AFRL-SR-BL-TR-00-

0169

REPORT DOCUMENTATION PAGE

Public reporting burden for this collection of information is estimated to average 1 hour per response, including the tim ... and maintaining the data needed, and completing and reviewing this collection of information. Send comments regarding this burden ... suggestions for reducing this burden to Washington Headquarters Services, Directorate for Information Operations and Reports, 1215 ... to the Office of Management and Budget, Paperwork Reduction Project (0704-0188), Washington, DC 20503

1. AGENCY USE ONLY (Leave blank)	2. REPORT DATE	3. REPORT TYPE AND DATES COVERED
	3/7/2000	Final

4. TITLE AND SUBTITLE

Spatial Soliton Interactions for Photonic Switching

Part 1

5. FUNDING NUMBERS

AFOSR/BMDO
F49620-96-1-0431

6. AUTHOR(S)

Kelvin H. Wagner and Steve Blair

7. PERFORMING ORGANIZATION NAME(S) AND ADDRESS(ES)

University of Colorado at Boulder
Optoelectronic Computing Systems Center
Campus Box 525
Boulder, CO 80309

8. PERFORMING ORGANIZATION REPORT NUMBER

N/A

9. SPONSORING / MONITORING AGENCY NAME(S) AND ADDRESS(ES)

Dr Alan Craig
AFSOR, Bldg 410
110 Duncan Ave, Suite B115
Bolling AFB, Washington DC 70332

10. SPONSORING / MONITORING AGENCY REPORT NUMBER

11. SUPPLEMENTARY NOTES

Companion report is F49620-95-1-0432

20000503 094

12a. DISTRIBUTION / AVAILABILITY STATEMENT

Full version of both reports available online at
http://optics.colorado.edu/~kelvin/links/soliton_report.ps.gz

UL

12b. DISTRIBUTION CODE

UL

13. ABSTRACT *(Maximum 200 Words)*

High-bandwidth optical communications will greatly benefit from optical switches since they could eliminate the optical/electronic conversion. Optical logic gates allowing data regeneration, gain, cascadability, would allow even more complex all-optical routing functions. In this work we report on an in-depth study of an optical logic gates based on spatial and spatio-temporal solitons. Optical solitons that propagate long distances without change, act as the natural carrier of binary data due to their stability to perturbations and intrinsic threshold. The non-diffracting nature of spatial optical solitons lends to their use in a class of angular deflection logic gates in which a weak signal can alter the propagation of a strong pump in order to change the device state from high to low, thereby implementing a controlled inverter which is cascadable to produce logically-complete, multi-input NOR.

Reduced forms of the multi-dimensional, nonlinear spatio-temporal wave equation are solved numerically to study the spatial collision and dragging interactions between orthogonally-polarized spatial solitons and spatio-temporal solitary waves. These three-terminal angular deflection gates, provide complete logic-level restoration, fanout greater than two with large noise margin, and cascadability. In addition, the spatio-temporal logic gates are expected to have pJ switching energies using enhanced nonlinear media, and ps switching times through temporal pipelined operation.

14. SUBJECT TERMS

Photonic switching, optical logic, nonlinear optics, optical solitons, spatiotemporal solitons, mulitple scales, derivation, nonlinear wave equation

15. NUMBER OF PAGES

16. PRICE CODE

17. SECURITY CLASSIFICATION OF REPORT	18. SECURITY CLASSIFICATION OF THIS PAGE	19. SECURITY CLASSIFICATION OF ABSTRACT	20. LIMITATION OF ABSTRACT
Unclassified	Unclassified	Unclassified	UL

NSN 7540-01-280-5500

Standard Form 298 (Rev. 2-89)
Prescribed by ANSI Std. Z39-18
298-102

DTIC QUALITY INSPECTED 3

Contents

I AFOSR Final report F49620-96-1-0431 3

1 Introduction, Motivation and Background 4
- 1.1 Outline . . . 4
- 1.2 Applications in Switching and Computing . . . 5
  - 1.2.1 Optical Communications Networks . . . 5
  - 1.2.2 Digital Optical Computing and Processing . . . 6
- 1.3 Requirements for Digital Switching and Logic Devices . . . 7
  - 1.3.1 Switching Devices . . . 7
  - 1.3.2 Logic Devices . . . 7
  - 1.3.3 Optical Devices . . . 9
- 1.4 Digital Optical Switching and Logic Devices . . . 9
  - 1.4.1 Nonlinear Directional Coupler . . . 9
  - 1.4.2 Kerr Gate . . . 13
  - 1.4.3 Nonlinear Optical Loop Mirror . . . 18
  - 1.4.4 Terahertz Optical Asymmetric Demultiplexor . . . 20
- 1.5 Optical Soliton Logic Devices . . . 23
  - 1.5.1 Temporal Soliton Dragging Gate . . . 24
  - 1.5.2 Angular Deflection Gate based on Spatial Soliton Dragging . . . 27

2 Optical Solitons 33
- 2.1 Historical Background . . . 33
- 2.2 Preliminaries . . . 35
- 2.3 1-D Spatial Optical Solitons . . . 35
  - 2.3.1 The Non-Paraxial Fundamental Soliton . . . 37
  - 2.3.2 The Paraxial Fundamental Soliton . . . 37
- 2.4 1-D Temporal Optical Solitons . . . 42
  - 2.4.1 The Non-SVEA Fundamental Soliton . . . 43
  - 2.4.2 The SVEA Fundamental Soliton . . . 44
  - 2.4.3 Higher-Order 1-D Temporal NLS Solitons . . . 48
  - 2.4.4 Higher-Order Temporal Effects . . . 49
- 2.5 2-D and 3-D Spatio-Temporal Solitary Waves . . . 53

3 The Vector Nonlinear Wave Equations 60
- 3.1 Derivation of the Vector Nonlinear Helmholtz Equation . . . 61
  - 3.1.1 The Linear Material Polarization . . . 64
  - 3.1.2 The Third-Order Nonlinear Material Polarization . . . 67
  - 3.1.3 The Fifth-Order Nonlinear Material Polarization . . . 70
  - 3.1.4 The Vector, Nonlinear Helmholtz Equation . . . 71
- 3.2 Multiple-Scales Derivation of the Nonlinear Wave Equation . . . 73
  - 3.2.1 Multiple-Scales in Maxwell's Equations . . . 73
  - 3.2.2 Derivation of the (3+1)-D Higher-Order Vector Nonlinear Schrödinger Equation . . . 77
  - 3.2.3 Reduction to (1+1)-D Spatial and (2+1)-D Spatio-Temporal Equations . . . 90

4 Spatio-Temporal Diffraction and the Split-Step Numerical Method **93**
4.1 Linear Spatio-Temporal Diffraction . . . 93
4.1.1 Spatio-Temporal Group-Velocity Space . . . 96
4.1.2 Linear Spatio-Temporal Propagation . . . 99
4.1.3 The Linear Terms in the Higher-Order NLS equation . . . 99
4.2 Derivation of the Split-Step Method . . . 103
4.2.1 Nonlinear Spatial Propagation . . . 105
4.2.2 Nonlinear Spatio-Temporal Propagation . . . 105
4.3 Implementation and Accuracy of the Split-Step Method . . . 107
4.3.1 (1+1)-D Spatial . . . 108
4.3.2 (2+1)-D Spatio-Temporal . . . 111

5 Conclusions **116**

A Symmetry Properties of the Nonlinear Susceptibility Tensors **130**
A.1 The Intrinsic Permutation Symmetry . . . 130
A.2 Symmetries of $\chi^{(3)}$ . . . 131
A.2.1 Nonlinear Refraction . . . 132
A.2.2 Third-Harmonic Generation . . . 134
A.2.3 Third-Harmonic Downconversion . . . 135
A.3 Symmetries of $\chi^{(5)}$ - Quintic Nonlinear Refraction and Three-Photon Absorption . . . 136

B The Raman Response Function and Raman Susceptibility **138**
B.1 Origin of The Raman Response . . . 138
B.2 The Raman Gain Spectrum . . . 140
B.3 The Raman Susceptibility . . . 145

C Derivation of the (2+1)-D Vector Nonlinear Schrödinger Equation for a Slab Waveguide **150**
C.1 Order ε - Effective Indices and Phase Velocity . . . 152
C.2 Order ε^2 - Group Velocity . . . 154
C.3 Order ε^3 - Coupled Nonlinear Schrödinger Equations . . . 157

D Optical Properties of Fused Silica **164**
D.1 Properties of Bulk Fused Silica . . . 164
D.2 Properties of Glass Waveguides . . . 167
D.2.1 Derivation of TE Mode . . . 168
D.2.2 Derivation of TM Mode . . . 169
D.2.3 Linear Waveguide Dispersion Properties . . . 170

Part I

AFOSR Final report F49620-96-1-0431

Chapter 1

Introduction, Motivation and Background

This thesis deals with the topic of ultrafast, all-optical switching and logic using spatial and spatio-temporal solitons. The main focus is on the accurate analytical and numerical modeling of the interaction among solitons in geometries that allow for logically-complete, cascadable logic gates with fanout and level restoration. Detailed modeling will assist in subsequent experimental investigation by identifying regions of stability, robust operation and reliability, and candidate material systems.

The work in this thesis makes significant contributions in the areas of fundamental nonlinear spatio-temporal propagation and optical switching and logic. The first contribution is the result of a multiple-scales derivation directly from Maxwell's equations, which results in a first-order, multi-dimensional, vectorial differential equation that is accurate beyond the standard paraxial and slowly-varying envelope and amplitude approximations. This result is fundamental to the studies of this thesis and will have application in other areas as well, such as optical communications, short-pulse passively mode-locked lasers, and atmospheric pulse propagation.

The second contribution arises from the systems-level approach taken to optical switching and logic. Most optical switching technologies do not satisfy the basic requirements for a logic gate, thereby rendering them of little use in applications beyond simple, single-stage switching operations. The novel logic gates studied here satisfy the necessary requirements and thus have the potential to make an impact in areas of ultra-high speed switching and logic systems. The desirable properties of these logic gates are facilitated by the non-diffracting and/or non-dispersing nature of optical solitons.

1.1 Outline

The remainder of this chapter briefly presents background in device requirements and optical switching and logic. Section 1.2 provides motivation and a brief overview of promising applications for optical logic. Section 1.3 covers generic requirements for switching and logic devices and additional specific requirements for optical devices. A brief review of other contemporary optical switching devices and their shortcomings is presented in section 1.4. Logic devices which specifically take advantage of the properties of optical solitons are discussed in section 1.5, which also provides an introduction to the optical soliton logic gates studied in this thesis.

Detailed background on optical solitons is given in Chapter 2. First, section 2.1 provides historical background in solitary wave and soliton phenomena. Section 2.2 covers some preliminary details that lead directly to the discussion of optical solitons and solitary waves. The following sections then discuss spatial (sec. 2.3), temporal (sec. 2.4), and spatio-temporal (sec. 2.5) optical solitons.

Chapter 3 derives the multi-dimensional vector wave equations necessary for the numerical simulations of the soliton-based logic gates presented in later chapters. Section 3.1 covers a standard treatment of a fully vectorial, nonlinear Helmholtz-type wave equation along with background on the linear and nonlinear susceptibilities. This second-order wave equation is unsuitable for the purposes of this thesis due to the difficulty in numerically propagating an initial field distribution because of the fast time and space scales in the equation. Instead, section 3.2 derives an asymptotic vector nonlinear wave equation directly from Maxwell's equations which is first-order in the propagation coordinate and depends only on the scales of the slowly-varying envelope, and is thus more suitable for numerical propagation. The importance of the results obtained in this chapter arises from the higher-order nature of the derived equation, which extends beyond the approximations made in the well-known multi-dimensional nonlinear Schrödinger (NLS) equation, resulting in the capability to describe propagation of vector optical field envelopes with very broad spectral content in both the spatial and temporal frequency domains, including the effects of higher-order nonlinearities.

Chapter 4 describes the split-step numerical method used to solve the vector nonlinear wave equations. The basis of

this method is to treat linear and nonlinear (inhomogeneous) propagation in separate steps, performing linear propagation in its natural Fourier domain and nonlinear propagation in the real-space domain. For a small step size, this splitting is a good approximation. Section 4.1 covers multi-dimensional linear spatio-temporal diffraction, which can be solved without approximation as an initial value problem. Noting that linear and nonlinear propagation are not separable, section 4.2 derives a split-step formulation which is approximately second-order accurate in step size. This formulation is then applied separately to (1+1)-D spatial and (2+1)-D spatio-temporal nonlinear propagation, to be used in later chapters. Finally, section 4.3 discusses the accuracy of the method as it applies to problems of later chapters.

The use of one-dimensional spatial soliton interactions for logic gates is presented in Chapter 5. The first section covers the basic soliton interaction geometries useful for three-terminal, restoring logic, noting that the collision and dragging geometries using orthogonally polarized solitons, which are of the general class of angular deflection gates, provide the best performance in terms of large gain with high contrast. Section 5.3 then examines the effects of linear and two-photon absorption on the propagation of a single spatial soliton and develops appropriate figures-of-merit for use in comparing the suitability of nonlinear materials for soliton logic gates. The collision and dragging logic gates are then compared in the presence of absorption using the material parameters of fused silica, where the spatial dragging gates generally perform better because of their shorter gate lengths. The final section (5.4) computes the transfer functions of the collision and dragging gates and determines the maximum fanout that these gates can provide in a cascaded system. The results of this chapter provide guidance for the spatio-temporal logic gates of the next chapter, which is of ultimate interest.

Logic gates based on the interactions between two-dimensional spatio-temporal solitary waves is the subject of Chapter 6, which have the potential for greater than THz switching rates with nJ to pJ switching energies. Section 6.1 discusses the propagation of a single spatio-temporal solitary wave with higher-order linear and nonlinear effects as derived in Chapter 4. This section shows numerically that stabilized solitary waves suitable for logic gates should exist. With these results, section 6.2 studies the vectorial interaction between these spatio-temporal solitary waves with emphasis on the dragging interaction. For completeness, section 6.3 presents results on cascaded logic. It is shown that the dragging logic gates can provide reasonable fanout in a cascaded, logically-complete, system, but also that, ultimately, the performance of the logic gate will be limited by the effects of Raman scattering.

Finally, Chapter 7 concludes, noting that this thesis provides the theoretical and numerical development that is necessary to study a novel class of all-optical logic gates. Numerical simulations have shown that these gates satisfy the system requirements that suggest their use beyond simple, single-stage operation, and paves the way for future theoretical and experimental work on ultrafast, all-optical logic systems.

1.2 Applications in Switching and Computing

The traditional advantages that optics hold over electronics are the inherent speed, parallelism, and lack of inductive or capacitive crosstalk, although crosstalk does occur to some extent in linear propagation due to scattering and diffraction, and in nonlinear propagation, which plays an important role in the topic of this thesis. These properties allow linear optics to map well onto problems in interconnection [1]. It is generally accepted that optical interconnects will replace electric transmission lines in many applications. Indeed, this is already occurring in long-haul communications networks and is expected to occur in short-haul and local-area networks as well. It is an open question to determine how far down the interconnect hierarchy this trend will reach, but it is fairly clear that it will extend to system level switching fabrics. In all of these cases though, the data is actually switched electronically, or under electronic control, and processed electronically.

It is less clear what role optics will play in switching and digital computing however. The soliton-based logic devices studied in this thesis are one approach to all-optical logic for switching and computing applications. Numerous all-optical switching and logic devices have been proposed, but none so far have reached the stage of practicality for real systems. There are certain minimum requirements for a logic device, and many of the optical approaches to logic fail to meet them. These requirements are discussed in section 1.3 and some contemporary optical switching devices and their failings are discussed in section 1.4. A clear understanding of these failings aids the present study of optical soliton-based logic devices. As section 1.5 explains, the soliton devices completely satisfy the fundamental requirements (and most of the practical requirements as well) for digital logic [2,3] and might succeed where the other optical approaches have failed.

The following sections discuss two general areas for which restoring, cascadable logic gates, such as those studied in later chapters of this thesis, might find widespread application.

1.2.1 Optical Communications Networks

With the advent of high-bandwidth optical communications [4], high-speed switching technology becomes a necessity. Because information will be transmitted optically, it makes sense to explore optical technologies and devices to perform (or at least assist

in) the switching necessary to multiplex, demultiplex, and route information to the correct destination. Future bandwidth needs will be too great for an electronic-only solution to the switching problem. An advantage of optical devices in communications systems is the ability to switch and/or perform logic at the bit rate. This means that switching and logic operations are performed at and scale with the rate of incoming data, which is especially important in Tb/s communications switching and routing applications. Conversely, interconnected electronic gates cannot arbitrarily scale with the data rates and may ultimately be limited to speeds of about 50 Gbit/s [5].

Optical switching and logic devices are well suited for time-division multiplexed (TDM) data transmission [6], in which many low bandwidth channels are interleaved into individual time slots within a single high bandwidth channel. Here, the aggregate data rate may exceed 100 Gb/s [7], which is well beyond the performance expectation of practical, low power, electronic or optoelectronic switching networks. Therefore, at the very least, optical switching technology will find use in the intermediate processing layer in which the individual channels are optically separated (demultiplexed) from the single, high-speed transmission channel, for subsequent processing in the electronic/optoelectronic domain. An additional area of use is in data regeneration within an optical transmission line, which requires an optical logic gate. Given sufficient noise margins, an optical logic gate regenerates a noisy or attenuated data stream with fresh pulses that are derived from a power supply or clock, such that timing, amplitude, shape, etc., are completely restored. This type of all-optical repeater may eliminate the need for high-speed, high-power electronic repeaters in long-haul transmission.

Currently, the most popular multiplexing technique for long-haul communications and local-area optical networks is wavelength division multiplexing (WDM), in which each low bandwidth source channel is assigned a slot in the optical frequency spectrum. WDM has the advantage that multiplexing and demultiplexing can be performed by spectrally selective, passive, optical elements. However, due to the difficulties in developing a large array of stable wavelength sources, the individual channels in a WDM system may exceed data rates of 10 Gb/s [8,9], which may be of sufficient bandwidths that other advantages of optical switching and logic devices, such as the elimination of the optoelectronic conversion process [10], potentially lower power, and the use of deep optical circulating delay lines [11] for contention resolution, may play a role in the choice of implementation technology.

More complex operations are required in packet switched optical networks [10, 12]. In these networks, at each node, a packet header is decoded, which determines the direction in which to route the packet. Header recognition is a simple digital correlation operation, but must be performed at the bit rate. Typical implementations based on optical switches [13] perform this operation in parallel, which results in a $1/N$ loss where N is the number of bits in the header. In order to reduce the latency at each node and avoid the fanout loss, a digital comparator, or shift register, could be used instead, based on optical logic gates. In addition, optical logic could be used for contention resolution, real-time encryption/decryption, and other complex tasks as well. Therefore, intelligent digital optical processing may play a significant role in the development in the next generation of high-speed optical communications networks.

1.2.2 Digital Optical Computing and Processing

Determining what role optics should play in general-purpose computing is an open question. The technological lead, resources, and infrastructures that electronics enjoy may be insurmountable for general-purpose optical computing. Even a compelling optical technology may not be enough to impact the future of digital computing, but there is potential in niche areas which are discussed in this section.

Simple digital optical logic circuits have been demonstrated [14, 15] and proposed [16], which pave the way for more complex systems. However, many of these studies have been based on optical switches or gates that do not completely satisfy the requirements for digital logic. For example, the nonlinear Fabry-Perot etalon [17] is a two-terminal device which must be biased about an operating point with a holding beam and is very sensitive to variations in device parameter (i.e. the transfer characteristics vary from device to device). All of these factors preclude their use in complex systems. The logic gates studied in this thesis, on the other hand, do not suffer from these problems and could serve as fundamental building blocks in more complex systems.

In the absence of high space-bandwidth optical interconnections, bit-serial computation and signal processing [18] is a promising application area, especially when the problems of interest can be processed in a highly pipelined manner [19]. General purpose optical computers [20] have even been demonstrated using the bit-serial approach. One potential limitation for ultra-fast digital optical computing is the memory store. It has been shown, however, that an optical delay line can be used to implement a general machine [16], at the cost of increased latency. These tradeoffs are based on the transformations of computational origami [21]. Even more computational capacity can be realized with the combination of optical logic gates with optical interconnection, for which the power of the interconnection network allows for the efficient mapping of problems that would be difficult to process electronically [22].

1.3 Requirements for Digital Switching and Logic Devices

Routing switches and logic elements must possess certain properties in order to function properly within a system. The major distinction made here between switching elements and logic gates is that switching elements physically direct electrons or photons from one or more input ports to one or more output ports, while logic gates replace electrons or photons on the input ports with "new" electrons or photons derived from a power supply which then appear at the output ports. The requirements for a switching device are much less stringent than those for a logic device and will be discussed first. Additional requirements for an optical logic device are discussed in the following section.

1.3.1 Switching Devices

Optical routing switches are typically used just in the first switching stage to reduce data bandwidth to a level that electronics can handle in subsequent stages. These switching elements use a control to physically direct light from one or more input ports to one or more output ports and thus can be used to implement multiplexing and demultiplexing functionality. The routing decision is based either on the intensity of the signal inputs or by the presence of an externally derived control which is independent of the switching fabric. Therefore, the control is typically not of the same format as the data, meaning that the output of the switch cannot directly serve as the control for another switch [3]. As a result, this type of routing switch has fewer requirements than a logic gate.

The most important requirement of a switching device is high contrast operation. In binary transmission, the contrast determines the threshold level which separates the high and low states. Higher contrast gives larger noise margin, resulting in lower bit-error-rate (BER). For the output of a switching element, the overall contrast depends both on the contrast of the data stream (the difference in signal level between the two binary states which depends on the modulation ratio at the input of the transmission line and on the transmission line itself) and the contrast of the switching operation.

Another important requirement is switch transparency. If the switch is lossy or only a small fraction of the input is diverted to the output by the switching action, then high-speed, single-shot detection may become impossible, resulting in information loss. This does not mean that the switching operation must provide gain, though. For high-contrast output, saturation of an external amplification stage can be used to restore the data signal levels, but the gain recovery time may limit the data rate and introduce inter-symbol interference, the contrast at the output of the amplifier may be reduced, and complete logic level restoration (as discussed later for optical devices) is not obtained. The amount of gain is also limited due to amplified-spontaneous emission (ASE) noise, which increases the noise floor.

Routing switches do not have signal level restoration (in the absence of external amplification or level shifting) and the outputs may degrade due to loss or crosstalk and therefore BER may suffer from a long cascade of switches. If data pass through many levels of switching, such as in a multi-level implementation of an N:N crossbar or the binary tree structure required for 1:N or N:1 multiplexors or demultiplexors constructed from 1:2 or 2:1 switches, then gain and level restoration as mentioned previously may be a necessity, subject to the limitations discussed in addition to ASE noise. Three-terminal operation also becomes necessary when many levels of switching elements are used such that the operation of the switch in unidirectional, which prevents any light entering the output ports from affecting the operation of the switch.

Therefore, in order to implement more complex, multi-level switching fabrics, or to handle data-dependent (i.e. self-routing) switching operations, switching elements must have the additional properties and fulfill the more demanding requirements of a logic gate. It is in these applications that most all-optical switching devices are inadequate, as discussed in section 1.4.

1.3.2 Logic Devices

A digital logic gate performs a Boolean operation on one or more binary inputs. All inputs and outputs are of the same physical format thus allowing control to be distributed throughout the switching fabric [3] such that one data stream can control another. The logic gate completely restores signal integrity and timing by replacing the electrons or photons at the input with new electrons or photons from the power supply that go to the output.

Logic levels (i.e. 0 or 1 in digital logic) are physically represented by signal levels, which may be voltage or current for electronics; or for the representationally richer case of optical logic, amplitude, phase, polarization, or color, and are differentiated by a threshold nonlinearity. Information is carried by the logic level and is determined by the interpretation of the signal level (based on the threshold). Since the signal level can be altered during a logic operation, small noise or loss can accumulate throughout the computation and cause information loss. A digital representation of information avoids this degradation if the signal level is restandardized at each step [23]. Restandardization means that the signal levels are restored to values (that are the same throughout the system) which represent valid logic states. As a result, a small deviation about a valid logic level propagates at most one stage and the logic level remains intact (within the allowable noise margin). The is termed logic level restoration.

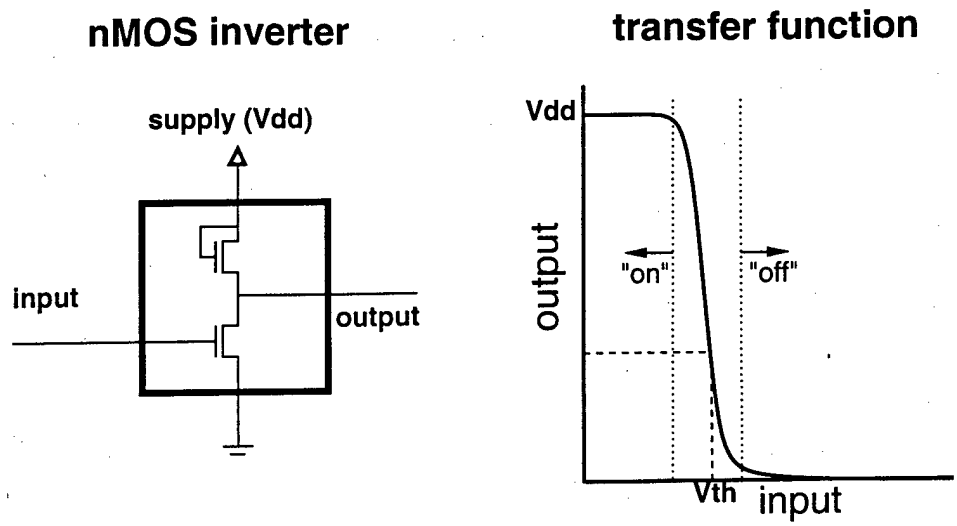

Figure 1.1: nMOS inverter circuit and associated transfer function. Near the threshold voltage is a region of small-signal gain. Large-signal gain is also provided ($V_{dd} > V_{th}$) and the high and low output states are saturated.

The properties required by a digital electronic [24] or optical [25] logic device are well known. Perhaps the most important requirements, upon which many other requirements depend, are gain, saturation, and threshold. These characteristics are illustrated in Figure 1.1, which shows the sigmoidal input-output relationship for a simple nMOS inverter. At the most fundamental level, a region (typically near the input threshold) of differential or small signal gain in the input-output transfer function, where a small change in the input produces a large change in the output, is required (but not sufficient) for a restoring logic gate [26]. Small-signal gain provides sharp switching characteristics and allows for low modulation depth on the input signal biased about the threshold level to produce high contrast switching. Outside the linear region of small-signal gain, saturated levels are key to providing large noise margin by attenuating small variations in the input about valid logic levels (i.e. inputs lying within the "on" and "off" regions shown in the figure), thus producing little change in the output.

Restoration of the logic level prevents accumulation of errors due to attenuation or crosstalk by providing fresh gate output levels directly from the power supply. In the case of an optical gate, logic level restoration must include, in addition to power levels, beam shape and position, pulse duration, color, polarization, and timing [25]. These levels are standardized throughout the entire system typically by the common power supply and ground. Standardization is possible because small-signal gain and saturated levels in the nonlinear transfer function allow for a wide tolerance to the variation in operational characteristics of the devices in the system [24].

Large-signal gain means that the output of the gate is larger than the input required (at least threshold) to switch the gate. Without large-signal gain, fanout, in which the output of a gate provides inputs to many gates in order to implement arbitrary logic functions, is impossible. Most optical logic gates cannot intrinsically provide large-signal gain, and in fact, the output is typically much smaller than the input. Although a separate, external amplification stage can be used, this may limit the bit rate and result in reduced contrast and increased BER when the amplifier noise exceeds the device noise margins. A logic gate with intrinsic gain, in which a small input controls a large power supply, does not suffer this source of noise.

Additional requirements for synthesis of arbitrary logic and switching are logical completeness and cascadability. A complete set of logic functions must include inversion [24]. Inversion is a basic function of MOSFET electronics and the inverter structure forms the basis towards implementing more complex Boolean operations such as multi-input and logically complete NOR. Cascadability means that the output of one gate can directly drive the input to the next and allows the direct implementation of multi-level logic. Logic level restoration and inputs and outputs of the same format are therefore crucial to allowing cascadability.

The most successful logic devices have three orthogonal ports (which can be separate in time, space, wavelength, or polarization) and input-output isolation. A three-terminal device, such as an electronic transistor, ensures that the output of the gate depends only on the inputs and the output does not perturb the operation of the gate [24]. This input-output isolation results in one-way operation and prevents downstream noise which enters the output port from affecting the operation of the gate. There are many examples of two-terminal devices in optics. The problem with two-terminal devices is that they work equally well in either direction [25]. The classic examples are the laser [27] (a two-terminal device with gain) and nonlinear Fabry-Perot etalon [17] which, when critically biased [28], can switch either through the input or through an unwanted reflection back into

the output.

1.3.3 Optical Devices

The main additional requirement for an optical logic device is operation independent of the relative phase between the beam or pulse of light that induces the switching operation and the one that is switched. Phase-sensitivity is not an issue in electronic devices since the phases of the interacting electrons are continuously randomized from phonon collisions [3]. Phase insensitive logic operation is critical in optics because of the coherence of laser sources and since phase is difficult to control in complex systems due to the small optical wavelength. An optical logic gate can be made insensitive to relative phase by using the interaction between optical inputs of orthogonal polarizations or inputs that are spectrally resolved in angle or frequency such that there is no linear interference, but there may be nonlinear interference.

Material nonlinearity is a necessary requirement in order to implement an optical logic gate. The desire for a low loss, ultrafast gate opposes the desire for low switching energy which can be achieved via the use of resonant nonlinearity. Because of the large loss associated with resonant nonlinearity, most ultrafast optical switching and logic gates utilize a much smaller nonresonant nonlinearity. A detailed exploration of the effect of loss on optical soliton logic gates is presented in section 5.3.

It is also desirable for the nonlinear coupling between the interacting optical fields to depend only on intensity, but this can only be guaranteed in certain situations, such as with orthogonal circular polarizations in bulk isotropic media [2, 29]. Other situations can reduce phase-dependent nonlinearity by using the accumulating phase difference between orthogonally polarized linear eigenmodes of naturally or artificially birefringent media to wash out the phase-dependent nonlinear effects.

1.4 Digital Optical Switching and Logic Devices

Some of the most promising all-optical devices for ultrafast switching and logic are the nonlinear directional coupler (NLDC), optical Kerr gate, nonlinear optical loop mirror (NOLM) or Sagnac gate, and the terahertz optical asymmetric demultiplexor (TOAD) and its variants. Even though these devices may possess a region of small-signal gain, only the NLDC has saturated levels in the device input-output curve and none intrinsically provide a robust way to obtain large-signal gain. As a result, the main requirements for these devices are those of a single-stage switch, the most important of which is high contrast, which results from complete switching.

In many of these devices, complete switching occurs upon accumulation of a π differential nonlinear phase shift. This phase is between two independent components of the same beam or pulse and is not to be confused with the relative phase between control and data as discussed earlier on phase-insensitive operation. The accumulated nonlinear phase shift can be written generically

$$\Delta\Phi = \delta \frac{2\pi n_2}{\lambda_f} |A|^2 d, \tag{1.1}$$

where n_2 is the nonlinear Kerr coefficient defined by the total index $n = n_0 + n_2 |A|^2$, λ_f is the free-space wavelength, d is the interaction length, A is the electric field amplitude of the light that induces the switching operation, and δ is a constant factor determined by the nonlinear interaction. The phase shift is proportional to the nonlinear index, the peak intensity, and the interaction length, and can be made large by an increase in any one of these parameters. At the output of the device, this phase shift manifests itself as an amplitude change, either as a rotation of the polarization followed by an analyzer or due to coherent beam combining at an output coupler.

Even though silica has a small nonlinear index for example (see Appendix D), low loss fiber can provide very long interaction lengths d with tight transverse confinement [30], thus making fiber based switching devices very popular [3]. Because switching occurs within the fiber, the control and data must be of different wavelengths and/or polarizations in order to avoid the power loss in coupling in the absence of phase locking and in order to discriminate the switched data from the control at the output. As a result, operation independent of the relative phase between data and control is achieved, but group-velocity or birefringence walkoff limits the interaction length (the walkoff must be less than the pulse durations) and therefore the data rate. These devices are now discussed individually in some detail.

1.4.1 Nonlinear Directional Coupler

This nonlinear switching device is based on the directional coupler as shown in Figure 1.2. The linear directional coupler relies on the coherent interaction between two waveguides placed near each other. The coherent interaction is due to evanescent overlap between fields confined within the individual waveguides and results in periodic energy exchange between the guides. The presence of nonlinearity frustrates this coherent exchange by detuning the waveguides and can result in intensity-dependent

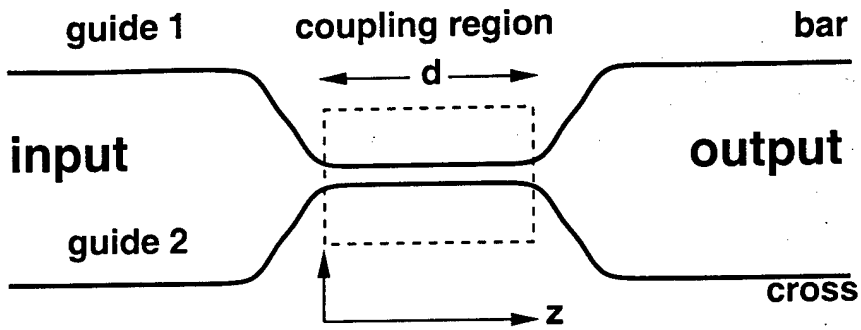

Figure 1.2: Directional coupler. In linear operation, energy is exchanged periodically between guides in the coupling region. Nonlinear operation can frustrate this coupling, resulting in controlled switching.

switching between the output ports. The NLDC was originally proposed [31] as an alternative to bistable switching devices such as the nonlinear Fabry-Perot etalon. More recently, it has received much attention, particularly in the capacity of a prototype all-optical switching device [32], and for ultrafast optical demultiplexing [33].

In the limit of weak coupling between identical guides, the coupled mode equations for the NLDC are

$$-i\frac{\partial A_1}{\partial z} = \kappa A_2 + k_f n_2 |A_1|^2 A_1 \tag{1.2}$$

$$-i\frac{\partial A_2}{\partial z} = \kappa A_1 + k_f n_2 |A_2|^2 A_2, \tag{1.3}$$

where κ is the linear coupling constant, and A_1 and A_2 represent the electric field amplitudes in guides 1 and 2 respectively. Assuming no nonlinearity, the amplitude in each guide can be written

$$\frac{\partial^2 A_1}{\partial z^2} = -\kappa^2 A_1 \quad \Rightarrow \quad A_1(z) = a_1 \cos(\kappa z) + b_1 \sin(\kappa z) \tag{1.4a}$$

$$\frac{\partial^2 A_2}{\partial z^2} = -\kappa^2 A_2 \quad \Rightarrow \quad A_2(z) = a_2 \cos(\kappa z) + b_2 \sin(\kappa z). \tag{1.4b}$$

With the boundary conditions $A_1(0) = A_0$ and $A_2(0) = 0$, the coefficients $b_1 = a_2 = 0$, leading to the result

$$A_1(z) = A_0 \cos(\kappa z) \tag{1.5a}$$

$$A_2(z) = A_0 \sin(\kappa z). \tag{1.5b}$$

The output intensities at the bar and cross ports are given by

$$I_1(d) = I_0 \cos^2(\pi d / L_{\text{coh}}) \tag{1.6a}$$

$$I_2(d) = I_0 \sin^2(\pi d / L_{\text{coh}}). \tag{1.6b}$$

where the coherence length is defined $L_{\text{coh}} = \pi/\kappa$ and is the length over which light is completely coupled from one guide to the other and back. Therefore, for a half-beat length coupler with $d = L_{\text{coh}}/2$, input into guide 1 emerges at the output from guide 2 (cross state).

In nonlinear operation, using the nonlinear coupled-mode equations, the fractional intensity in each guide is written [31]

$$\frac{I_1(d)}{I_0} = \frac{1}{2}\left\{1 + \text{cn}\left(\frac{2\pi d}{L_{\text{coh}}}, \left[\frac{I}{I_{\text{crit}}}\right]^2\right)\right\} \tag{1.7a}$$

$$\frac{I_2(d)}{I_0} = \frac{1}{2}\left\{1 - \text{cn}\left(\frac{2\pi d}{L_{\text{coh}}}, \left[\frac{I}{I_{\text{crit}}}\right]^2\right)\right\}, \tag{1.7b}$$

where cn() is a Jacobi elliptic function. As before, this solution assumes that there is no light initially launched into guide 2. The critical intensity is defined as

$$I_{\text{crit}} = \frac{\lambda_f}{n_2^I L_{\text{coh}}}, \tag{1.8}$$

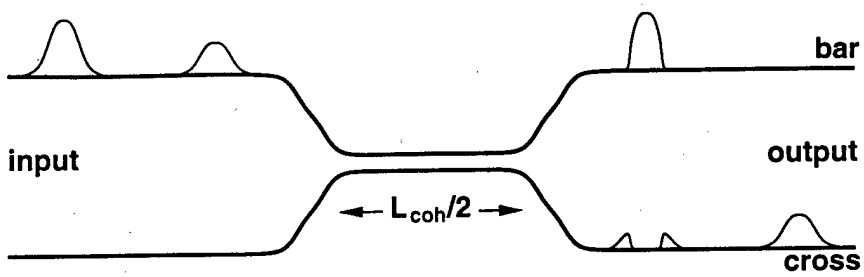

Figure 1.3: Operation of half-beat length nonlinear directional coupler. For low power, or linear, operation, the input pulse exits the cross port (guide 2) while in nonlinear operation, the central portions of the pulse, which exceed the critical intensity, exit the bar port (guide 1) with the wings exiting the cross port.

and represents the input intensity for which the light is divided equally between the two output ports [31]. For a half-beat length coupler, the critical intensity results in a π phase shift for the field in guide 1, and $\delta = 1$ in equation 1.1. Above the critical intensity, the fraction of light exiting the bar port increases towards unity. This two-terminal device performs a switching operation since photons from the data stream are directed into one of two output ports.

A half-beat length NLDC is shown schematically in Figure 1.3, where a low-power data pulse couples to the cross port while a high-power data pulse remains in guide 1 (bar state). The high-power case can be understood intuitively by considering the nonlinear increase in the core index which more strongly guides the light, thus detuning the coupler. Notice that only the central portion of the high-power pulse exceeds the critical intensity and remains in guide 1. This effect is called partial switching, or pulse breakup, and is characteristic of many optical switching devices and results in reduced integrated energy contrast [33]. In fact, partial switching is a problem with all of the non-soliton devices discussed in this section. Solutions to this problem are the use of square pulses [34] such that the intensity is constant across the pulse duration, or the use of temporal solitons [35–37], which propagate unchanged and tend to switch as a unit because of uniform phase across the pulse profile [38].

Figure 1.4 shows a plot of the switching fraction into the bar output port versus normalized peak pulse intensity launched into guide 1 for the half-beat length NLDC. The solid curve shows the fraction of the light that remains in the bar state assuming a constant intensity square-top pulse as given directly by equation 1.7a. The curve for the soliton case has similar shape with sharp switching characteristics [35], but the switching intensity threshold is about twice the critical intensity because the induced nonlinear phase is half that of the plane wave case, as shown in section 2.2. The dashed curve shows the light fraction assuming a non-soliton $\text{sech}^2()$ input intensity profile and takes into account partial switching which leads to reduced contrast operation as indicated by the greatly reduced switching fraction. In either case, at low input levels, all of the light switches over to the cross port, while at high inputs, most of the light exits the bar port.

Direct cascadability can also be addressed using Figure 1.4, where the dotted line represents the input threshold for which the output of the bar port exceeds I_{crit}. Figure 1.5, which shows the transfer function for each port of the device, provides the same information more clearly. As shown in the figure, for a square-top pulse, an input intensity greater than 1.1 I_{crit} is required to exceed the threshold intensity at the bar port. In this case, the output of the bar port can be used as the input to another device resulting in 50% switching of that second device. Therefore, much higher inputs than 1.1 I_{crit} are necessary to cascade to another device, but, due to the lack of large-signal gain and in the absence of external amplification, any optical losses in the system will eventually result in the degradation of the signal level to the point that switching ceases. The situation is worse in the case of a nonuniform pulse. Here, a peak input intensity of greater than 1.6 I_{crit} is required for at least 50% switching of a subsequent device. Indeed, because of partial switching, attempts at cascading two such devices have met with limited success [39]. A final point to note is that when designed as a half-beat-length coupler in linear operation, the NLDC transfer function has quasi-saturated levels which attenuate fluctuation in the input level and allow for some noise margin.

As described so far, the NLDC is a two-terminal device whose switching operation is determined by the intensity of the input signals. A three-terminal version can also be constructed by using a high-power control pulse to switch a low-power data pulse as shown in Figure 1.6, but this device is not directly cascadable either due to the lack of large-signal gain and inconsistent signal representation (using different wavelengths). The control pulse must be of different central frequency or polarization in order to avoid phase-sensitivity and to extract the data at the output with zero background. Experimental demonstrations have used different frequencies because of the large difference in coherence lengths between orthogonal polarizations [33]. There are still partial switching problems if the control pulse does not have constant amplitude. An additional problem is dispersive walkoff, which will be discussed in more detail for the Kerr gate. A recent demultiplexing demonstration [33] used a longer control pulse length and allowed the data pulse to walk-through the control to achieve complete switching, and therefore, high contrast. Lengthening of the control pulse means that the separation between data pulses needs to be larger, thereby reducing

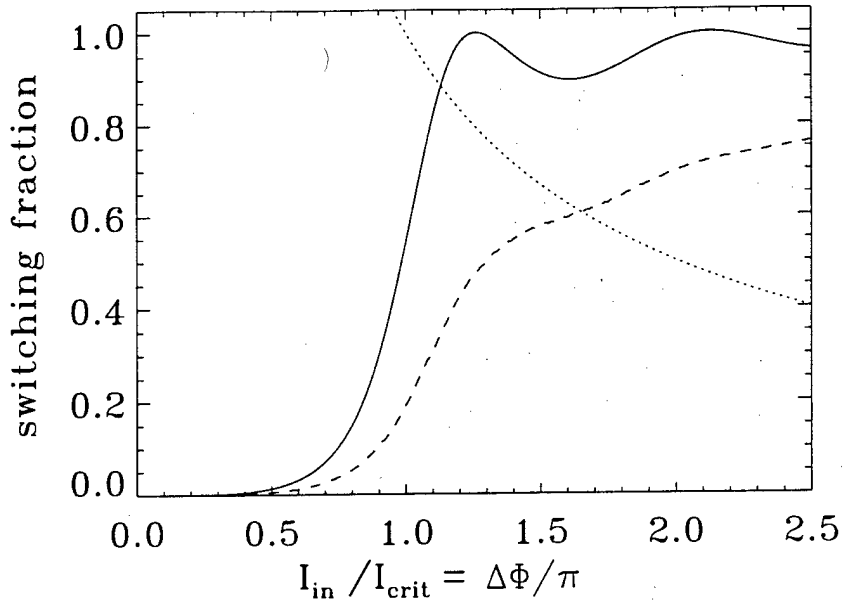

Figure 1.4: Switching fraction into the bar port for a half-beat length NLDC versus input peak intensity. The fraction into the cross port is inverse of the curves shown. The solid curve is for a square-top pulse while the dashed curve is for a non-soliton $\text{sech}^2()$ intensity profile pulse indicating incomplete switching. The dotted curve shows the threshold for which the bar state output exceeds the critical intensity.

the data rate and increasing the switching energy, but also allows for some tolerance to timing jitter.

Because of the region of small-signal gain shown in Figure 1.5, it is possible to obtain large-signal gain with this device, based on the process of light-induced symmetry breaking [40], as originally studied using a phase-dependent interaction between light input into each port. The input into port 1 is biased with a "power supply" or clock pulse near the critical intensity, which is an unstable operating point. Due to small-signal gain, a weak control input into port 2 is amplified, resulting in complete switching into either the bar or cross state depending on the relative phase between the inputs in ports 1 and 2. For a multiple of 2π relative phase, the inputs add constructively and the output emerges from the bar state, while for π relative phase, the inputs add destructively causing the output to emerge from the cross state. This switching is critically dependent on the relative phase between the data and control, and therefore cascadability may be difficult to achieve if the phase of the output depends on the intensity of the inputs. It also appears that such a device would be sensitive to variation in waveguide parameters.

A phase-independent version of this three-terminal device with gain can be realized using weak amplitude to initiate switching into the bar port, thereby providing a controlled inversion operation at the cross port. This device must therefore meet the more demanding requirements of a logic gate. Again, if port 1 is biased by a clock pulse at some level less than the critical intensity such that the clock exits the cross port, then additional light of orthogonal polarization or color entering port 1 can activate switching into the bar port. Therefore, logic level restoration is obtained since only the power supply or clock pulse (from the cross port) is passed to subsequent gates when the control pulse is blocked by an analyzer or spectral amplitude filter. For instance, referring to Figure 1.5, for bias in port 1 of 0.8 I_{crit}, then an additional contribution of 0.6 I_{crit} (for cross-phase modulation coefficient of 2/3) can cause complete switching into the bar port. This example illustrates a gain of 1.3, which is the maximum for the standard device and may not be achievable in practice because there is strong variation in switching intensity with power supply and device variations will not allow for level standardization. It is clear that the larger the small-signal gain, the less the input required to switch the state of the device. Because of the ripples in the transfer function, a control pulse of intensity 1.2 will allow for an output level of 0.2 at the cross port, thereby significantly reducing the contrast of the gate. When the switching is incomplete, though, the small-signal gain may be less than unity, precluding the possibility for large-signal gain, as illustrated by the transfer function for the non-soliton $\text{sech}^2()$ (in intensity) pulse.

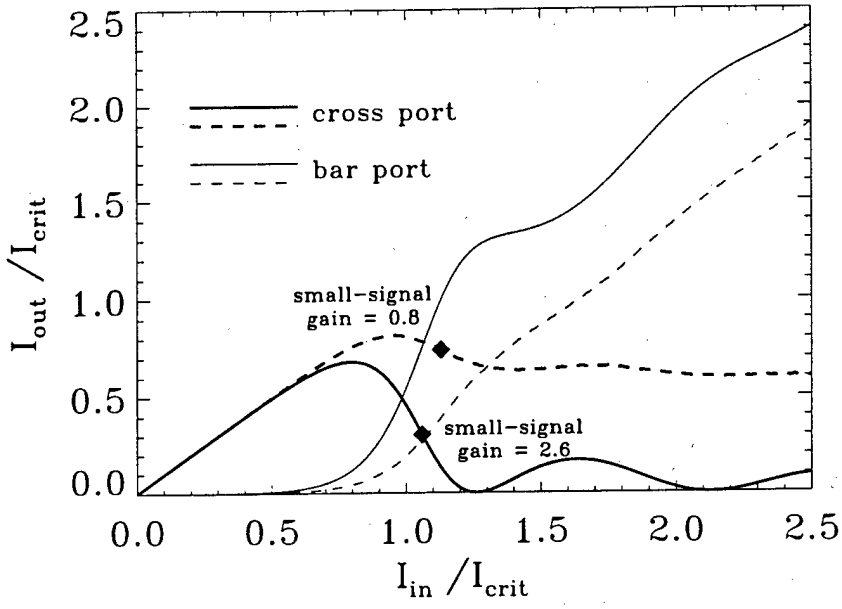

Figure 1.5: Output intensity into the cross and bar states as a function of input peak intensity the half-beat length NLDC. The solid curve is for a square-top pulse while the dashed curve is for a non-soliton $\text{sech}^2()$ pulse.

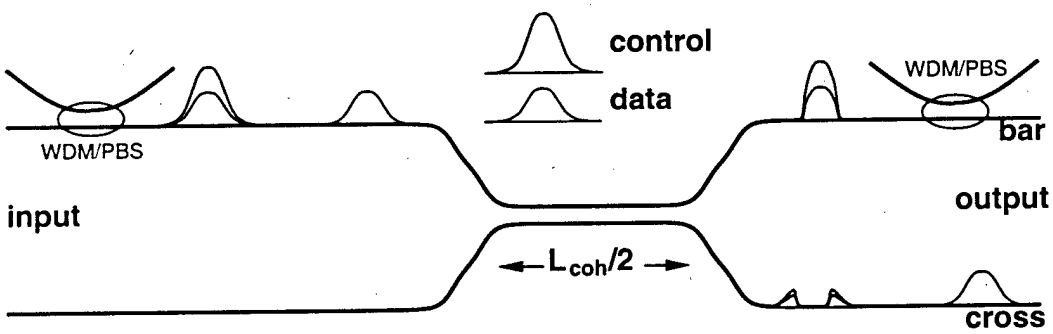

Figure 1.6: Three-terminal half-beat length NLDC. The control pulse is of a different color or polarization than the data pulse.

1.4.2 Kerr Gate

The optical Kerr gate was proposed as an ultrafast photonic gating device [41]. In the implementations discussed here, the Kerr gate is a three-terminal device in which data is either passed or blocked at the output. Since logic-level restoration is not possible, this device is simply an optical switch. The bulk geometry is shown in Figure 1.7. By virtue of the difference between self-phase modulation and cross-phase modulation, the gate beam A_1 induces a differential phase shift which rotates the polarization of the signal beam A_2, as long as there is nonzero projection of the polarization of A_2 onto a direction orthogonal to the polarization of A_1. Assuming plane waves interacting at small angles, the total electric field at the input can be written

$$E(0) = \hat{x}\left[A_1(0)e^{-i\omega_0 t} + \cos\theta A_2(0)e^{-i\omega_0 t} + \text{cc}\right] + \hat{y}\left[\sin\theta A_2(0)e^{-i\omega_0 t} + \text{cc}\right], \tag{1.9}$$

where θ is the angle that the polarization vector of A_2 makes with the x axis, which is the assumed polarization direction of A_1. Note that in practice beams must be used in order to spatially separate A_1 and A_2 at the output, where the angle of interaction is greater than the diffraction angle of either beam such that the beams are spatially resolvable in the far field. An additional consideration when dealing with beams (or pulses as in the fiber geometry) is that partial switching occurs analogous to the situation with the NLDC. For simplicity, the plane-wave analysis is used and is sufficient for the present purposes.

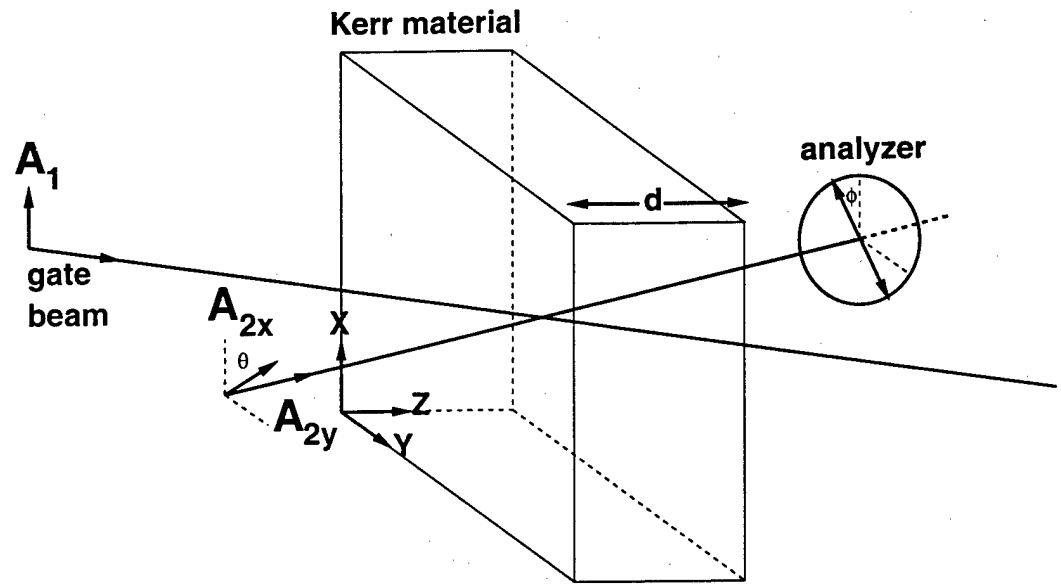

Figure 1.7: Bulk Kerr gate geometry. The polarization of the signal (or data) A_2 rotates based on the intensity of the gate (or control) A_1. In the absence of A_1, A_2 is blocked by the analyzer at the output. For A_1 of sufficient intensity, A_2 is transmitted by the analyzer.

After a propagation distance d in the nonlinear medium, the polarization components accumulate linear and nonlinear phase

$$A_1(d) = A_1(0)e^{ik_0 d}e^{i\Phi_1} \tag{1.10}$$

$$A_{2x}(d) = A_{2x}(0)e^{ik_0 d}e^{i\Phi_{2x}} \tag{1.11}$$

$$A_{2y}(d) = A_{2y}(0)e^{ik_0 d}e^{i\Phi_{2y}}, \tag{1.12}$$

where the nonlinear phases are written as

$$\Phi_1 = \frac{2\pi n_2}{\lambda_f}\int_0^d \left[|A_1(z)+A_{2x}(z)|^2 + 2\Delta\,|A_{2y}(z)|^2\right] dz \tag{1.13}$$

$$\Phi_{2x} = \frac{2\pi n_2}{\lambda_f}\int_0^d \left[|A_1(z)+A_{2x}(z)|^2 + 2\Delta\,|A_{2y}(z)|^2\right] dz \tag{1.14}$$

$$\Phi_{2y} = \frac{2\pi n_2}{\lambda_f}\int_0^d \left[|A_{2y}(z)|^2 + 2\Delta\,|A_1(z)+A_{2x}(z)|^2\right] dz. \tag{1.15}$$

The factor 2Δ denotes the cross-phase modulation coefficient and is equal to 2/3 in isotropic media. Assuming that $|A_1| \gg |A_2|$, thus precluding the possibility for large-signal gain, and that there is no absorption or power exchange throughout the interaction, the nonlinear phase induced on A_2 can be simplified to

$$\Phi_{2x} = \frac{2\pi n_2}{\lambda_f}|A_1(0)|^2 d \tag{1.16}$$

$$\Phi_{2y} = 2\Delta\frac{2\pi n_2}{\lambda_f}|A_1(0)|^2 d, \tag{1.17}$$

with the differential change in phase between the polarization components of A_2 written

$$\Delta\Phi = \Phi_{2x} - \Phi_{2y} = \frac{2\pi n_2}{\lambda_f}[1-2\Delta]\,|A_1(0)|^2 d, \tag{1.18}$$

such that $\delta = 1 - 2\Delta$.

In terms of a Jones vector, the output A_2 before the analyzer can be written

$$A_2(d) = A_2(0)e^{ik_0 d}e^{i\Phi_{2y}}\begin{bmatrix}\cos\theta e^{i\Delta\Phi}\\ \sin\theta\end{bmatrix}. \tag{1.19}$$

The transmission of a linear polarizer (analyzer) oriented at an angle ϕ relative to the x axis is [42]

$$T(\phi) = \begin{bmatrix} \cos^2\phi & \sin\phi\cos\phi \\ \sin\phi\cos\phi & \sin^2\phi \end{bmatrix}. \tag{1.20}$$

The output intensity of the signal beam after passing through the analyzer is therefore

$$\begin{aligned} I_2(d) = I_2(0) \Big[&\sin^2\phi\cos^2\phi + \cos^2\theta\cos^4\phi + \sin^2\theta\sin^4\phi \\ &+ 2\cos\theta\sin\theta\cos\phi\sin\phi\cos\Delta\Phi \Big], \end{aligned} \tag{1.21}$$

where the intensity $I_2(0) = \varepsilon_0 c n_0 |A_2(0)|^2/2$.

Typically, $\phi = \theta \pm \pi/2$ so that complete extinction is obtained with no nonlinear phase shift, thus implementing a pass gate. In this case, the output intensity is

$$I_2(d) = 2I_2(0)\cos^2\theta\sin^2\theta\,[1 - \cos\Delta\Phi]. \tag{1.22}$$

In order to maximize the contrast of the device, $\theta = \pi/4$, leading to the final result

$$I_2(d) = I_2(0)\sin^2(\Delta\Phi/2). \tag{1.23}$$

Therefore, a minimum of a π phase shift is again needed for complete switching, but over switching results when $\Delta\Phi > \pi$. A contrast ratio can be defined based on the difference between the high and low output states of a single port

$$\rho \equiv \frac{I_2(d)|_{\text{high}} - I_2(d)|_{\text{low}}}{I_2(d)|_{\text{high}} + I_2(d)|_{\text{low}}}. \tag{1.24}$$

In the case of the pass gate, $\rho = 1$, assuming an analyzer with perfect extinction.

An inverter can also be realized by setting $\phi = \theta$. The output intensity is

$$I_2(d) = I_2(0)\left\{1 - 2\cos^2\theta\sin^2\theta\,[1 - \cos\Delta\Phi]\right\}. \tag{1.25}$$

Again, $\theta = \pi/4$ maximizes the contrast, leading to the result

$$I_2(d) = I_2(0)\left[1 - \sin^2(\Delta\Phi/2)\right], \tag{1.26}$$

with $\Delta\Phi = \pi$ for complete extinction of the signal. The contrast ratio of the Kerr gate inverter is

$$\rho = \frac{\sin^2(\Delta\Phi/2)}{2 - \sin^2(\Delta\Phi/2)} \qquad 0 \le p \le 1. \tag{1.27}$$

Now the contrast is limited by the precision to which the intensity of the gate beam can be controlled in order to exactly achieve the condition $\Delta\Phi = \pi$ for complete extinction of the signal.

Figure 1.8 shows the input-output relationships for the pass gate and inverter geometries. The maximum small-signal gain occurs when $\Delta\Phi = (2m+1)\,\pi/2$, but, since $I_1 \gg I_2$, small-signal gain is always much less than unity. In addition, there are quasi-saturated levels for $\Delta\Phi = m\pi$, where m is a positive integer. The most important point to note is that over switching can occur. As $\Delta\Phi$ increases towards π, the pass gate switches on and the inverter switches off, but as $\Delta\Phi$ increases past π, the pass gate switches off and the inverter switches on. Therefore, there are no true saturated levels giving rise to stable states insensitive to variations in the gate beam intensity.

Because of the condition $I_1(0) \gg I_2(d)$, large-signal gain is not intrinsically possible with the Kerr gate either. In other words, it takes a high intensity gating beam to switch a small intensity signal beam. External amplification can be used to bring the high output state after the analyzer to the level required for switching a subsequent stage, but because of the over-switching problems inherent in the device, this process may not stable and could eventually lead to attenuation of the signal level after a long cascade of devices due to unavoidable amplitude fluctuations. This process can be made stable through the use of a saturating amplifier, but the gain recovery time of the amplifier will place a limit on the data rate.

As an example of the switching intensities needed for the Kerr gate, consider a 1 cm thick sample of fused silica, with $n_2^I = 3.3 \times 10^{-16}$ cm^2/W at $\lambda_f = 1.55$ μm (see Appendix D). In this situation, a gate intensity of $I_1(0) = 700$ GW/cm^2 is required. This intensity can be lowered by orders of magnitude by going to a fiber geometry in which the interaction length can be extended to many km's, as shown in Figure 1.9. For a 1 km fiber gate, $I_1(0) = 3.5$ MW/cm^2. Another advantage of the fiber

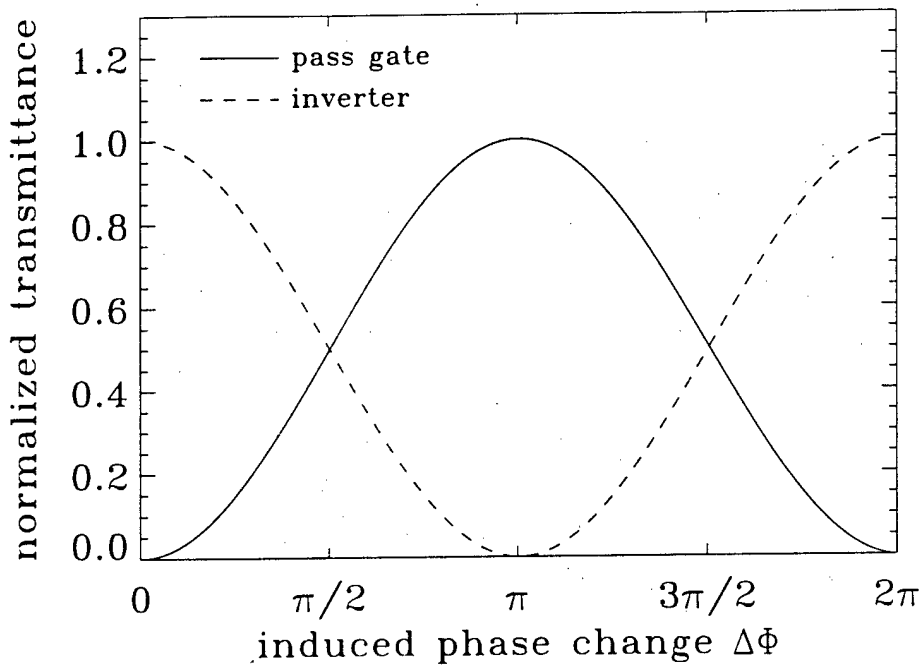

Figure 1.8: Transfer functions for the Kerr gate. The solid curve shows the normalized output versus induced phase shift $\Delta\Phi$ for the pass gate geometry, while the dashed curve shows the same information for the inverter.

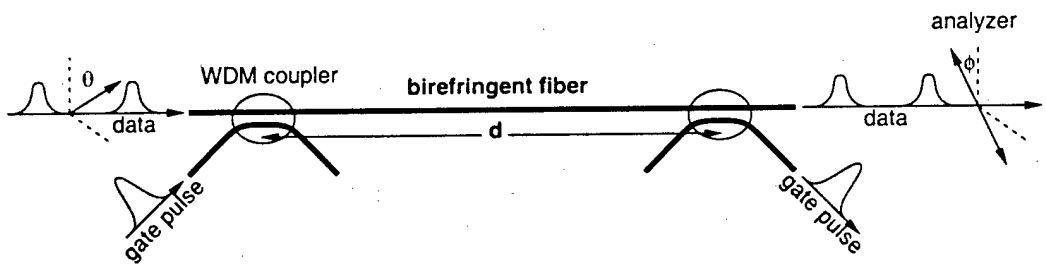

Figure 1.9: Fiber Kerr gate geometry. The gate and data pulses are of different central wavelengths. The gate pulse is timed to co-propagate with and extract one data pulse. Wavelength-division multiplexing (WDM) couplers launch the gate pulse into the interaction region and extract the gate pulse at the output for background-free operation. The bulk analyzer shown can be replaced by an in-fiber polarizer.

geometry in communications situations is that there is no need to couple the signal, or data, pulses out of and back into the fiber in order to achieve the desired switching operation.

Since the pump and data pulses must be separated at the output for background-free operation (i.e. high contrast), the two pulses must be of different color. An additional constraint is that the fiber must be polarization preserving, or birefringent, in order to keep the polarization of the data pulses from randomly evolving due to thermal or stress variations. As a result, the polarization components of the data pulses pick up a nonzero relative phase due to the intrinsic birefringence

$$A_{2x}(d) = A_{2x}(0)e^{ik_x d}e^{i\Phi_{2x}} \tag{1.28}$$

$$A_{2y}(d) = A_{2y}(0)e^{ik_y d}e^{i\Phi_{2y}}, \tag{1.29}$$

where $k_x = 2\pi n_x/\lambda_f$, $k_y = 2\pi n_y/\lambda_f$ and n_x and n_y are the indices of refraction along the principal axes of the fiber. The final polarization state without the gate pulse is in general elliptical, but the original state of polarization can be recovered using a

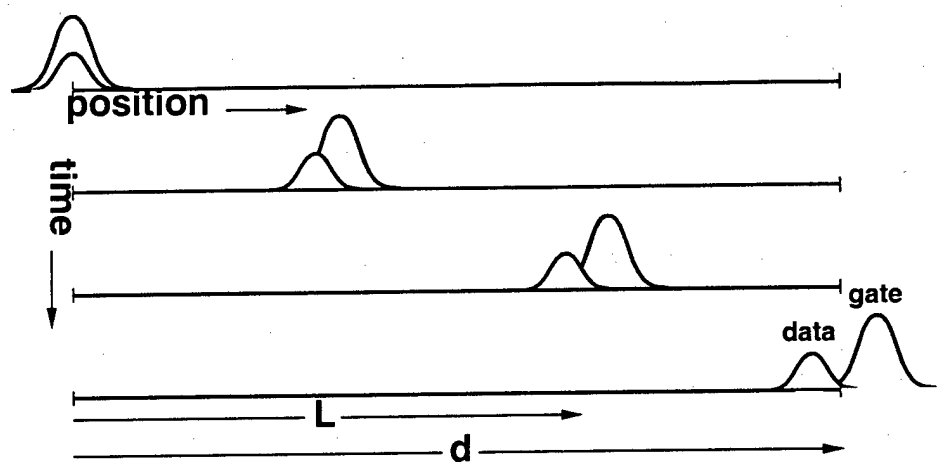

Figure 1.10: Pulse walkoff in fiber Kerr gate geometry. The fiber length is denoted by d, but the interaction length is limited to the birefringent or dispersive walkoff distance L. This diagram illustrates the dispersive walkoff between the gate and same-polarized data. The birefringence walkoff between the two components of the data pulse is similar.

compensator plate. Now, the nonlinear phases are written

$$\Phi_{2x} = 2\frac{2\pi n_2}{\lambda_f}|A_1(0)|^2 d \tag{1.30}$$

$$\Phi_{2y} = 2\Delta\frac{2\pi n_2}{\lambda_f}|A_1(0)|^2 d, \tag{1.31}$$

where the factor of 2 in the x phase is due to the interaction between waves of different frequency, and the four-wave mixing terms have been neglected. The differential phase is

$$\Delta\Phi = \frac{4\pi n_2}{\lambda_f}[1-\Delta]|A_1(0)|^2 d, \tag{1.32}$$

which, when $\Delta = 1/3$, is a factor of 2 larger than in the bulk geometry due to the increased cross-phase modulation coefficient between different colors in the same polarization state.

In an early Kerr gate demultiplexing experiment in fiber [43], it was recognized that birefringent and dispersive walkoff would limit the performance of the device due to the long interaction lengths needed to obtain a π phase shift with low switching energies. The result of walkoff is the reduction of the interaction distance as given by the length of the fiber, as shown in Figure 1.10, to an effective interaction distance given by one of the walkoff lengths. If the gate and data pulses have temporal duration τ, then the walkoff lengths can be defined

$$L_{\text{bire}} = \frac{\tau}{|k_x'(\omega_d) - k_y'(\omega_d)|} \approx \frac{c\tau}{|n_x - n_y|} \tag{1.33}$$

$$L_{\text{disp}} = \frac{\tau}{|k_x'(\omega_d) - k_x'(\omega_g)|} \approx \frac{\tau^2}{k_x''(\omega_d)}, \tag{1.34}$$

where $k_x'(\omega_d)$ and $k_y'(\omega_d)$ are the group delay coefficients for the polarization components at the data wavelength, $k_x'(\omega_g)$ is the group delay coefficient at the gate wavelength, $\Delta\omega \sim 1/\tau$ is the approximate spectral separation (by one FWHM), and $k_x''(\omega_d)$ is the group delay dispersion coefficient. For $\tau = 1$ ps pulses (for a data rate $\sim$ 100 Gb/sec with pulse separation 10 τ), typical walkoff lengths in silica fiber are $L_{\text{bire}} = 30$ m for $|n_x - n_y| \sim 10^{-5}$ and $L_{\text{disp}} = 35$ m, using $k_x''(\omega_d) = -2.79 \times 10^{-8}$ ps$^2/\mu$m from Appendix D.

The birefringence walkoff length is the distance over which the two polarization components of the data pulse maintain overlap by at least their temporal FWHM. This is also the distance over which the gate pulse and the orthogonal polarization of the signal pulse maintain overlap. The dispersive walkoff length is the distance over which the gate pulse and the same polarization of the signal pulse maintain overlap. In the worst-case scenario, the gate pulse propagates down the fast (slow) axis of the fiber and has the greater (lesser) group velocity. The interaction distance is therefore limited to the minimum of

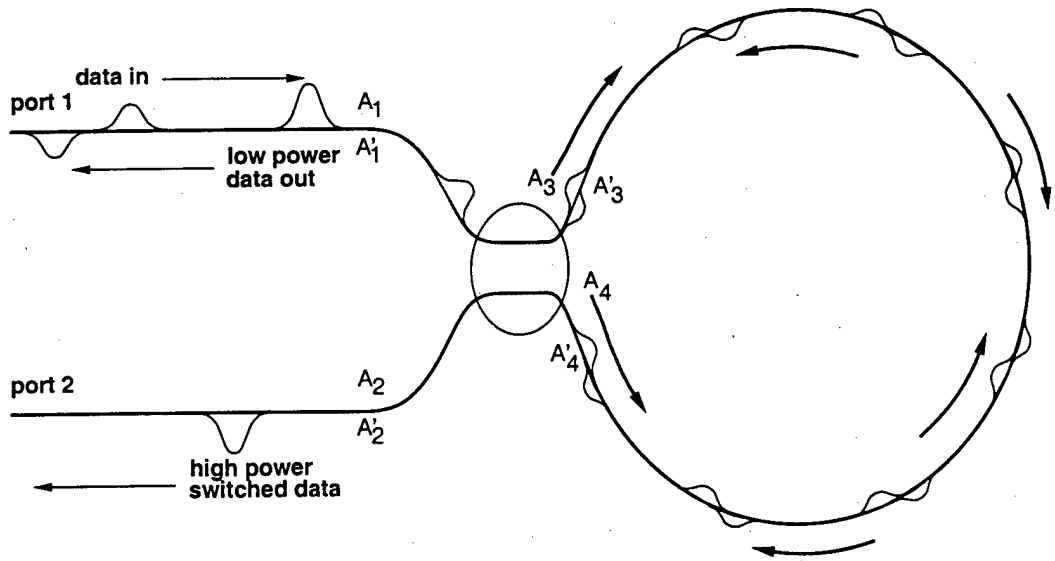

Figure 1.11: Diagram of the two-terminal nonlinear optical loop mirror in the intensity-dependent switching mode.

the birefringent and dispersive walkoff distances. The best-case is for the gate to propagate down the fast (slow) axis and have the lesser (greater) group velocity. Here, the interaction distance is limited to the birefringent walkoff length between the polarization components of the data pulse.

The effective interaction distance can be increased to twice the walkoff length by launching the slower pulse one pulse duration ahead of the faster pulse, but this technique still does not solve the underlying problem. Birefringent walkoff can be effectively eliminated by cross-axis splicing the polarization maintaining fiber such that the distance between each splice is less than the walkoff length L_{bire} [43]. The effects of dispersive walkoff can be reduced by decreasing the spectral separation between the data and gating pulses, thus limiting the data rate because $1/\tau \sim \Delta\omega$, or by equally spacing the central wavelengths about the zero dispersion wavelength such that both pulses travel with the same group velocities. This does not allow for both pulses to be temporal solitons, however.

A recent fiber Kerr gate demonstration used a 1.5 cm length of silica fiber (which is about L_{disp} for the experimental pulse duration) to perform demultiplexing of a 460 Gb/s data stream [44]. In the experiment, the peak gate intensity 43 GW/cm^2 (about 5 nJ pulse energy) resulted in a gating efficiency of less than 10%. A π phase change requires peak gate pulse intensity of nearly 235 GW/cm^2 (about 25 nJ pulse energy), which, except for the benefits of compactness and increased coupling efficiency, eliminates the original advantages of going to the fiber geometry.

1.4.3 Nonlinear Optical Loop Mirror

The nonlinear optical loop mirror [38], or NOLM, has been used extensively in ultrafast all-optical demultiplexing experiments [45,46]. Studies have also focused on the use of NOLMs to realize simple logic gates [45] and more complicated logic circuits [16]. The most basic two-terminal configuration is shown in Figure 1.11. A pulse which enters port 1 is split at a 2x2 fiber coupler into two counter-propagating pulses which recombine at the coupler. For a perfectly symmetric device, the pulses constructively interfere at the coupler and exit from port 1, thus acting as a mirror. Deviations from symmetry result in light exiting both ports 1 and 2. In nonlinear operation of a non-symmetric device, the pulse intensity can control the ratio of light exiting each output port.

Immediately after the coupler, the field amplitude in each counter-propagating direction of the loop can be written

$$A_3 = tA_1 \qquad A'_3 = A_4 e^{i\phi_{\text{ccw}}} \tag{1.35}$$

$$A_4 = irA_1 \qquad A'_4 = A_3 e^{i\phi_{\text{cw}}} \tag{1.36}$$

when it is assumed that no light enters port 2. The unprimed quantities represent the amplitudes before propagation around the loop while the primed quantities are after propagation around the loop and just before the coupler. The phases around the loop are allowed to be different as justified later. Here t is the (real) amplitude transmission coefficient and r is the (real) amplitude reflection coefficient. When the angle of incidence is less than the critical angle (as it must be here), there is a π phase shift upon

reflection from one of the coupler interfaces. Since the 3dB fiber coupler is symmetric, this phase is distributed symmetrically with the reflection coefficient in each direction. The amplitudes at the output ports are then

$$A_1' = tA_3' + irA_4' = itrA_1 e^{i\phi_{ccw}} \left[1 + e^{i\Delta\Phi}\right] \tag{1.37}$$

$$A_2' = tA_4' + irA_3' = A_1 e^{i\phi_{ccw}} \left[t^2 e^{i\Delta\Phi} - r^2\right], \tag{1.38}$$

where $\Delta\Phi = \phi_{cw} - \phi_{ccw}$. Finally, the output intensities are written

$$I_1' = 2r^2[1-r^2][1+\cos\Delta\Phi]I_1 = 4I_1 r^2[1-r^2]\cos^2(\Delta\Phi/2) \tag{1.39}$$

$$I_2' = I_1 - 4I_1 r^2[1-r^2]\cos^2(\Delta\Phi/2), \tag{1.40}$$

assuming a lossless system such that $r^2 + t^2 = 1$.

For the original NOLM device which switches based on the intensity of the incoming data pulses, the phases are

$$\phi_{ccw} = k_0 L + \frac{2\pi n_2}{\lambda_f}\int_0^L |A_4(z)|^2 dz \approx k_0 L + \frac{2\pi n_2 L}{\lambda_f}|A_4(0)|^2 \tag{1.41}$$

$$\phi_{cw} = k_0 L + \frac{2\pi n_2}{\lambda_f}\int_0^L |A_3(z)|^2 dz \approx k_0 L + \frac{2\pi n_2 L}{\lambda_f}|A_3(0)|^2, \tag{1.42}$$

where the differential phase is written

$$\Delta\Phi = \frac{2\pi n_2 L}{\lambda_f}\left[|A_3(0)|^2 - |A_4(0)|^2\right] = \frac{2\pi n_2 L}{\lambda_f}\left[1-2r^2\right]|A_1(0)|^2, \tag{1.43}$$

and $\delta = 1 - 2r^2$. For a symmetric device in which $r^2 = 0.5$, the phase shift is zero and all the light exits port 1, independent from the strength of the nonlinear interaction. Therefore, the loop must be unbalanced in order for self-switching to occur, in which the light exits port 2.

An example of the self-switching of the NOLM is shown in Figure 1.12, which plots the peak intensity in each of the two output ports (assuming square-top pulses) using $r^2 = 0.25$. This figure is different than Figure 1.8 of the Kerr gate, which plots the switching fraction, not the output intensity. This is done here to emphasize the low contrast of the two-terminal NOLM. Like the Kerr gate, over switching can occur for input intensity beyond that required for $\Delta\Phi = \pi$, thus making this device difficult to cascade. It should also be noted that partial switching will occur if square-top or soliton pulses are not used.

Because the self-switching behavior is similar to the two-terminal NLDC, a three-terminal NOLM with large-signal gain can be constructed in the same way, by biasing the device with a strong power supply or clock pulse and using a weaker control or data pulse (of different polarization or color) to initiate switching, thereby providing complete logic level restoration. Unlike the NLDC, the NOLM switching function does not possess saturated levels, thus making the device sensitive to input fluctuations, but also allowing for multiple intensity levels for the clock pulse (spaced by even intervals on the figure) to achieve inverting operation. Because the switching intensity is fixed at $1/2\Delta$ for the coordinate system used in the figure, the large-signal gain can be arbitrarily high (subject to limitations placed by nonlinear absorption, for example). The output from either port 1 or port 2 can be used. The contrast from port 1 is unity, but since this is also the input port, a coupling loss must be taken both at the input and at the output in order to extract the switched data.

The contrast of the NOLM at output port 2 is

$$\rho = \frac{2r^2[1-r^2]}{1-2r^2[1-r^2]}, \tag{1.44}$$

which is maximized when $r^2 = 0.5$. The peak intensity required for a π phase shift is

$$I_1 = \frac{\lambda_f}{2n_2' L[1-2r^2]}, \tag{1.45}$$

which is infinite when $r^2 = 0.5$. Here, the intensity I_1 represents the data pulse intensity plus any additional control pulse intensity. For example, $I_1 = I_{data} + 2\Delta I_{control}$, in the case of the biased device. The minimum required intensity is when $r = 0$, but the contrast is 0. Therefore, in the two-terminal or biased three-terminal NOLM, there is a tradeoff between high contrast operation and low switching intensity (energy).

Some of these problems can be solved by using a balanced (r^2=0.5) and un-biased three-terminal NOLM [47]. This configuration is shown in Figure 1.13, in which an external control pulse of different polarization or wavelength is used to

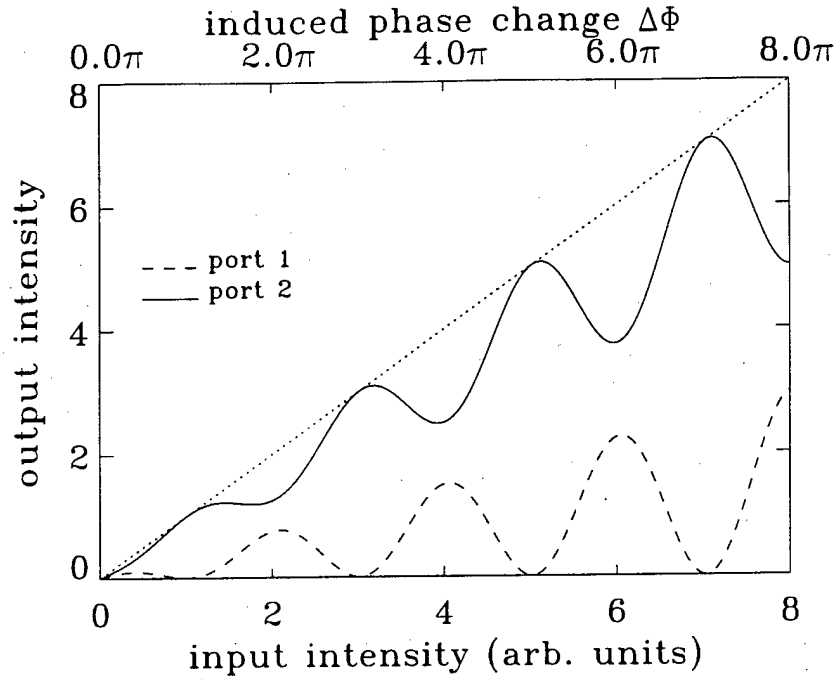

Figure 1.12: Switching characteristics of the two-terminal NOLM. If a non-square-top or non-soliton pulse is used, the output energy will not follow the intensity curve and the energy contrast will be reduced over the ideal case of unity for port 1 or as given by equation 1.44 for port 2. The amplitude reflection coefficient of the 2x2 fiber coupler is set to $r = 0.5$, giving a reflectance of $r^2 = 0.25$.

switch a much weaker data pulse by inducing a π phase shift on the counter-clockwise pulse via cross-phase modulation. In this case, the phases of the counter-propagating pulses can be written

$$\phi_{ccw} = k_0 L + 2\Delta \frac{2\pi n_2 L}{\lambda_f} |A_{ctl}(0)|^2 \qquad (1.46)$$
$$\phi_{cw} = k_0 L.$$

where A_{ctl} is the amplitude of the control pulse, which co-propagates A_{ccw} and therefore counter-propagates A_{cw}, inducing negligible nonlinear effect on the latter. For orthogonal polarizations, $2\Delta = 2/3$, while for different wavelengths, $2\Delta = 2$. In this device, the switching intensity and contrast are independent of r, because the change in phase is

$$\Delta\Phi = 2\Delta \frac{2\pi n_2 L}{\lambda_f} |A_{ctl}(0)|^2 \qquad (1.47)$$

and the contrast at output port 2 is $\rho = 1$ assuming that the control pulse intensity can be maintained to achieve $\Delta\Phi = \pi$.

Due to the long interactions lengths of 10 km or more [46], these switching elements suffer from polarization or dispersive pulse walkoff (unlike the fiber Kerr gate, the control pulse does not have to be of different polarization *and* wavelength). Walkoff can be minimized by using cross-spliced polarization maintaining fiber or choosing the control and data wavelengths symmetrically about the zero dispersion wavelength [45], as discussed for the fiber Kerr gate. Recent experiments have achieved demultiplexing of 100 Gbit/s data streams [48] in a 6 km loop using 1 pJ control pulses, and two-stage cascadability using low birefringence fiber loops with an amplification stage in between [49].

1.4.4 Terahertz Optical Asymmetric Demultiplexor

The terahertz optical asymmetric demultiplexor [50], or TOAD, was developed to reduce the long latency inherent in the NOLM and reduce switching energies by asymmetrically positioning a thin, highly (resonant) nonlinear element on one side of center of a fiber loop mirror, as shown in Figure 1.14. The fiber nonlinearity is not utilized and therefore the fiber loop can be on the order of meters in length rather than kilometers.

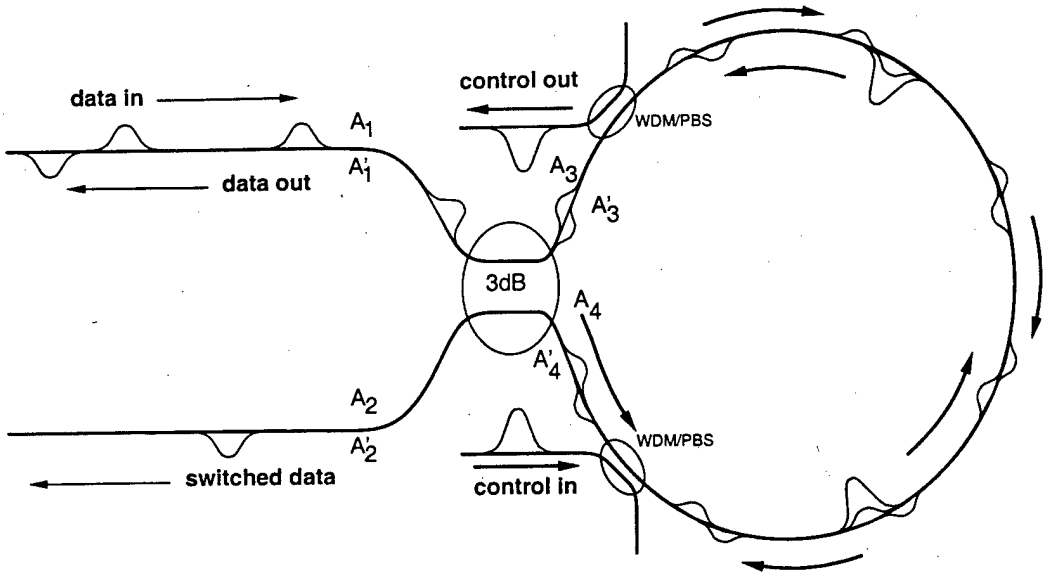

Figure 1.13: Three-terminal NOLM in two-pulse configuration. Wavelength division multiplexing (WDM) or polarizing (PBS) couplers transfer the control pulse into and out of the loop with nearly unity efficiency. For polarizing couplers, the fiber loop must be polarization maintaining. The control pulse only propagates counter-clockwise, and only interacts strongly with the counter-clockwise component of the data pulse.

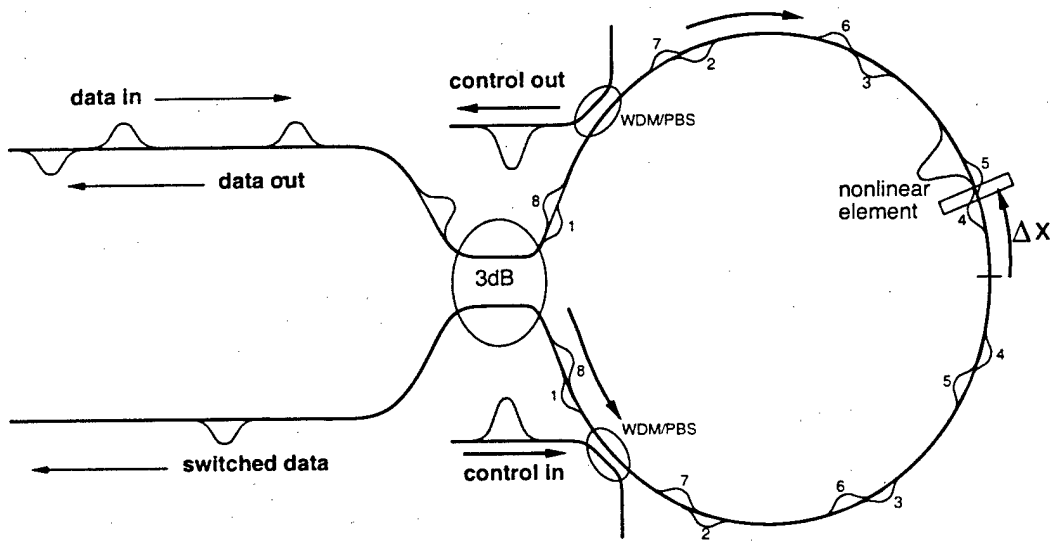

Figure 1.14: Three-terminal terahertz optical asymmetric demultiplexor. The nonlinear phase shift is provided by the control pulse excitation of an asymmetrically placed nonlinear element.

The TOAD switch works similarly to the three-terminal NOLM by imposing a π phase shift in one arm (direction) of the loop, and cannot be configured as a true logic gate. The differentiating factor from the NOLM is that a thin nonlinear element excited by the control pulse is responsible for the nonlinear phase shift induced on the data pulses. In the diagram, pulses 1-3 pass through the nonlinear element before the control pulse and experience no nonlinear phase shift in the clockwise and counter-clockwise parts because the nonlinear element is in the un-excited state. As a result, there is no differential phase shift ($\Delta\Phi = 0$) and the pulses exit the input port (or reflect). Pulses 5-8 pass through the element after the control pulse, but now each direction experiences a nonlinear phase shift, but, given constraints of long relaxation time of the nonlinear element as discussed later, experience no significant differential phase shift and also exit the input port. Pulse 4, on the other hand, switches out the other port because the clockwise propagating part of the pulse passes through the nonlinear element before the control pulse and experiences no nonlinear phase shift, but the counter-clockwise part reaches the nonlinear element just after

excitation by the control pulse and experiences a nonlinear phase shift. If the differential phase shift $\Delta\Phi = \pi$, then the pulse will exit the output port.

The counter-clockwise and clockwise phases can be written

$$\phi_{\rm ccw} = k_0 L + \Delta\frac{2\pi d}{\lambda_f}\Delta n(t_i - t_{\rm ctl} + 2\Delta x/v_g) \tag{1.48}$$

$$\phi_{\rm cw} = k_0 L + \Delta\frac{2\pi d}{\lambda_f}\Delta n(t_i - t_{\rm ctl}), \tag{1.49}$$

where t_i is the time that the clockwise portion of the ith pulses reaches the nonlinear element, $t_i + 2\Delta x/v_g$ is the time that the counter-clockwise portion of the same pulse reaches the nonlinear element, $t_{\rm ctl}$ is the time that the control pulse excites the nonlinearity, and v_g is the group velocity. The time-dependent nonlinear index change is written

$$\Delta n(t) = \int_0^\infty R(\tau)\,|A_{\rm ctl}(t-\tau)|^2\,d\tau \qquad t \geq 0 \tag{1.50}$$

$$= 0 \qquad t < 0, \tag{1.51}$$

where $R(\tau)$ is a nonlinear response function, typically of the form of an exponential decay. It is clear that, assuming an instantaneous rise time,

$$t_i < t_{\rm ctl} < t_i + 2\Delta x/v_g, \tag{1.52}$$

in order to switch the ith pulse. A much more complete analysis has been performed [51], with the basic conclusion that the nonzero length of the nonlinear element places a restriction on the minimum duration of the switching window, which must be at least twice the transit time through the element plus the rise time of the nonlinearity. The relaxation time of the nonlinearity sets the lower bound on the frame time because the nonlinear material must be in the ground state before re-excitation by another control pulse. These requirements are expressed by [50]

$$\tau_{\rm rise} + 2\tau_{\rm transit} < T_{\rm bit} \ll \tau_{\rm fall} < T_{\rm frame}, \tag{1.53}$$

where $\tau_{\rm rise}$ is the rise-time of the nonlinearity and can usually be considered instantaneous, $\tau_{\rm transit}$ is the transit time through the nonlinear element, $T_{\rm bit}$ is the time between adjacent bits in the data stream, $\tau_{\rm fall}$ is the fall time of the nonlinearity and does not have to be instantaneous as in the other devices which require $\tau_{\rm fall} \ll T_{\rm bit}$, and $T_{\rm frame}$ is the frame time for time-division multiplexed data. The fall time $\tau_{\rm fall}$ must be greater than the time difference $2\Delta x/v_g$ between when the two parts of the same pulse pass through the nonlinear element so that the clockwise and counter-clockwise portions accumulate approximately the same nonlinear phase shift. A disadvantage is that only one data pulse can be switched within the relaxation time of the nonlinear element, so that the switching events must occur at least $\tau_{\rm fall}$ apart. Unlike the other devices, the TOAD is relatively insensitive to timing jitter between the control and data pulses. All that is required is that the control pulse arrives (up to one bit time) at the nonlinear element before the intended data pulse. The amount of timing jitter that can be tolerated is limited to $T_{\rm bit} - \tau_{\rm rise}$.

Because the nonlinearity need not be instantaneous (and in fact the fall time must be long), very large, resonant nonlinearity, such as that produced by real particle excitation and decay, can be used. The optical path length of the nonlinear element must be less than that between the element and center and, since the nonlinear phase shift is proportional to the product of nonlinear index, control pulse intensity, and the thickness of the nonlinear element, the latter is perhaps the main limitation on high contrast, low energy switching for THz data streams. A recent demonstration [52] showed single-pulse demultiplexing of 250 Gbit/s data with 0.8 pJ switching energy.

A related device, based on a Mach-Zehnder configuration with asymmetric placement of a nonlinear element in each of the two arms (where the difference between the distance from the coupler to each element is Δx), has also been demonstrated [53]. As in the TOAD device, a control pulse is used to excite the nonlinear elements, where the time difference between the excitation of each element leads to a switching window of duration $\Delta x/v_g$, but again, large-signal gain cannot be realized. Because the two arms are physically distinct, any differential environmental variations can disturb the operation of the gate, but the effect is less important for an integrated device.

Another variation, which perhaps is more akin to the fiber Kerr gate, is the so-called ultrafast nonlinear interferometer [54], or UNI. This device is shown in Figure 1.15. The input data pulses split equally along the polarization axes of birefringent fiber. Because the group velocity is different along each axis, the polarization components walk-off from each other in time. The time difference between the leading and trailing components allows for asymmetric excitation of the nonlinear element by a strong gate pulse such that the leading pulse is affected only by the amplification process of the device (the device is electrically pumped) and the trailing pulse is affected by the device after gain saturation by the strong gate. Therefore, due to sub-ps carrier

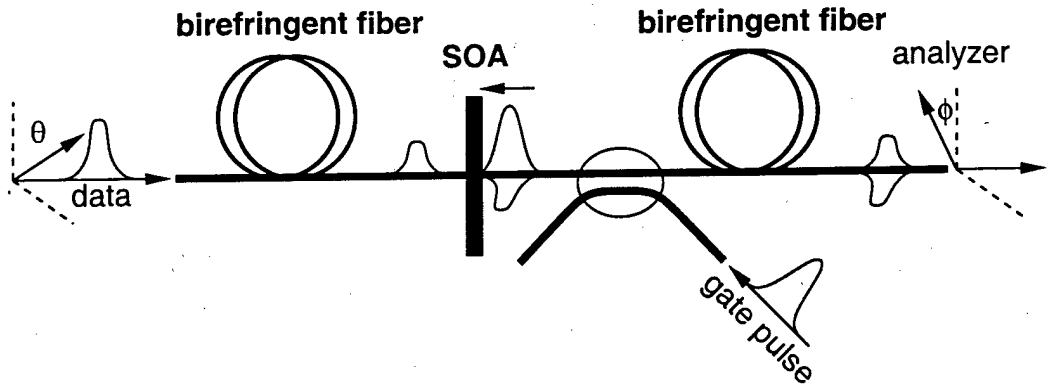

Figure 1.15: Three-terminal ultrafast nonlinear interferometer. A differential phase shift is imparted onto the data pulse at the semiconductor optical amplifier (SOA) by asymmetric excitation with the gate pulse.

heating and gain depletion, and virtual electronic processes, both differential amplitude and phase changes are induced between the data components. Long-lived carrier population and thermal nonlinearities ensure that no differential change is induced between subsequent data pulse components. After traveling through another length of birefringent fiber with fast and slow axes reversed, the components overlap at an analyzer biased to produce the desired logic operation. For example, if the analyzer is set to pass the data pulse in the absence of the gate pulse, then the device will act as an inverter, albeit without logic level restoration and large-signal gain.

Like the TOAD, the switching rate is limited by the gain recovery time of the SOA, but it should be noted that only enough recovery time is needed so that the control pulse can induce another π phase shift. If only TDM de-multiplexing is performed, then recovery time only limits the frame period, while the bit rate is limited by the optical thickness of the element and the rise time of the nonlinearity. For switching operations that occur on a bit-by-bit basis, then the π phase shift recovery time places the main limitation on bit rate, which can be as high as 100 Gb/s [55]. A recent experiment [11] demonstrated the cascadability of this three-terminal device by implementing a 40 Gb/s inverting shift register. A fiber amplifier was used to bring the inverted data output of the device up to the necessary 0.1 pJ switching energy.

1.5 Optical Soliton Logic Devices

The devices discussed in the previous section all suffer from drawbacks that may limit their use in cascaded digital logic and switching systems. Except for variations of the nonlinear directional coupler (NLDC) and nonlinear optical loop mirror (NOLM), none of these switching devices has complete logic level restoration with large-signal gain. In the standard configurations, the data pulse itself is transmitted to the output. The strong control pulse only initiates the switching and is thrown away afterwards. As a result, the transmitted data is never restored allowing signal level variations to build up over time. The roles of control and data can be reversed such that weak "power supply" pulses are passed on to subsequent gates, and are controlled by strong data pulses. Here, restoration is almost complete, with the lack of obtaining a valid signal level without external amplification which introduces ASE noise and bandwidth limitations. The biased three-terminal NLDC and NOLM have complete logic level restoration because of large-signal gain, but the gain of the NLDC is very limited and suffers from low contrast in practice, and the NOLM does not possess saturated levels and is lossy in order to achieve high contrast.

In the three-terminal configurations, these devices are only directly cascadable when using control or gate pulses of orthogonal polarization to the data pulses. Cascadability is achieved simply by using a half-wave plate to rotate the polarization of the output to serve as a control input. Using different colors also allows for cascadability, but the system becomes more complicated. In the first realization, the output of the gate must be converted through some nonlinear process such as three- or four-wave mixing, to the appropriate control input color. A second realization is to alternate the correct control color at each stage such that no wavelength conversion is necessary, but this may require two device designs in order to achieve optimum performance. These two-color schemes are the only way to cascade the fiber Kerr gate, since different colors are necessary in the fiber geometry, and the NLDC, because the use of different polarizations greatly reduces the switching performance [33].

The Kerr gate, NOLM, and terahertz optical asymmetric demultiplexor (TOAD) all suffer from over switching, although saturated gain in the nonlinear element can clamp the total induced phase shift in the latter device. In each of these three devices, a control intensity higher than that required for a π phase shift will cause over switching [45] and result in reduced contrast. Therefore, each gate in the system must be precisely toleranced if high contrast operation is required, but because of

unavoidable variations, the signal level will be attenuated through a long cascade with eventual loss of the logic level.

The performance of all of the devices, except TOAD, is reduced considerably by walkoff and incomplete switching. Means of reducing walkoff were discussed for each device, but it should be noted that, since the use of orthogonal polarizations is more practical for cascadability considerations, cross-axis splicing is an elegant solution. Because square-top pulses possess high frequency components at the leading and trailing edges leading to rapid pulse broadening, the most robust way to eliminate incomplete switching is to use temporal solitons for the control and data pulses. The use of temporal solitons can also reduce or eliminate walkoff by the mechanism of temporal trapping [56,57].

The limitations of these devices motivates the study of a new class of devices based on optical solitons, which make full use of the soliton properties. Because solitons are threshold phenomena, they are natural carriers of digital information. Below a critical power or energy, a nonlinear wave will asymptotically disperse, but above the critical power or energy, a nonlinear wave will evolve into one or more stable (possibly higher-order) solitons. Therefore, binary logic levels can be represented by the amount of detected power or energy, or even by spatial or temporal size (a soliton could readily pass through a spatial or temporal aperture, while the majority of a dispersive wave would not). A related issue is resolvability. Since solitons beat the linear diffraction/dispersion limits, a logic gate (without absorption) could be arbitrarily long. This property is used to great advantage in the soliton collision and dragging gates as discussed later, where a small angular/frequency change (induced by a nonlinear phase shift less than π) manifests itself as a resolvable spatial/temporal shift.

Other benefits arise from the use of solitons in digital logic systems. Solitons are stable to weak perturbations meaning that the soliton tends to maintain its shape in the presence of material inhomogeneities or input profile variations, which is an important property for logic restoration. In fact, the original amplitude and shape can be restored even after absorption by the use of adiabatic amplification. This property is useful for logic restoration and in long haul communications. Additionally, in some cases, solitons will maintain their shape even after collision with another soliton, which turns out to be a disadvantage for optical switching. The logic gates presented in this thesis use a configuration in which the interaction is inelastic such that soliton shape is not necessarily maintained after collision. The most important benefit to optical switching is that solitons (or nonlinear waves in general) can exert a force on one another, unlike light in linear propagation. These forces can alter the direction in space or velocity in time of one or both solitons resulting in a switching or logical operation.

In order to achieve low switching energy per gate operation, the ideal optical soliton logic gate should be based on one of the three geometries that allow for complete three-dimensional confinement [2]: 1-D temporal solitons in fiber, 2-D spatio-temporal solitary waves in slab waveguides, and 3-D light bullets. The advantage of spatio-temporal solitary waves over temporal solitons for switching and logic is the removal of one or two transverse dimensions of linear confinement. This allows for spatial parallelism (without the loss of ultrafast temporal pipelining) and the freedom to use spatial interactions with much easier output state discrimination [2,58] than their temporal counterparts [59] in order to implement amplitude keyed logic for eventual conversion to the electronic domain. Even though one dimension of spatial parallelism is lost, the 2-D solitary wave has the important advantages over the 3-D "light bullet" case in that it should be more easily realizable experimentally [60], and the slab waveguide geometry allows for the possibility for tailoring of the dispersion properties [61], photolithographic circuit definition, and cooling through the area of the substrate. The (2+1)-D case also presents an efficient test bed allowing for the study of the effects of higher-order terms in the evolution equation by retaining full spatio-temporal dynamics without resorting to the time-consuming (3+1)-D simulation.

The remainder of this section briefly discusses two soliton-based logic gates based on the trapping interaction. These gates satisfy the requirements for a logic device, including large signal gain and logic level restoration. The first device is the temporal soliton dragging gate [62], and the second is the related spatial dragging gate [58], which is the main subject of this thesis. Note that other soliton interactions can be used for logic devices and are discussed further in Chapter 5.

1.5.1 Temporal Soliton Dragging Gate

The soliton trapping [62] and dragging [59] gates are based on the temporal trapping mechanism [56, 57]. Two nonlinear waves of different polarization and/or wavelength propagate down a fiber with different group velocities. If they are initially overlapping in time, in linear propagation, one will reach the end of the fiber before the other. In nonlinear propagation though, they can trap each other through nonlinear attractive forces such that they both propagate at the same group velocity. In this case, each wave must experience a frequency shift in order to propagate at the common, weighted-mean, group velocity. The two nonlinear waves do not need to be of the same size (in terms of pulse area) in order for trapping to occur [57], and the frequency shift experienced by the smaller wave is greater than that experienced by the larger wave.

Figure 1.16 shows the generic three-terminal gate geometry. In the most basic geometry as shown, these gates perform an inversion operation in which the pump is passed in the absence of the signal and blocked by a spectral filter or time gate (as discussed later) in the presence of the signal. Note that the signal is always blocked at the output and the pump of one gate becomes the signal of the next, resulting in true three-terminal operation. Since the pump pulse may be passed on to later gates,

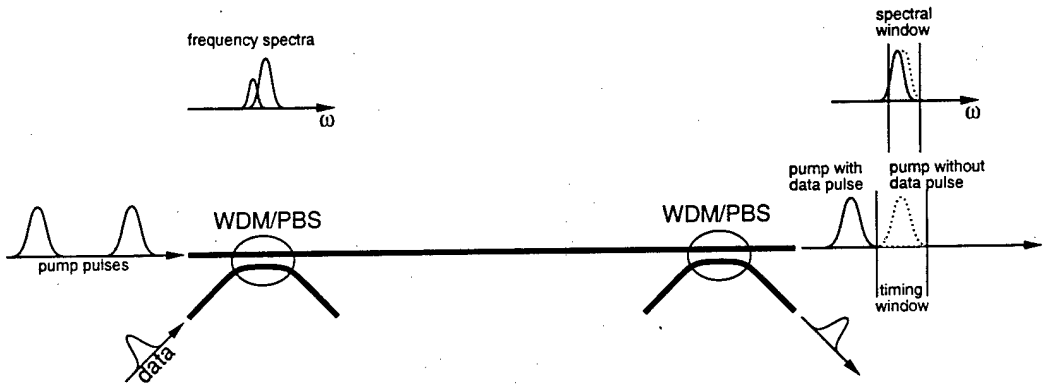

Figure 1.16: Temporal soliton trapping/dragging gate. Soliton pump pulses (always present) initially overlap in time with (non-soliton) data or signal pulses of different wavelength and/or polarization. Cross-induced chirp causes the pump and signal to propagate with the same group velocity. This frequency shift must be resolvable for the trapping gate. The change in group velocity becomes an arbitrarily large timing shift after propagation through a dispersive fiber delay line. For the dragging gate, this timing shift must be resolvable.

it is convenient for it to be a temporal soliton in order to maintain its shape after propagation through many tens to hundreds of meters of fiber, thereby ensuring logic level restoration. The trapping and dragging gates use pulses of the same wavelength but with orthogonal polarizations. Note that similar type gates can be constructed using pulses of different wavelength [63], based on the analogous trapping mechanism [64], but this gate is not readily cascadable because frequency shifters are necessary to drive the subsequent gate, while in the case of different polarizations, a wave plate can be used to rotate the output pump polarization to the correct state. In either case, the gate operation is independent of the relative phase between the pump and signal [1].

The soliton trapping gate relies on a resolvable spectral shift of the pump soliton [62], so that an unshifted pump will pass through a spectral bandpass filter while a shifted pump (in the presence of the signal) will not. This results in amplitude keyed logic and is compatible with common high-speed optical detectors for eventual conversion into an electronic signal. In order for this to occur, the fiber birefringence must be sufficiently large to produce the necessary difference in group velocity between the pulse propagating down the slow axis and the pulse propagating down the fast axis, which when compensated due to trapping, results in a spectrally resolved shift. The pump and signal pulses must also be of nearly the same amplitude so that the shift is not weighted preferentially towards the signal. As a result, this gate cannot provide significant large-signal gain. In fact, the first experimental demonstrations [62, 65] used solitons of 300 fs duration and 42 pJ energies for the pump and signal. A final note is that, because complete trapping can occur in a few soliton periods, the gate length need only be a few tens of meters in length, thereby reducing latency.

The temporal soliton dragging logic gate utilizes the fiber dispersive delay line as a "lever-arm" in order to allow a weak control or signal soliton to "drag" a strong pump in time [3]. In this way, even a small spectral shift of the pump (i.e. less than a π phase shift induced by a weak signal pulse) can result in a large time delay due to non-zero group delay dispersion. Because the pump is a temporal soliton and does not broaden in time, a resolvable temporal shift can be achieved by choosing the appropriate length delay line, according to the expression

$$\Delta\omega k_0'' L > \tau_{\mathrm{FWHM}}, \tag{1.54}$$

where the frequency shift $\Delta\omega$ is a function of the pump and signal pulses and the birefringence, and $k_0'' L$ is the group-delay dispersion. Therefore, there is a tradeoff between gain and fiber birefringence (which determine the amount of spectral shift) and gate length. If the pump were a linearly dispersive wave, broadening occurs at the same rate as the temporal delay (neglecting higher-order dispersion) and temporal resolvability can only be achieved by a resolvable spectral shift.

Temporal dragging logic must be time-shift keyed, which is still fully cascadable in the optical domain (but may limit bit rate somewhat) for a clocked system, but not compatible with high-speed electronic detection. Detection can be achieved by using a trapping gate in the last stage [3] or an ultrafast optical gating mechanism, such as the Kerr gate. One problem with time-shift keyed logic is that the dragged pump is difficult to remove from the system (although it is blocked by the polarization beam splitter at the output of every second dragging gate) and may cause interference in subsequent switching stages. Note that, in contrast to the problems imposed by birefringent walkoff on the previous fiber gates, the temporal soliton trapping/dragging

[1] when neglecting the nonlinear four-wave mixing effects

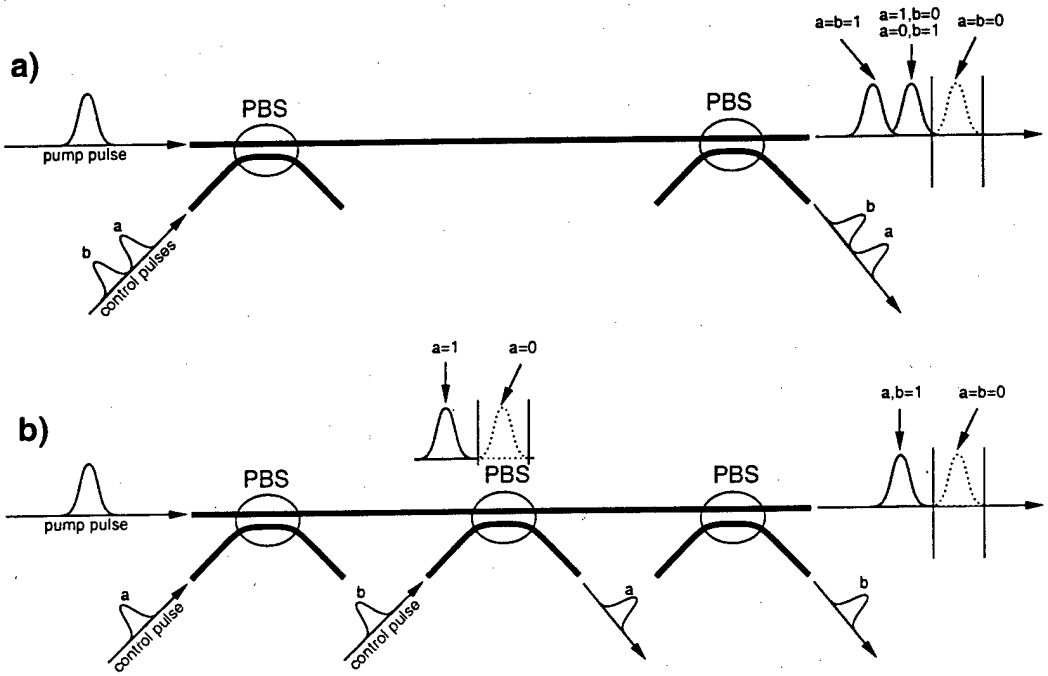

Figure 1.17: Temporal soliton dragging NOR gate geometries. Diagram a) shows a two-input soliton dragging gate which implements NOR. Diagram b) show two cascaded single-input soliton dragging gates which also implements NOR.

gates use birefringent walkoff (in combination with nonlinear cross-phase modulation) to induce the switching operation. The only constraint is that the walkoff length should be greater than about one soliton period because the bulk of the interaction occurs within that distance [66].

The first demonstration [59] of temporal soliton dragging was of a two-input, logically complete NOR gate. Two possible realizations of this logic gate are shown in Figure 1.17, where the first geometry is the one used in the experiment. In this experiment, the 300 fs pump pulse had energy of 132 pJ, while the non-soliton control pulses had 30 pJ energy, realizing a gain of 4.5 with high contrast. The fiber length was 75 meters, giving a gate latency of 360 ns. A cascading demonstration was also performed using a geometry similar to that shown in Figure 1.17 a). This demonstration suffered from the effects of Raman amplification, in which lower spectral components of a pulse are amplified at the expense of higher spectral components, resulting in asymmetric temporal broadening of the pump pulse, and may limit cascadability due to the shift in mean frequency. When both control pulses are present, the output of the device is sensitive to the relative phase between the control inputs.

Using the geometry of b), a follow-on work [66] obtained switching with reduced control pulse energy and no phase sensitivity. In this demonstration, a 500 fs, 54 pJ pump pulse was used along with 6 pJ control pulses. The pulse durations were lengthened and energies were lowered to reduce the effects of Raman gain. For this geometry, the length of fiber between the coupling region for each control pulse need only be that required for the interaction to occur (about 75 meters in this case). The long dispersive delay line (350 meters) can be placed at the end in order to achieve the timing shift due to the spectral shift induced by either control. This is one instantiation of the more general time-domain chirp architecture [3]. Dragging was obtained with lower control pulse energies because each control pulse completely overlapped the pump pulse in time, resulting in a stronger interaction than in the partial overlap geometry of a).

Subsequent extensions to the time-domain chirp architecture used 30 m of moderately birefringent fiber in which the spectral shift occurred, followed by 2 km of polarization maintaining fiber as the dispersive delay line to obtain the timing shift [3]. In this case, the control pulse energy was about 1 pJ. Another modification used a short ($\sim$ 2 mm), highly nonlinear semiconductor as the nonlinear chirping element, followed by 600 m of fiber. Control energies were on the order of 100 pJ because the control and pump were slightly offset in time to achieve spectral shift upon trapping due to the lack of strong group velocity mismatch in the semiconductor.

These trapping and dragging interactions are described by the coupled, temporal NLS equations [67]

$$2ik_0\left[\frac{\partial A_1}{\partial z}+\frac{1}{2}\Delta k_0'\frac{\partial A_1}{\partial T}\right]-k_0k_0''\frac{\partial^2 A_1}{\partial T^2}+2k_0^2\frac{n_2}{n_0}\left[|A_1|^2+2\Delta|A_2|^2\right]A_1=0 \tag{1.55a}$$

$$2ik_0\left[\frac{\partial A_2}{\partial z}-\frac{1}{2}\Delta k_0'\frac{\partial A_2}{\partial T}\right]-k_0k_0''\frac{\partial^2 A_2}{\partial T^2}+2k_0^2\frac{n_2}{n_0}\left[|A_2|^2+2\Delta|A_1|^2\right]A_2=0, \tag{1.55b}$$

where $\Delta k_0'$ is the difference between the group delay coefficients, and the reduced time is defined $T=t-k_0'z$ with k_0' being the average group delay coefficient. Here, the group-delay dispersion coefficients are assumed equal and A_1 and A_2 represent the orthogonal polarizations. Note that the vector four-wave mixing terms have been neglected due to unavoidable intrinsic, stress-induced, or bend-induced birefringence which leads to accumulating phase difference between the orthogonal polarizations. Much more will be said about this fundamental system of equations in later chapters of this thesis.

1.5.2 Angular Deflection Gate based on Spatial Soliton Dragging

Spatial dragging gates [58] are one instantiation of a more general class of angular deflection logic gates studied in this thesis. The first spatial trapping gate was demonstrated experimentally [68] using spatial solitons of the same polarization (i.e. phase-dependent), but propagating at different angles. Due to cross-focusing, which is the spatial analogy to cross-phase modulation, the solitons mutually attract and under the right condition, form a trapped pair. The analogous temporal trapping interaction between two temporal solitons of different color (and hence different group velocities), has been studied analytically [64] and experimentally [63]. The direct spatial analogy to the Islam temporal trapping [62] and dragging [59] gates is the interaction between spatial solitons in the orthogonal eigenpolarization states of a uniaxial crystal [69]. In linear propagation, these eigenstates would normally walk-off in space, but nonlinear cross-focusing causes trapping or dragging to occur. A different arrangement, which is the one used in this thesis, has also been analyzed theoretically [58, 70], in which the interaction occurs between tilted orthogonally-polarized spatial solitons in linearly isotropic media. The temporal analog to this interaction is temporal solitons of different color and orthogonal polarization.

The use of solitons or solitary waves in optical logic is critical in that solitons beat the diffraction and/or dispersion limit over distances much longer than the characteristic linear lengths. Here, the main interest is in the use of lateral spatial confinement over distances larger than the linear diffraction distance. The key idea is illustrated in Figure 1.18, which shows the basic angular deflection logic gate. A pump soliton (left-hand side) propagates the length of the gate (which is assumed to be in a slab waveguide geometry) and passes through a spatial aperture at the output, forming the high output state of the device. Because the spatial soliton does not diffract, the size of the aperture can be the same as the size of the wave at the input, independent of the actual gate length.

The switching operation is performed by disturbing the propagation of the pump beam such it does not exit the spatial aperture, thus providing the low output state of the device. This can be accomplished by inducing a change in propagation angle which leads to a spatially-resolved shift at the output. If the beam propagates linearly (as shown on the right-hand side), a spatially-resolved shift can only be produced by inducing a change in the propagation angle (with a change in phase across the aperture of the beam of at least π) that is greater than twice the linear diffraction angle. In nonlinear soliton propagation, an induced angle change that is less than linearly resolvable (i.e. less than a π phase change across the spatial aperture) results in a differential spatial shift which can be integrated over non-diffracting propagation such that a spatially-resolvable shift occurs at the output. Thus, as shown in the figure, the gate length must be at least the minimum resolvable dragging distance, which depends on the spatial width of the soliton beam and the amount of angular change, much like the case of the deflection of a linear pump by a much larger angle and well within the linear diffraction length.

The angular change is produced through the nonlinear interaction between the pump and another, orthogonally-polarized beam, called the signal, which initially overlaps the pump and propagates at a non-zero relative angle. The signal beam must be strong enough to induce a nonlinear index change felt by the pump through cross-focusing. If the pump propagates linearly, then large-signal gain is not possible because the signal beam is necessarily stronger. In this case, there is no mutual nonlinear interaction and the nominal effect of the signal is to create a nonlinear prism which deflects the pump in the direction of the signal. The deflection angle depends on the relative propagation angle and intensity of the signal, with the maximum angle occurring when the pump is completely guided, or trapped, by the signal. Therefore, the angle θ must be at least the diffraction angle of the pump because the deflected pump will be nonlinearly guided by the signal, which may be a spatial soliton in the limiting case.

If the pump is a spatial soliton, then large-signal gain is possible, but the interaction is more complicated due to mutual nonlinear coupling:

$$2ik_0\frac{\partial A_y}{\partial z}+2ik_x\frac{\partial A_y}{\partial x}+\frac{\partial^2 A_y}{\partial x^2}+2k_0^2\frac{n_2}{n_0}\left[|A_y|^2+2\Delta|A_x|^2\right]A_y=0 \tag{1.56a}$$

$$2ik_0\frac{\partial A_x}{\partial z}+\frac{\partial^2 A_x}{\partial x^2}+2k_0^2\frac{n_2}{n_0}\left[|A_x|^2+2\Delta|A_y|^2\right]A_x=0, \tag{1.56b}$$

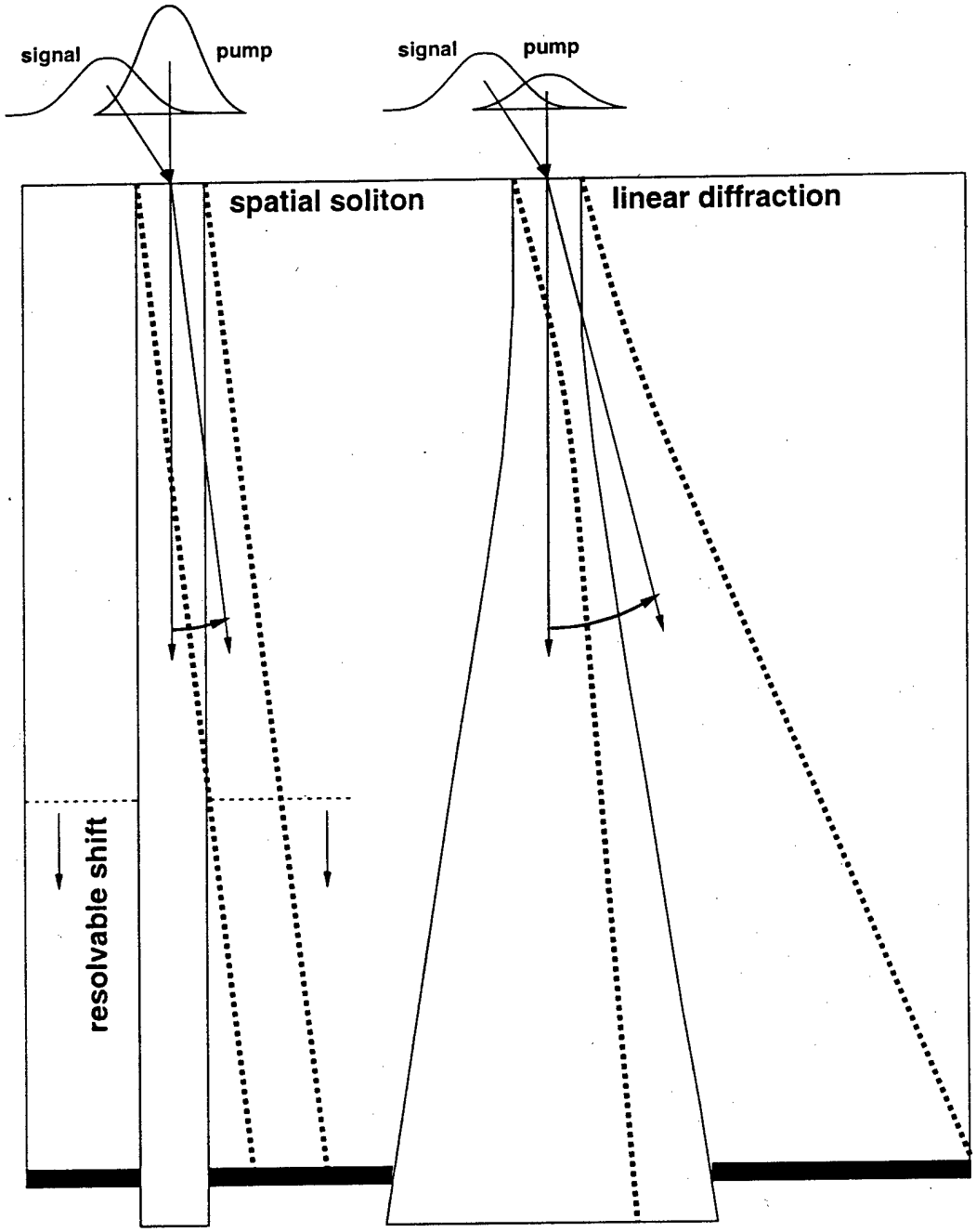

Figure 1.18: Logic gate geometry based upon the light-induced deflection of an optical "pump" beam away from a spatial aperture at the output. At one extreme, the pump can propagate nonlinearly as a spatial soliton (left), or at the other extreme, the pump can propagate linearly and diffract (right). Deflection is induced by the cross nonlinear interaction with a signal beam which is tilted with respect to the pump. The dashed contours represent the deflected pump.

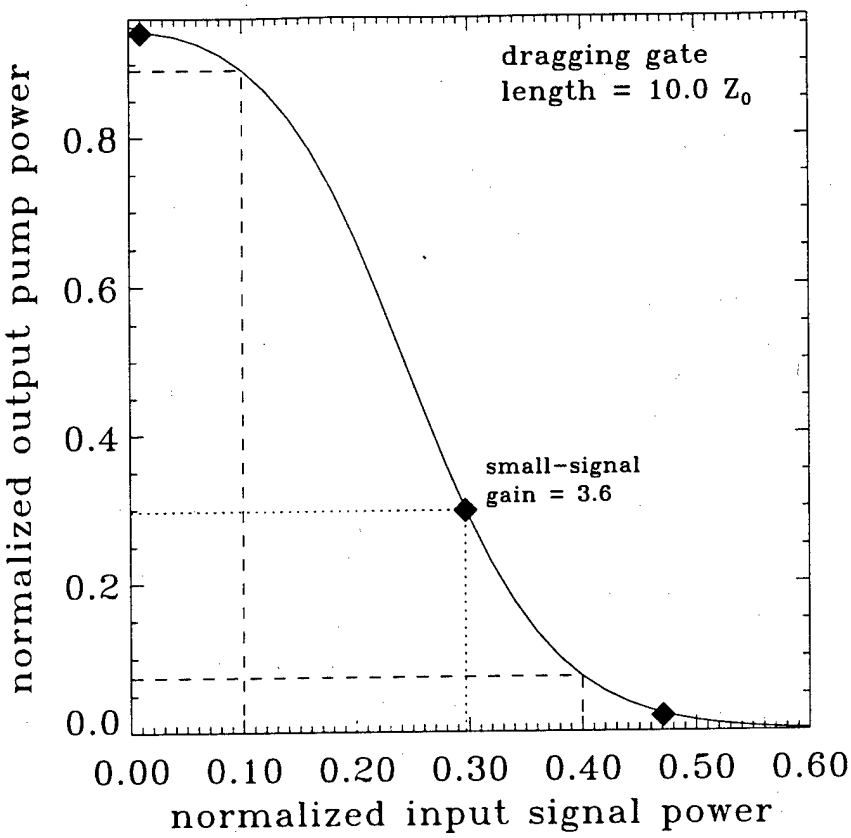

Figure 1.19: Transfer function for spatial soliton dragging logic gate demonstrating small-signal gain and saturated levels. The pump and signal are fundamental solitons of width w_0. The signal soliton amplitude is varied to obtain the increasing input power as indicated on the horizontal scale. This transfer curve illustrates a large-signal gain of 2.0, as discussed in section 5.4.

where, for consistency with temporal interaction equations, the angle of propagation θ of the signal A_y (which is analogous to group delay) is included explicitly in the paraxial approximation such that $\theta = k_x/k_0$. Here, k_0 is the wavenumber, n_2 is the nonlinear Kerr index, and A_x is the pump envelope. This is the base system of equations used in Chapter 5 for the study of the interaction between spatial solitons. Now, during propagation, each beam affects the other through cross-focusing. If large-signal gain is realized, then the pump exerts a greater attractive force on the signal than the signal does on the pump. Nevertheless, as mentioned previously, only a small angular deviation of the pump is needed. As in the case with the linear pump, two interaction scenarios can occur: each soliton simply deflects the other, or they form a bound, orbiting pair propagating at the weighted-mean angle [58]. The former is typically referred to as dragging [59], while the latter is referred to as trapping [65]. Soliton trapping is more likely to occur when the relative propagation angle is small and the solitons are nearly the same size, while deflection, or dragging, occurs for large angles and/or large gain. Note also that the optimal interaction may not occur in complete trapping, in which case part of the signal, the "shadow" [71], may remain bound to the pump, while the rest propagates at a much larger angle as an unbound linear diffractive wave. Therefore, this interaction will be generically referred to as dragging since the high gain situation is of ultimate interest.

Figure 1.19 shows a typical input-output relation for the spatial dragging logic gate. Note that the same function would be obtained for the temporal dragging gate as well. The most important feature to note is the region of small-signal gain at the input threshold level near 0.3, surrounded by saturated levels. The transfer function shows that the dragging gate has the same operational characteristics as an nMOS inverter [26], as shown in Figure 1.1. Here, the role of the electric power supply is provided by the pump wave and the role of the gate voltage is played by the signal wave. The presence of small-signal gain at the threshold level allows the output to be driven low with very sharp switching characteristics. The threshold level is the point on the curve in which the input and output levels are the same. For an input level beyond threshold, the output of the device is switched into a valid low state; therefore, the threshold level is the minimum input signal level required to switch the output

state of the device, and determines the operating point on the transfer curve where large signal gain is unity. When small signal gain is greater than unity at the threshold level, then the input switching level can be chosen such that large signal gain and contrast greater than unity can be obtained. The transfer curve is terminated by saturated levels, showing that over switching is not possible. As a result, when operating well into the "on" and "off" regimes, small variations in the input signal level are attenuated and do not affect proper gate operation, thus providing large noise margin. A more detailed examination of soliton logic gates, based on spatial interactions, is presented in Chapters 5 and 6.

Because these gates have two inputs and only one output, they are three-terminal devices with input-output isolation. Only the undeflected pump is passed on to subsequent gates, and it is important that the pump propagate stably over the length of the gate with little change in its physical parameters. This allows for restoration of not only the logic level (because of small-signal gain), but also restoration of timing, position, polarization, color, and shape, which is crucial to cascaded operation [25]. Cascading of these gates can result in more complex logic functionality, as discussed in the next paragraph. Since the pump and signal have orthogonal polarizations, the interaction between them is phase insensitive. In the case of linear polarizations, this is not strictly true because of the presence of phase-dependent vectorial four-wave mixing terms in the nonlinear polarization. Here, it is assumed that these terms can be neglected because of waveguide birefringence, which causes each polarization to propagate with a different phase velocity. This assumption is valid when the interaction length is much greater than the birefringence beat-length.

In analogy with temporal dragging logic gate [66] of Figure 1.17 b), logically complete, n-input NOR gates can be implemented with spatial dragging in an n-stage system in which a cascaded pump is dragged to the side and blocked by the presence of a signal in any stage, thereby producing a low output, as shown in Figure 5.35 for a two-input NOR. In this implementation, the same pump is passed through two (or more) subsequent stages, so that standardized output levels (in terms of both the inverter and the multi-input NOR) may not obtained due to absorption incurred in the additional stages. Complete logic level restoration is not strictly obtained either, because broadening of the pump in the presence of absorption also depends on total propagation distance, as discussed in section 5.3, such that the shape is not necessarily restored. However, complete logic level restoration is not necessary for a small cascade of gates (just as with electronic pass gates) and it is important to note that the pump soliton is the one that passes through multiple levels. Absorption will be the ultimate limit to the fan-in (number of stages) of this type of NOR gate. Another implementation, in which the total length of a multi-input NOR gate is held constant, so that the length of each signal input stage gets smaller with the degree of fan-in, results in both standardized output levels and complete restoration, and is discussed in more detail in sections 5.4.3 and 6.3.2.

The main benefit of the spatial dragging logic gate over the temporal dragging gate is that amplitude keyed logic is straightforward to implement while providing gain. In the spatial case, an aperture can be used to discriminate the output. For temporal dragging though, an ultrafast time gating mechanism is required to implement amplitude keyed logic instead of the more natural time-shift keyed logic [3]. A spectral filter is all that is necessary to implement amplitude keyed logic for temporal trapping, but the leverage of the dispersive delay line is lost and gain cannot be provided. Therefore, only the spatial dragging geometry has the simultaneous advantages of simple output state determination and the leverage of non-diffracting propagation which allows for large-signal gain. Additional advantages are spatial parallelism, as discussed previously, and latency. Typical spatial soliton logic gates as studied in this thesis are on the order of cm's long, while typical temporal soliton gates are on the order of 10's of m's. This results in a factor of 1000 reduction in latency. Much shorter temporal solitons can be used to reduce the length of the fiber-based gates, but higher-order temporal effects can cause problems as discussed in Chapter 6.

Spatial dragging of purely spatial solitons loses the advantages of gate-level temporal pipelining and low energies (due to complete confinement) of the temporal dragging gates, though, and spatial dragging between non-soliton pulses could yield partial switching behavior with low contrast, as shown in previous sections. That is why, in Chapter 6, this thesis studies spatial dragging of spatio-temporal solitary waves in order to retain the best features of short gate lengths, ultrafast operation and temporal pipelining, and low switching energies. The spatial dragging gate utilizing spatio-temporal solitons is perhaps the only all-optical switching and logic technology that satisfies all of the requirements for digital switching and logic and has the potential for implementation into large scale systems utilizing the high degrees of spatial and temporal parallelism available to optics.

Figure 1.20 shows the generalization of the deflection gate architecture to the use of 2-D spatio-temporal solitary waves. Utilization of fully-confined spatio-temporal waves allows for low energy operation and the additional flexibility to use spatial and/or temporal interactions. Here the focus is on spatial dragging, but temporal trapping/dragging may also occur and allow for the reduction of the requirements on allowable timing jitter between the pump and signal. Note that after the first gate, timing is restored in the system (because only the undeviated pump clock stream is passed) such that jitter no longer becomes a concern. Also, since the solitary wave does not disperse, temporal pipelining can be employed at the gate level, resulting in very high throughput which is independent of actual gate length. This architecture maps well onto the processing of a large number of independent data streams, such as ultra-fast time-division multiplexed transmission, bit-serial computation [20], and bit-serial digital signal processing [18], as discussed briefly in section 1.2.

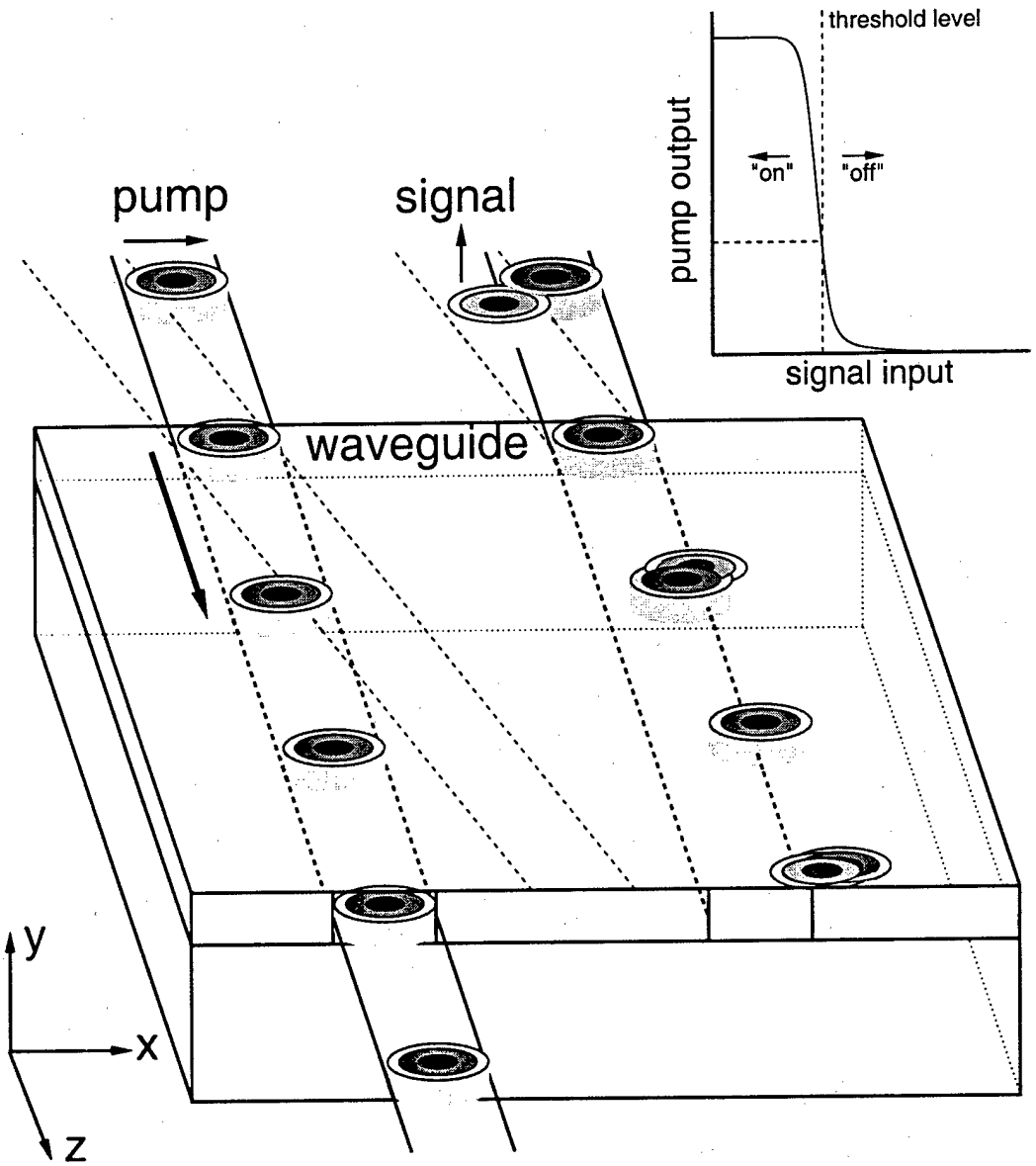

Figure 1.20: Spatio-temporal solitary wave dragging logic gate. A pump solitary wave (left) will propagate the length of the gate and pass through a spatial aperture at the output. In the presence of a tilted, orthogonally-polarized signal (right), mutual deflection will cause the pump to shift to the side and not pass through the aperture. The inset schematically shows the input-output relation for the gate. The threshold level is set at the point where the input and output are equal. This gate performs an inversion operation and can achieve large-signal gain.

It is important to make clear that dragging is an asymmetric interaction. The nonlinear waves are brought into temporal and/or spatial coincidence in linear propagation, such that they overlap at the beginning of nonlinear propagation. For a symmetric interaction, such as collision, the waves are brought into coincidence in purely nonlinear propagation where the nonlinear interaction forces are present both before and after the point of overlap. These interaction forces are symmetric in that the net change in frequency or angle is zero (the change before complete overlap is exactly compensated by the equal and opposite change after overlap), but with a small (not resolvable) residual temporal or spatial shift. Since the dragging interaction is asymmetric, the nonlinear interaction forces occur only after the point of overlap such that the frequency or angular change is not compensated. This is the key point in understanding the advantages of soliton dragging over other, symmetric, collision geometries.

Chapter 2

Optical Solitons

Outside of the communications, switching, and computing applications, optical solitary waves and optical solitons (and solitons in general) are interesting in their own right. An entire field of mathematics is devoted to the study of nonlinear integrable equations and their soliton solutions [131]. These nonlinear equations are associated with a linear scattering problem and time-evolution equation. The bound-state eigenvalues of the linear scattering equation correspond to the soliton solutions and only those solutions remain in the asymptotic limit of large time (or long distance). The nonlinear evolution of an arbitrary initial condition is described by decomposing into the linear eigenfunction basis set given by the scattering problem. These eigenvalues are then iso-spectrally evolved and transformed back to the original space using the inverse scattering transformation [73, 161, 162]. This thesis will not make direct use of the inverse scattering transform because in general the multi-dimensional vector nonlinear wave equations employed are not known to be integrable [163] and can be solved instead via more simple numerical and approximate analytical techniques.

Numerous examples of these integrable and non-integrable nonlinear wave equations exist in physics, but the examples from optics are most closely related to this thesis. There are many mechanisms of optical nonlinearity through which solitons or solitary waves can form, many of which will be discussed in section 2.1. The most ubiquitous example is the optical Kerr nonlinearity (section 2.2), which gives rise to the integrable (1+1)-D nonlinear Schrödinger (or NLS) equation, in both spatial (section 2.3) and temporal (section 2.4) forms. The multi-dimensional NLS equation (section 2.5) is not known to be integrable [163] and describes the propagation of optical waves with additional dimensions of linear and nonlinear behavior. With suitable modifications, the NLS equation serves as the basis for describing the soliton behavior necessary for the logic gates studied in this thesis.

2.1 Historical Background

A solitary wave is a nonlinear wave phenomenon that propagates without change. The most notable recorded discovery of a solitary wave occurred in 1834 when J. Scott Russell observed a solitary water wave in the Edinburgh-Glasgow canal [164,165]. Through laboratory experiments, Russell deduced that the wave speed is proportional to its amplitude, i.e. taller waves travel faster than shorter waves. This wave phenomenon is termed a gravity wave. He also deduced that an arbitrary initial profile will asymptotically evolve into multiple solitary waves, and that two solitary waves, with the taller one overtaking the shorter one, will interact and emerge undistorted [165]. These solitary waves were later called solitons by Zabusky and Kruskal [166]. In 1871 and 1876, respectively, Boussinesq and Lord Raleigh showed that, by assuming that the length of the solitary wave is much greater the water depth, such a solitary wave has a $\text{sech}^2()$ amplitude profile. At this point it was realized that the length of the solitary wave is inversely proportional to its amplitude, such that a shorter wave is longer than a taller wave.

The governing nonlinear wave equation for shallow water waves was derived by Korteweg and deVries in 1895 [167], now known as the KdV equation:

$$\frac{\partial u}{\partial t} + 6u\frac{\partial u}{\partial x} + \frac{\partial^3 u}{\partial x^3} = 0, \tag{2.1}$$

written in normalized form where u is the normalized amplitude of the wave as a function of position and time. In 1955, Fermi, Pasta, and Ulam [168] studied a numerical model closely related to discrete KdV, and in 1965, Zabusky and Kruskal numerically solved the KdV equation with periodic boundary conditions [166] and found that two or more KdV solitary waves do not break up upon collision. This particle-like nature led them to coin the term "soliton". In this thesis, the term solitary wave is used when it is not known that the nonlinear wave is indeed a soliton.

The first study of solitary wave phenomena in optics was the self-trapping of one- and two-dimensional filaments [169]. This was one study out of a large body of theoretical work that arose from experimental observations of beam filamentation due to self-focusing in liquids [170], bulk glasses and crystals [171, 172], and atomic gases [173]. Self-focusing was also determined responsible for anomalously low stimulated Raman scattering threshold intensities [174]. It was quickly realized in numerical studies based on the radial NLS equation [175] that two-dimensional nonlinear propagation could become unstable when diffraction does not balance self-focusing, leading to a focusing singularity. In fact, in two and three dimensions, the operating point representing the stationary solution where nonlinearity and diffraction balance is unstable, and results in the well-known critical collapse or blow-up phenomenon due to form instability [176], referred to as large-scale self-focusing [177] in two spatial dimensions. At some point in the process of focusing to a point, the beam breaks up into many filaments giving rise to small-scale self-trapping [178, 179] and is a result of modulational instability such that small transverse amplitude or phase perturbations cause a plane wave (or large scale filament) to decay into individual beams whose subsequent propagation dynamics depend on the scale of the perturbation [178].

Blow-up is an unphysical manifestation of the multi-dimensional NLS equation and indicates that the original assumptions used in the derivation of the equation break down. One mechanism of arresting this behavior is to include saturation of the nonlinear index [180, 181], resulting in stable self-trapping, thus explaining the stability of small-scale filaments. Another numerical study [179] showed the formation of small-scale filaments by following the self-focusing of a beam and subsequent breakup into an annular structure with the center portion resembling a small-scale filament. This ring structure was a result of the analysis being based on a radial nonlinear wave equation and by symmetry is the only structure possible, but will be indicative of an experimental situation in an isotropic medium in which strict radial symmetry of the initial conditions is maintained. The full picture of filamentary structure via transverse instability can only be captured with a two-dimensional analysis [178]. It was also realized that other higher-order nonlinear effects such as Raman and Brillouin scattering arrested collapse. The vector nonlinear wave equation derived in Chapter 3 includes non-paraxial terms which should also be included in the study of two-dimensional self-focusing, and will always prevent self-focusing to transverse cross-sectional areas smaller than order λ^2.

In 1972, Zakharov and Shabat [73] published the seminal paper on the inverse scattering transform for the (1+1)-D spatial optical NLS equation. A year later, Hasegawa and Tappert [132] derived the (1+1)-D temporal NLS equation for single-mode optical fiber and proposed the use of temporal solitons as data carriers for long-haul communications. It wasn't until 1980, though, that the first temporal optical soliton was observed experimentally [182]. This experiment was made possible by the availability of low-loss optical fiber in the anomalous dispersion regime (i.e. wavelengths longer than about 1.28 μm in fused silica fiber) and the color-center laser producing ps pulses in that regime. More recent work has focused attention on the modifications of the base NLS equation required to adequately describe long distance, short-pulse propagation in fiber. These modifications include: higher-order dispersion [30], such as third- and fourth-order; optical shock [183] (also called self-steepening or the intensity-dependent group-velocity [184]); and stimulated Raman scattering [185, 186] (responsible for the soliton self-frequency shift [145, 187]). Spatial optical solitons have also been realized experimentally in liquid CS_2 [188, 189], glass [118, 120] and AlGaAs [190] slab waveguides, and in CS_2 cells using highly elliptical beams [191] to avoid critical collapse inherent in (2+1)-D nonlinear propagation [175]. Much more theoretical and experimental attention has been paid to temporal solitons, though, due to their potential for important applications, such as long-distance fiber communications.

The previous paragraphs discussed optical solitons formed through the Kerr nonlinearity, but there are other nonlinear mechanisms in optics that also allow for solitons or solitary wave behavior. It has been known since the early 1970s that a third-order like nonlinearity can be obtained by cascading two second-order nonlinearities, such as occurs with the interaction between a fundamental and a field generated through DC rectification [192] or a generated second-harmonic [193]. The former mechanism has been shown theoretically [194, 195] to be described by the Davey-Stewartson (or Benny-Roskes) equation that exhibits stabilized 2-D spatio-temporal solitons [162], but to date, these solitons have not been observed experimentally. The latter mechanism has generated a new field of study in nonlinear optics as a means of producing extremely large, ultrafast third-order nonlinear effects [196]. Second-harmonic cascading been shown theoretically [197, 198] and experimentally to support bright spatial [199] and temporal solitons.

Other nonlinear mechanisms that support solitons include: formation of temporal solitons in the Stokes pulse via stimulated inter-pulse Raman scattering (SRS) [200, 201], dark 1-D [84] and stable 2-D vortex [202] spatial solitons in self-defocusing media with thermal nonlinearity, plasma filaments in air [203], and so-called photorefractive solitons [204]. These nonlinear mechanisms do not respond on the fs time scales of the Kerr and cascaded nonlinearities and, as a result, may not be as useful for ultrafast optical switching.

2.2 Preliminaries

This thesis concentrates on bright one-dimensional spatial solitons and multi-dimensional spatio-temporal solitary waves in media exhibiting optical Kerr nonlinearity. The entire class of dark solitons are omitted from study because they have nonzero boundary conditions at infinity, implying the requirement of infinite power/energy. This boundary condition can be relaxed somewhat by embedding a dark stripe or vortex within a localized bright diffracting background. A multi-dimensional hybrid bright/dark solitary wave, or symbion, may also exist for either bright in time and dark in space (which might be important for materials with $n_2 < 0$ and normal dispersion [205]), or bright in space and dark in time (which might be important for materials with $n_2 > 0$ and normal dispersion).

In one dimension of space, a spatial soliton exists through the balance between linear diffraction and nonlinear self-focusing [73, 169]. In time, a temporal soliton exists through the balance between linear dispersion and nonlinear self-phase modulation [132]. Kerr-type (nonresonant and non-dispersive) refractive nonlinearity is responsible for both self-focusing and self-phase modulation and is the fundamental requirement for the so-called nonlinear Schrödinger (NLS) solitons in optics which are the subject of this thesis. In one dimension, NLS solitons are stable, meaning that small amplitude or phase perturbations do not upset the balance between the opposing linear and nonlinear effects.

Under special conditions on the amplitude and beam width/pulse duration, optical solitons can form when the total refractive index is well-described by the expression

$$n = n_0 + n_2 |A|^2, \tag{2.2}$$

where n_0 is the linear index of refraction at some frequency ω_0 and n_2 is the total ultrafast nonlinear index, or Kerr index, with units of $\mathrm{cm}^2/\mathrm{V}^2$, and A is the electric field envelope with units $\mathrm{V}^2/\mathrm{cm}^2$. The definition of the nonlinear index in terms of the third-order susceptibility, given by equation 3.59, was chosen such that the above expression for the total refractive index is valid. A further generalization includes the quintic contribution to the refractive index through ultrafast $\chi^{(5)}$,

$$n = n_0 + n_2 |A|^2 + n_4^{\mathrm{eff}} |A|^4, \tag{2.3}$$

where the effective quintic index, with units $\mathrm{cm}^4/\mathrm{V}^4$, is defined as

$$n_4^{\mathrm{eff}} = n_4 - \frac{n_2^2}{2n_0}, \tag{2.4}$$

ignoring the cascaded contribution. The direct quintic index n_4 is discussed in section 3.1.3. In this case, the relative dielectric constant takes the form

$$\varepsilon = n^2 = n_0^2 + 2n_0 n_2 |A|^2 + 2n_0 n_4 |A|^4 + \cdots. \tag{2.5}$$

It is now seen that the second term in the definition of n_4^{eff} is the result of taking the square-root of the dielectric constant to obtain the refractive index. An additional contribution, produced through the process of cascading between the fundamental and third-harmonic, is derived in the multiple-scales analysis of section 3.2.

The quintic nonlinearity will be used in the multi-dimensional solitary wave case as a means for providing stability, but first 1-D spatial and temporal solitons as described by the cubic NLS equation will be discussed in detail.

2.3 1-D Spatial Optical Solitons

Spatial solitons result from the balance between linear diffraction and nonlinear self-focusing as shown in Figure 2.1. In one transverse spatial dimension, these solitons are stable such that the balance between the linear and nonlinear effects prevents small amplitude or phase perturbations from destroying the soliton. If a perturbation acts to widen the soliton, nonlinear self-focusing overpowers diffraction to restore balance. In the opposite case, if a perturbation narrows the soliton, linear diffraction overtakes self-focusing.

The analytical study of spatial solitons begins with the scalar Helmholtz equation which describes the propagation of a monochromatic beam in weakly inhomogeneous media

$$\nabla^2 \bar{A} + k^2 \bar{A} = 0 \tag{2.6}$$

where $E = \frac{1}{2}\bar{A}(x,y,z)e^{-i\omega_0 t} + \mathrm{cc}$ is the time-harmonic electric field, $k = \omega_0 n(\mathbf{r}, \omega_0)/c$ is allowed to have weak spatial variation, and the over bar indicates the presence of a fast phase variation due to propagation. Assuming for the moment that k has no spatial variation, equation 2.6 can be transformed into the spatial frequency, or Fourier, domain

$$\left[k_x^2 + k_y^2 + k_z^2\right] \bar{A} = k_0^2 \bar{A}, \tag{2.7}$$

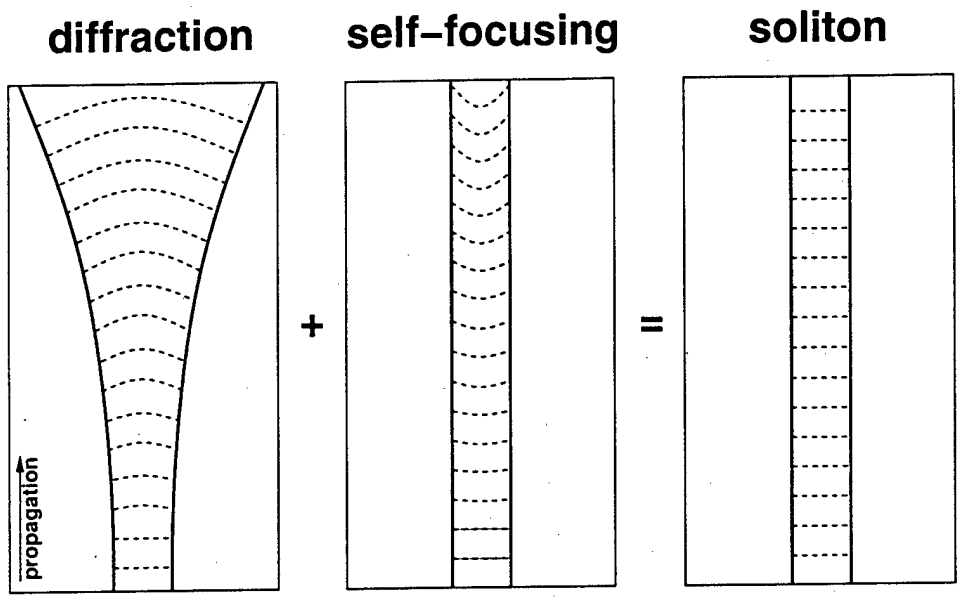

Figure 2.1: Illustration of the balance between linear diffraction and nonlinear self-focusing in the formation of a spatial optical soliton. The $1/e^2$ beam radius is plotted along with the dashed lines which represent the phase fronts.

where k_x, k_y and k_z are spatial frequency variables representing the Cartesian components of the optical wave vector. The solution to this equation is

$$\sqrt{k_x^2 + k_y^2 + k_z^2} = k_0, \tag{2.8}$$

which describes the momentum sphere of isotropic propagation and prescribes one spatial frequency component when the other two are known. This sets up an initial-value problem for propagation, such that when the electric field is known on a plane for example, guaranteeing that two of the three components of momentum are known, propagation to another parallel plane at an arbitrary distance is then fully determined by specifying the third component using equation 2.8. If z is the direction of propagation, then the initial-value problem has the solution in the Fourier domain

$$\tilde{A}(k_x, k_y, z) = e^{\pm i\sqrt{k_0^2 - k_x^2 - k_y^2}z}\tilde{A}(k_x, k_y, 0), \tag{2.9}$$

where $\tilde{A}(k_x, k_y, 0)$ is known by the Fourier transform of the initial field on the input plane. The field distribution $\overline{A}(x, y, z)$ at the observation plane is calculated by the inverse Fourier transform of $\tilde{A}(k_x, k_y, z)$. Linear diffraction is described in more detail in section 2.3.2 and Chapter 4.

In media of isotropic symmetry class with Kerr-type nonlinear index n_2, the inhomogeneous wave number is

$$k^2(|A|) = k_0^2 + 2k_0^2\frac{n_2}{n_0}|A|^2 \tag{2.10}$$

where the quintic nonlinear index is neglected. Substituting into equation 2.6 results in

$$\nabla^2\bar{A} + k_0^2\bar{A} + 2k_0^2\frac{n_2}{n_0}|A|^2\bar{A} = 0. \tag{2.11}$$

This equation describes the (2+1)-D spatial propagation of a beam in a weakly inhomogeneous, weakly nonlinear medium. Since the 1-D spatial soliton is of present interest, it is assumed that the beam is confined in the y dimension by a slab waveguide. As a result, assuming that the linearly guided and nonlinear soliton envelopes are separable, i.e.

$$\bar{A}(x, y, z) = \Phi(y)\bar{A}(x, z), \tag{2.12}$$

where $\Phi(y)$ represents the guided profile and is real and of unity magnitude, the nonlinear Helmholtz equation 2.11 reduces to

$$\frac{\partial^2\bar{A}}{\partial z^2} + \frac{\partial^2\bar{A}}{\partial x^2} + k_0^2\bar{A} + 2k_0^2\frac{n_2}{n_0}|A|^2\bar{A} = 0 \tag{2.13}$$

and is the starting point for the following analysis of 1-D spatial solitons.

Note that the effects of waveguide confinement have been formally neglected in equation 2.13. This omission can be remedied by using an effective wavenumber β^{eff} and nonlinear coefficient n_2^{eff} determined by the appropriate modal overlap integrals, but the analysis in the next two sections neglects the effects of transverse waveguide confinement for simplicity. The fully confined case of 2-D spatio-temporal solitary waves in a slab waveguide is discussed in full in Appendix C.

2.3.1 The Non-Paraxial Fundamental Soliton

A soliton is by definition a stationary solution, therefore, using the field amplitude ansatz

$$\bar{A}(x,z) = A(x)e^{i\beta z} \tag{2.14}$$

in equation 2.13, the stationary transverse envelope becomes the eigenfunction of the ordinary nonlinear differential equation

$$\frac{d^2A(x)}{dx^2} + \left[k_0^2 - \beta^2 + 2k_0^2\frac{n_2}{n_0}|A(x)|^2\right]A(x) = 0, \tag{2.15}$$

where β^2 is the eigenvalue and β represents the total wavenumber and contains both linear and nonlinear contributions.

The transverse envelope is assumed to be of the form [169]

$$A(x) = A_0 \operatorname{sech}\left(\frac{x}{w_0}\right), \tag{2.16}$$

where A_0 is the real amplitude and w_0 is a measure of the beam width. Since the soliton is non-diffracting, there is no transverse phase variation. The stationary solution is given by

$$A_0 = \frac{1}{k_0 w_0}\sqrt{\frac{n_0}{n_2}} \tag{2.17}$$

$$\beta^2 = k_0^2 + \frac{1}{w_0^2} = k_0^2\left[1 + \frac{n_2 A_0^2}{n_0}\right], \tag{2.18}$$

with the total wavenumber $\beta \approx k_0 + k_f n_2 A_0^2/2$ when the induced nonlinearity is small.

Since equation 2.13 is invariant under the unitary transformation

$$\begin{bmatrix} x' \\ z' \end{bmatrix} = \begin{bmatrix} \cos\theta & \sin\theta \\ -\sin\theta & \cos\theta \end{bmatrix}\begin{bmatrix} x \\ z \end{bmatrix}, \tag{2.19}$$

a more general stationary solution is given by

$$A(x',z') = A_0 \operatorname{sech}\left[\frac{\cos\theta\, x' - \sin\theta\, z'}{w_0}\right] e^{i\beta[\cos\theta\, z' + \sin\theta\, x']}. \tag{2.20}$$

Equation 2.20 is a fully linear and nonlinear non-paraxial solution when the optical field polarization is in the y direction such that vectorial effects are absent. Unfortunately, it is mathematically and numerically difficult to propagate this (or other) solution using the evolution equation 2.13; therefore, a common practice is to reduce this full Helmholtz equation to a parabolic one so that robust numerical techniques based on finite-difference or split-step methods, and analytic techniques such as the scattering/inverse-scattering transform, can be used. This procedure is carried out formally in Chapter 3 for the fully vectorial (3+1)-D and (2+1)-D evolution equations which uncovers the linear and nonlinear physics buried in the second-order equation 2.6, but done in an ad-hoc manner in the next section for the (1+1)-D case.

2.3.2 The Paraxial Fundamental Soliton

Paraxial propagation is described about some mean direction of propagation. For simplicity, choosing z to be this direction, the electric field envelope is assumed to be of the form

$$\bar{A}(x,z) = A(x,z)e^{ik_0 z}, \tag{2.21}$$

where $k_0 = \omega_0 n_0/c$ is the bulk propagation constant or wave number. The fast phase due to propagation is explicitly removed from the transverse envelope so that the slowly-varying amplitude (SVA) and paraxial approximations can be made. Substituting this expression into the nonlinear Helmholtz equation 2.13, and making the approximation

$$\left|\partial^2 A/\partial z^2\right| = \frac{1}{2k_0}\left|\frac{\partial^3 A}{\partial z^3} + \frac{\partial^3 A}{\partial z \partial x^2} + 2k_0^2 \frac{n_2}{n_0}\frac{\partial |A|^2 A}{\partial z}\right| \ll \left|2k_0 \partial A/\partial z\right|, \tag{2.22}$$

results in the (1+1)-D spatial NLS equation

$$2ik_0 \frac{\partial A}{\partial z} + \frac{\partial^2 A}{\partial x^2} + 2k_0^2 \frac{n_2}{n_0}|A|^2 A = 0. \tag{2.23}$$

The first two terms in equation 2.23 simply describe linear diffraction in the paraxial approximation which is seen by taking a transverse spatial Fourier transform

$$\frac{\partial \tilde{A}}{\partial z} = -i\frac{k_x^2}{2k_0}\tilde{A} \quad \Rightarrow \quad \tilde{A}(z) = \tilde{A}(0)e^{-i[k_x^2/2k_0]z}, \tag{2.24}$$

and reduces the z-directed accumulated phase from the maximum value k_0 to $k_0\left[1 - k_x^2/2k_0^2\right]$ due to the off-axis projection of the phase-velocity onto the mean direction of propagation z. This expression only allows for propagation in one direction (along z or very near to it) and is the result of the using the slowly-varying amplitude approximation which reduces the Helmholtz equation to a uni-directional wave equation. The SVAA is valid when backscattered radiation from linear or nonlinear inhomogeneity can be neglected to a given order of approximation, as discussed in Chapter 3.

Figure 2.2 illustrates diffraction in spatial frequency space. For full (2+1)-D spatial diffraction in isotropic space, the surface of allowed k vectors is a sphere. Diffraction in (1+1)-D as shown in the figure is represented by slicing the sphere with a plane passing through the origin, resulting in a circle. The paraxial approximation represents this circle as a parabola and is valid for small transverse spatial frequencies (small angular bandwidths). Linear propagation is described by appropriately phasing each transverse spatial frequency component $\tilde{A}(k_x)$ with $\exp(ik_z z)$, where $k_z = \sqrt{k_0^2 - k_x^2}$ in the non-paraxial case and $k_z \approx k_0 - k_x^2/2k_0$ in the paraxial case.

Figure 2.3 shows the diffraction of an initial $\mathrm{sech}(x/w_0)$ profile beam over 5 confocal distances. Here the confocal distance $Z_0 = \pi^2 w_0^2/\lambda$ is twice the Rayleigh range, which represents the distance over which the FWHM intensity pattern increases by $\sqrt{2}$ [1]. Note that the intensity FWHM is $1.7627 w_0$ [30].

Neglecting the diffraction term in equation 2.23 results in the nonlinear equation

$$i\frac{\partial A}{\partial z} + k_f n_2 |A|^2 A = 0, \tag{2.25}$$

where $k_f = \omega_0/c$ is the free-space wavenumber. The solution to this equation is written in the real space domain as

$$A(x,z) = e^{i\phi^{NL}(x,z)}A(x,0) \tag{2.26}$$

with the nonlinear phase accumulation

$$\phi^{NL}(x,z) = k_f n_2 \int_0^z \left|A(x,z')\right|^2 dz'. \tag{2.27}$$

For small $z = \Delta z$, the nonlinear phase is approximated by the expression

$$\phi^{NL}(x,\Delta z) \approx k_f n_2 \left|A(x,\Delta z/2)\right|^2 \Delta z \tag{2.28}$$

which is second-order accurate in Δz. This nonlinearly induced phase is illustrated in Figure 2.4 for propagation distance Δz and peak amplitude chosen such that the maximum nonlinear phase is 4 radians.

The spatial frequency space is the natural domain in which to solve the linear diffraction problem, while real space is the natural domain in which to solve the nonlinear problem (ignoring diffraction). This insight will be used in the development of the split-step Fourier method outlined in Chapter 4, which efficiently implements nonlinear propagation by switching between the two domains for linear diffraction and nonlinear refraction.

[1] Unlike the case for Gaussian beams, in the case of a sech(), this distance is not the same as that obtained by interpolating the far-field diffraction pattern, which results in a confocal distance $1.605\pi^2 w_0^2/\lambda$

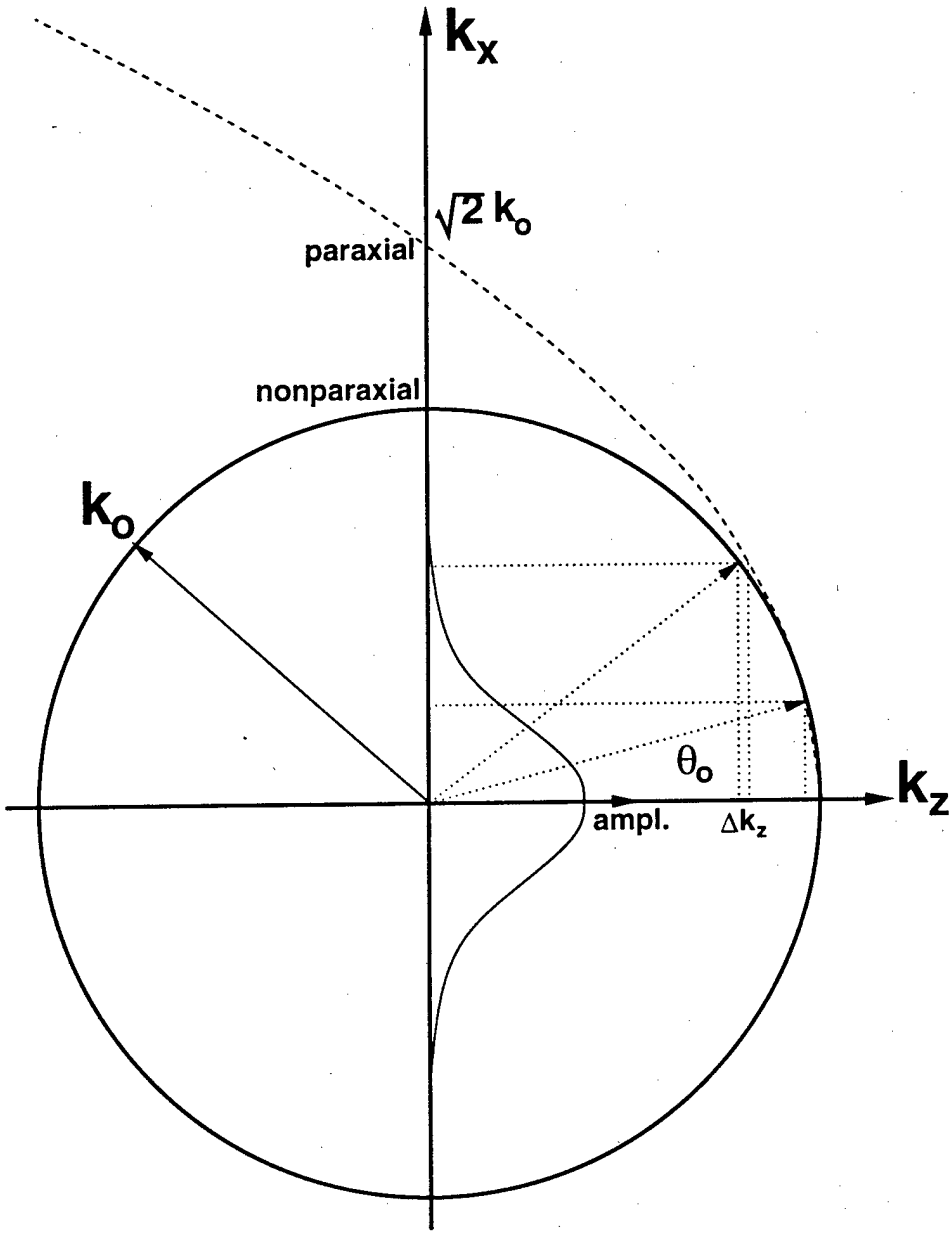

Figure 2.2: k-space diagram graphically showing the z-projected wavenumber k_z as a function of the transverse wavenumber k_x. The paraxial approximation is illustrated by the dashed curve. The transverse spatial frequency spectrum of a beam is shown in order to illustrate propagation by associating k_z with every k_x of the spectrum. The paraxial approximation is good for small k_x but breaks down for larger k_x where the associated value for k_z deviates significantly from the exact result.

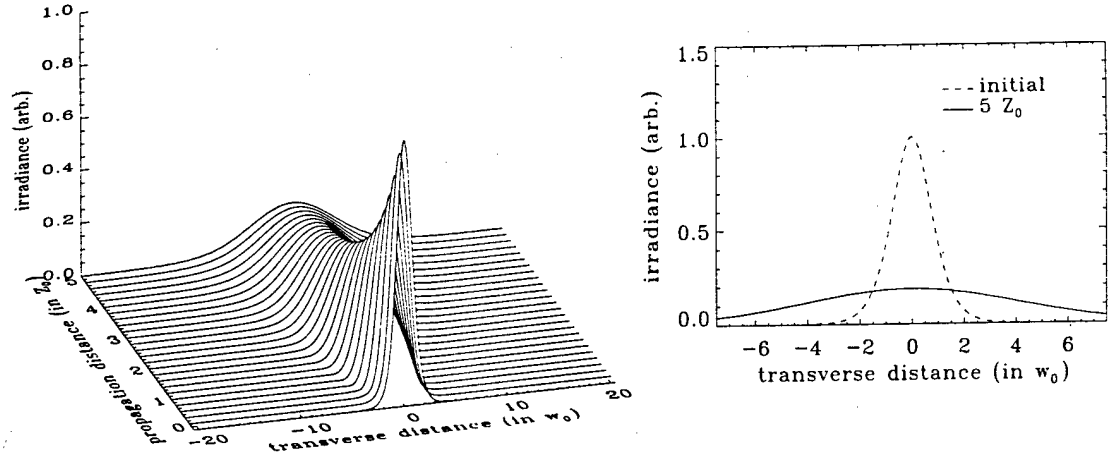

Figure 2.3: Diffraction of a beam of initial $\mathrm{sech}(x/w_0)$ profile, and intensity profile $\mathrm{sech}^2(x/w_0)$, where $w_0 = 14.2\ \mu$m and intensity FWHM 25 μm. After propagating 5 Z_0, where $Z_0 = \pi^2 w_0^2/\lambda = 1.85$ mm is the confocal distance, the intensity FWHM broadens to 140 μm.

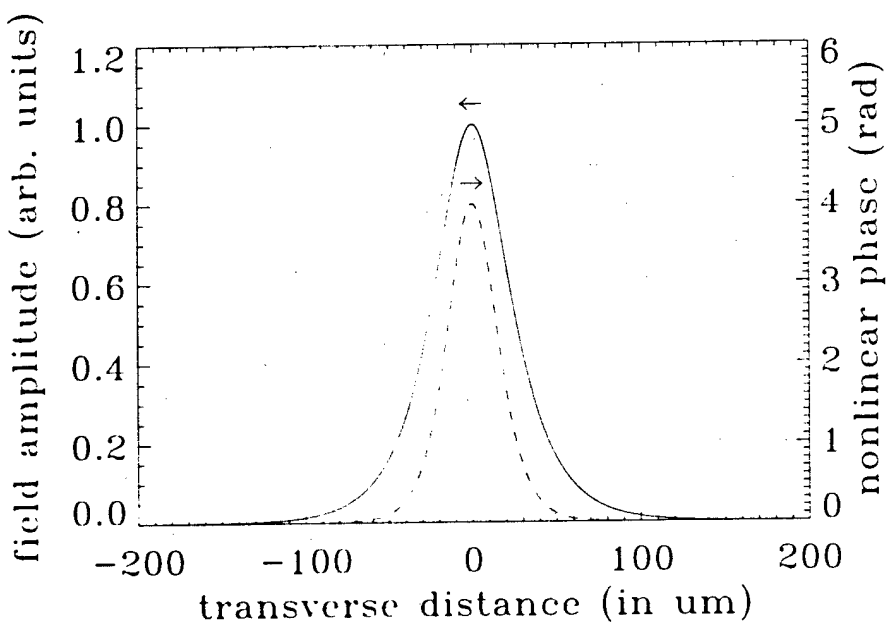

Figure 2.4: The nonlinear phase (dashed curve) induced by an electric field envelope (solid curve). The induced phase is proportional to the local intensity and in a material with positive Kerr nonlinearity, tends to reduce the phase velocity of the central portion of the beam resulting in a focusing, or lensing, effect.

Now, looking for a paraxial soliton solution, the stationary ansatz 2.14 is substituted into equation 2.23 with the result

$$\frac{d^2A(x)}{dx^2} + 2k_0\left[-\beta + k_f n_2 |A(x)|^2\right]A(x) = 0. \tag{2.29}$$

Assuming the fundamental soliton form of equation 2.16, the amplitude and phase become

$$A_0 = \frac{1}{k_0 w_0}\sqrt{\frac{n_0}{n_2}} \tag{2.30}$$

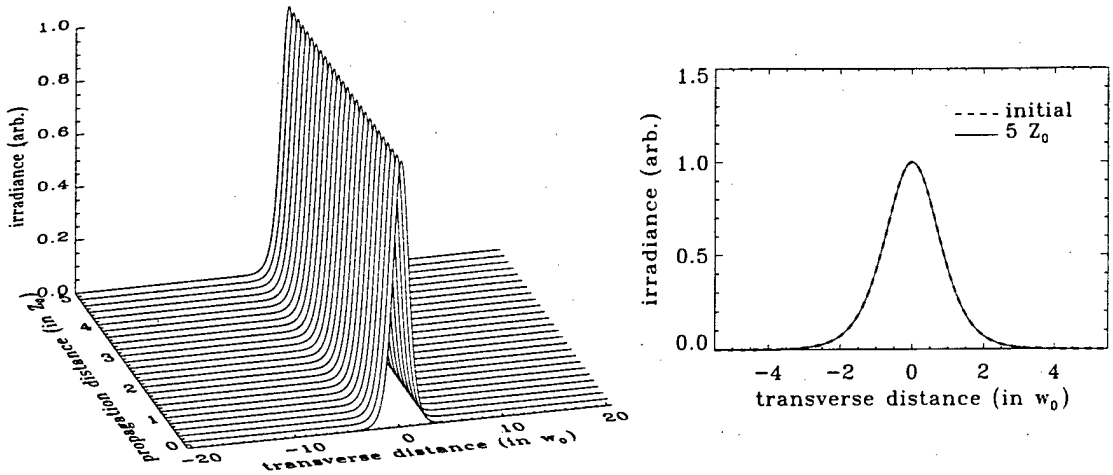

Figure 2.5: Spatial soliton beam of initial $\mathrm{sech}(x/w_0)$ amplitude profile, where $w_0 = 14.2\ \mu$m and intensity FWHM 25 μm. Even after propagating 5 Z_0, where $Z_0 = 1.85$ mm, the beam width and position are unchanged.

$$\beta = 1/2k_0w_0^2 = k_f n_2 A_0^2/2, \tag{2.31}$$

where the amplitude is the same as in the non-paraxial solution and β represents the slow phase nonlinear correction to the fast phase linear wavenumber k_0. The total wavenumber $k_0 + \beta$ is the same as that obtained in the non-paraxial case given by equation 2.18 when $w_0 \gg \lambda$. The nonlinear correction to the wave number β is half that obtained for a plane wave of amplitude A_0, and simply reflects the fact that the soliton does not have constant amplitude.

The full paraxial solution is written

$$\bar{A}(x,y,z) = \frac{1}{k_0 w_0}\sqrt{\frac{n_0}{n_2}}\,\Phi(y)\,\mathrm{sech}\left(\frac{x}{w_0}\right)e^{i[k_0+1/2k_0w_0^2]z}, \tag{2.32}$$

where the linearly guided profile $\Phi(y)$ and linear wavenumber k_0 are added for completeness. Spatial soliton propagation using the split-step numerical scheme of section 4.2.1 is shown in Figure 2.5 with $w_0 = 14.2\ \mu$m. After a propagation distance of 5 Z_0, the soliton is unchanged, thereby beating the limits imposed by linear diffraction as shown in Figure 2.3, which would result in spatial broadening by a factor of 5.6.

Defining the optical intensity with units W/cm^2

$$I(x,y,z) = \frac{\varepsilon_0 c n}{2}|A(x,y,z)|^2 = \frac{1}{2\eta}|A(x,y,z)|^2, \tag{2.33}$$

and neglecting the nonlinear contribution to the index and impedance, the intensity of the fundamental soliton is written

$$I(x,y,z) = \frac{\varepsilon_0 c}{2k_f^2 w_0^2 n_2}\,\Phi^2(y)\,\mathrm{sech}^2\left(\frac{x}{w_0}\right), \tag{2.34}$$

for n_2 in units of V^2/cm^2. The power of the soliton is

$$P(z) = \int\int I(x,y,z)dx\,dy = \frac{\varepsilon_0 c}{k_f^2 w_0 n_2}\int \Phi^2(y)dx \tag{2.35}$$

and has units of W. Note that $\int \mathrm{sech}^2(x/w_0)dy = 2w_0$.

From these expressions, it is clear that the peak intensity of the soliton increases inversely proportionally to the square of the width and the power of the soliton increases inversely proportionally to the width, so that a narrow soliton requires more power to launch and propagate than a broader one.

A further generalization of the paraxial soliton solution is given by

$$A(x,z) = A_0\,\mathrm{sech}\left(\frac{x-\theta z}{w_0}\right)e^{i[\delta k_x x+\beta z]}. \tag{2.36}$$

Substituting this expression into the NLS equation 2.23 results in

$$A_0 = \frac{1}{k_0 w_0}\sqrt{\frac{n_0}{n_2}} \tag{2.37}$$

$$\theta = \delta k_x / k_0 \tag{2.38}$$

$$\beta = \frac{1}{2k_0 w_0^2} - \frac{\delta k_x^2}{2k_0}, \tag{2.39}$$

which is the paraxial version of equation 2.20. Notice that, like the non-paraxial soliton solution, the NLS soliton solution has two free parameters: the width w_0 and angle of propagation θ.

2.4 1-D Temporal Optical Solitons

Temporal optical solitons result from the balance between linear dispersion and nonlinear self-phase modulation (SPM). In order to arrive at this one-dimensional system, the temporal soliton is confined transversely in an optical fiber. Even though the nonlinearity of silica glass is very small, optical fiber is an ideal system in which to perform experimental studies because of the very low linear loss ~ 0.2 dB/km ($\sim 5\times 10^{-7}$ cm^{-1}) and long interaction lengths [30]. Because a temporal soliton is inherently a one-dimensional nonlinear phenomenon described by the NLS equation, stability is guaranteed as it is in the one-dimensional spatial case.

The scalar wave equation describing temporal propagation in fiber is

$$\frac{\partial^2 \bar{A}}{\partial z^2} + k^2\left(\omega_0 + i\frac{\partial}{\partial t}\right)\bar{A} + 2\frac{n_0 n_2}{c^2}\left[\omega_0 + i\frac{\partial}{\partial t}\right]^2 |A|^2 \bar{A} = 0, \tag{2.40}$$

where the electric field $E = \frac{1}{2}\bar{A}(x,y,z,t)e^{-i\omega_0 t} + \text{cc}$ and Raman scattering has been neglected. The wave number function of the operator $\frac{\partial}{\partial t}$ is interpreted by its Taylor expansion [194], as shown in equation 2.44. Here, parenthesis enclose function arguments, while braces and brackets are used for grouping. The effects of Raman scattering are considered in section 2.4.3. Equation 2.40 describes the evolution of the pulse envelope, therefore soliton solutions are termed envelope solitons, in contrast to field soliton solutions of other nonlinear wave equations such as KdV.

In the following analysis it is assumed that $\bar{A}$ has the separable form $\bar{A} = \Phi(x,y)\bar{A}(z,t)$, where Φ is the transversely guided profile of unity magnitude. The effects of transverse guidance will be neglected for simplicity, as already done in equation 2.40. In Appendix C, the derivation in the case of spatio-temporal propagation in a slab waveguide is presented in full.

The linear part of equation 2.40 has the simple solution in the temporal frequency domain

$$\tilde{A}(\Delta\omega, z) = e^{\pm ik(\omega_0+\Delta\omega)z}\tilde{A}(\Delta\omega, 0). \tag{2.41}$$

The term $\Delta\omega$ describes some (small) frequency variation about the central frequency ω_0. Similar to the case for linear diffraction, linear dispersive propagation is fully described by phasing each temporal frequency component $\tilde{A}(\omega_0 + \Delta\omega)$ using the appropriate dispersive wave number $k(\omega_0 + \Delta\omega)$.

The variation in wavenumber k with wavelength is shown in Figure 2.6 for bulk silica glass, where waveguide dispersion is neglected. The linear and nonlinear optical properties of silica are discussed in more detail in Appendix D. Also shown is the wavelength dependence of the group delay coefficient, which is related to the wavenumber by $k' = \partial k/\partial\omega$, and can be evaluated in two forms

$$k'(\omega) = \frac{1}{c}\left[n(\omega) + \frac{\omega}{c}\frac{\partial n(\omega)}{\partial\omega}\right] \tag{2.42}$$

$$k'(\lambda) = \frac{1}{c}\left[n(\lambda) - \lambda\frac{\partial n(\lambda)}{\partial\lambda}\right]. \tag{2.43}$$

It is clear from the figure that when $\lambda > 1.28\ \mu$m, shorter wavelengths are delayed less than longer wavelengths, meaning that shorter wavelengths (higher frequencies) travel with a greater group velocity than longer wavelengths. This is the anomalous dispersion regime and is the regime in which bright temporal solitons can form with positive Kerr nonlinearity.

Much effort has been placed on using waveguide dispersion of fiber to tailor the overall dispersion characteristics. One example of this is dispersion-shifted fiber, in which the zero value of group-delay dispersion is shifted to longer wavelengths, particularly near 1.55 μm where the fiber loss is minimum. Double or quadruple clad fiber has flattened dispersion characteristics where the GDD is small and nearly uniform over a 25 nm range [30]. Both of these examples are used mainly for linear propagation where dispersion is not compensated by SPM. Appendix D briefly covers the effects of waveguide parameters on the overall linear dispersion relation.

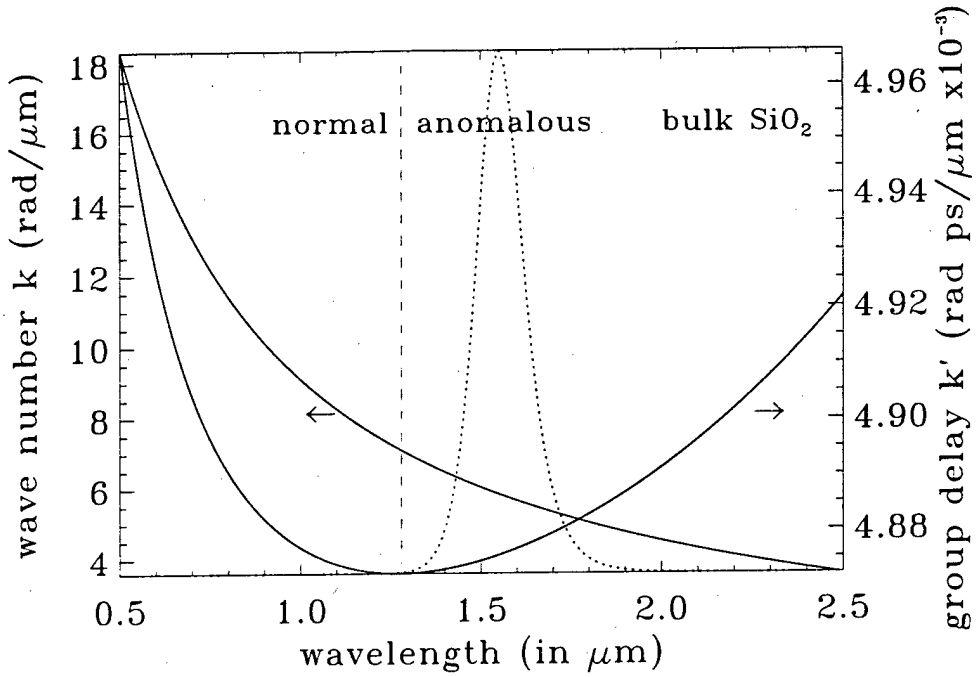

Figure 2.6: Wave number and group delay versus wavelength for bulk silica. The dashed vertical line separates the normal (NGDD) and anomalous (AGDD) dispersion regimes. The spectrum of a 16.5 fs intensity FWHM sech() pulse with time-bandwidth product 0.316 is also shown. Linear dispersive propagation occurs by phasing each temporal frequency component using the appropriate wave number.

2.4.1 The Non-SVEA Fundamental Soliton

It is not known that equation 2.40 has a general solution. There are solutions for specific material parameter values when the full dispersion relation $k^2(\omega)$ is truncated at a given order. This truncation amounts to making the slowly-varying envelope approximation (SVEA), although the standard SVEA keeps terms only up to second-order in time derivatives and results in the temporal NLS equation.

An analytic solution to equation 2.40 has been obtained [206] keeping linear dispersion terms up to fourth-order in time derivatives and all nonlinear terms, excluding Raman scattering. To fourth order, the linear dispersion is

$$k^2\left(\omega_0 + i\frac{\partial}{\partial t}\right) \approx k_0^2 + 2ik_0k_0'\frac{\partial}{\partial t} - \left[k_0'^2 + k_0k_0''\right]\frac{\partial^2}{\partial t^2} - \frac{i}{3}\left[3k_0'k_0'' + k_0k_0'''\right]\frac{\partial^3}{\partial t^3} + \frac{1}{12}\left[3k_0''^2 + 4k_0'k_0''' + k_0k_0''''\right]\frac{\partial^4}{\partial t^4}. \tag{2.44}$$

With this approximation, equation 2.40 can be rewritten

$$\frac{\partial^2\bar{A}}{\partial z^2} + k_0^2\bar{A} + 2ik_0k_0'\frac{\partial\bar{A}}{\partial t} - \left[k_0'^2 + k_0k_0''\right]\frac{\partial^2\bar{A}}{\partial t^2} - \frac{i}{3}\left[3k_0'k_0'' + k_0k_0'''\right]\frac{\partial^3\bar{A}}{\partial t^3} + \frac{1}{12}\left[3k_0''^2 + 4k_0'k_0''' + k_0k_0''''\right]\frac{\partial^4\bar{A}}{\partial t^4} + 2n_0n_2\left[k_f^2 + \frac{2ik_f}{c}\frac{\partial}{\partial t} - \frac{1}{c^2}\frac{\partial^2}{\partial t^2}\right]|A|^2\bar{A} = 0. \tag{2.45}$$

Notice that the SVAA has not been made, even though the SVEA has been made to fourth-order in time derivatives. Equation 2.45 will still be referred to as a non-SVEA equation because it includes two orders of time derivatives beyond the standard SVEA equation.

A solitary wave solution to equation 2.45 is given by [206]

$$\bar{A}(z,t) = A_0 \operatorname{sech}\left(\frac{t - z/v}{\tau_0}\right) e^{i[\beta z - \delta\omega t]}, \tag{2.46}$$

where the expressions for the quantities A_0, ν, τ_0, β and $\delta\omega$ can be found in the reference. One important property of the solution is that all of the parameters are determined by the material constants; there are no free parameters so only one solitary wave profile can be a self-consistent solution. This is unlike the NLS case in which there are two free parameters - width/duration (or amplitude) and propagation angle/frequency [117]. A condition on the existence of the solution 2.46 is that the material dispersion parameters k_0'', k_0''' and k_0'''' are negative, which can be accomplished using quadruple-clad fiber for example [207].

Another property of this solution is that, like the non-paraxial spatial soliton solution of the previous section, there is no backscatter of radiation from the induced inhomogeneity due to the nonlinear index. This is because the wave is a stationary state and does not change with propagation, therefore there is no energy loss due to scattering. The stability properties of this non-SVEA solution have not been studied to date, and it should be pointed out that experimental realization may be difficult due to the restrictive nature of the solution.

2.4.2 The SVEA Fundamental Soliton

Writing the field amplitude in terms of a fast propagation phase and slowly-varying envelope,

$$\bar{A}(z,t) = A(z,t)e^{ik_0 z}, \tag{2.47}$$

and substituting into equation 2.40, the (1+1)-dimensional scalar nonlinear wave equation usually considered for soliton propagation in optical fiber [132] is obtained

$$2ik_0\left[\frac{\partial A}{\partial z} + k_0'\frac{\partial A}{\partial t}\right] - k_0 k_0''\frac{\partial^2 A}{\partial t^2} + 2k_0^2\frac{n_2}{n_0}|A|^2 A = 0, \tag{2.48}$$

where the slowly-varying amplitude and envelope approximations have been made. The quantity in brackets simply indicates that the wave nominally moves at the group velocity $v_g = 1/k_0'$. This quantity can be simplified by making the transformation into the reduced time coordinates

$$\begin{aligned} T &= t - k_0' z \\ Z &= z. \end{aligned} \tag{2.49}$$

and noting that

$$\frac{\partial}{\partial t} = \frac{\partial T}{\partial t}\frac{\partial}{\partial T} + \frac{\partial Z}{\partial t}\frac{\partial}{\partial Z} = \frac{\partial}{\partial T} \tag{2.50}$$

$$\frac{\partial}{\partial z} = \frac{\partial T}{\partial z}\frac{\partial}{\partial T} + \frac{\partial Z}{\partial z}\frac{\partial}{\partial Z} = -k_0'\frac{\partial}{\partial T} + \frac{\partial}{\partial Z}. \tag{2.51}$$

With these substitutions, equation 2.48 can be written

$$2ik_0\frac{\partial A}{\partial z} - k_0 k_0''\frac{\partial^2 A}{\partial T^2} + 2k_0^2\frac{n_2}{n_0}|A|^2 A = 0, \tag{2.52}$$

which is the temporal nonlinear Schrödinger (NLS) equation. Apart from a scaling factor, this equation is the same as the (1+1)-D spatial NLS equation. For bright soliton solutions analogous to equation 2.32, it is clear that $k_0'' < 0$, meaning that the wave propagates in the anomalous dispersion regime.

By using the transformation 2.49, the coordinate system is changed such that the pulse moving with the group velocity $1/k_0'$ is stationary on the reduced time axis T, instead of moving on the time axis t at the group velocity. This results in the leading-order frequency-dependent correction to the wavenumber k_0 being proportional to the group-delay dispersion coefficient k_0'', or

$$k(\omega) \approx k_0 + \frac{1}{2}\Delta\omega^2 k_0'', \tag{2.53}$$

where $k_0 = k(\omega_0)$ and $\Delta\omega = \omega - \omega_0$.

The linear part of equation 2.52 has a simple solution in the temporal frequency domain

$$\tilde{A}(\Delta\omega, z) = e^{i[k_0''\Delta\omega^2/2]z}\tilde{A}(\Delta\omega, 0). \tag{2.54}$$

Analogous to paraxial linear spatial diffraction, linear dispersion is described by phasing each temporal frequency component with the appropriate quadratic phase factor $e^{ik_0''\Delta\omega^2 z/2}$ in this case where SVEA was made such that higher-order dispersion is

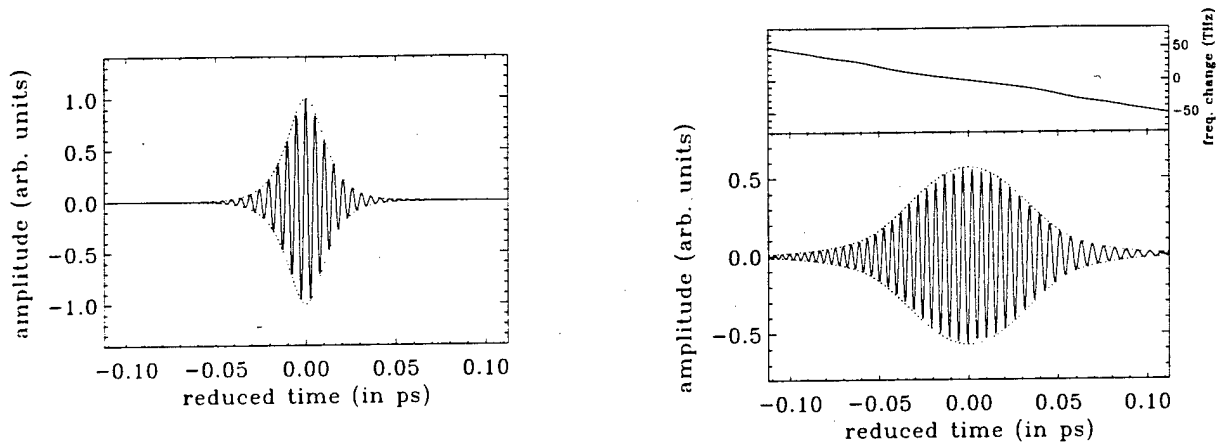

Figure 2.7: Effect of negative group-delay dispersion on a 16.5 fs quasi-monochromatic wavepacket with $\lambda_f = 1.55\ \mu$m. The initial sech() packet is shown on the left and the dispersed packet on the right. The electric field oscillation at optical frequencies is shown for illustrative purposes.

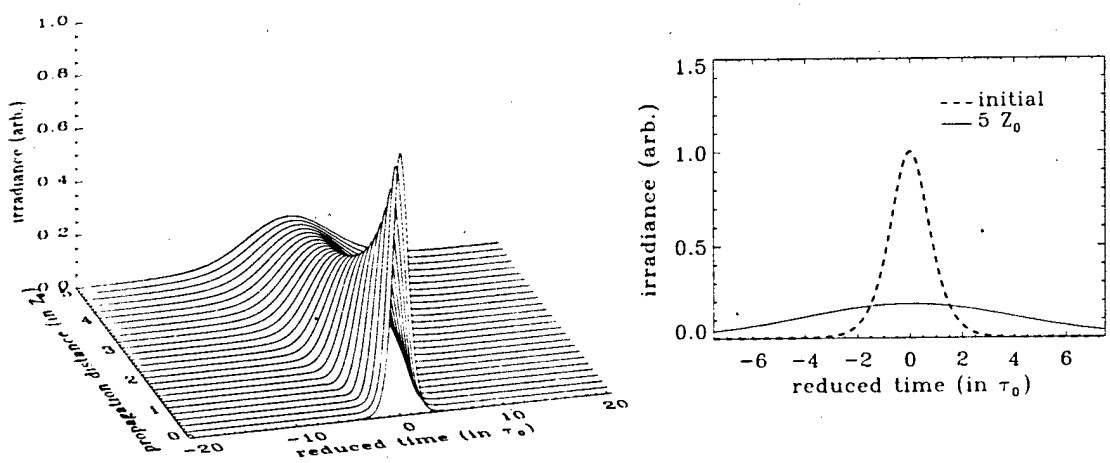

Figure 2.8: Dispersion of a pulse of initial sech(T/τ_0) amplitude profile, where τ_0 = 9.36 fs and intensity FWHM duration 16.5 fs. After propagating 5 Z_0, where $Z_0 = \pi\tau_0^2/2|k_0''|$ = 4.93 mm = $2L_D/\pi$ is the dispersive confocal distance and L_D is the standard dispersion length, the pulse FWHM broadens to 91.5 fs.

neglected. The dispersion of a wavepacket is illustrated in Figure 2.7 in the time domain. Even though group delay dispersion is an envelope phenomenon, the local phase of the envelope affects the underlying carrier. The figure indicates that in the dispersed envelope, higher frequencies move towards the pulse leading edge (negative time) and lower frequencies move towards the trailing edge (positive time), characteristic of the AGDD regime.

Figure 2.8 shows the effect of group-delay dispersion on a 16.5 fs FWHM pulse envelope over the dispersive equivalent distance of 5 Z_0. Note that higher-order dispersive effects must be considered for this wavepacket, but are presently neglected for illustrative purposes. The definition of Z_0 is obtained by using the substitution $\tau_0 \rightarrow w_0\sqrt{k_0|k_0''|}$ in the definition of the confocal distance used for spatial diffraction of the sech(x/w_0) profile. With the consideration of only group-delay dispersion, the broadening of the temporal profile depends on the magnitude of GDD, not the sign. The chirp of the carrier does depend on the sign of GDD, as shown in Figure 2.7.

The nonlinear part of equation 2.52 has the solution

$$A(T,z) = e^{i\phi^{NL}(T,z)}A(0) \tag{2.55}$$

with the nonlinear phase accumulation

$$\phi^{NL}(T,z) = k_f n_2 \int_0^z |A(T,z')|^2 dz'. \tag{2.56}$$

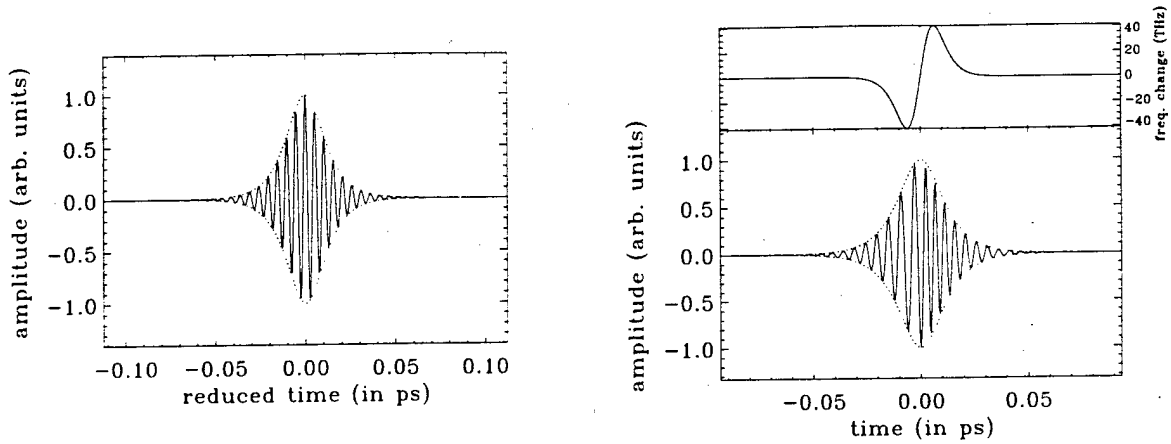

Figure 2.9: Effect of positive self-phase modulation on a 16.5 fs quasi-monochromatic wavepacket where the initial sech() packet is on the left and the nonlinearly modulated packet on the right, with π peak nonlinear phase change. Positive self-phase modulation reduces the phase velocity proportionally to the square of the field envelope resulting in an instantaneous frequency shift (top right), such that the pulse leading edge is downshifted and the pulse trailing edge is upshifted.

Because of the nonlinear phase modulation, there is an instantaneous frequency change across the pulse envelope. This frequency shift is defined as

$$\delta\omega = -\frac{\partial\phi^{\mathrm{NL}}}{\partial T} \approx -k_f n_2 \Delta z \frac{\partial |A(T,\Delta z/2)|^2}{\partial T}, \tag{2.57}$$

and is known as self-phase modulation (SPM) [30]. This effect is illustrated in Figure 2.9. The frequencies at the center of the pulse are not shifted because the derivative there is zero. At the inflection points of the envelope the derivative is maximum resulting in the largest frequency shift such that the leading edge is downshifted while the trailing edge is upshifted for positive SPM. Therefore, in the anomalous dispersion regime, the leading edge will travel with a slower group velocity than the trailing edge. The net effect is a narrowing, or compression, of the pulse and a temporal soliton results from the dynamical balance between positive SPM and linear dispersion in the anomalous regime. This balance is the reason for the existence of stable temporal solitons. In the normal regime, pulse lengthening is enhanced due to positive SPM.

It is clear from Figure 2.9 that, even though the envelope amplitude is unchanged, SPM alters the phase and hence the spectral content. This phenomenon is known as SPM-induced spectral broadening and is shown in Figure 2.10 by comparing the temporal Fourier transforms of the two wavepackets in Figure 2.9, where significant spectral broadening has occurred. In the absence of asymmetric, higher-order effects, spectral broadening is symmetric about the central frequency.

By analogy with the 1-D spatial soliton, the existence of a temporal soliton of the form

$$A(T,z) = A_0 \operatorname{sech}\left(\frac{T}{\tau_0}\right) e^{i\beta z} \tag{2.58}$$

is postulated where β is the nonlinear wave number correction. Using this trial solution in equation 2.52 results in

$$A_0^2 = -\frac{k_0'' n_0}{k_0 n_2 \tau_0^2} \tag{2.59}$$

$$\beta = -k_0''/2\tau_0^2 = k_f n_2 A_0^2/2. \tag{2.60}$$

In order for the amplitude A_0 to be real, $k_0'' < 0$, which is the anomalous dispersion regime as anticipated. By comparing the expression for the amplitude in the temporal and spatial cases, there is a correspondence between the temporal duration and spatial width give by $\tau_0 = \sqrt{-k_0 k_0''}\, w_0$, also indicating that $k_0'' < 0$ in order for τ_0 to be real.

The full SVEA temporal soliton solution is then

$$\bar{A}(x,y,z,T) = \frac{1}{\tau_0}\sqrt{\frac{-k_0'' n_0}{k_0 n_2}}\, \Phi(x,y) \operatorname{sech}\left(\frac{T}{\tau_0}\right) e^{i[k_0 - k_0''/2\tau_0^2]z}, \tag{2.61}$$

where the guided profile $\Phi(x,y)$ and linear wave number k_0 are added for completeness. The numerical propagation of a temporal soliton is shown in Figure 2.11 over 5 Z_0. As for the spatial soliton, the pulse duration and position in the reduced time coordinate frame are unchanged.

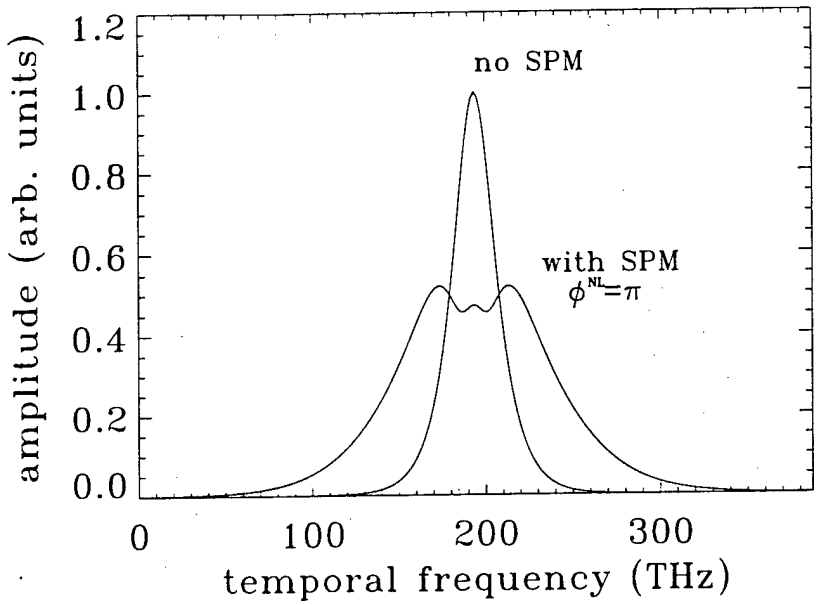

Figure 2.10: Self-phase modulation induced spectral broadening. The peak nonlinear phase change is π, resulting in spectral broadening by greater than a factor of 2. Subsequent pulse compression utilizing the appropriate net negative group-delay dispersion will result in a pulse shorter than the initial pulse.

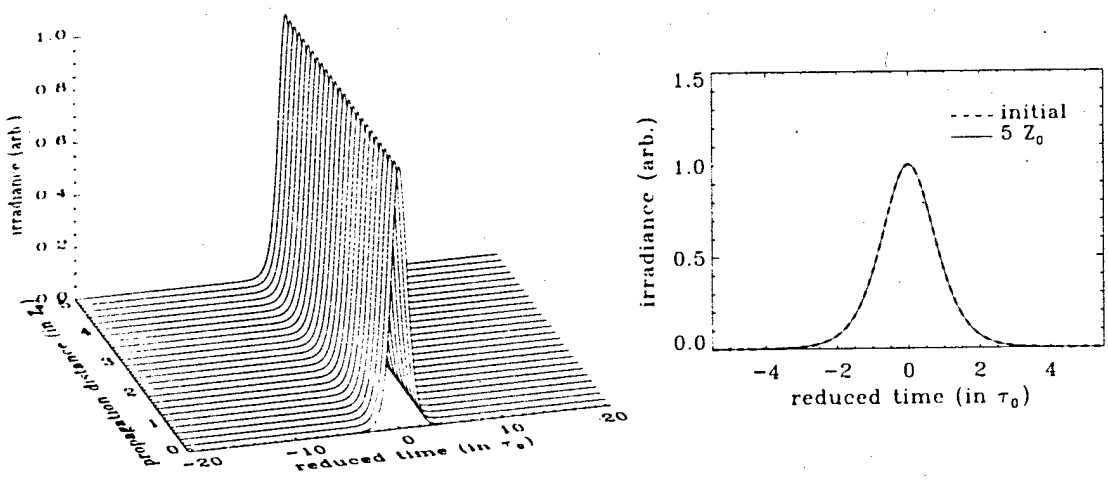

Figure 2.11: Temporal soliton pulse of initial sech(T/τ_0) profile, where $\tau_0 = 9.36$ fs and intensity FWHM duration 16.5 fs. After propagating 5 Z_0, where Z_0 = 4.93 mm, the pulse duration and position are unchanged.

The optical intensity is given by

$$I(x,y,z,T) = -\frac{\varepsilon_0 c n(x,y) k_0''}{2k_f \tau_0^2 n_2}\, \Phi^2(x,y)\, \mathrm{sech}^2\left(\frac{T}{\tau_0}\right), \tag{2.62}$$

where the spatial variation of the linear refractive index responsible for transverse guidance is retained. The optical power of the soliton is

$$P(z,T) = -\frac{\varepsilon_0 c n_0 k_0'' A_{\mathrm{eff}}}{2k_f \tau_0^2 n_2}\, \mathrm{sech}^2\left(\frac{T}{\tau_0}\right), \tag{2.63}$$

and the effective transverse spatial area is defined by the expression

$$A_{\text{eff}} = \frac{1}{n_0} \int\int n(x,y)\, \Phi^2(x,y)\, dxdy. \tag{2.64}$$

The total energy of the soliton is then

$$E = -\frac{\varepsilon_0 c n_0 k_0'' A_{\text{eff}}}{k_f \tau_0 n_2}, \tag{2.65}$$

with the same scaling as the 1-D spatial soliton.

As was done for the spatial paraxial soliton solution, the temporal SVEA soliton solution can be generalized to the form

$$A(z,T) = A_0 \operatorname{sech}\left(\frac{T - \delta k_0' z}{\tau_0}\right) e^{i[\beta z - \delta\omega T]}. \tag{2.66}$$

Substituting into the temporal NLS equation 2.52 results in

$$A_0^2 = -\frac{k_0'' n_0}{k_0 n_2 \tau_0^2} \tag{2.67}$$

$$\beta = -\frac{k_0''}{2\tau_0^2} + \frac{\delta\omega^2 k_0''}{2} \tag{2.68}$$

$$\delta k_0' = \delta\omega k_0''. \tag{2.69}$$

This result simply means that a change in optical frequency $\delta\omega$ changes the linear wave number from k_0 to $k_0 + \delta\omega^2 k_0''/2$ and the group delay from k_0' to $k_0' + \delta\omega k_0''$. Notice that the amplitude is unchanged which is the result of neglecting the third-order dispersion contribution k_0''' in the NLS equation.

2.4.3 Higher-Order 1-D Temporal NLS Solitons

Taking the temporal nonlinear wave equation one order of approximation beyond SVEA results in the modified NLS, or mNLS, equation

$$\begin{aligned} 2ik_0 \frac{\partial A}{\partial z} - k_0 k_0'' \frac{\partial^2 A}{\partial T^2} - \frac{i}{3} k_0 k_0''' \frac{\partial^3 A}{\partial T^3} \\ + 2k_0^2 \frac{n_2}{n_0} |A|^2 A + 4ik_f n_2 \left[\frac{n_0}{c} - \frac{k_0'}{2}\right] \frac{\partial |A|^2 A}{\partial T} = 0. \end{aligned} \tag{2.70}$$

A similar equation was previously considered [140] but lacked the correct form of the shock term. As shown in Chapter 3, this is the order at which the effects of stimulated Raman scattering also appear for the given scalings. Raman scattering is a dissipative effect and is considered in the next section on higher-order temporal effects.

A solution to the mNLS equation is given by

$$A(z,T) = A_0 \operatorname{sech}\left(\frac{T - \delta k_0' z}{\tau_0}\right) e^{i[\beta z - \delta\omega T]}, \tag{2.71}$$

with the following parameter values

$$A_0^2 = -\frac{k_0 k_0'''}{6 k_f n_2 \tau_0^2 \left[n_0/c - k_0'/2\right]} \tag{2.72}$$

$$\beta = -\frac{1}{2\tau_0^2}\left[k_0'' + \delta\omega k_0'''\right] + \frac{\delta\omega^2 k_0''}{2} + \frac{\delta\omega^3 k_0'''}{6} \tag{2.73}$$

$$\delta k_0' = \delta\omega k_0'' + \frac{\delta\omega^2 k_0'''}{2} - \frac{k_0'''}{6\tau_0^2} \tag{2.74}$$

$$\delta\omega = \frac{k_0}{4\left[n_0/c - k_0'/2\right]} - \frac{3k_0''}{2k_0'''}. \tag{2.75}$$

The only free parameter is the pulse duration τ_0, which allows for multiple solitons of different durations/amplitudes to be used for switching. Stability has not been investigated theoretically, but numerical simulation verifies that the solution propagates

stably. Note that this solution is a generalization of that obtained previously [140] in which temporal walkoff in the reduced time coordinate frame was not allowed, resulting in no free parameters. This is explained further below.

There are two special cases of interest in which $\delta k_0' = 0$ and $\delta\omega = 0$. When $\delta k_0' = 0$, there is no pulse walkoff in the reduced-time coordinate frame. In this case there are no free parameters [140] since the pulse duration is now fixed at the value

$$\tau_0^2\big|_{\delta k_0'=0} = \frac{k_0'''}{6\left[\delta\omega k_0'' + \frac{1}{2}\delta\omega^2 k_0'''\right]}. \tag{2.76}$$

Another way of expressing this relationship is to determine the value of TOD needed to sustain a given pulse duration. Therefore, choosing the pulse duration τ_0 as a "free" parameter, the following conditions hold

$$\delta\omega\big|_{\delta k_0'=0} = \frac{2\tau_0 k_0 - \sqrt{4k_0^2\tau_0^2 - 16\left[n_0/c - k_0'/2\right]^2}}{4\tau_0\left[n_0/c - k_0'/2\right]} \tag{2.77}$$

$$k_0'''\big|_{\delta k_0'=0} = -\frac{6\delta\omega k_0''\tau_0^2}{3\delta\omega^2\tau_0^2 - 1}, \tag{2.78}$$

where the '-' sign was chosen in front of the square-root as the proper solution which is verified by numerical simulation.

The other interesting case is when $\delta\omega = 0$, meaning that the original choice of center frequency ω_0 is a solution to the mNLS equation. This can only occur when the material dispersion parameters satisfy the condition

$$k_0'''\big|_{\delta\omega=0} = \frac{6k_0''\left[n_0/c - k_0'/2\right]}{k_0}, \tag{2.79}$$

such that the change in group delay is written

$$\delta k_0'\big|_{\delta\omega=0} = -\frac{k_0''\left[n_0/c - k_0'/2\right]}{k_0\tau_0^2}. \tag{2.80}$$

Note that τ_0 remains a free parameter. The temporal walkoff in the reduced time coordinate frame can be eliminated by redefining the coordinate transformation as $T = t - (k_0' + \delta k_0')z$.

A special case of mNLS, written in normalized form, is known to be integrable [208]

$$i\frac{\partial u}{\partial z} + \frac{1}{2}\frac{\partial^2 u}{\partial T^2} + |u|^2 u + i\beta\left[\frac{\partial^3 u}{\partial T^3} + 6|u|^2\frac{\partial u}{\partial T}\right] = 0 \tag{2.81}$$

because it is a member of the NLS hierarchy and has an associated scattering problem and inverse scattering transform. This equation is not of interest here because, like the general mNLS solution with $\delta\omega = 0$, it places restrictions on the material constants which may not be feasible to satisfy. Instead, this thesis deals with more general, non-integrable cases using parameters of materials currently in use for nonlinear optical switching.

2.4.4 Higher-Order Temporal Effects

The previous section considered additional non-SVEA terms to the NLS equation that still allowed for analytic soliton-like solutions. This section considers additional terms that result from the scalar, temporal reduction of the full evolution equation derived in Chapter 3 for use in spatio-temporal propagation. The additional terms included here that are not present in equation 2.70 are fourth-order dispersion (FOD) and stimulated Raman scattering:

$$\begin{aligned} 2ik_0\frac{\partial A}{\partial z} - k_0 k_0''\frac{\partial^2 A}{\partial T^2} - \frac{i}{3}k_0 k_0'''\frac{\partial^3 A}{\partial T^3} + \frac{1}{12}k_0 k_0''''\frac{\partial^4 A}{\partial T^4} \\ + 2k_0^2\frac{n_K}{n_0}|A|^2 A + 4ik_f n_K\left[\frac{n_0}{c} - \frac{k_0'}{2}\right]\frac{\partial |A|^2 A}{\partial T} \\ + \frac{k_f}{2}\left\{k_f + i\frac{2}{n_0}\left[\frac{n_0}{c} - \frac{k_0'}{2}\right]\frac{\partial}{\partial T}\right\}\int_0^\infty R_R(\tau)\,|A(T-\tau)|^2 A\,d\tau = 0. \end{aligned} \tag{2.82}$$

Here, k_0'''' is the fourth-order dispersion coefficient, n_K is the nonlinear Kerr index, and $R_R(\tau)$ is the Raman response function. To date, there is no known analytic solution to this equation. As a result, the effects of these higher-order temporal terms on the fundamental NLS soliton are now discussed.

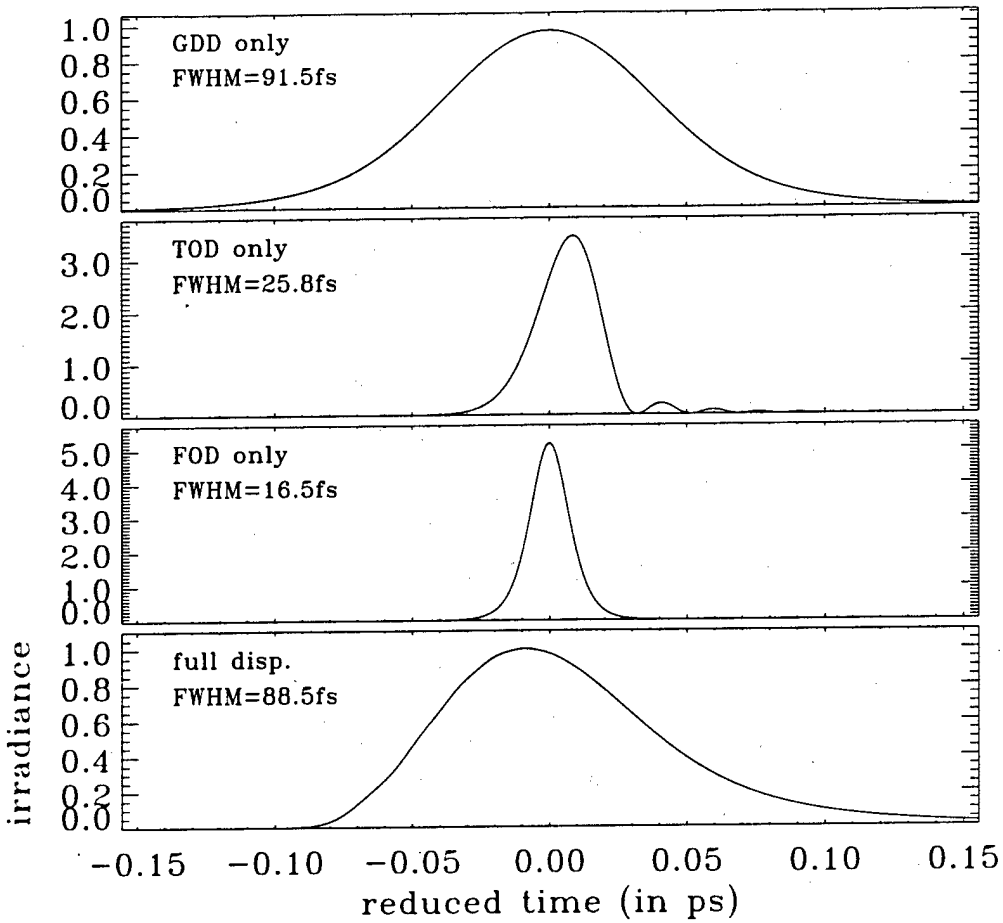

Figure 2.12: Effects of linear dispersion on a sech() pulse with initial intensity temporal FWHM of 16.5 fs. Based on the dispersion properties of fused silica, the group-delay dispersion (GDD) coefficient $k_0'' < 0$, the third-order dispersion (TOD) coefficient $k_0''' > 0$, and the fourth-order dispersion (FOD) coefficient $k_0'''' < 0$. The propagation distance in each figure is 5 Z_0.

Higher-Order Linear Dispersion

First, the effects of higher-order linear dispersion will be considered in the absence of nonlinearity. In this case, equation 2.82 reduces to

$$2ik_0\frac{\partial A}{\partial z} - k_0k_0''\frac{\partial^2 A}{\partial T^2} - \frac{i}{3}k_0k_0'''\frac{\partial^3 A}{\partial T^3} + \frac{1}{12}k_0k_0''''\frac{\partial^4 A}{\partial T^4} = 0. \tag{2.83}$$

The group delay as a function of frequency, as shown in Figure 2.6, can be written $k'(\omega) = k_0' + \Delta k'(\Delta\omega)$, where the approximation

$$\Delta k'(\Delta\omega) \approx \Delta\omega k_0'' + \frac{1}{2}\Delta\omega^2 k_0''' + \frac{1}{6}\Delta\omega^3 k_0'''', \tag{2.84}$$

is made and is cubic in frequency deviation about ω_0.

The effects of linear dispersion on a temporal wavepacket are shown in Figure 2.12. The top plot shows temporal broadening due to GDD alone, and is based on the same data used for Figure 2.8. The symmetry of the broadening can be understood by considering the change in group delay, which is linear in $\Delta\omega$. Therefore, symmetric deviation about the center frequency results in anti-symmetric deviation in group delay about k_0', such that

$$k'(\omega_0 \pm \Delta\omega) \approx k_0' \pm \Delta\omega k_0''. \tag{2.85}$$

As a result, GDD leads to symmetric broadening, with red-shifted frequencies trailing blue-shifted frequencies in the AGDD regime.

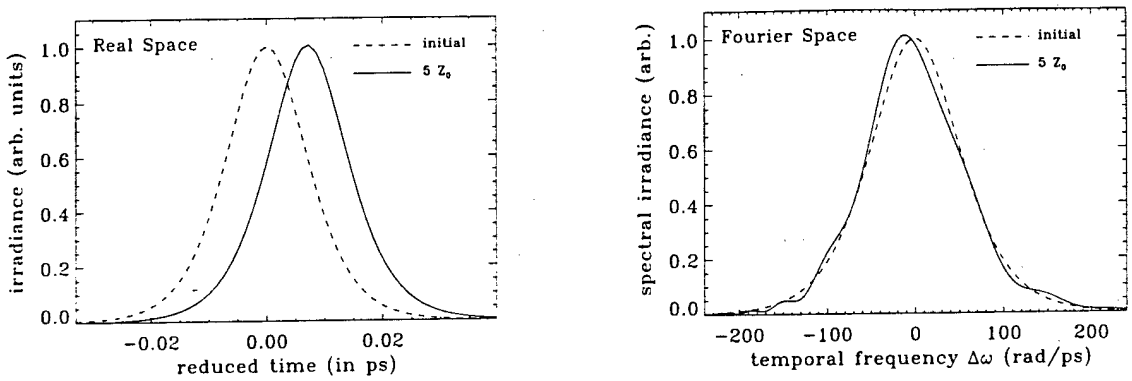

Figure 2.13: Effects of higher-order linear dispersion on a temporal soliton with initial intensity temporal FWHM of 16.5 fs. The initial (dashed curve) and final (solid curve, after 5 Z_0) temporal envelopes are shown on the left plot, while the initial (dashed) and final (solid) spectral envelopes are shown on the right. The soliton is delayed by 7.25 fs and narrows slightly to 16.2 fs.

The second plot shows temporal broadening due to TOD alone. In this case, the group delay

$$k'(\omega_0 \pm \Delta\omega) \approx k_0' + \frac{1}{2}\Delta\omega^2 k_0''', \tag{2.86}$$

which results in a symmetric change in group delay with frequency. This expression indicates that both red-shifted and blue-shifted frequencies will move towards the leading edge (TOD<0) or trailing edge (TOD>0). For positive TOD as shown, the peak will be delayed in the reduced time coordinate frame with steepening of the trailing edge and oscillations in the tail [30].

The third plot shows the effect of FOD alone. The group delay can be written

$$k'(\omega_0 \pm \Delta\omega) \approx k_0' \pm \frac{1}{6}\Delta\omega^3 k_0'''', \tag{2.87}$$

which, like GDD, is anti-symmetric. Again, broadening will be symmetric, but with much stronger change in group delay for frequencies far removed from ω_0. FOD can either enhance (same sign) or oppose (opposite sign) the broadening due to GDD. As shown in the plot, the FOD coefficient of fused silica is small enough that its effect is negligible for the choice of initial pulse duration and propagation distance.

Finally, the fourth plot shows the temporal broadening due to the combined effects of all dispersion terms. In fact, the full dispersion relation using the Sellmeier coefficients for fused silica (see Appendix D) is used, but the primary effects arise from GDD and TOD. Because of TOD, broadening is asymmetric. The signs of GDD (<0) and TOD (>0) indicate that TOD opposes the change in group delay due to GDD when $\Delta\omega > 0$, and enhances the change due to GDD when $\Delta\omega < 0$, as shown in Figure 2.6. Therefore, the broadening of the red-shifted trailing edge will be increased while broadening of the blue-shifted leading edge will be reduced. Opposite to the case of TOD alone, the peak is now slightly advanced.

The effect of higher-order dispersion on a temporal soliton is shown in Figure 2.13, as described by the evolution equation

$$2ik_0\frac{\partial A}{\partial z} - k_0 k_0''\frac{\partial^2 A}{\partial T^2} - \frac{i}{3}k_0 k_0'''\frac{\partial^3 A}{\partial T^3} + \frac{1}{12}k_0 k_0''''\frac{\partial^4 A}{\partial T^4} + 2k_0^2\frac{n_2}{n_0}|A|^2 A = 0, \tag{2.88}$$

where $n_2 = n_K + \frac{1}{4n_0}\int_0^\infty R_R(\tau)d\tau$ is the total instantaneous nonlinear refractive index. Because AGDD is balanced with self-phase modulation, the soliton is delayed by 7.25 fs in the reduced coordinates. This delay is primarily the result of positive TOD, and is similar to the case previously discussed with TOD acting alone on a linear pulse, where the delay was 7.08 fs. The peak of the spectrum is also downshifted, as shown on the right-hand plot, which corresponds to the delay experienced in time. Except for the delay, in real space, the soliton is mostly unaffected by higher-order dispersion, a testament to (1+1)-D stability.

Optical Shock

Optical shock [183] is the first-order time derivative of the nonlinearity and gives rise to an intensity-dependent group delay [184]. The evolution equation describing nonlinear refraction and optical shock is

$$2ik_0\frac{\partial A}{\partial z} + 2k_0^2\frac{n_2}{n_0}|A|^2 A + 4ik_f n_2\left[\frac{n_0}{c} - \frac{k_0'}{2}\right]\frac{\partial |A|^2 A}{\partial T} = 0. \tag{2.89}$$

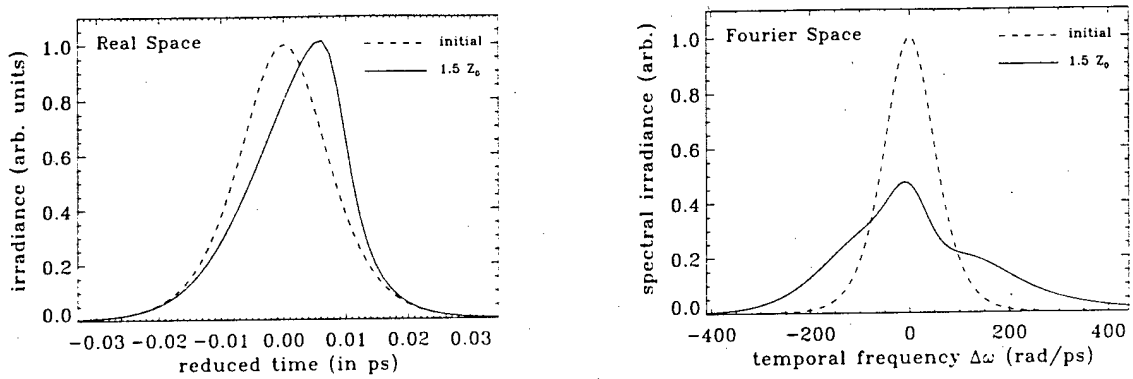

Figure 2.14: Effects of optical shock on a 16.5 fs wavepacket for a propagation distance of 1.5 Z_0. The left-hand plot shows the initial (dashed) and final (solid) temporal intensity envelopes and indicates slight narrowing to 16.3 fs and delay of the peak by 5.68 fs. The right-hand plot shows the initial (dashed) and final (solid) spectral envelopes and indicates spectral broadening from 19.1 THz to 33.9 THz due to SPM with asymmetry caused by shock.

The optical shock expression obtained here has two contributions, one (proportional to phase delay) directly from Maxwell's equation in the time derivative of the nonlinear polarization, and one (proportional to group delay) due to the removal of the SVE approximation by one order.

Expressing the field envelope as

$$A = |A|\, e^{i\phi}, \tag{2.90}$$

equation 2.89 can be written as the coupled differential equations

$$\frac{\partial |A|}{\partial z} = 6\frac{n_2}{n_0}\left[\frac{k_0'}{2} - \frac{n_0}{c}\right]|A|^2 \frac{\partial |A|}{\partial T} \tag{2.91a}$$

$$\frac{\partial \phi}{\partial z} = k_f n_2 |A|^2 + \frac{n_2}{n_0}\left[\frac{k_0'}{2} - \frac{n_0}{c}\right]|A|^2 \frac{\partial \phi}{\partial T}. \tag{2.91b}$$

The first equation has the simple solution

$$|A(T,z)| = |A(z - v_{gv} T)|, \tag{2.92}$$

where the intensity-dependent group velocity is defined

$$v_{gv} = \frac{1}{6\frac{n_2}{n_0}\left[\frac{k_0'}{2} - \frac{n_0}{c}\right]|A|^2}. \tag{2.93}$$

Therefore, the group velocity is reduced with increasing intensity.

The self-steepening effect due to optical shock is shown in Figure 2.14. The peak is delayed more than the wings resulting in a steepening of the trailing edge. An estimate of the time delay of the peak is

$$\Delta T = \frac{dZ_0}{v_{gv}} = \frac{3}{2}\lambda d\left[\frac{n_0}{c} - \frac{k_0'}{2}\right], \tag{2.94}$$

which gives the value ΔT = 5.73 fs using the parameters of the simulations. This compares very well with the value of 5.68 fs obtained by numerically locating the peak. The second plot shows that the spectral broadening due to self-phase modulation (as shown in Figure 2.10) becomes asymmetric, with slight down-shift of the peak corresponding to delay in the temporal domain.

The steepening of the trailing edge results in broad frequency content. Therefore, dispersion must be considered, which dissipates steepening. The following evolution equation well describes the effects of shock and dispersion

$$\begin{aligned} 2ik_0\frac{\partial A}{\partial z} - k_0 k_0''\frac{\partial^2 A}{\partial T^2} - \frac{i}{3}k_0 k_0'''\frac{\partial^3 A}{\partial T^3} + \frac{1}{12}k_0 k_0''''\frac{\partial^4 A}{\partial T^4} \\ + 2k_0^2\frac{n_K}{n_0}|A|^2 A + 4ik_f n_K\left[\frac{n_0}{c} - \frac{k_0'}{2}\right]\frac{\partial |A|^2 A}{\partial T} = 0, \end{aligned} \tag{2.95}$$

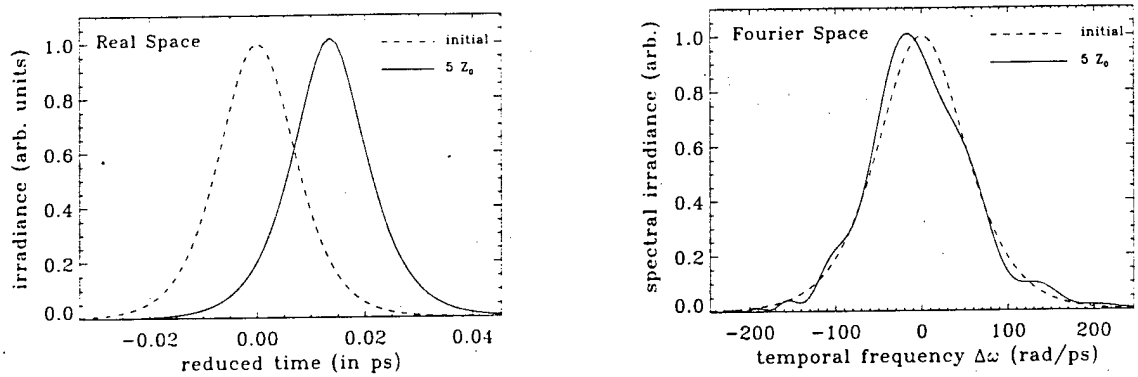

Figure 2.15: Effects of optical shock and higher-order dispersion on a 16.5 fs wavepacket for a propagation distance of 5 Z_0. The left-hand plot shows the initial (dashed) and final (solid) temporal intensity envelopes and indicates slight narrowing to 15.8 fs and overall (centroid) delay of 13.7 fs. The right-hand plot shows the initial (dashed) and final (solid) spectral envelopes and indicates asymmetry due to shock and TOD.

and is used for the simulation results presented in Figure 2.15, using the fundamental soliton A=sech(T/τ_0) as the initial condition. Dispersion dissipates the shock and the balance between AGDD and SPM stabilizes the pulse. As a result, the effect of shock is to delay the entire pulse. The overall delay of 15.8 fs is due to both shock and positive TOD, where the delay without shock is 7.25 fs, as shown in Figure 2.13.

Raman Scattering

This section considers the full evolution equation 2.82, which includes higher-order dispersion, shock and Raman scattering. The Raman nonlinearity is described via the full Raman response function [186] for a single resonance:

$$R_R(\tau) = \frac{R_0 e^{-\gamma\tau/2}\sin(\Omega_R\tau)}{\Omega_R}. \tag{2.96}$$

where $\Omega_R = \sqrt{\Omega_f - \gamma^2/4}$ is the optical phonon frequency, Ω_f is the natural oscillation frequency and γ is the damping constant. Raman scattering results in a continuous frequency down-shift by providing gain at lower frequencies at the expense of higher frequencies, as discussed in Appendix B. This effect is often referred to as the soliton self-frequency shift [145]. In the AGDD regime, the downshifted frequencies travel with a greater group delay (slower group velocity) thereby delaying the wave in the reduced time coordinates, as shown in Figure 2.16.

Spectral narrowing and downshift are clearly seen on the right-hand plot. The peak of the Raman gain in fused silica is 13.2 THz (or 82.9 rad/ps). The peak of the downshifted spectrum is about 80 rad/ps below the knee of the high frequency side of the curve, indicating that the low frequencies are amplified and the high frequencies are attenuated, resulting in spectral narrowing. Spectral four-wave mixing continuously creates new frequencies, called the Stokes (low-frequency) and anti-Stokes (high-frequency) side bands, allowing for a Raman downshift which exceeds the original spectral bandwidth. The manifestation of these effects in the temporal domain is temporal broadening (due to spectral narrowing) and delay (due to downshift). Note that the delay of 20.0 fs is only slightly greater than the delay of 13.7 fs without the Raman term. This indicates that, in this case, the Raman effect is about the same order as the other higher-order temporal effects, but because of the large, continuous spectral downshift, the Raman term will manifest itself over much longer distances and eventually dominate.

2.5 2-D and 3-D Spatio-Temporal Solitary Waves

The propagation and interaction of multi-dimensional spatio-temporal solitary waves, which are stationary in both space and time, is of ultimate interest to this thesis. These multi-dimensional nonlinear phenomena are termed solitary waves instead of solitons because, like solitons, they are stationary, but may not satisfy the additional properties of solitons such as inelastic collisions (which preserve the soliton eigenvalues) and integrability of the defining equations. Like temporal solitons in fiber, these multi-dimensional solitary waves are fully confined, either by complete nonlinear self-confinement in the case of the 3-D light bullet or with one dimension of linear confinement by a planar waveguide in the 2-D self-confined case, such that the

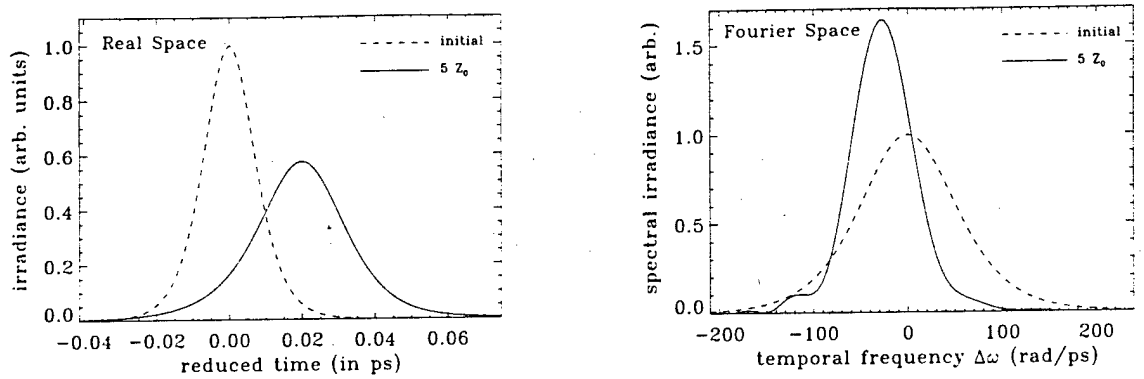

Figure 2.16: Effects of Raman scattering, including shock and higher-order dispersion, on a 16.5 fs wavepacket for a propagation distance of 5 Z_0. The left-hand plot shows the initial (dashed) and final (solid) temporal intensity envelopes and indicates broadening to 27.4 fs and overall (centroid) delay of 20.0 fs. The right-hand plot shows the initial (dashed) and final (solid) spectral envelopes and indicates spectral narrowing from 19.1 THz to 11.7 THz and overall downshift by 4.23 THz.

energy requirement is low. A brief discussion of 2-D spatio-temporal solitary waves is presented here with more detail on propagation and interaction provided in Chapter 6.

The most straightforward means of describing the propagation of 2-D spatio-temporal solitary waves is the direct extension of the (1+1)-D nonlinear Schrödinger (NLS) equation

$$2ik_0\frac{\partial A}{\partial z} + \frac{\partial^2 A}{\partial x^2} - k_0 k_0''\frac{\partial^2 A}{\partial T^2} + 2k_0^2\frac{n_2}{n_0}|A|^2 A = 0, \tag{2.97}$$

but it is well known that the solitary wave solutions are unstable to propagation [209]. This instability can result in critical collapse, or blow-up, when nonlinearity overtakes diffraction/dispersion, or in broadening when diffraction/dispersion overtakes nonlinearity. In the case of (2+1)-D spatial and spatio-temporal in the AGDD regime, and (3+1)-D spatio-temporal in the AGDD regime, blow-up is the result [176], which indicates that the evolution equation does not take into account additional physics which arrest this behavior. The inclusion of non-paraxial and non-SVEA terms results instead in spatio-temporal broadening.

Since the pump must propagate the length of the logic gate undisturbed (i.e. with final size about the same as the initial size), mechanisms to stabilize propagation need to be investigated. Multi-dimensional propagation can be stabilized by the inclusion of a suitable nonlinear index saturation mechanism [2,210] such as ultrafast quintic nonlinearity of opposite sign to the cubic Kerr nonlinearity, i.e. $n = n_0 + n_2|A|^2 + n_4^{\text{eff}}|A|^4$ where A is a scalar field and $n_4^{\text{eff}} < 0$ accounts for the refractive part of the effective quintic nonlinearity. Examples of this type of saturation behavior are the nonresonant nonlinearities of semiconducting AlGaAs [143] at sub-half bandgap or the organic single-crystal PTS [125, 147]. Ultrafast saturation from the quintic nonlinearity is the stabilization mechanism discussed in this thesis, but it should be noted that the balancing between third-order dispersion (plus space-time focusing) and shock as shown in section 2.4.3 for 1-D temporal solitons may also serve as a stabilization mechanism for multi-dimensional propagation [139].

The scalar (2+1)-D cubic-quintic NLS equation is

$$2ik_0\frac{\partial A}{\partial z} + \frac{\partial^2 A}{\partial x^2} - k_0 k_0''\frac{\partial^2 A}{\partial T^2} + 2k_0^2\frac{n_2}{n_0}\left[|A|^2 + \frac{n_4^{\text{eff}}}{n_2}|A|^4\right]A = 0. \tag{2.98}$$

Along with the quintic term, any additional terms to the (2+1)-D nonlinear evolution equation that have comparable effect must also be considered, and the conditions determined under which they can be neglected. This motivates the multiple-scales derivation of Chapter 3, in which a full vectorial derivation directly from Maxwell's equation is performed and results in a coupled, non-paraxial, non-slowly-varying envelope (SVE), first-order vectorial differential equation for the propagation of orthogonal linear polarizations including nonlinear couplings with the weak longitudinally-projected field. In Chapter 6, reduced, paraxial, versions of these equations are used to study the propagation of a single pump solitary wave and the vectorial interaction between pump and signal solitary waves. It is shown that quintic index saturation can stabilize against the effects of other, comparable, higher-order terms.

The scalar equation suitable for the propagation of a single spatio-temporal nonlinear wave under the conditions of present

interest is, from section 3.2.3,

$$
\begin{aligned}
2ik_0\frac{\partial A}{\partial z} &+ \frac{\partial^2 A}{\partial x^2} - k_0 k_0''\frac{\partial^2 A}{\partial T^2} - \frac{i}{3}k_0 k_0'''\frac{\partial^3 A}{\partial T^3} - i\frac{k_0'}{k_0}\frac{\partial^3 A}{\partial T\partial x^2} \\
&+ \frac{1}{12}k_0 k_0''''\frac{\partial^4 A}{\partial T^4} + 2k_0^2\frac{n_K}{n_0}|A|^2 A + 4ik_f n_K\left[\frac{n_0}{c} - \frac{k_0'}{2}\right]\frac{\partial |A|^2 A}{\partial T} \\
&+ \frac{k_f}{2}\left\{k_f + i\frac{2}{n_0}\left[\frac{n_0}{c} - \frac{k_0'}{2}\right]\frac{\partial}{\partial T}\right\}\int_0^\infty R_R(\tau)\,|A(T-\tau)|^2 A d\tau \\
&+ 2k_0^2\frac{n_4^{\text{eff}}}{n_0}|A|^4 A = 0.
\end{aligned}
\tag{2.99}
$$

The first term in equation 2.99 is the first-order propagator along the z direction. The reduced time transformation $T = t - k_0' z$, where k_0' is the group-delay, is made such that propagation is nominally stationary in the new coordinate system. Paraxial diffraction along the x direction and group-delay dispersion are represented by the next two terms, where k_0'' is the group-delay dispersion coefficient and describes pulse lengthening under the SVE approximation. Third-order dispersion, with coefficient k_0''', and space-time focusing [144] follow, and are the first non-SVE corrections. The space-time focusing term describes the (paraxial) curvature of the energy front due to spatio-temporal diffraction. The final linear term is fourth-order dispersion.

The first nonlinear term in equation 2.99 represents third-order nonlinear refraction followed by optical shock. The following terms describe the Raman nonlinearity. The effective quintic nonlinear index n_4^{eff} consists of three distinct contributions: directly from the fifth-order polarization, from the product of the third-order polarization with itself due to the reduction from Maxwell's equations to a first-order equation, and a "cascaded" contribution due to the nonlinear coupling between the fundamental and third-harmonic, which can be tuned via phase-matching [211]. A simple estimate of the size of the cascaded quintic nonlinear index suggests that [134] $n_4^{\text{eff}} \approx -20n_2^2$, which is negative as desired for multi-dimensional stability.

The initial conditions used in the simulations of Chapter 6 are the numerically-computed eigenmodes of the normalized scalar (2+1)-D cubic-quintic NLS equation:

$$
i\frac{\partial u}{\partial \tilde{z}} + \frac{\partial^2 u}{\partial \tilde{x}^2} + s\frac{\partial^2 u}{\partial \tilde{T}^2} + 2|u|^2 u + 2q|u|^4 u = 0,
\tag{2.100}
$$

where the following definitions are made: $u = k_0 w_0\sqrt{n_2/n_0}A$ where $n_2 = n_K + \frac{1}{4n_0}\int_0^\infty R_R(\tau)d\tau$ is the total instantaneous nonlinear refractive index, $\tilde{z} = z/2k_0 w_0^2$, $\tilde{x} = x/w_0$, $\tilde{T} = T/w_0\sqrt{|k_0 k_0''|}$, $s = -\text{sign}(k_0'')$, and $q = n_0 n_4^{\text{eff}}/n_2^2 k_0^2 w_0^2$ with w_0 a measure of the transverse spatial width of the solitary-wave. For a bright spatio-temporal solitary wave with $n_2 > 0$, operation must be in a region of anomalous group-delay dispersion (AGDD) such that $s = +1$. The symmetry of this cubic-quintic equation allows it to be transformed into an ordinary differential equation [2] and subsequently solved via standard fourth-order Runge-Kutta [212].

The existence of a radially-symmetric stationary solution to equation 2.100 of the form

$$
u(\tilde{x}, \tilde{T}, \tilde{z}) = U(\rho)\exp(i\beta\tilde{z})
\tag{2.101}
$$

is postulated, where $\rho = \sqrt{\tilde{x}^2 + \tilde{T}^2}$. Substituting this ansatz into equation 2.100 results in the ordinary nonlinear differential equation

$$
\frac{d^2 U}{d\rho^2} + \frac{1}{\rho}\frac{dU}{d\rho} + \left[2U^2 + 2qU^4 - \beta\right]U = 0,
\tag{2.102}
$$

which has fundamental and higher-order solutions corresponding to increasing optical energies, physical size, and number of zero crossings of the field [2].

For the purposes of optical switching, only the fundamental eigenmode solutions to equation 2.102 are of interest, which possess the minimum size and energy [2]. It should also be noted that the higher-order modes are unstable to angular perturbations even with a saturating nonlinearity [213]. There is a family of such fundamental solutions of different widths and amplitudes parameterized by the value of q. Using the relationship between the field amplitude A and the normalized amplitude u, the q parameter can be rewritten as

$$
q = \frac{n_4^{\text{eff}}|A_0|^2}{n_2 U_0^2},
\tag{2.103}
$$

where $|A_0|$ and U_0 are real and represent the peak value of the field amplitude in real and normalized units respectively. Now the quintic nonlinear index n_4^{eff} is written in the convenient form

$$
n_4^{\text{eff}} = -\frac{n_2}{A_{\text{sat}}^2},
\tag{2.104}
$$

where A_{sat} is a real constant saturation amplitude. With this definition, the total refractive index seen by a scalar field is

$$n = n_0 + n_2 \left[1 - \frac{|A|^2}{A_{sat}^2} \right] |A|^2, \tag{2.105}$$

such that, for a peak field amplitude $|A_0| = \sqrt{\sigma} A_{sat}$, the induced nonlinear index will be reduced from the purely Kerr value of n_2 to $[1-\sigma]n_2$, where $\sigma = |A_0|^2 / A_{sat}^2$ is the saturation parameter. The definition 2.104 is used so that the form of equation 2.105 is consistent with the first two terms of the Taylor expansion of the two-level system saturation [214].

Including only the cubic and quintic contributions as shown in equation 2.105 cannot result in true saturation. When $n_2 > 0$ and $n_4^{eff} < 0$ as in the situation here, the induced nonlinearity reaches a peak at $|A|^2 = A_{sat}^2/2$, then decreases and eventually becomes negative when $|A|^2 > A_{sat}^2$. This behavior is an indication that higher-order terms in the material polarization expansion may need to be included, but one experimental measurement of the induced nonlinear index in PTS at $\lambda_f = 1.064\ \mu m$ shows that this roll-over into a negative contribution does indeed occur [147]. Nevertheless, when $\sigma < 0.5$, equation 2.105 mimics true saturation behavior.

Combining equations 2.103 and 2.104 and substituting into the eigenvalue equation 2.102 and noting that $U_0^2/U_{sat}^2 = |A_0|^2/A_{sat}^2$, results in the following ordinary differential eigenvalue equation

$$\frac{d^2U}{d\rho^2} + \frac{1}{\rho}\frac{dU}{d\rho} + 2\left[1 - \frac{U^2}{U_{sat}^2}\right] U^3 - \beta U = 0. \tag{2.106}$$

Figure 2.17 illustrates a few fundamental eigenmode solutions of equation 2.106 calculated as a function of peak normalized amplitude U_0 using the normalized saturation amplitude $U_{sat} = \sqrt{16.0}$. The heavy solid line ($U_0 = 1$) corresponds to the

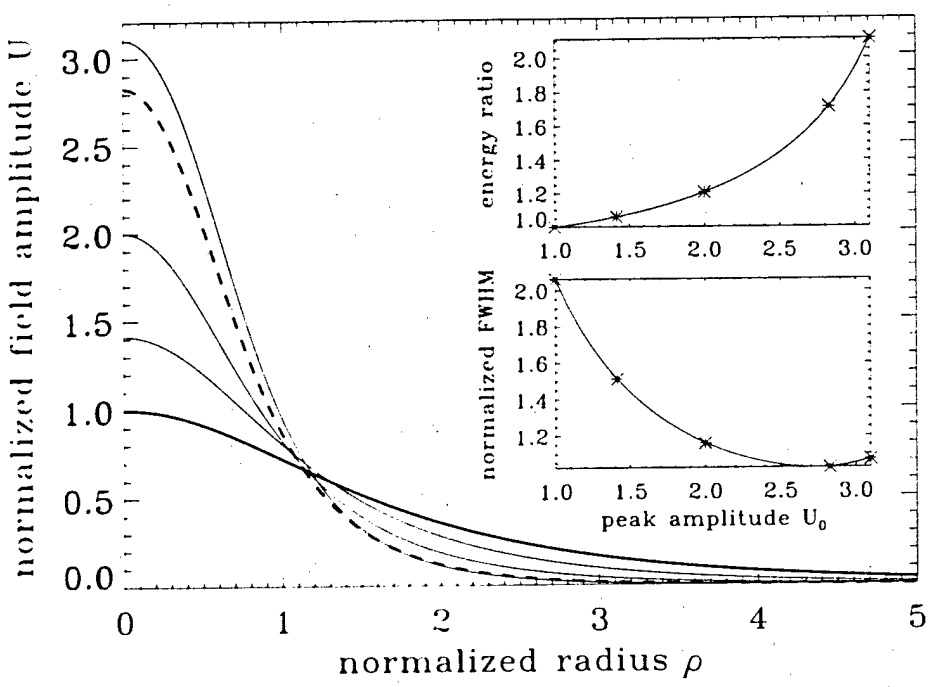

Figure 2.17: Fundamental eigenmodes of equation 2.106 plotted as a function of peak normalized amplitude. Here, the normalized saturation amplitude $U_{sat} = 4$, and $\sigma = 0.0625, 0.125, 0.25, 0.5$, and 0.6 for $U_0 = 1.0, 1.41, 2.0, 2.83$, and 3.1, respectively. The inset plots show energy ratio (top) and normalized FWHM (bottom) as a function of U_0, with asterisks denoting the positions of the eigenmodes in the main figure.

saturation parameter $\sigma = 0.0625$, while the heavy dashed line ($U_0 = 2.83$) corresponds to $\sigma = 0.5$. The top inset shows the energy ratio as a function of peak amplitude when the $\sigma = 0.0625$ eigenmode is used as the signal spatio-temporal wave. When using $\sigma = 0.5$ for the pump, the energy ratio is 1.712. The energy ratio increases with increasing σ, but when $\sigma > 0.5$, the

induced index as given by equation 2.105 begins to decrease from the maximum when $\sigma = 0.5$. The lower inset shows the variation in intensity full-width at half-maximum (FWHM). The FWHM initially decreases with σ, reaches a minimum near $\sigma = 0.5$, then increases as $\sigma \to 1$.

Figure 2.18 plots the $\sigma = 0.5$ fundamental eigenmode (dashed curve) of equation 2.106 along with $\sigma = 0$ eigenmodes (no saturation, solid curves) of peak normalized amplitudes of $U_0 = 2.83$ and $U_0 = 1.94$. The non-saturated $U_0 = 1.94$ eigenmode

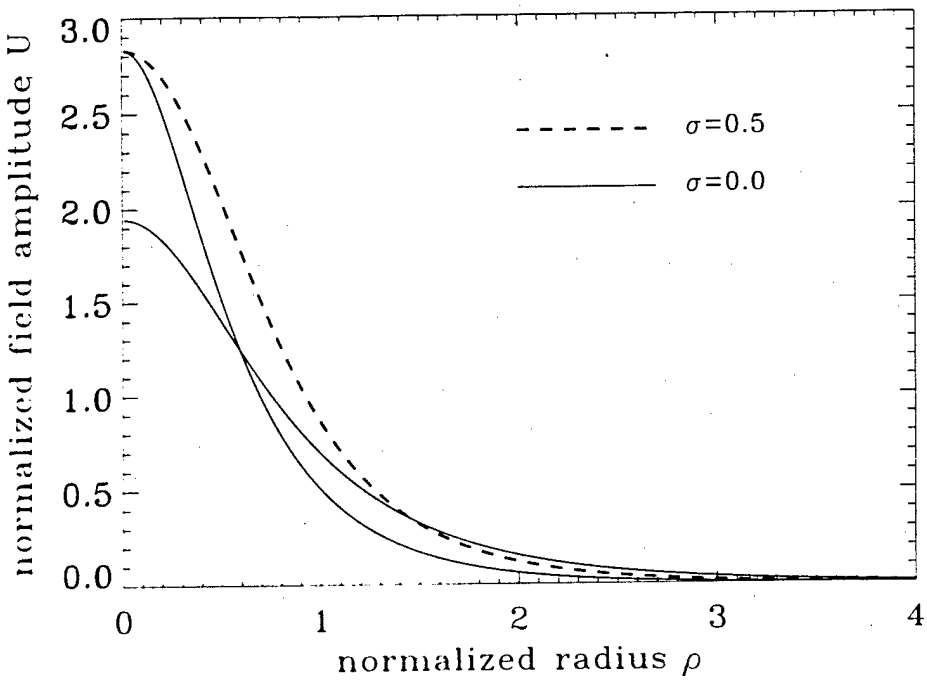

Figure 2.18 Numerically computed eigenmodes of equation 2.106 for the saturation parameter $\sigma = 0.5$ and normalized peak amplitude $U_0 = 2.83$ (dashed curves) and for the saturation parameter $\sigma = 0$ with $U_0 = 2.83$ and $U_0 = 1.94$ (solid curves). The effect of saturation is to broaden the width of the eigenmode near the peak where the saturation has its greatest effect. The space/time-bandwidth products are 0.312 for the saturated eigenmode and 0.242 for the non-saturated eigenmodes.

is a scaled version of the $U_0 = 2.83$ non-saturated eigenmode with the same normalized half-width at half-maximum (HWHM) of 0.5135 as the saturated $\sigma = 0.5$ eigenmode, and will be used in Chapter 6 to compare the effects of the higher-order temporal terms on the pump with and without saturation in section 6.1. Note that for the same HWHM, the saturated eigenmode will have a larger value of U_0 than the non-saturated one. The normalized FWHM of the intensity profiles of these eigenmodes is 1.027, while the FWHM of the $\sigma = 0.0625$ signal eigenmode is 2.063.

Stability of the cubic-quintic eigenmodes can be examined by the evaluation of the stability parameter [209]

$$S = \frac{\partial P}{\partial \beta}, \tag{2.107}$$

where P is the integration over the eigenmode profile and represents power in the 2-D spatial case and energy in the 3-D spatio-temporal case. Stability is ensured when $S > 0$, which is true for (1+1)-D NLS propagation, otherwise, propagation is unstable. For (2+1)-D propagation, $S = 0$, and for (3+1)-D, $S < 0$ [2]. The first condition is the result of the fact that the power of the 2-D eigenmode is constant with respect to width and eigenvalue [169], such that an increase in width, which reduces diffraction/dispersion, is exactly compensated by nonlinearity, and a decrease in width, which enhances nonlinearity, is exactly compensated by diffraction/dispersion. The second condition results from the fact that the energy of the 3-D eigenmode decreases with decreasing width and increasing eigenvalue [2], which is opposite to the 1-D case, such that an increase in width results in diffraction/dispersion overtaking nonlinearity, and a decrease in width results in nonlinearity overtaking diffraction/dispersion.

Figure 2.19 plots the eigenmode power (top) and stability parameter (bottom) versus eigenvalue for the (2+1)-D cubic-quintic NLS equation 2.106. It is shown that, like the 1-D case, the power increases with increasing eigenvalue (decreasing

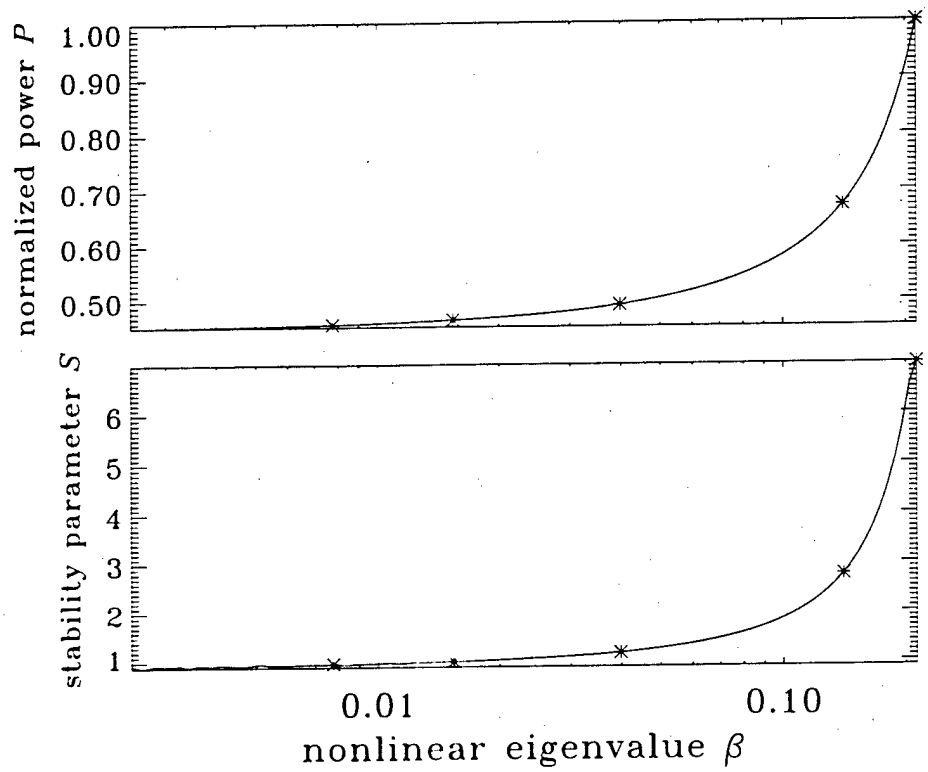

Figure 2.19: Plot of power and stability versus nonlinear eigenvalue, indicating that quintic saturation results in stable (2+1)-D eigenmodes. The asterisks denote the positions of the fundamental eigenmodes of Figure 2.17.

width), indicating stability, and S is always positive. The figure also indicates that eigenmodes with greater β (i.e. greater saturation) are more stable than eigenmodes with small β. The stability parameter asymptotically approaches zero with decreasing β which is expected since $\sigma \to 0$ as well.

Stable propagation of the $\sigma = 0.5$ cubic-quintic eigenmode is verified by numerical simulation of equation 2.98, as shown in Figure 2.20. The width parameter is chosen as $w_0 = 39.6\ \mu$m, which results in intensity spatial FWHM of 40.7 μm, and temporal FWHM of 16.5 fs. The propagation distance is 15 Z_0, over which the spatio-temporal solitary wave is unchanged. The same stabilized solitary-wave behavior occurs in the fully 3-D case as well [2]. The confocal distance $Z_0 = 0.559 k_0 w_0^2$ = 5.14 mm, and is calculated numerically. For the simulation, the parameters of fused silica (see Appendix D) are used at $\lambda_l = 1.55\ \mu$m. The first section of Chapter 6 studies the effects of the higher-order terms of equation 2.99 on stability of this $\sigma = 0.5$ cubic-quintic pump solitary wave eigenmode, and shows that stabilization does occur, albeit with some spatio-temporal broadening due to Raman scattering.

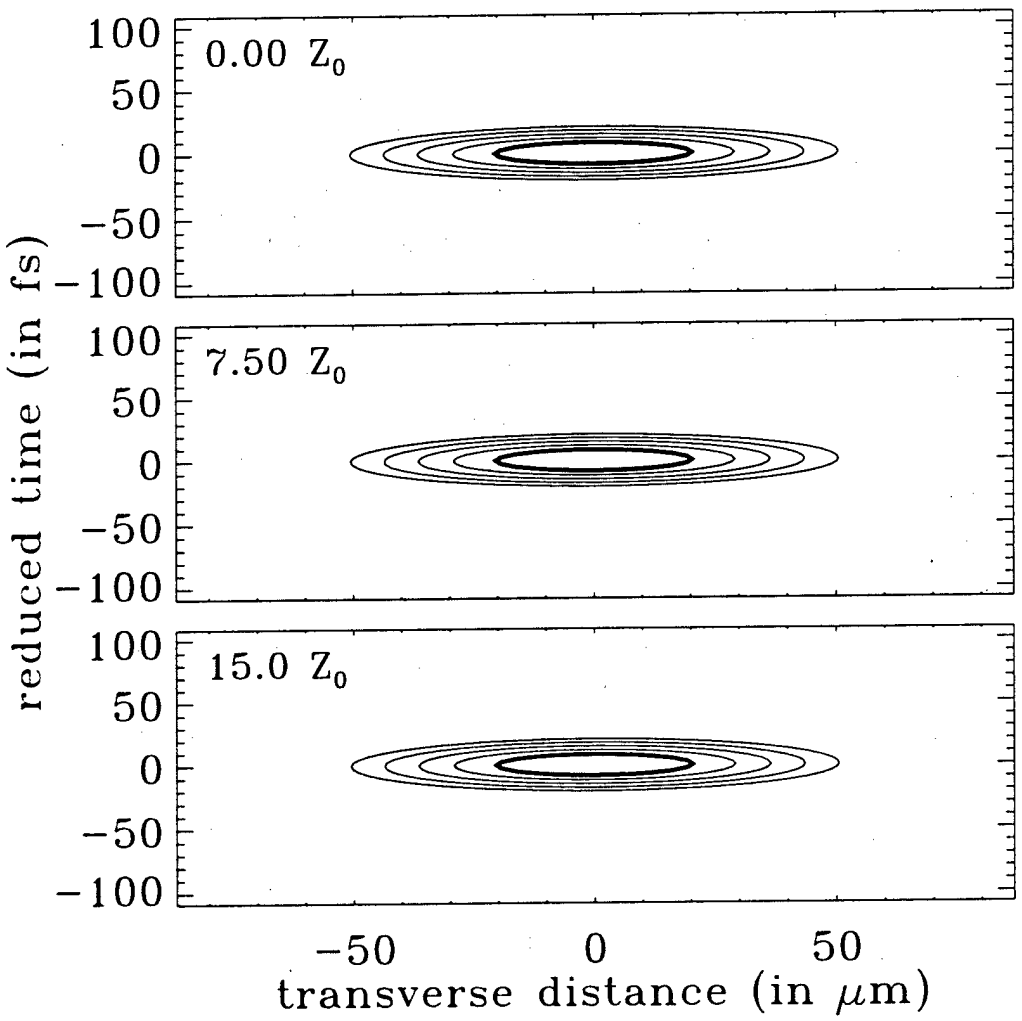

Figure 2.20: Stable propagation of the $\sigma = 0.5$ eigenmode of the cubic-quintic NLS equation without the effects of the higher-order terms. The spatio-temporal wave of transverse FWHM 40.7 μm and temporal FWHM 16.5 fs remains unchanged after propagating 15 confocal distances. The contours are at -3 dB intervals relative to the peak intensity in each frame.

Chapter 3

The Vector Nonlinear Wave Equations

Optical nonlinear interactions generally fall into three regimes of operation: parametric, dynamic and transient coherent. Operating very far from resonance, where the material simply serves as an intermediary for the interaction between coherent light beams or pulses, is known as the parametric regime. In this regime, the nonlinear response is purely reactive (real nonlinear susceptibilities) because material transitions are virtual, meaning that there is no exchange of energy between light and matter because the nonlinear response is a result of wavefunction deformation and is essentially instantaneous and lossless. As a result, energy is conserved among the beams or pulses of light and the Manley-Rowe relations hold [215]. The particular parametric case of the third-order nonlinear material polarization responsible for self-focusing and self-phase modulation is known as the optical Kerr effect, and is of fundamental importance for the optical nonlinear Schrödinger-type (NLS-type) equations derived in the chapter.

The dynamic and transient coherent regimes are resonant and differentiated by the ratio between the pulse duration and T_2, the transverse relaxation (or transverse dephasing) time of the resonant excited state. The transverse relaxation time is related to the homogeneous linewidth by $T_2 = 1/\pi\Gamma_h$. The homogeneous linewidth typically lies in the range GHz-THz for optical materials at room temperature, but in solid persistent spectral hole burning materials at low temperature, Γ_h can be as narrow as 100 Hz [216]. Indeed, much effort is directed at finding materials with slow dephasing at low temperature (along with broad inhomogeneous bandwidths) for applications in time-domain holography [217,218] and frequency-domain data storage [219]. Note that the inhomogeneous dephasing time is defined $T_2^* = 1/\pi\Gamma_i$, where Γ_i is the inhomogeneous linewidth. The longitudinal relaxation time T_1 of the excited state leads to the "sluggish" nature of nonlinearity and corresponds to the decay time-constant of the induced population change of the excited state.

The dynamic regime of optical nonlinearity occurs near resonance when the pulse duration is greater than T_2. Operating in the dynamic regime ensures that light-induced coherence is lost within the pulse duration and is obviously satisfied by continuous-wave irradiation. This nonlinearity produces real excitations because energy is exchanged between light and matter, and due to resonant enhancement, nonlinearity can be very large, but at the expense of large absorption. The transient-coherent regime is when the optical excitation is on a shorter time scale than T_2; therefore light-induced coherence persists longer than the excitation. Interesting effects arise in this regime such as [214] self-induced transparency (SIT), photon echos, and free-induction decay, and may allow for large nonlinearity with small absorption (but long response time) for specially designed pulses.

The parametric and dynamic regimes of operation are studied in this thesis for optical soliton switching and computing. The tradeoff between the parametric and dynamic regimes is typically between low absorption and large (resonantly-enhanced) nonlinearity. The simulations of soliton interactions in Chapter 5 include absorption, and material figures-of-merit are derived in order to determine the maximum gain that can be obtained by the logic gate due to the presence of absorption in candidate materials. These figures-of-merit show that the tradeoff must be made in favor of small nonlinearity and low absorption, restricting attention mainly to the parametric regime of operation.

This chapter derives the fundamental nonlinear wave equation, which is a multi-dimensional and higher-order extension to the nonlinear Schrödinger (NLS) equation, appropriate for describing propagation in media of isotropic symmetry class and, with minor modifications, the cubic 432, $\bar{4}$3m and m3m symmetry classes. These choices are motivated by the presently available materials fused silica (isotropic) and AlGaAs (cubic $\bar{4}$3m), each of which satisfy the material figures-of-merit. Section 3.1 starts with Maxwell's equations and the material polarization expansion and derives the vector nonlinear Helmholtz equation. In the parametric and dynamic regimes, the nonlinear polarization can be represented by a Taylor series expansion [220], and is the approach taken here. The general integral forms of the first, third, and fifth terms of the polarization expansion are manipulated into differential form thereby transforming the integral-differential nonlinear Helmholtz equation into a purely differential one. The resulting second-order differential equation is difficult to handle numerically in multiple dimensions when long-time

evolution is desired, as it is here. As a result, a first-order equation is derived in section 3.2, with the two leading-order scales of the Helmholtz equation removed, which can readily describe long-time evolution. This section uses the asymptotic multiple-scales technique to derive the uni-directional, fully vectorial, nonlinear wave equation directly from Maxwell's equations for (3+1)-D propagation in weakly nonlinear media. This equation is reduced to forms suitable to describe the (1+1)-D spatial and (2+1)-D spatio-temporal simulations presented in thesis which are the starting points for numerical analysis based on the split-step method discussed in Chapter 4.

3.1 Derivation of the Vector Nonlinear Helmholtz Equation

In this section, the vector nonlinear Helmholtz equation valid for refractive and absorptive effects first-, third-, and fifth-order in the electric field is derived. The forms of these polarizations are then specified and examined separately in detail. The complete causal dispersive character of the linear susceptibility is retained in a compact time-domain formulation (Section 3.1.1) valid for less than unity fractional temporal bandwidths, while the third-order response is reduced from full nonlinear dispersion to the dominant time-domain forms describing the optical Kerr effect and fully dispersive stimulated Raman scattering (SRS) (Section 3.1.2), and the fifth-order response is reduced to instantaneous form (Section 3.1.3) where dispersion is assumed weak enough to be neglected.

The starting point for deriving the vector nonlinear wave equations is Maxwell's equations, written in differential form:

$$\nabla \times \mathbf{E} = -\frac{\partial \mathbf{B}}{\partial t} \tag{3.1}$$

$$\nabla \times \mathbf{H} = \mathbf{J}_f + \frac{\partial \mathbf{D}}{\partial t} \tag{3.2}$$

$$\nabla \cdot \mathbf{D} = \rho_f \tag{3.3}$$

$$\nabla \cdot \mathbf{B} = 0 \tag{3.4}$$

where $\mathbf{E}$ is the electric field, $\mathbf{H}$ is the magnetic field, $\mathbf{D}$ is the electric displacement, $\mathbf{B}$ is the magnetic induction, $\mathbf{J}_f$ is the free current (or source current) and ρ_f is the density of free charge. Boldfaced variables represent vector quantities. In the dielectric media appropriate for studies in optics, $\mathbf{J}_f = \rho_f = 0$. In order to couple the material response with the electromagnetic radiation, Maxwell's equations must be amended with the constitutive relations

$$\mathbf{B} = \mu_0 \mathbf{H} \tag{3.5}$$

$$\mathbf{D} = \varepsilon_0 \bar{\bar{\varepsilon}} \mathbf{E} = \varepsilon_0 \mathbf{E} + \mathbf{P} \tag{3.6}$$

where $\bar{\bar{\varepsilon}}$ is the relative material dielectric tensor, ε_0 is the free-space dielectric constant, $\mathbf{P}$ is the material polarization and μ_0 is the permeability of free-space. Note that the material is assumed to be non-magnetizable, i.e. $\mu = \mu_0$.

Using the Maxwell's equations 3.1 and 3.2 and the constitutive relation 3.5

$$\nabla \times [\nabla \times \mathbf{E}] = -\frac{\partial}{\partial t}(\nabla \times \mathbf{B}) = -\mu_0 \frac{\partial^2 \mathbf{D}}{\partial t^2}, \tag{3.7}$$

which can be rewritten using the constitutive relation 3.6

$$\nabla \times [\nabla \times \mathbf{E}] = -\frac{1}{c^2}\frac{\partial^2 \mathbf{E}}{\partial t^2} - \mu_0 \frac{\partial^2 \mathbf{P}}{\partial t^2} \tag{3.8}$$

where $c = \sqrt{1/\mu_0 \varepsilon_0}$ is the velocity of light in free-space.

The material polarization $\mathbf{P}$ consists of linear and nonlinear contributions:

$$\mathbf{P} = \mathbf{P}^{\mathrm{L}} + \mathbf{P}^{\mathrm{NL}} = \mathbf{P}^{\mathrm{L}} + \mathbf{P}^{(2)} + \mathbf{P}^{(3)} + \cdots, \tag{3.9}$$

where $\mathbf{P}^{(2)}$ is the second-order polarization, etc, and the expansion of the material polarization in a Taylor's series converges when the material response is sufficiently nonresonant [220], such as in the parametric or dynamic regimes.

Since this thesis is concerned with multi-dimensional and higher-order generalizations of the (NLS) equation, it is assumed that the lowest-order nonlinear contribution is $\mathbf{P}^{(3)}$. The derivations are directly valid for the isotropic symmetry class, but are also valid for cubic 432, $\bar{4}$3m and m3m with minor modifications. In centrosymmetric media, such as media of isotropic or cubic m3 and m3m symmetry classes, $\chi^{(2\ell)} = 0$, where ℓ is a positive integer. Cubic classes 432, $\bar{4}$3m and 23, have non-zero $\chi^{(2\ell)}$. For the latter three cubic classes, second-harmonic generation can usually be neglected because the cubic classes are

linearly isotropic and phase matching is difficult to achieve. In addition, resonant generation of radiation around DC due to optical rectification can also be ignored because the phase velocity near DC is typically much smaller than the group velocity of the optical driving field, although important effects can occur even in the nonresonant case [195], but are not considered in this thesis.

Separating the linear and nonlinear parts of the material polarization, the fully vectorial, nonlinearly-driven wave equation is

$$\nabla \times [\nabla \times \mathbf{E}] + \frac{1}{c^2}\frac{\partial^2 \mathbf{E}}{\partial t^2} + \mu_0 \frac{\partial^2 \mathbf{P}^{\mathrm{L}}}{\partial t^2} = -\mu_0 \frac{\partial^2 \mathbf{P}^{\mathrm{NL}}}{\partial t^2}, \tag{3.10}$$

or, in the alternate form

$$\nabla^2 \mathbf{E} - \nabla[\nabla \cdot \mathbf{E}] - \frac{1}{c^2}\frac{\partial^2 \mathbf{E}}{\partial t^2} - \mu_0 \frac{\partial^2 \mathbf{P}^{\mathrm{L}}}{\partial t^2} = \mu_0 \frac{\partial^2 \mathbf{P}^{\mathrm{NL}}}{\partial t^2}, \tag{3.11}$$

where the vector identity $\nabla \times [\nabla \times \mathbf{E}] = \nabla[\nabla \cdot \mathbf{E}] - \nabla^2 \mathbf{E}$ is used. These equations are generally valid for nonlinear optics. The forms of the polarizations are now specified.

The Material Polarization

The most general form for the linear material polarization, for example, including the full spatial and temporal response, is [221]

$$\mathbf{P}^{\mathrm{L}}(\mathbf{r},t) = \varepsilon_0 \int_{-\infty}^{\infty}\int_0^{\infty} \overline{\overline{R}}(\mathbf{r}',\tau) \cdot \mathbf{E}(\mathbf{r}-\mathbf{r}',t-\tau)\, d\mathbf{r}' d\tau, \tag{3.12}$$

which describes nonlocal behavior in space, such as diffusion of real carriers, and causal nonlocal behavior in time. By employing the electric dipole approximation [221], and thereby ignoring optical activity as well, the spatial response will not be considered in this thesis. Therefore, the material polarization convolution integrals describe only spatially localized material response but still retain non-zero time response. The form taken for the linear polarization is then

$$\mathbf{P}^{\mathrm{L}}(\mathbf{r},t) = \varepsilon_0 \int_0^{\infty} \overline{\overline{R}}(\mathbf{r},\tau) \cdot \mathbf{E}(\mathbf{r},t-\tau)\, d\tau, \tag{3.13}$$

where $\cdot$ is a contraction operator and the impulse-response function is allowed to vary spatially as would occur for layered media. The linear impulse-response function $\overline{\overline{R}}$ is a second-rank tensor and causality requires that the response is zero for $\tau < 0$ (for $\tau < 0$, the material polarization would depend on values of the field $\mathbf{E}(t-\tau)$ that haven't yet arrived), justifying the lower bound on the integral. A second condition is that the response function must be real because both the driving field and material polarization are real. Another common way of writing the linear polarization is

$$P_j^{\mathrm{L}}(\mathbf{r},t) = \varepsilon_0 \int_0^{\infty} R_{jk}(\mathbf{r},\tau) E_k(\mathbf{r},t-\tau)\, d\tau \tag{3.14}$$

where $j,k \in \{x,y,z\}$ and the Einstein summation convention over repeated indices is used.

Similarly, the form for the third-order nonlinear material polarization is

$$\mathbf{P}^{(3)}(\mathbf{r},t) = \varepsilon_0 \int_0^{\infty}\int_0^{\infty}\int_0^{\infty} \overline{\overline{\overline{\overline{R}}}}(\mathbf{r},\tau_1,\tau_2,\tau_3) \vdots \mathbf{E}(\mathbf{r},t-\tau_1)\mathbf{E}(\mathbf{r},t-\tau_2) \times \mathbf{E}(\mathbf{r},t-\tau_3)\, d\tau_1 d\tau_2 d\tau_3, \tag{3.15}$$

where the third-order impulse response function $\overline{\overline{\overline{\overline{R}}}}$ is a fourth-rank tensor, $\vdots$ is a contraction operator and the induced material polarization depends on the product of three fields. Here, spatial dispersion can additionally arise from the diffusion or propagation of real particles, such as electrons or phonons (i.e. heat), which are created by the nonlinear light-matter interaction. These effects are neglected by assuming sufficient distance from resonance. As before, the third-order nonlinear polarization is written in component form using the triple Einstein summation convention over repeated indices

$$P_j^{(3)}(\mathbf{r},t) = \varepsilon_0 \int_0^{\infty}\int_0^{\infty}\int_0^{\infty} R_{jklm}(\mathbf{r},\tau_1,\tau_2,\tau_3) E_k(\mathbf{r},t-\tau_1) \times E_l(\mathbf{r},t-\tau_2) E_m(\mathbf{r},t-\tau_3)\, d\tau_1 d\tau_2 d\tau_3. \tag{3.16}$$

The third-order nonlinear polarization is responsible for four-wave mixing effects such as nonlinear refraction (self- and cross-focusing and self- and cross-phase modulation), Raman and Brillouin scattering, and third-harmonic generation.

For ultrashort pulses with large temporal bandwidths, such that the excitation duration is much shorter than the medium response time T_1, the time-domain formulation of the nonlinear material response is the appropriate representation [150,220] because the electric field can be considered a delta function and the convolution integral trivially evaluated. In the opposite limit where the optical excitation lasts much longer than the material response time, the frequency-domain susceptibility formulation is most commonly used, such as the case for the mixing of monochromatic beams, because the material response function takes on a constant value. This thesis deals with an intermediate nonresonant situation for which part of the nonlinear response can be considered instantaneous and hence represented by a constant in the frequency-domain, while part of the response is non-instantaneous such that the material polarization is nontrivial in either formulation. With these arguments in mind then, instead of using the more general form for the third-order nonlinear impulse response function in equation 3.16 (which is valid for nonresonant as well as near-resonant processes [220]), the following form can be used that is appropriate for the nonresonant processes just discussed [145,222]

$$\begin{aligned} R_{jklm}(\mathbf{r},\tau_1,\tau_2,\tau_3) &= R^{\mathrm{K}}_{jklm}(\mathbf{r})\delta(\tau_1)\delta(\tau_2)\delta(\tau_3) \\ &\quad + R^{\mathrm{R}}_{jklm}(\mathbf{r},\tau_1,\tau_2)\delta(\tau_1-\tau_2)\delta(\tau_3) \end{aligned} \tag{3.17}$$

where the constant $R^{\mathrm{K}}_{jklm}(\mathbf{r})$ accounts for the strength of the instantaneous electronic, or Kerr, response and the Raman response function [150] $R^{\mathrm{R}}_{jklm}(\mathbf{r},\tau_1,\tau_2)$ accounts for the slower nuclear response. This form does not describe general nonlinear dispersion, but does describe the most important effects to this thesis - nonlinear refraction (in both instantaneous and delayed forms) and third-harmonic generation and down-conversion.

Raman scattering is a nonlinear refractive/absorptive effect that arises from the rotational or vibrational response of a nucleus to the time-varying electric field. In the quantum picture, Raman scattering is the interaction between photons and optical phonons (i.e. high-frequency phonons with non-zero dipole moments). This effect is described by a time-dependent nonlinear refractive index [222] as evident by using the impulse response function of equation 3.17 in the convolution integral of equation 3.16

$$\begin{aligned} P^{(3)}_j(\mathbf{r},t) &= \varepsilon_0 R^{\mathrm{K}}_{jklm}(\mathbf{r})E_k(\mathbf{r},t)E_l(\mathbf{r},t)E_m(\mathbf{r},t) \\ &\quad + \varepsilon_0\int_0^\infty R^{\mathrm{R}}_{jklm}(\mathbf{r},\tau)E_k(\mathbf{r},t-\tau)E_l(\mathbf{r},t-\tau)E_m(\mathbf{r},t)d\tau, \end{aligned} \tag{3.18}$$

where $\tau \equiv \tau_1 = \tau_2$. The Raman response is studied further in Appendix B.

The corresponding fifth-order polarization is

$$P^{(5)}_j(\mathbf{r},t) = \varepsilon_0 R^{\mathrm{I}}_{jklmno}(\mathbf{r})E_k(\mathbf{r},t)E_l(\mathbf{r},t)E_m(\mathbf{r},t)E_n(\mathbf{r},t)E_o(\mathbf{r},t), \tag{3.19}$$

and is treated only in instantaneous form responsible for nonlinear refraction.

Since the terms in the material polarizations depend on time history, it is useful to define the temporal Fourier-transform pair

$$\mathbf{E}(\mathbf{r},t) = \frac{1}{2\pi}\int \tilde{\mathbf{E}}(\mathbf{r},\omega)e^{-i\omega t}d\omega \tag{3.20a}$$

$$\tilde{\mathbf{E}}(\mathbf{r},\omega) = \int \mathbf{E}(\mathbf{r},t)e^{i\omega t}dt \tag{3.20b}$$

in order to examine the linear and nonlinear polarizations in the temporal frequency domain. For compactness of notation, all integrals without limits are taken to extend from $-\infty$ to $+\infty$. Using the Fourier transform relations and performing Taylor's expansions in the temporal frequency domain, the convolution integrals of equations 3.14 and 3.18 can be rewritten in differential forms for pulses of finite temporal bandwidths, as shown in sections 3.1.1 and 3.1.2, respectively. The reason for writing the material response in differential form is that the integral-differential wave equations 3.10 and 3.11 become purely differential. Before this is done, though, the quasi-monochromatic representation, which is key to writing the material response as differential operators on the pulse envelope, is examined.

The Quasi-Monochromatic Representation

In this thesis, the quasi-monochromatic representation of the optical field is used such that in the time-domain

$$\mathbf{E}(\mathbf{r},t) = \frac{1}{2}\left[\overline{\mathbf{A}}(\mathbf{r},t)e^{-i\omega_0 t} + \overline{\mathbf{A}}^*(\mathbf{r},t)e^{i\omega_0 t}\right]. \tag{3.21}$$

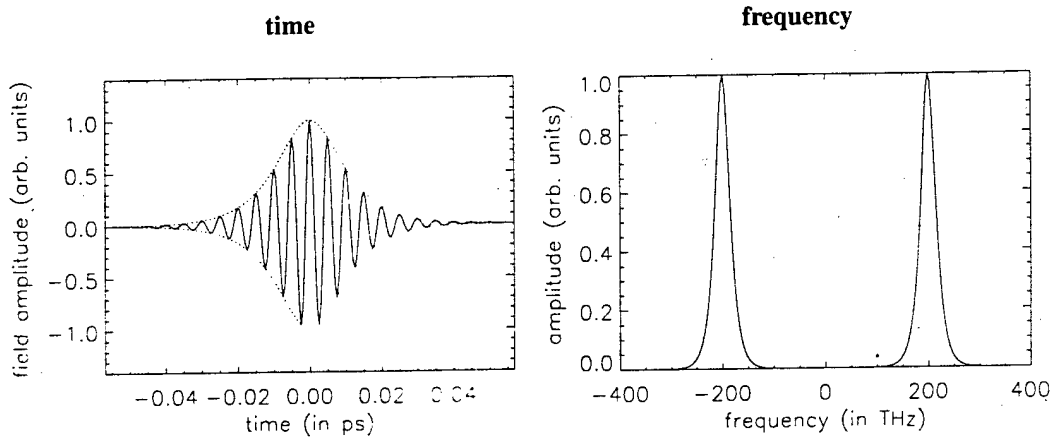

Figure 3.1: Quasi-monochromatic wavepacket of fractional bandwidth $\eta = 0.12$. The left figure shows the representation in time and the right figure shows the representation in frequency. The dotted lines in the time-domain plot illustrate the pulse envelope.

The quasi-monochromatic representation assumes that the field has some finite bandwidth centered about the carrier frequency ω_0, meaning that the fast temporal phase variation is removed leaving only slower temporal variation in the envelope. In fact, the notion of an optical envelope has been shown to be valid down to the single-cycle regime [223], but the Taylor expansion of the linear and nonlinear convolution integrals performed in the subsequent sections of this chapter does not converge in this regime where the fractional temporal bandwidth approaches or even exceeds unity. For generality, the envelope still retains a fast propagation phase variation, which is denoted by the over-bar. The quasi-monochromatic representation is illustrated more clearly upon transformation into the temporal frequency domain

$$\begin{aligned}\tilde{\mathbf{E}}(\mathbf{r},\omega) &= \frac{1}{2}\left[\bar{\tilde{\mathbf{A}}}(\mathbf{r},\omega) * \delta(\omega-\omega_0) + \bar{\tilde{\mathbf{A}}}^*(\mathbf{r},\omega) * \delta(\omega+\omega_0)\right] \\ &= \frac{1}{2}\left[\bar{\tilde{\mathbf{A}}}(\mathbf{r},\omega-\omega_0) + \bar{\tilde{\mathbf{A}}}^*(\mathbf{r},\omega+\omega_0)\right] \end{aligned} \tag{3.22}$$

where $*$ is the convolution operator. In the following sections, these expressions will be used to examine the material response in the temporal-frequency domain and define the susceptibility tensors.

The time and frequency domain representations of a quasi-monochromatic wavepacket are shown in Figure 3.1. The fractional bandwidth is defined as the full-width at half-maximum frequency bandwidth $\Delta\omega_{\mathrm{FWHM}}$ divided by the center frequency ω_0,

$$\eta = \frac{\Delta\omega_{\mathrm{FWHM}}}{\omega_0}, \tag{3.23}$$

where the quasi-monochromatic representation is valid to the point where $\eta \sim 1$. In the multiple-scales analysis of section 3.2, η will serve as a small expansion parameter; therefore, the situation of interest is when $\eta < 1$. Note that when the third-harmonic is considered, an additional slowly-varying envelope about $3\omega_0$ must be defined, otherwise the fractional bandwidth of the envelope $\bar{\mathbf{A}}$ about the fundamental would exceed unity.

3.1.1 The Linear Material Polarization

This section transforms the convolution integral of equation 3.14 into the temporal frequency domain representation $\tilde{\mathbf{P}}^{\mathrm{L}}(\omega)$. The linear susceptibility is defined and Taylor-expanded such that the inverse Fourier transformation into the time domain results in a much simpler differential representation of 3.14. The derivation is presented in detail here in order to shorten the similar procedure used for the third-order polarization in the following section.

Using the time/frequency Fourier transform relation, the linear material polarization given by equation 3.14 can be rewritten as

$$\begin{aligned} P_j^{\mathrm{L}}(\mathbf{r},t) &= \frac{\varepsilon_0}{2\pi}\int_0^\infty R_{jk}(\mathbf{r},\tau)\left[\int \tilde{E}_k(\mathbf{r},\omega)e^{-i\omega[t-\tau]}d\omega\right]d\tau \\ &= \frac{\varepsilon_0}{2\pi}\int\left[\int \Theta(\tau)R_{jk}(\mathbf{r},\tau)e^{i\omega\tau}d\tau\right]\tilde{E}_k(\mathbf{r},\omega)e^{-i\omega t}d\omega \end{aligned}$$

$$= \frac{\varepsilon_0}{2\pi}\int \chi_{jk}(\mathbf{r},\omega)\tilde{E}_k(\mathbf{r},\omega)e^{-i\omega t}d\omega \tag{3.24}$$

where the order of integration is changed in the second step, $\Theta(\tau)$ is the unit step (Heaviside) function required by causality and normally incorporated into the definition of R, and the linear susceptibility is defined

$$\chi_{jk}(\mathbf{r},\omega) \equiv \int \Theta(\tau)R_{jk}(\mathbf{r},\tau)e^{i\omega\tau}d\tau, \tag{3.25}$$

which guarantees that $\chi_{jk}(-\omega) = \chi^*_{jk}(\omega)$ since R_{jk} is real. An interesting manifestation of causality in equation 3.25 is the Kramers-Kronig relations. Equation 3.25 can be rewritten [224]

$$\begin{aligned}\chi_{jk}(\omega) &= \chi_{jk}(\omega) * \left[\frac{\delta(\omega)}{2} + \frac{i}{2\pi\omega}\right] \\ &= -\frac{i}{\pi}\mathcal{P}\int \frac{\chi_{jk}(\Omega)}{\Omega-\omega}d\Omega,\end{aligned} \tag{3.26}$$

where $\mathcal{P}$ represents the principal value. The linear susceptibility consists of real and imaginary parts $\chi_{jk} = \mathcal{R}e\{\chi_{jk}\} + i\,Im\{\chi_{jk}\}$ so that equation 3.26 is rewritten

$$\mathcal{R}e\{\chi_{jk}(\omega)\} = \frac{1}{\pi}\mathcal{P}\int \frac{Im\{\chi_{jk}(\Omega)\}}{\Omega-\omega}d\Omega \tag{3.27}$$

$$Im\{\chi_{jk}(\omega)\} = -\frac{1}{\pi}\mathcal{P}\int \frac{\mathcal{R}e\{\chi_{jk}(\Omega)\}}{\Omega-\omega}d\Omega \tag{3.28}$$

which are the linear Kramers-Kronig relations.

The linear material polarization is now written completely in the temporal frequency domain,

$$\begin{aligned}\tilde{P}^L_j(\mathbf{r},\omega) &= \frac{\varepsilon_0}{2\pi}\int\left[\int \chi_{jk}(\mathbf{r},\omega_1)\tilde{E}_k(\mathbf{r},\omega_1)e^{-i\omega_1 t}d\omega_1\right]e^{i\omega t}dt \\ &= \frac{\varepsilon_0}{2\pi}\int\left[\int \chi_{jk}(\mathbf{r},\omega_1)e^{-i(\omega_1-\omega)t}dt\right]\tilde{E}_k(\mathbf{r},\omega_1)d\omega_1 \\ &= \varepsilon_0\int \chi_{jk}(\mathbf{r},\omega_1)\tilde{E}_k(\mathbf{r},\omega_1)\delta(\omega-\omega_1)d\omega_1 \\ &= \varepsilon_0\chi_{jk}(\mathbf{r},\omega)\tilde{E}_k(\mathbf{r},\omega).\end{aligned} \tag{3.29}$$

which indicates that the linear polarization is simply the product of the linear dispersive susceptibility with the amplitude of the temporal frequency spectrum of the field.

Substituting the wavepacket representation into equation 3.29 results in

$$\tilde{P}^L_j(\mathbf{r},\omega) = \frac{\varepsilon_0}{2}\chi_{jk}(\mathbf{r},\omega)\left[\tilde{\bar{A}}_k(\mathbf{r},\omega-\omega_0) + \tilde{\bar{A}}^*_k(\mathbf{r},\omega+\omega_0)\right]. \tag{3.30}$$

Since the wavepacket representation is centered about ω_0 (and the conjugate about $-\omega_0$), equation 3.30 can be rewritten by Taylor-expanding $\chi(\mathbf{r},\omega)$ about the central frequency ω_0 (and $-\omega_0$)

$$\begin{aligned}\tilde{P}^L_j(\mathbf{r},\omega) = &\frac{\varepsilon_0}{2}\left[\chi_{jk}(\mathbf{r},\omega_0) + \sum_{s=1}^{\infty}\frac{[\omega-\omega_0]^s}{s!}\cdot\frac{\partial^s\chi_{jk}(\mathbf{r},\omega)}{\partial\omega^s}\bigg|_{\omega=\omega_0}\right]\tilde{\bar{A}}_k(\mathbf{r},\omega-\omega_0) \\ &+ \frac{\varepsilon_0}{2}\left[\chi_{jk}(\mathbf{r},-\omega_0) + \sum_{s=1}^{\infty}\frac{[\omega+\omega_0]^2}{s!}\cdot\frac{\partial^s\chi_{jk}(\mathbf{r},\omega)}{\partial\omega^s}\bigg|_{\omega=-\omega_0}\right]\tilde{\bar{A}}^*_k(\mathbf{r},\omega+\omega_0).\end{aligned} \tag{3.31}$$

Considering now only the linear polarization near the center frequency ω_0, and defining $\omega' = \omega - \omega_0$, the polarization is inverse transformed into the time domain

$$P^{L+}_j(\mathbf{r},t) = \frac{\varepsilon_0}{2}\int\left[\chi_{jk}(\mathbf{r},\omega_0) + \sum_{s=1}^{\infty}\frac{[\omega']^s}{s!}\cdot\frac{\partial^s\chi_{jk}(\mathbf{r},\omega)}{\partial\omega^s}\bigg|_{\omega=\omega_0}\right]\tilde{\bar{A}}_k(\mathbf{r},\omega')e^{-i\omega t}d\omega$$

$$
\begin{aligned}
&= \frac{\varepsilon_0}{2}\int\left[\chi_{jk}(\mathbf{r},\omega_0)+\sum_{s=1}^{\infty}\frac{[\omega']^s}{s!}\cdot\frac{\partial^s\chi_{jk}(\mathbf{r},\omega)}{\partial\omega^s}\bigg|_{\omega=\omega_0}\right]\tilde{\overline{A}}_k(\mathbf{r},\omega')e^{-i[\omega'+\omega_0]t}d\omega' \\
&= \frac{\varepsilon_0}{2}\left[\chi_{jk}(\mathbf{r},\omega_0)\overline{A}_k(t)+\sum_{s=1}^{\infty}\frac{i^s}{s!}\cdot\frac{\partial^s\chi_{jk}(\mathbf{r},\omega)}{\partial\omega^s}\bigg|_{\omega=\omega_0}\cdot\frac{\partial^s\overline{A}_k(\mathbf{r},t)}{\partial t^s}\right]e^{-i\omega_0 t} \\
&= \frac{\varepsilon_0}{2}\left[\chi_{jk}\left(\mathbf{r},\omega_0+i\frac{\partial}{\partial t}\right)\overline{A}_k(\mathbf{r},t)\right]e^{-i\omega_0 t}. \qquad (3.32)
\end{aligned}
$$

Here, the function of the operator is interpreted by its Taylor's expansion about the central frequency ω_0.

Using equation 3.32, the vector Helmholtz equation 3.11 can be rewritten for the quasi-monochromatic envelope

$$
\begin{aligned}
&\nabla^2\overline{A}_j(\mathbf{r},t)e^{-i\omega_0 t}-\frac{\partial}{\partial j}\sum_{k\in\{x,y,z\}}\frac{\partial\overline{A}_k(\mathbf{r},t)}{\partial k}e^{-i\omega_0 t}= \qquad (3.33)\\
&\frac{1}{c^2}\frac{\partial^2}{\partial t^2}\left\{\overline{A}_j(\mathbf{r},t)e^{-i\omega_0 t}+\left[\chi_{jk}\left(\mathbf{r},\omega_0+i\frac{\partial}{\partial t}\right)\overline{A}_k(\mathbf{r},t)\right]e^{-i\omega_0 t}\right\}\\
&+2\mu_0\frac{\partial^2 P_j^{\mathrm{NL}+}(\mathbf{r},t)}{\partial t^2},
\end{aligned}
$$

with the corresponding conjugate expression. Here $P_j^{\mathrm{NL}+}$ means the nonlinear polarization associated with the phase factor $e^{-i\omega_0 t}$. An additional equation is required to describe the evolution of any additional radiation well separated from ω_0, such as the third-harmonic, otherwise the fractional bandwidth of a single envelope would exceed unity and the functional representation of the linear material polarization would become invalid.

Defining the linear dielectric tensor

$$\varepsilon_{jk}^{\mathrm{L}}(\mathbf{r},\omega)\equiv 1+\chi_{jk}(\mathbf{r},\omega), \qquad (3.34)$$

the vector Helmholtz equation becomes

$$
\begin{aligned}
&\nabla^2\overline{A}_j(\mathbf{r},t)e^{-i\omega_0 t}-\frac{\partial}{\partial j}\sum_{k\in\{x,y,z\}}\frac{\partial\overline{A}_k(\mathbf{r},t)}{\partial k}e^{-i\omega_0 t}= \qquad (3.35)\\
&\frac{1}{c^2}\frac{\partial^2}{\partial t^2}\left\{\left[\varepsilon_{jk}^{\mathrm{L}}\left(\mathbf{r},\omega_0+i\frac{\partial}{\partial t}\right)\overline{A}_j(\mathbf{r},t)\right]e^{-i\omega_0 t}\right\}+2\mu_0\frac{\partial^2 P_j^{\mathrm{NL}+}(\mathbf{r},t)}{\partial t^2}.
\end{aligned}
$$

The second-order time derivative of the linear polarization is evaluated

$$
\begin{aligned}
&\frac{1}{c^2}\frac{\partial^2}{\partial t^2}\left\{\left[\varepsilon_{jk}^{\mathrm{L}}\left(\mathbf{r},\omega_0+i\frac{\partial}{\partial t}\right)\overline{A}_k(\mathbf{r},t)\right]e^{-i\omega_0 t}\right\}\\
&=\frac{1}{c^2}\left\{\left[\frac{\partial^2}{\partial t^2}-2i\omega_0\frac{\partial}{\partial t}-\omega_0^2\right]\left[\varepsilon_{jk}^{\mathrm{L}}\left(\mathbf{r},\omega_0+i\frac{\partial}{\partial t}\right)\overline{A}_k(\mathbf{r},t)\right]\right\}e^{-i\omega_0 t}\\
&=-\frac{1}{c^2}\left\{\left[\omega_0+i\frac{\partial}{\partial t}\right]^2\left[\varepsilon_{jk}^{\mathrm{L}}\left(\mathbf{r},\omega_0+i\frac{\partial}{\partial t}\right)\overline{A}_k(\mathbf{r},t)\right]\right\}e^{-i\omega_0 t}. \qquad (3.36)
\end{aligned}
$$

In general, the linear dielectric tensor is composed of 9 independent elements. For the purpose of this thesis, the material symmetry classes will be restricted to those in which the linear dielectric tensor is isotropic. Isotropic refers to the case when all three elements of this diagonalized tensor are equal [225], i.e.

$$\overline{\overline{\varepsilon}}(\omega)=\begin{bmatrix}\varepsilon(\omega) & 0 & 0\\ 0 & \varepsilon(\omega) & 0\\ 0 & 0 & \varepsilon(\omega)\end{bmatrix}, \qquad (3.37)$$

otherwise the material is anisotropic. The linearly isotropic symmetry classes are cubic and isotropic. Note that the isotropic symmetry class is not a crystal class but a macroscopic description of liquids, gases or disordered or amorphous solids such as glass.

The linear propagation and absorption functions are defined

$$\left[k(\mathbf{r},\omega)+i\frac{\alpha(\mathbf{r},\omega)}{2}\right]^2\equiv\frac{\omega^2\varepsilon^{\mathrm{L}}(\mathbf{r},\omega)}{c^2} \qquad (3.38)$$

where $k(\mathbf{r},\omega)$ is the frequency-dependent linear propagation constant and $\alpha(\mathbf{r},\omega)$ is the frequency-dependent linear intensity absorption coefficient, and both are allowed to be functions of space to represent material inhomogeneity. The tensor notation is dropped for the linearly-isotropic classes because the dielectric tensor becomes scalar. Assuming that linear absorption is small compared to the propagation constant, equation 3.38 can be approximated

$$k^2(\mathbf{r},\omega)+ik(\mathbf{r},\omega)\alpha(\mathbf{r},\omega)\approx\frac{\omega^2}{c^2}\left[\varepsilon^{\mathrm{L}}_{\mathcal{R}}(\mathbf{r},\omega)+i\varepsilon^{\mathrm{L}}_{I}(\mathbf{r},\omega)\right], \tag{3.39}$$

where the following definitions are made:

$$\varepsilon^{\mathrm{L}}_{\mathcal{R}}(\mathbf{r},\omega)\equiv\mathcal{R}e\left\{\varepsilon^{\mathrm{L}}(\mathbf{r},\omega)\right\} \tag{3.40}$$

$$\varepsilon^{\mathrm{L}}_{I}(\mathbf{r},\omega)\equiv Im\left\{\varepsilon^{\mathrm{L}}(\mathbf{r},\omega)\right\}. \tag{3.41}$$

Now the linear propagation and absorption constants are written

$$k^2(\mathbf{r},\omega)=\frac{\omega^2}{c^2}\varepsilon^{\mathrm{L}}_{\mathcal{R}}(\mathbf{r},\omega) \tag{3.42}$$

$$\alpha(\mathbf{r},\omega)=\frac{\omega}{c}\varepsilon^{\mathrm{L}}_{I}(\mathbf{r},\omega)/\sqrt{\varepsilon^{\mathrm{L}}_{\mathcal{R}}(\mathbf{r},\omega)}. \tag{3.43}$$

With these replacements, the Helmholtz equation is now written

$$\begin{aligned}\nabla^2\overline{A}_j(\mathbf{r},t)e^{-i\omega_0 t}-\frac{\partial}{\partial j}\sum_{k\in\{x,y,z\}}\frac{\partial\overline{A}_k(\mathbf{r},t)}{\partial k}e^{-i\omega_0 t}&=2\mu_0\frac{\partial^2 P_j^{\mathrm{NL}+}(\mathbf{r},t)}{\partial t^2}\\ -\left\{k\left(\mathbf{r},\omega_0+i\frac{\partial}{\partial t}\right)\left[k\left(\mathbf{r},\omega_0+i\frac{\partial}{\partial t}\right)+i\alpha\left(\mathbf{r},\omega_0+i\frac{\partial}{\partial t}\right)\right]\overline{A}_j(\mathbf{r},t)\right\}e^{-i\omega_0 t},\end{aligned} \tag{3.44}$$

where only the form of the nonlinear polarization remains to be specified.

3.1.2 The Third-Order Nonlinear Material Polarization

This section examines more closely the third-order material polarization, beginning first with the general response of nonlinear refraction. Using the same steps as for the linear material polarization, the third-order response integral is transformed into the temporal frequency domain. The frequency-domain representation is approximated for finite bandwidth excitation and transformed back into the time domain. Using the results of Appendix A, the tensor structure is reduced for the isotropic (and cubic 432, $\bar{4}3$m and m3m) symmetry class. Finally, the fully general case is reduced to a form suitable for the description of the nonresonant Kerr and Raman nonlinearities as previously discussed, which are used throughout the remaining chapters of this thesis.

Following the procedure used for transforming the linear response integral in section 3.1.1, the nonlinear polarization 3.16 is written in the temporal frequency domain as

$$\begin{aligned}\tilde{P}_j^{(3)}(\mathbf{r},\omega)=\varepsilon_0\int\int\int\chi_{jklm}(\omega;\mathbf{r},\omega_1,\omega_2,\omega_3)\tilde{E}_k(\mathbf{r},\omega_1)\tilde{E}_l(\mathbf{r},\omega_2)\times\\ \tilde{E}_m(\mathbf{r},\omega_3)\delta(\omega-\omega_1-\omega_2-\omega_3)d\omega_1 d\omega_2 d\omega_3,\end{aligned} \tag{3.45}$$

where the factors of $1/2\pi$ have been neglected for simplicity, and the third-order nonlinear susceptibility tensor is defined

$$\begin{aligned}\chi_{jklm}(\omega;\mathbf{r},\omega_1,\omega_2,\omega_3)\equiv\int\int\int\Theta(\tau_1)\Theta(\tau_2)\Theta(\tau_3)R_{jklm}(\mathbf{r},\tau_1,\tau_2,\tau_3)\times\\ e^{i[\omega_1\tau_1+\omega_2\tau_2+\omega_3\tau_3]}d\tau_1 d\tau_2 d\tau_3.\end{aligned} \tag{3.46}$$

The Heaviside functions are included to enforce causality with infinite limits of integration. Again, because the third-order nonlinear response function R_{jklm} is real,

$$\chi_{jklm}(\omega;\mathbf{r},-\omega_1,-\omega_2,-\omega_3)=\chi^*_{jklm}(\omega;\mathbf{r},\omega_1,\omega_2,\omega_3). \tag{3.47}$$

In this thesis, the nonlinear processes of interest are those which are nearly frequency-degenerate, such that any generated frequencies are near that of the driving field at ω_0, and those involving the third-harmonic. These latter third-harmonic processes are discussed in Appendix A.

Using the quasi-monochromatic representation 3.21, equation 3.45 can be written

$$\begin{aligned}\tilde{P}_j^{(3)+}(\mathbf{r},\omega) = \frac{\varepsilon_0}{8}\int\int\int \chi_{jklm}(\omega;\mathbf{r},\omega_1,\omega_2,\omega_3)\times \\ \Big[\tilde{\bar{A}}_k^*(\mathbf{r},\omega_1+\omega_0)\tilde{\bar{A}}_l(\mathbf{r},\omega_2-\omega_0)\tilde{\bar{A}}_m(\mathbf{r},\omega_3-\omega_0) \\ +\tilde{\bar{A}}_k(\mathbf{r},\omega_1-\omega_0)\tilde{\bar{A}}_l^*(\mathbf{r},\omega_2+\omega_0)\tilde{\bar{A}}_m(\mathbf{r},\omega_3-\omega_0) \\ +\tilde{\bar{A}}_k(\mathbf{r},\omega_1-\omega_0)\tilde{\bar{A}}_l(\mathbf{r},\omega_2-\omega_0)\tilde{\bar{A}}_m^*(\mathbf{r},\omega_3+\omega_0)\Big]\times \\ \delta(\omega-\omega_1-\omega_2-\omega_3)d\omega_1 d\omega_2 d\omega_3,\end{aligned} \tag{3.48}$$

which is valid for fully-dispersive nonlinear refraction. Now, the third-order susceptibility tensor is Taylor-expanded in the three frequency space $[\omega_1,\omega_2,\omega_3]$ about the center frequency ω_0 and its conjugate $-\omega_0$. Taking the first term in equation 3.48 for example

$$\begin{aligned}\chi_{jklm}(\omega;\omega_1,\omega_2,\omega_3)\tilde{\bar{A}}_k^*(\omega_1+\omega_0)\tilde{\bar{A}}_l(\omega_2-\omega_0)\tilde{\bar{A}}_m(\omega_3-\omega_0) = \\ \Bigg[\chi_{jklm}(\omega_0;-\omega_0,\omega_0,\omega_0) + [\omega_1+\omega_0]\left.\frac{\partial\chi_{jklm}(\omega_0;\omega_1,\omega_0,\omega_0)}{\partial\omega_1}\right|_{\omega_1=-\omega_0} \\ + [\omega_2-\omega_0]\left.\frac{\partial\chi_{jklm}(\omega_0;-\omega_0,\omega_2,\omega_0)}{\partial\omega_2}\right|_{\omega_2=\omega_0} \\ + [\omega_3-\omega_0]\left.\frac{\partial\chi_{jklm}(\omega_0;-\omega_0,\omega_0,\omega_3)}{\partial\omega_3}\right|_{\omega_3=\omega_0} + \cdots\Bigg]\times \\ \tilde{\bar{A}}_k^*(\omega_1+\omega_0)\tilde{\bar{A}}_l(\omega_2-\omega_0)\tilde{\bar{A}}_m(\omega_3-\omega_0),\end{aligned} \tag{3.49}$$

where the spatial dependence is dropped for notational convenience here and throughout the rest of this section.

Using the proper Taylor expansions for the remaining terms in equation 3.48 and transforming back into the time domain results in (cf equation A.10)

$$\begin{aligned}P_j^{(3)+}(t) = \frac{\varepsilon_0}{8}\Bigg[\chi_{jklm}\left(\omega_0;-\omega_0+i\frac{\partial}{\partial t},\omega_0+i\frac{\partial}{\partial t},\omega_0+i\frac{\partial}{\partial t}\right)\bar{A}_k^*(t)\bar{A}_l(t)\bar{A}_m(t) \\ +\chi_{jklm}\left(\omega_0;\omega_0+i\frac{\partial}{\partial t},-\omega_0+i\frac{\partial}{\partial t},\omega_0+i\frac{\partial}{\partial t}\right)\bar{A}_k(t)\bar{A}_l^*(t)\bar{A}_m(t) \\ +\chi_{jklm}\left(\omega_0;\omega_0+i\frac{\partial}{\partial t},\omega_0+i\frac{\partial}{\partial t},-\omega_0+i\frac{\partial}{\partial t}\right)\bar{A}_k(t)\bar{A}_l(t)\bar{A}_m^*(t)\Bigg]e^{-i\omega_0 t}.\end{aligned} \tag{3.50}$$

The operator arguments are interpreted as before and the derivative operations are only performed on the corresponding field envelopes; thus, ordering of the field envelopes is important. Using the intrinsic and spatial symmetry properties discussed in section A.2, equation 3.50 reduces to (cf equation A.11)

$$\begin{aligned}P_j^{(3)+}(t) = \frac{3\varepsilon_0}{8}\Bigg[\chi_{jjjj}\left(\omega_0;-\omega_0+i\frac{\partial}{\partial t},\omega_0+i\frac{\partial}{\partial t},\omega_0+i\frac{\partial}{\partial t}\right)\bar{A}_j^*(t)\bar{A}_j(t)\bar{A}_j(t) \\ +2\chi_{jkkj}\left(\omega_0;-\omega_0+i\frac{\partial}{\partial t},\omega_0+i\frac{\partial}{\partial t},\omega_0+i\frac{\partial}{\partial t}\right)\bar{A}_k^*(t)\bar{A}_k(t)\bar{A}_j(t) \\ +\chi_{jjkk}\left(\omega_0;-\omega_0+i\frac{\partial}{\partial t},\omega_0+i\frac{\partial}{\partial t},\omega_0+i\frac{\partial}{\partial t}\right)\bar{A}_j^*(t)\bar{A}_k(t)\bar{A}_k(t)\Bigg]e^{-i\omega_0 t},\end{aligned} \tag{3.51}$$

where the subscripts $j \neq k$.

In general, as given by equation 3.46, all terms in the Taylor's expansion of the third-order susceptibility about $\pm\omega_0$ have real and imaginary parts. This is a result of retaining the fully dispersive character. As mentioned previously, this thesis is concerned with the instantaneous and Raman responses. Even though the instantaneous response strictly means that the susceptibility does not vary over the excitation bandwidth, this thesis retains both the real and imaginary parts of the "instantaneous" susceptibility without considering the fully dispersive character. The reason for doing this is because the delayed response given by the Raman effect should dominate the remaining dispersive terms. In contrast to the instantaneous susceptibility, the frequency dependence

of the Raman susceptibility is retained such that the even-order terms in the Raman susceptibility expansion are real (giving rise to nonlinear refraction effects) while the odd-order terms are imaginary (giving rise to nonlinear gain/absorption effects).

The full derivation including both the instantaneous and Raman nonlinear response is carried out in section B.3. The result, given by equation B.78, is repeated here for convenience

$$
\begin{aligned}
P_j^{(3)+}(t) = \frac{3\varepsilon_0}{8}\Big[& \chi^{\mathrm{K}}_{jjjj}(\omega_0;-\omega_0,\omega_0,\omega_0)\overline{A}_j^*(t)\overline{A}_j(t)\overline{A}_j(t) \\
& +2\chi^{\mathrm{K}}_{jkkj}(\omega_0;-\omega_0,\omega_0,\omega_0)\overline{A}_k^*(t)\overline{A}_k(t)\overline{A}_j(t) \\
& +\chi^{\mathrm{K}}_{jjkk}(\omega_0;-\omega_0,\omega_0,\omega_0)\overline{A}_j^*(t)\overline{A}_k(t)\overline{A}_k(t)\Big]e^{-i\omega_0 t} \\
+\frac{\varepsilon_0}{4}\Big\{ & \Big[\chi^{\mathrm{R}}_{jjjj}(\omega_0;0)\overline{A}_j^*(t)\overline{A}_j(t)+\chi^{\mathrm{R}}_{jkkj}(\omega_0;0)\overline{A}_k^*(t)\overline{A}_k(t)\Big]\overline{A}_j(t) \\
& +\chi^{\mathrm{R}}_{jjkk}(\omega_0;0)\Big[\overline{A}_k^*(t)\overline{A}_j(t)+\overline{A}_j^*(t)\overline{A}_k(t)\Big]\overline{A}_k(t)\Big\}e^{-i\omega_0 t} \\
-\frac{\varepsilon_0}{4}\Big\{ & \Big[T^{\mathrm{R}}_{jjjj}\frac{\partial\overline{A}_j^*(t)\overline{A}_j(t)}{\partial t}+T^{\mathrm{R}}_{jkkj}\frac{\partial\overline{A}_k^*(t)\overline{A}_k(t)}{\partial t}\Big]\overline{A}_j(t) \\
& +T^{\mathrm{R}}_{jjkk}\Big[\frac{\partial\overline{A}_k^*(t)\overline{A}_j(t)}{\partial t}+\frac{\partial\overline{A}_j^*(t)\overline{A}_k(t)}{\partial t}\Big]\overline{A}_k(t)\Big\}e^{-i\omega_0 t} \\
-\frac{\varepsilon_0}{8}\Big\{ & \Big[\chi^{\mathrm{R}''}_{jjjj}(\omega_0;0)\frac{\partial^2\overline{A}_j^*(t)\overline{A}_j(t)}{\partial t^2}+\chi^{\mathrm{R}''}_{jkkj}(\omega_0;0)\frac{\partial^2\overline{A}_k^*(t)\overline{A}_k(t)}{\partial t^2}\Big]\overline{A}_j(t) \\
& +\chi^{\mathrm{R}''}_{jjkk}(\omega_0;0)\Big[\frac{\partial^2\overline{A}_k^*(t)\overline{A}_j(t)}{\partial t^2}+\frac{\partial^2\overline{A}_j^*(t)\overline{A}_k(t)}{\partial t^2}\Big]\overline{A}_k(t)\Big\}e^{-i\omega_0 t}.
\end{aligned}
\tag{3.52}
$$

The third-order polarization includes scalar and vectorial (coupled) forms of nonlinear refraction, two-photon absorption, first-order Raman gain, and second-order dispersion of Raman nonlinear refraction. The phase-dependent vectorial terms are absent if orthogonal circular polarizations are chosen as the basis set rather than linear polarizations [226]. Here, the linear polarization, or Cartesian, basis set was chosen because these polarizations are also the eigenvectors for a planar waveguide.

Defining the Kerr nonlinear index, the two-photon absorption coefficient, the Raman nonlinear index, the Raman time constant, and the Raman index dispersion coefficient, respectively,

$$n_K = \frac{3}{8n_0}\mathcal{R}e\left\{\chi^{\mathrm{K}}_{jjjj}(\omega_0;-\omega_0,\omega_0,\omega_0)\right\} \tag{3.53}$$

$$\beta_2 = \frac{3k_0}{4n_0}Im\left\{\chi^{\mathrm{K}}_{jjjj}(\omega_0;-\omega_0,\omega_0,\omega_0)\right\} \tag{3.54}$$

$$n_R = \frac{1}{4n_0}\chi^{\mathrm{R}}_{jjjj}(\omega_0;0) \tag{3.55}$$

$$\tau_R = \frac{T^{\mathrm{R}}_{jjjj}}{\chi^{\mathrm{R}}_{jjjj}(\omega_0;0)}\cdot\frac{n_R}{n_K+n_R} \tag{3.56}$$

$$n_R'' = \frac{1}{4n_0}\chi^{\mathrm{R}''}_{jjjj}(\omega_0;0). \tag{3.57}$$

and the nonlinear anisotropy ratios

$$\begin{aligned}
\Delta_K &= \chi^{\mathrm{K}}_{jkkj}/\chi^{\mathrm{K}}_{jjjj} & \Delta_R &= \chi^{\mathrm{R}}_{jkkj}/\chi^{\mathrm{R}}_{jjjj} = T^{\mathrm{R}}_{jkkj}/T^{\mathrm{R}}_{jjjj} \\
\gamma_K &= \chi^{\mathrm{K}}_{jjkk}/\chi^{\mathrm{K}}_{jjjj} & \gamma_R &= \chi^{\mathrm{R}}_{jjkk}/\chi^{\mathrm{R}}_{jjjj} = T^{\mathrm{R}}_{jjkk}/T^{\mathrm{R}}_{jjjj},
\end{aligned}$$

equation 3.52 reduces to

$$
\begin{aligned}
P_j^{(3)+}(t) = \varepsilon_0 n_0 n_2\Big\{ & \Big[|A_j(t)|^2+2\Delta|A_k(t)|^2\Big]\overline{A}_j(t)+\gamma\overline{A}_j^*(t)\overline{A}_k(t)\overline{A}_k(t)\Big\}e^{-i\omega_0 t} \\
+ i\frac{\varepsilon_0\beta_2}{2k_f}\Big\{ & \Big[|A_j(t)|^2+2\Delta_K|A_k(t)|^2\Big]\overline{A}_j(t)+\gamma_K\overline{A}_j^*(t)\overline{A}_k(t)\overline{A}_k(t)\Big\}e^{-i\omega_0 t} \\
-\varepsilon_0 n_0 n_2\tau_R\Big\{ & \Big[\frac{\partial\overline{A}_j^*(t)\overline{A}_j(t)}{\partial t}+\Delta_R\frac{\partial\overline{A}_k^*(t)\overline{A}_k(t)}{\partial t}\Big]\overline{A}_j(t)
\end{aligned}
\tag{3.58}
$$

$$+\gamma_R\left[\frac{\partial\overline{A}_k^*(t)\overline{A}_j(t)}{\partial t}+\frac{\partial\overline{A}_j^*(t)\overline{A}_k(t)}{\partial t}\right]\overline{A}_k(t)\Bigg\}e^{-i\omega_0 t}$$
$$-\frac{\varepsilon_0 n_0 n_R''}{2}\Bigg\{\frac{\partial^2\overline{A}_j^*(t)\overline{A}_j(t)}{\partial t^2}\overline{A}_j(t)+\Delta_R\frac{\partial^2\overline{A}_k^*(t)\overline{A}_k(t)}{\partial t^2}\overline{A}_j(t)$$
$$+\gamma_R\left[\frac{\partial^2\overline{A}_k^*(t)\overline{A}_j(t)}{\partial t^2}+\frac{\partial^2\overline{A}_j^*(t)\overline{A}_k(t)}{\partial t^2}\right]\overline{A}_k(t)\Bigg\}e^{-i\omega_0 t},$$

where the total instantaneous nonlinear refractive index and the overall nonlinear anisotropy factors are defined

$$n_2 = n_K + n_R \tag{3.59}$$
$$\Delta = \frac{2n_K\Delta_K + n_R[\Delta_R+\gamma_R]}{2[n_K+n_R]} \tag{3.60}$$
$$\gamma = \frac{n_K\gamma_K + n_R\gamma_R}{n_K+n_R}. \tag{3.61}$$

Here, $n_K = [1-f_R]n_2$, $n_R = f_R n_2$, and f_R represents the fractional Raman contribution to the ultrafast nonlinear index. Note that for the isotropic symmetry class,

$$2\Delta_K + \gamma_K = 1 \tag{3.62}$$
$$\Delta_R + 2\gamma_R = 1, \tag{3.63}$$

and under Kleinman symmetry, $\Delta_K = \gamma_K$ and $\Delta_R = \gamma_R$.

The form of equation 3.58 is suitable for the multiple-scales analysis of section 3.2 because the terms are easily ordered based upon peak intensity and pulse duration. For the nonlinear Helmholtz equation of this section and the numerics of Chapter 4 though, the full Raman response can be used. The time-domain form is

$$P_j^{(3)+}(t) = \tag{3.64}$$
$$\varepsilon_0 n_0 n_K\left\{\left[\,|A_j(t)|^2+2\Delta_K|A_k(t)|^2\right]\overline{A}_j(t)+\gamma_K\overline{A}_j^*(t)\overline{A}_k(t)\overline{A}_k(t)\right\}e^{-i\omega_0 t}$$
$$+i\frac{\varepsilon_0\beta_2}{2k_f}\left\{\left[\,|A_j(t)|^2+2\Delta_K|A_k(t)|^2\right]\overline{A}_j(t)+\gamma_K\overline{A}_j^*(t)\overline{A}_k(t)\overline{A}_k(t)\right\}e^{-i\omega_0 t}$$
$$+\frac{\varepsilon_0}{4}\Bigg[\int_0^\infty R^{\mathrm{R}}_{jjjj}(\tau)\overline{A}_j^*(t-\tau)\overline{A}_j(t-\tau)\overline{A}_j(t)d\tau$$
$$+\Delta_R\int_0^\infty R^{\mathrm{R}}_{jjjj}(\tau)\overline{A}_k^*(t-\tau)\overline{A}_k(t-\tau)\overline{A}_j(t)d\tau$$
$$+\gamma_R\int_0^\infty R^{\mathrm{R}}_{jjjj}(\tau)\overline{A}_k^*(t-\tau)\overline{A}_j(t-\tau)\overline{A}_k(t)d\tau$$
$$+\gamma_R\int_0^\infty R^{\mathrm{R}}_{jjjj}(\tau)\overline{A}_j^*(t-\tau)\overline{A}_k(t-\tau)\overline{A}_k(t)d\tau\Bigg]e^{-i\omega_0 t}.$$

In the numerics, the convolution integral with the Raman response function is easily evaluated in the temporal-frequency domain using instead the Raman susceptibility.

3.1.3 The Fifth-Order Nonlinear Material Polarization

The direct extension of the nonlinear polarization to fifth-order is, in the frequency domain,

$$\tilde{P}_j^{(5)}(\omega) = \varepsilon_0\int\int\int\int\int\chi_{jklmno}(\omega;\omega_1,\omega_2,\omega_3,\omega_4,\omega_5)\times \tag{3.65}$$
$$\tilde{E}_k(\omega_1)\tilde{E}_l(\omega_2)\tilde{E}_m(\omega_3)\tilde{E}_n(\omega_4)\tilde{E}_o(\omega_5)\times$$
$$\delta(\omega-\omega_1-\omega_2-\omega_3-\omega_4-\omega_5)d\omega_1 d\omega_2 d\omega_3 d\omega_4 d\omega_5.$$

Neglecting nonlinear dispersion and using the quasi-monochromatic wavepacket, the fifth-order nonlinear polarization at ω_0 responsible for nonlinear refraction, written in the time-domain, is

$$P_j^{(5)+}(t) = \tag{3.66}$$

$$\frac{\varepsilon_0}{32}\Big[\chi_{jklmno}(\omega_0;-\omega_0,-\omega_0,\omega_0,\omega_0,\omega_0)\,\overline{A}_k^*(t)\overline{A}_l^*(t)\overline{A}_m(t)\overline{A}_n(t)\overline{A}_o(t)$$
$$+\chi_{jklmno}(\omega_0;-\omega_0,\omega_0,-\omega_0,\omega_0,\omega_0)\overline{A}_k^*(t)\overline{A}_l(t)\overline{A}_m^*(t)\overline{A}_n(t)\overline{A}_o(t)$$
$$+\cdots$$
$$+\chi_{jklmno}(\omega_0;\omega_0,\omega_0,\omega_0,-\omega_0,-\omega_0)\overline{A}_k(t)\overline{A}_l(t)\overline{A}_m(t)\overline{A}_n^*(t)\overline{A}_o^*(t)\Big]e^{-i\omega_0 t},$$

where there are ${}_5C_2 = 10$ total terms.

From Appendix A, the fifth-order nonlinear refraction for isotropic symmetry is (cf equation A.23)

$$P_j^{(5)+}(t) = \frac{5\varepsilon_0}{16}\chi_{jjjjjj}(\omega_0;-\omega_0,-\omega_0,\omega_0,\omega_0,\omega_0)\,e^{-i\omega_0 t}\times \tag{3.67}$$
$$\Big[|A_j(t)|^4 A_j(t) + \frac{3}{5}|A_k(t)|^4 A_j(t) + \frac{6}{5}|A_j(t)|^2|A_k(t)|^2 A_j(t)$$
$$+\frac{2}{5}|A_k(t)|^2 A_k^2(t)A_j^*(t) + \frac{3}{5}A_j^{*2}(t)A_k^2(t)A_j(t) + +\frac{1}{5}A_j^2(t)A_k^{*2}(t)A_j(t)$$
$$+\frac{2}{5}|A_k(t)|^2 A_l^2(t)A_j^*(t) + \frac{1}{5}A_k^{*2}(t)A_l^2(t)A_j(t) + \frac{2}{5}|A_k(t)|^2|A_l(t)|^2 A_j(t)\Big],$$

where $j \neq k \neq l$ and Kleinman symmetry has been invoked for simplicity, leaving only one independent component of the sixth-rank tensor [226]. Analogous to the cubic nonlinear index n_2 and two-photon absorption coefficient β_2, the quintic nonlinear index and three-photon absorption coefficients are defined

$$n_4 = \frac{5}{16n_0}\mathcal{R}e\left\{\chi_{jjjjjj}(\omega_0;-\omega_0,-\omega_0,\omega_0,\omega_0,\omega_0)\right\} \tag{3.68}$$

$$\beta_3 = \frac{5k_f}{8}Im\left\{\chi_{jjjjjj}(\omega_0;-\omega_0,-\omega_0,\omega_0,\omega_0,\omega_0)\right\}. \tag{3.69}$$

Note that the fully-dispersive fifth-order Raman response is not considered. In fact, the zeroth-order refractive part of the fifth-order Raman response can be assumed to be included in the definition of n_4, where χ_{jjjjjj} is redefined to include both the instantaneous and Raman contributions.

Using the quintic nonlinear index and three-photon absorption coefficient, the fifth-order nonlinear refraction polarization is finally written

$$P_j^{(5)+}(t) = \varepsilon_0\left[n_0 n_4 + i\frac{\beta_3}{2k_f}\right]\Big[|A_j(t)|^4\overline{A}_j(t) + \frac{3}{5}|A_k(t)|^4\overline{A}_j(t) \tag{3.70}$$
$$+\frac{6}{5}|A_j(t)|^2|A_k(t)|^2\overline{A}_j(t) + \frac{2}{5}|A_k(t)|^2\overline{A}_k^2(t)\overline{A}_j^*(t)$$
$$+\frac{3}{5}\overline{A}_j^{*2}(t)\overline{A}_k^2(t)\overline{A}_j(t) + \frac{1}{5}\overline{A}_j^2(t)\overline{A}_k^{*2}(t)\overline{A}_j(t) + \frac{2}{5}|A_k(t)|^2\overline{A}_l^2(t)\overline{A}_j^*(t)$$
$$+\frac{1}{5}\overline{A}_k^{*2}(t)\overline{A}_l^2(t)\overline{A}_j(t) + \frac{2}{5}|A_k(t)|^2|A_l(t)|^2\overline{A}_j(t)\Big]e^{-i\omega_0 t}.$$

Again, the phase-dependent vectorial terms are included, but eventually will be removed due to the assumption of phase-velocity mismatch between the orthogonal modes of a waveguide, which washes out their effects over distances longer than the beat length. The phase-dependent vectorial terms are rigorously absent for the circular polarization basis set [226].

An additional, effective, quintic refraction contribution arises from the cascaded interaction between the fundamental at ω_0 and the third-harmonic. This contribution will be derived in the multiple-scales analysis even though the result is valid for the Helmholtz development of this section as well. This cascaded contribution is the higher-order analogy of second-harmonic cascading, which leads to an effective third-order nonlinear refractive effect [193], and has been studied recently because of the possibility for producing a large Kerr-like nonlinear index [196]. Note that an additional quintic contribution proportional to the square of the cubic Kerr index is obtained in the next section, and is the result of the derivation of a first-order equation.

3.1.4 The Vector, Nonlinear Helmholtz Equation

Using the third- and fifth-order polarizations from sections 3.1.2 and 3.1.3, the nonlinear Helmholtz equation 3.44 can be written

$$\nabla^2\overline{A}_j(t) - \frac{\partial}{\partial j}\sum_{k\in\{x,y,z\}}\frac{\partial\overline{A}_k(t)}{\partial k} = \tag{3.71}$$

$$
\begin{aligned}
&-k\left(\omega_0+i\frac{\partial}{\partial t}\right)\left[k\left(\omega_0+i\frac{\partial}{\partial t}\right)+i\alpha\left(\omega_0+i\frac{\partial}{\partial t}\right)\right]\overline{A}_j(t)\\
&-\frac{2}{c^2}\left[n_0n_K+i\frac{\beta_2}{2k_f}\right]\left[\omega_0+i\frac{\partial}{\partial t}\right]^2\Big[\left|A_j(t)\right|^2\overline{A}_j(t)+2\Delta_K\left|A_k(t)\right|^2\overline{A}_j(t)\\
&\qquad\qquad+\gamma_K\overline{A}_k^2(t)\overline{A}_j^*(t)\Big]\\
&-\frac{1}{2c^2}\left[\omega_0+i\frac{\partial}{\partial t}\right]^2\Big[\int_0^\infty R^{\mathrm{R}}_{jjjj}(\tau)\left|A_j(t-\tau)\right|^2\overline{A}_j d\tau\\
&\qquad+\Delta_R\int_0^\infty R^{\mathrm{R}}_{jjjj}(\tau)\left|A_k(t-\tau)\right|^2\overline{A}_j d\tau\\
&\qquad+\gamma_R\int_0^\infty R^{\mathrm{R}}_{jjjj}(\tau)\overline{A}_k^*(t-\tau)\overline{A}_j(t-\tau)\overline{A}_k d\tau\\
&\qquad+\gamma_R\int_0^\infty R^{\mathrm{R}}_{jjjj}(\tau)\overline{A}_j^*(t-\tau)\overline{A}_k(t-\tau)\overline{A}_k d\tau\Big]\\
&-\frac{2}{c^2}\left[n_0n_4+i\frac{\beta_3}{2k_f}\right]\left[\omega_0+i\frac{\partial}{\partial t}\right]^2\Big[\left|A_j(t)\right|^4\overline{A}_j(t)+\frac{3}{5}\left|A_k(t)\right|^4\overline{A}_j(t)\\
&\qquad+\frac{6}{5}\left|A_j(t)\right|^2\left|A_k(t)\right|^2\overline{A}_j(t)+\frac{2}{5}\left|A_k(t)\right|^2\overline{A}_k^2(t)\overline{A}_j^*(t)\\
&\qquad+\frac{3}{5}\overline{A}_j^{*2}(t)\overline{A}_k^2(t)\overline{A}_j(t)+\frac{1}{5}\overline{A}_j^2(t)\overline{A}_k^{*2}(t)\overline{A}_j(t)\\
&\qquad+\frac{2}{5}\left|A_k(t)\right|^2\overline{A}_l^2(t)\overline{A}_j^*(t)+\frac{1}{5}\overline{A}_k^{*2}(t)\overline{A}_l^2(t)\overline{A}_j(t)\\
&\qquad+\frac{2}{5}\left|A_k(t)\right|^2\left|A_l(t)\right|^2\overline{A}_j(t)\Big].
\end{aligned}
$$

Equation 3.71 describes the general evolution of multi-dimensional vector waves including the effects of full linear refractive and absorptive dispersion, third-order nonlinear refraction, fully-dispersive third-order Raman scattering, and fifth-order nonlinear refraction (neglecting the third-harmonic cascading term) and two- and three-photon absorption. This equation also describes omni-directional and inhomogeneous propagation in that scattering from linear or nonlinearly-induced inhomogeneities is fully treated. In fact, the only approximations made in the derivation from Maxwell's equations lie in the material polarization, and the neglect of frequencies far removed from the fundamental ω_0 which could be generated by a nonlinear interaction such as third-harmonic generation (which will be treated in the multiple-scales analysis).

The vector nonlinear Helmholtz equation has no known analytic solutions, although approximate stationary solutions to reduced versions may be obtainable, for example for a scalar equation with truncated linear and nonlinear dispersion [139]. These approximate solutions must be numerically propagated in order to test for stability. Therefore, what is most useful for the soliton and solitary wave propagation and interaction studies of this thesis is the nonlinear evolution of an initial vector field distribution into the far field (of linear propagation). As a result, equation 3.71 must be treated as an initial value problem rather than a boundary-value problem, which can only determine the equilibrium solutions, if any. Evolution over time is the most natural, but also the most difficult because the nonlinear Helmholtz equation is differential in space and integral in time due to linear and nonlinear dispersion.

One numerical method to evolve a unidirectional wave by a second-order differential equation is the Nyström method [227], which is analogous to Runge-Kutta for first-order differential equations. Nevertheless, second-order equations such as 3.71 are difficult to solve numerically for problems where long time/distance evolution is desired. The main contributing factor is the leading-order scales, which leads to restrictive requirements on sampling. This difficulty plagues numerical techniques that directly solve Maxwell's equations, such as finite-difference time-domain (FDTD) [228], as well, and motivates a different approach in which a first-order, vector nonlinear evolution equation for the slowly-varying field envelope is utilized. This equation is derived in section 3.2.

The Helmholtz equation retains the fast variation due to propagation, which is approximately e^{ik_0z}. For wide angular spectra and backscattered radiation, this phase must be properly sampled. The largest propagating longitudinal or transverse wave number is $k_0 = 2\pi/\lambda$, where λ is the material wavelength, and $\nu = 1/\lambda$ is the largest propagating spatial frequency. The upper bound on sampling is given by the Nyquist limit, meaning that in order to properly sample the highest spatial frequency, the samples must be at $\lambda/2$ intervals or less. Two additional considerations must be made. The transverse wave number for evanescent fields is larger than k_0, and the linear interference between forward- and backward-propagating radiation produces fringes with spacing $\lambda/2$. Therefore, the spatial sampling must be $\lambda/4$ or smaller in order to Nyquist sample these

oscillations. As a result, sampling at $\lambda/10$ is generally considered a rule of thumb for linear problems using a second-order accurate numerical scheme [229]; for nonlinear problems, sampling at $\lambda/100$ is commonly used. When nonlinear evolution into the far field is important (as it is here), it is difficult to formulate an accurate numerical technique that can resolve both fast and slow scales, because these fast scales dominates the calculation and any variation occurring on a slower scale becomes difficult to detect.

Much work has been done on a technique known as homogenization, in which the fast and slow scales are separated before the numerical calculation. The multiple-scales analysis performed in the next section is a form of homogenization, where the mean propagation phase and group velocity are removed in the development of a first-order evolution equation. Therefore, the two shortest distance scales, which are order 1 and $1/\varepsilon$ where ε is a small parameter, are removed, with the leading-order distance scale, $1/\varepsilon^2$, representing diffraction and dispersion (which are far-field effects), and nonlinear self-focusing and self-phase modulation. As a result, sampling can be larger than a wavelength since the finest scale to be resolved is that of the field envelope. Of course, in the non-paraxial and non-SVEA regime, sampling still must approach $\lambda/2$. The advantage here is that the sampling scales inversely with the bandwidth of the envelope; in the other schemes based on the second-order equation, the sampling is based on λ, independent of the envelope.

3.2 Multiple-Scales Derivation of the Nonlinear Wave Equation

This section uses the asymptotic method of multiple-scales to derive the basic equations needed for the theoretical and numerical studies of optical solitons and their interactions presented in this thesis. Because of the numerical difficulties that the Helmholtz equation 3.71 poses, a different approach to describing the nonlinear spatio-temporal evolution of wavepackets is developed in this section. This equation is first-order in the evolution variable and possesses good scales in the sense that all fast variations are removed.

The multiple-scales analysis separates the fast scales from the slow, resulting in a nonlinear wave equation that can describe long time/distance evolution; this is especially important in the waveguide derivation of Appendix C where variation in one transverse direction is fast. From the derivation, the multi-dimensional nonlinear Schrödinger (NLS) equation is obtained, which evolves over a distance scale $1/\varepsilon^2$, while higher-order terms that evolve over distance scales $1/\varepsilon^3$ and $1/\varepsilon^4$ are obtained in subsequent sub-sections. The point of this analysis is to remove the order 1 and $1/\varepsilon$ scales from the wave equation, allowing for the use of much simpler numerical techniques.

At each step in the perturbation expansion, an evolution equation is derived that contains all terms with significant contribution within some characteristic propagation distance. Higher-order equations subsequently extend the region of validity. The first-order equation accounts for wave propagation of the optical carrier, which is sufficient over a few wavelengths over which the field envelope does not change. A second-order envelope equation determines the group-velocity and is valid over distances smaller than the characteristic diffraction/dispersion/nonlinear lengths. Paraxial diffraction, group-delay dispersion, and cubic nonlinear refraction are added at third-order to reveal the multi-dimensional NLS equation. For distances well beyond the characteristics lengths, higher-order perturbation theory is required. The fourth-order equation adds perturbations to the NLS equation that describe linear and two-photon absorption and the first-order non-slowly varying envelope (non-SVEA) terms of third-order dispersion, space-time focusing, optical shock, and Raman gain. The fifth-order equation includes second-order non-SVEA terms, non-paraxial terms, Raman index dispersion, longitudinal field coupling, and quintic nonlinear refraction with contribution due to third-harmonic cascading.

3.2.1 Multiple-Scales in Maxwell's Equations

Once again, the starting point is Maxwell's equations, written in a form appropriate for dielectric media

$$\nabla \times \mathbf{E} = -\mu_0 \frac{\partial \mathbf{H}}{\partial t} \tag{3.72}$$

$$\nabla \times \mathbf{H} = \varepsilon_0 \frac{\partial \mathbf{E}}{\partial t} + \frac{\partial \mathbf{P}}{\partial t} \tag{3.73}$$

$$\nabla \cdot \mathbf{E} = -\frac{1}{\varepsilon_0} \nabla \cdot \mathbf{P} \tag{3.74}$$

$$\nabla \cdot \mathbf{H} = 0, \tag{3.75}$$

where the constitutive relations have been used to eliminate the electric and magnetic displacements. Spatial and temporal functional dependence is generally neglected for simplicity. Note that, with the use of the constitutive relations, the vector

Maxwell's equations contain six unknowns in the vector electric and magnetic fields, but separate into eight equations relating those fields. The divergence equations are unnecessary, but will be retained in the analysis because they provide direct relationships for the longitudinally-projected fields.

As before in the discussion of the linear and nonlinear polarizations, the quasi-monochromatic wavepacket representation is used for both the electric and magnetic fields

$$\mathbf{E} = \frac{1}{2}\overline{\mathbf{A}}e^{-i\omega_0 t} + \frac{1}{2}\overline{\mathbf{S}}e^{-3i\omega_0 t} + \text{cc} \tag{3.76}$$

$$\mathbf{H} = \frac{1}{2}\overline{\mathbf{B}}e^{-i\omega_0 t} + \frac{1}{2}\overline{\mathbf{T}}e^{-3i\omega_0 t} + \text{cc}, \tag{3.77}$$

where it is assumed that the fractional temporal bandwidths of the fundamental and third-harmonic envelopes are each less than unity. The over-bar denotes the retention of a fast phase variation due to linear propagation. This fast phase will be explicitly removed in the multiple-scales analysis. The mean direction of propagation is chosen to be along the z axis, which is fully general for the isotropic symmetry class, but only strictly applies to cubic classes when propagation is nominally along one of the crystal axes. The third-harmonic is included in order to obtain the cascaded contribution to the quintic nonlinearity.

With this wavepacket assumption, quasi-monochromatic Maxwell's equations can be written in terms of the fundamental envelopes $\overline{\mathbf{A}}$ and $\overline{\mathbf{B}}$,

$$\nabla \times \overline{\mathbf{A}} = i\mu_0 \left[\omega_0 + i\frac{\partial}{\partial t}\right]\overline{\mathbf{B}} \tag{3.78a}$$

$$\nabla \times \overline{\mathbf{B}} = -i\varepsilon_0 \left[\omega_0 + i\frac{\partial}{\partial t}\right]\left[\varepsilon^{\mathrm{L}}\left(\omega_0 + i\frac{\partial}{\partial t}\right)\overline{\mathbf{A}} + \frac{2}{\varepsilon_0}\overline{\mathbf{P}}^{\mathrm{NL}}\right] \tag{3.78b}$$

$$\varepsilon^{\mathrm{L}}\left(\omega_0 + i\frac{\partial}{\partial t}\right)\left[\nabla \cdot \overline{\mathbf{A}}\right] = -\frac{2}{\varepsilon_0}\nabla \cdot \overline{\mathbf{P}}^{\mathrm{NL}} \tag{3.78c}$$

$$\nabla \cdot \overline{\mathbf{B}} = 0, \tag{3.78d}$$

and in terms of the third-harmonic envelopes $\overline{\mathbf{S}}$ and $\overline{\mathbf{T}}$,

$$\nabla \times \overline{\mathbf{S}} = i\mu_0 \left[3\omega_0 + i\frac{\partial}{\partial t}\right]\overline{\mathbf{T}} \tag{3.79a'}$$

$$\nabla \times \overline{\mathbf{T}} = -i\varepsilon_0 \left[3\omega_0 + i\frac{\partial}{\partial t}\right]\left[\varepsilon^{\mathrm{L}}\left(3\omega_0 + i\frac{\partial}{\partial t}\right)\overline{\mathbf{S}} + \frac{2}{\varepsilon_0}\overline{\mathbf{P}}_3^{\mathrm{NL}}\right] \tag{3.79b'}$$

$$\varepsilon^{\mathrm{L}}\left(3\omega_0 + i\frac{\partial}{\partial t}\right)\left[\nabla \cdot \overline{\mathbf{S}}\right] = -\frac{2}{\varepsilon_0}\nabla \cdot \overline{\mathbf{P}}_3^{\mathrm{NL}} \tag{3.79c'}$$

$$\nabla \cdot \overline{\mathbf{T}} = 0, \tag{3.79d'}$$

with the corresponding conjugate expressions. Here, the material polarization is separated into linear dispersive and nonlinear parts. The fundamental and third-harmonic envelopes must satisfy the above equations in order that the total electric and magnetic fields $\mathbf{E}$ and $\mathbf{H}$, as given by equations 3.76 and 3.77 respectively, satisfy Maxwell's equations.

Key to the multiple-scales analysis is the suitable choice of small parameters that serve to scale the slow variables. The slow transverse variables are defined $X \equiv \kappa x$, $Y \equiv \kappa y$, which are responsible for diffraction. The small parameter $\kappa \sim \lambda/w_0 < 1$, where w_0 is a measure of the beam width, guarantees that the width of the transverse angular spectrum $\Delta k_T \sim 2\pi/w_0$ is small compared to the linear propagation constant $k_0 = 2\pi/\lambda$, otherwise known as the paraxial assumption. In linearly isotropic media, only even-order powers of the small parameter κ occur in the derivation, and the standard paraxial approximation truncates the diffraction expansion at κ^2 resulting in the parabolic representation of the k-space surface. In this derivation, the expansion will be taken to order κ^4, which goes one step beyond the paraxial approximation.

The slow time variable is defined $T \equiv \eta t$, where $\eta \sim \Delta\omega/\omega_0 < 1$ is the fractional temporal bandwidth. The small parameter η allows for the representation of linear and nonlinear dispersion by Taylor expansion in terms of time derivative operators instead of convolution integrals, as developed in section 3.1.1. Dispersion effects appear at all positive powers of η. For example, writing the linear dielectric constant in terms of real (dispersive) and imaginary (absorptive) parts

$$\varepsilon^{\mathrm{L}}\left(\omega_0 + i\eta\frac{\partial}{\partial T}\right) = \varepsilon_{\mathcal{R}}^{\mathrm{L}}\left(\omega_0 + i\eta\frac{\partial}{\partial T}\right) + i\varepsilon^3\varepsilon_I^{\mathrm{L}}\left(\omega_0 + i\eta\frac{\partial}{\partial T}\right), \tag{3.80}$$

the following expansion can be made

$$\begin{aligned}\varepsilon^{L}\left(\omega_0+i\eta\frac{\partial}{\partial T}\right) &= \varepsilon^{L}_{\mathcal{R}}(\omega_0)+i\eta\varepsilon^{L'}_{\mathcal{R}}(\omega_0)\frac{\partial}{\partial T}-\frac{\eta^2}{2}\varepsilon^{L''}_{\mathcal{R}}(\omega_0)\frac{\partial^2}{\partial T^2} \\ &\quad -i\frac{\eta^3}{6}\varepsilon^{L'''}_{\mathcal{R}}(\omega_0)\frac{\partial^3}{\partial T^3}+\frac{\eta^4}{24}\varepsilon^{L''''}_{\mathcal{R}}(\omega_0)\frac{\partial^4}{\partial T^4}+\cdots \\ &\quad +i\varepsilon^3\varepsilon^{L}_{I}(\omega_0)-\varepsilon^3\eta\varepsilon^{L'}_{I}(\omega_0)\frac{\partial}{\partial T}+\cdots,\end{aligned} \tag{3.81}$$

where ε is a small parameter that scales absorption and is defined later. If the envelope possesses fast temporal variations about the carrier ω_0, i.e. greater than unity fractional bandwidth, then the slow variable T can not be defined and the dispersion expansions are not valid. The slowly-varying envelope approximation (SVEA) truncates this expansion at η^2, while the non-SVEA development here extends the expansion to η^4 as shown. The imaginary part of the dielectric constant responsible for linear absorption is scaled three-orders smaller than the real part in order to appear in the derivation as a first-order correction to NLS. This is justified by noting that the development of the nonlinear polarization assumed that the optical frequencies were not in one-photon resonance with the medium and by the fact that only materials with small linear absorption are of interest for soliton switching, as discussed in Chapter 5, which amounts to the requirement that absorption is small over the diffraction length, which is the length scale of NLS.

Weak nonlinearity is assumed such that wave propagation is linear to lowest order. This is ensured by redefining the envelopes as small - $\nu\overline{\mathbf{A}}$ and $\nu\overline{\mathbf{B}}$ for the fundamental - where the small amplitude parameter $\nu\sim\sqrt{n_2/n_0}|A|$ scales the material polarization expansion. Since third-order nonlinear effects contain the product of three fields, nonlinearity will enter the wave equation two orders higher than first-order linear effects, which depend on only one field. Using the results of sections 3.1.2 and 3.1.3, the nonlinear polarization with time dependence centered about the fundamental frequency ω_0 is

$$\begin{aligned}\overline{P}^{NL}_{j} &= \nu^3\varepsilon_0 n_0 n_2\left\{\left[\,|A_j|^2+2\Delta|A_k|^2\right]\overline{A}_j+\gamma\overline{A}^*_j\overline{A}_k\overline{A}_k\right\} \\ &\quad +i\varepsilon\nu^3\frac{\varepsilon_0\beta_2}{2k_f}\left\{\left[\,|A_j|^2+2\Delta_K|A_k|^2\right]A_j+\gamma_K A^*_j A_k A_k\right\} \\ &\quad -\eta\nu^3\varepsilon_0 n_0 n_2\tau_R\left\{\left[\frac{\partial|A_j|^2}{\partial T}+\Delta_R\frac{\partial|A_k|^2}{\partial T}\right]\overline{A}_j+\gamma_R\left[\frac{\partial\overline{A}^*_k\overline{A}_j}{\partial T}+\frac{\partial\overline{A}^*_j\overline{A}_k}{\partial T}\right]\overline{A}_k\right\} \\ &\quad -\eta^2\nu^3\frac{\varepsilon_0 n_0 n''_R}{2}\left\{\left[\frac{\partial^2|A_j|^2}{\partial T^2}+\Delta_R\frac{\partial^2|A_k|^2}{\partial T^2}\right]\overline{A}_j+\gamma_R\left[\frac{\partial^2\overline{A}^*_k\overline{A}_j}{\partial T^2}+\frac{\partial^2\overline{A}^*_j\overline{A}_k}{\partial T^2}\right]\overline{A}_k\right\} \\ &\quad +\nu^5\varepsilon_0\left[n_0 n_4+i\frac{\beta_3}{2k_f}\right]\left\{\left[|A_j|^4+\frac{3}{5}|A_k|^4+\frac{6}{5}|A_j|^2|A_k|^2+\frac{2}{5}|A_k|^2|A_l|^2\right]\overline{A}_j\right. \\ &\qquad +\left[\frac{3}{5}\overline{A}^{*2}_j\overline{A}^2_k+\frac{1}{5}\overline{A}^2_j\overline{A}^{*2}_k+\frac{1}{5}\overline{A}^{*2}_k\overline{A}^2_l\right]\overline{A}_j \\ &\qquad \left.+\left[\frac{2}{5}|A_k|^2\overline{A}^2_k+\frac{2}{5}|A_k|^2\overline{A}^2_l\right]\overline{A}^*_j\right\} \\ &\quad +\nu^3\frac{3\varepsilon_0}{8}\chi_{jjjj}(\omega_0;3\omega_0,-\omega_0,-\omega_0)\left\{\overline{S}_j\left[\overline{A}^{*2}_j+\gamma_K\overline{A}^{*2}_k\right]+2\Delta_K\overline{S}_k\overline{A}^*_k\overline{A}^*_j\right\},\end{aligned} \tag{3.82}$$

where $j\neq k\neq l$. The terms responsible for two-photon absorption are scaled one order smaller than the refractive parts so that two-photon absorption also appears one order beyond NLS. This is also justified by noting that the development of the third-order nonlinear polarization assumed distance from two-photon resonance. As shown in Chapter 5, it is desirable for soliton switching (and true for nonlinear optical switching in general [115]) that two-photon absorption is weak relative to nonlinear refraction, which appears at the order of the NLS equation. Note that the term responsible for three-photon absorption is allowed to be the same size as fifth-order nonlinear refraction, however. The reasons for this are discussed later. The last term describes third-harmonic downconversion, and the form is derived in section A.2.3.

The pertinent nonlinear polarization at the third-harmonic is (c.f. equation A.16)

$$\begin{aligned}\overline{P}^{NL}_{j,3} &= \frac{\nu^3\varepsilon_0}{8}\left[\chi_{jjjj}(3\omega_0;\omega_0,\omega_0,\omega_0)\overline{A}_j\overline{A}_j\overline{A}_j\right. \\ &\quad \left.+\,3\chi_{jkkj}(3\omega_0;\omega_0,\omega_0,\omega_0)\overline{A}_k\overline{A}_k\overline{A}_j\right].\end{aligned} \tag{3.83}$$

The third-harmonic electric field **S** generated by this nonlinear polarization is assumed not to be present at the beginning of nonlinear propagation, but is generated by the fundamental through a non-resonantly phase-matched process. For a single incident linearly-polarized wave (at ω_0), the only susceptibility tensor component that will produce a third-harmonic polarization within the limit of the fifth-order derivation presented here is the scalar $\chi_{jjjj}(3\omega_0;\omega_0,\omega_0,\omega_0)$. For other states of incident polarization, or for the interaction between orthogonally-polarized waves of interest here, more components are required as shown.

The slow evolution scales are defined $Z_i \equiv \varepsilon^i z$, where propagation is assumed to be nominally along the z-direction and powers of ε determine the scale of the overall variation of the envelope due to diffraction, dispersion, nonlinearity, and absorption. At each order $i+1$ in the analysis, a differential equation in Z_i is obtained which groups all envelope variations of size ε^{i+1}. To this end, the envelopes are expanded in power series in ε:

$$\begin{aligned}
\overline{\mathbf{A}} &= \overline{\mathbf{A}}_1 + \varepsilon\overline{\mathbf{A}}_2 + \varepsilon^2\,\overline{\mathbf{A}}_3 + \cdots \\
\overline{\mathbf{S}} &= \varepsilon^2\,\overline{\mathbf{S}}_3 + \cdots \\
\overline{\mathbf{B}} &= \overline{\mathbf{B}}_1 + \varepsilon\overline{\mathbf{B}}_2 + \varepsilon^2\,\overline{\mathbf{B}}_3 + \cdots \\
\overline{\mathbf{T}} &= \varepsilon^2\,\overline{\mathbf{T}}_3 + \cdots.
\end{aligned} \tag{3.84}$$

The higher-order terms in the expansion represent corrections to the initial envelopes $\overline{\mathbf{A}}_1$ and $\overline{\mathbf{B}}_1$. Each step in the analysis forces the long-distance behavior (at Z_i) of the envelopes such that equation 3.84 remains a uniform asymptotic expansion. The scaling for the third-harmonic $\overline{\mathbf{S}}$ (in which the first contribution appears at the third-order of the analysis) is set to be consistent with generation by the product of three fundamental envelopes $\overline{\mathbf{A}}_1$. The third-harmonic interacts with the fundamental to produce a cascaded fifth-order nonlinearity [211] of sign and magnitude which are adjustable through phase-matching. Fifth and higher odd-order harmonics could also be generated, but do not affect the nonlinear wave equation for the fundamental at the order of the present derivation and are therefore ignored.

The small parameters, κ for the fractional angular bandwidth, η for the fractional temporal bandwidth, ν for the fractional change of the dielectric constant due to nonlinearity, and ε as an overall scaling factor, determine the relative scaling among terms (and physical effects) in the perturbative expansion. The perturbation expansion follows a particular connected path through the three-dimensional lattice of terms indexed by powers of κ, η, and ν; higher-order terms (more distant from the origin) are always smaller. A particular physical situation determines the sizes of the small parameters relative to ε, and allows for the derivation of the appropriate evolution equation. For example, a nonlinear spatio-temporal wave of short duration and large transverse size will result in the scaling $\kappa = \eta^2 = \nu^2 \equiv \varepsilon^2$. The terms associated with diffraction will then be driven to higher order and the resulting evolution equation at third-order perturbation theory, or ε^3, will be temporal NLS. Subsequent orders ε^4 and higher will reveal non-SVEA terms (and paraxial diffraction at ε^5). Conversely, a spatio-temporal wave of long duration and narrow transverse size is described by the scaling $\eta = \kappa^2 = \nu^2 \equiv \varepsilon^2$, moving the ultrafast terms to higher order and yielding the spatial NLS equation at ε^3 after transforming into a coordinate system to remove the group delay. Again, further analysis will reveal non-paraxial terms (and group-delay dispersion) at ε^5.

The most general equation, retaining as many terms as possible under the initial assumption of weakly nonlinear propagation of a field envelope, occurs when all physical effects manifest themselves over commensurate distances of propagation and results from the scaling $\kappa = \eta = \nu \equiv \varepsilon$. One result of this condition is that the multi-dimensional nonlinear Schrödinger (NLS) equation is obtained at order ε^3. Any other choice of initial scalings, such as the scalings valid for the numerical simulations presented later, would lead to one or more effects being less important than the others, resulting in the paraxial or SVE approximation, as previously discussed. In terms of the slow variables, the time and space derivative operators become

$$\frac{\partial}{\partial t} \to \varepsilon\frac{\partial}{\partial T} \tag{3.85}$$

$$\begin{aligned}
\nabla &= \hat{x}\frac{\partial}{\partial x} + \hat{y}\frac{\partial}{\partial y} + \hat{z}\frac{\partial}{\partial z} \\
&\to \hat{x}\varepsilon\frac{\partial}{\partial X} + \hat{y}\varepsilon\frac{\partial}{\partial Y} + \hat{z}\left[\frac{\partial}{\partial z} + \varepsilon\frac{\partial}{\partial Z_1} + \varepsilon^2\frac{\partial}{\partial Z_2} + \cdots\right],
\end{aligned} \tag{3.86}$$

where Z_0 is replaced by z so that uppercase represents slow (envelope) variables and lowercase represents fast (propagation phase) variables. In the analysis, Z_0 represents zeroth-order perturbation theory with characteristic length scale on the order of the carrier oscillation, Z_1 is first-order perturbation theory with length scale of group delay, Z_2 is second order resulting in NLS, and so on. Note that now the field envelopes are functions of z and the slow variables, i.e.,

$$\overline{\mathbf{A}} \to \overline{\mathbf{A}}(X, Y, Z_{i>0}, T, z), \tag{3.87}$$

where the fast z dependence will be removed in the analysis.

Now, the quasi-monochromatic Maxwell's equations for the fundamental can be written, in component form,

$$\hat{x}: \ \varepsilon\frac{\partial\overline{A}_z}{\partial Y} - \left[\frac{\partial}{\partial z} + \varepsilon\frac{\partial}{\partial Z_1} + \cdots\right]\overline{A}_y = i\mu_0\left[\omega_0 + i\varepsilon\frac{\partial}{\partial T}\right]\overline{B}_x \tag{3.88a}$$

$$\hat{y}: \ \left[\frac{\partial}{\partial z} + \varepsilon\frac{\partial}{\partial Z_1} + \cdots\right]\overline{A}_x - \varepsilon\frac{\partial\overline{A}_z}{\partial X} = i\mu_0\left[\omega_0 + i\varepsilon\frac{\partial}{\partial T}\right]\overline{B}_y \tag{3.88b}$$

$$\hat{z}: \ \varepsilon\frac{\partial\overline{A}_y}{\partial X} - \varepsilon\frac{\partial\overline{A}_x}{\partial Y} = i\mu_0\left[\omega_0 + i\varepsilon\frac{\partial}{\partial T}\right]\overline{B}_z, \tag{3.88c}$$

which is Faraday's Law and relates the electric and magnetic fields such that a time-varying magnetic field serves as a source for the orthogonal rotation of the electric field,

$$\hat{x}: \ \varepsilon\frac{\partial\overline{B}_z}{\partial Y} - \left[\frac{\partial}{\partial z} + \varepsilon\frac{\partial}{\partial Z_1} + \cdots\right]\overline{B}_y = -i\varepsilon_0\left[\omega_0 + i\varepsilon\frac{\partial}{\partial T}\right]\left[\varepsilon^{\mathrm{L}}\left(\omega_0 + i\varepsilon\frac{\partial}{\partial T}\right)\overline{A}_x + \frac{2}{\varepsilon_0}\overline{P}_x^{(\mathrm{NL})+}\right] \tag{3.89a}$$

$$\hat{y}: \ \left[\frac{\partial}{\partial z} + \varepsilon\frac{\partial}{\partial Z_1} + \cdots\right]\overline{B}_x - \varepsilon\frac{\partial\overline{B}_z}{\partial X} = -i\varepsilon_0\left[\omega_0 + i\varepsilon\frac{\partial}{\partial T}\right]\left[\varepsilon^{\mathrm{L}}\left(\omega_0 + i\varepsilon\frac{\partial}{\partial T}\right)\overline{A}_y + \frac{2}{\varepsilon_0}\overline{P}_y^{(\mathrm{NL})+}\right] \tag{3.89b}$$

$$\hat{z}: \ \varepsilon\frac{\partial\overline{B}_y}{\partial X} - \varepsilon\frac{\partial\overline{B}_x}{\partial Y} = -i\varepsilon_0\left[\omega_0 + i\varepsilon\frac{\partial}{\partial T}\right]\left[\varepsilon^{\mathrm{L}}\left(\omega_0 + i\varepsilon\frac{\partial}{\partial T}\right)\overline{A}_z + \frac{2}{\varepsilon_0}\overline{P}_z^{(\mathrm{NL})+}\right], \tag{3.89c}$$

which is Amperes Law (modified by Maxwell) and states that a time-varying electric displacement drives orthogonal circulation of the magnetic field,

$$\varepsilon^{\mathrm{L}}\left(\omega_0 + i\varepsilon\frac{\partial}{\partial T}\right)\left\{\varepsilon\frac{\partial\overline{A}_x}{\partial X} + \varepsilon\frac{\partial\overline{A}_y}{\partial Y} + \left[\frac{\partial}{\partial z} + \varepsilon\frac{\partial}{\partial Z_1} + \cdots\right]\overline{A}_z\right\} = -\frac{2}{\varepsilon_0}\left\{\varepsilon\frac{\partial\overline{P}_x^{(\mathrm{NL})+}}{\partial X} + \varepsilon\frac{\partial\overline{P}_y^{(\mathrm{NL})+}}{\partial Y} + \left[\frac{\partial}{\partial z} + \varepsilon\frac{\partial}{\partial Z_1} + \cdots\right]\overline{P}_z^{(\mathrm{NL})+}\right\}, \tag{3.90}$$

which is Gauss's Law and constrains the longitudinal electric field polarization in order to guarantee that the electric displacement is divergence free, and finally

$$\varepsilon\frac{\partial\overline{B}_x}{\partial X} + \varepsilon\frac{\partial\overline{B}_y}{\partial Y} + \left[\frac{\partial\overline{B}_z}{\partial z} + \varepsilon\frac{\partial\overline{B}_z}{\partial Z_1} + \cdots\right] = 0, \tag{3.91}$$

which states that there is no isolated magnetic charge and ensures the magnetic field is divergence free by proper choice of longitudinally-polarized magnetic field.

These equations serve as the starting point for the next section which presents the derivation of the (3+1)-D vector nonlinear wave equation for the Cartesian polarization components. This choice of the polarization basis set is arbitrary. The reduced dimensional derivation appropriate for nonlinear propagation in a planar waveguide is presented in Appendix C. In this case, a (2+1)-D vector nonlinear wave equation results because of one dimension of linear confinement by the waveguide. Again, the Cartesian polarization components are used, but now this choice is not arbitrary since the TE and TM modes of the waveguide appear in orthogonal linear polarization states. Slight modification of the above set of Maxwell equations is necessary in the guided case since, in one dimension transverse to the mean direction of propagation, the material polarization depends on position, and the envelope in that dimension may no longer be slowly varying.

3.2.2 Derivation of the (3+1)-D Higher-Order Vector Nonlinear Schrödinger Equation

The propagation of and interaction between optical solitons is of primary interest to this thesis. The use of one field envelope $\overline{A}$ does not preclude the description of multiple soliton interaction with arbitrary states of polarization. Indeed, a first-order nonlinear wave equation will be derived for each polarization component in Cartesian coordinates, and any number of soliton

envelopes of arbitrary polarization state can be decomposed into this basis set. For example, for the interaction between two solitons of orthogonal linear polarizations, the initial conditions would be

$$A_{1x} = f_x(X,Y,0,T) \qquad (3.90)$$
$$A_{1y} = f_y(X,Y,0,T),$$

where f_x and f_y represent the envelopes of the individual solitons. Using solitons of orthogonal circular polarizations,

$$A_{1x} = \frac{1}{\sqrt{2}}[f_+(X,Y,0,T) + f_-(X,Y,0,T)] \qquad (3.91)$$
$$A_{1y} = \frac{i}{\sqrt{2}}[f_+(X,Y,0,T) - f_-(X,Y,0,T)],$$

where

$$f_+(X,Y,0,T)\,\frac{\hat{x}+i\hat{y}}{\sqrt{2}} \qquad (3.92)$$
$$f_-(X,Y,0,T)\,\frac{\hat{x}-i\hat{y}}{\sqrt{2}} \qquad (3.93)$$

represent the soliton envelopes of right- and left-hand circular polarizations.

As a result of the choice of optic axis, $\hat{z}$, the wave equations for the x and y polarizations will be identical in form due to the isotropic and cubic symmetry. Now the terms are grouped in powers of ε. At all orders, A_x and A_y satisfy similar equations, while A_z is different due to linear vector coupling in Maxwell's equations and the fact that propagation is along the z direction.

Order ε - Phase Velocity

At the lowest order, Maxwell's equations constrain the phase velocity. Writing out the coefficients of ε, in Cartesian form,

$$\hat{x}: \quad \frac{\partial \overline{A}_{1x}}{\partial z} = -i\mu_0\omega_0\overline{B}_{1x} \qquad (3.94a)$$
$$\hat{y}: \quad \frac{\partial \overline{A}_{1x}}{\partial z} = i\mu_0\omega_0\overline{B}_{1y} \qquad (3.94b)$$
$$\hat{z}: \quad 0 = i\mu_0\omega_0\overline{B}_{1z}, \qquad (3.94c)$$

which allows the electric fields to be determined from the magnetic fields,

$$\hat{x}: \quad \frac{\partial \overline{B}_{1y}}{\partial z} = i\varepsilon_0\omega_0\varepsilon^{\mathrm{L}}_{\mathcal{R}}(\omega_0)\overline{A}_{1x} \qquad (3.95a)$$
$$\hat{y}: \quad \frac{\partial \overline{B}_{1x}}{\partial z} = -i\varepsilon_0\omega_0\varepsilon^{\mathrm{L}}_{\mathcal{R}}(\omega_0)\overline{A}_{1y} \qquad (3.95b)$$
$$\hat{z}: \quad 0 = i\varepsilon_0\omega_0\varepsilon^{\mathrm{L}}_{\mathcal{R}}(\omega_0)\overline{A}_{1z}, \qquad (3.95c)$$

which allows the magnetic fields to be determined from the electric fields, and

$$\frac{\partial \overline{A}_{1z}}{\partial z} = 0 \qquad (3.96)$$
$$\frac{\partial \overline{B}_{1z}}{\partial z} = 0, \qquad (3.97)$$

which provide no new information.

It is immediately seen that the longitudinal electric and magnetic field polarizations are zero to this order, leaving only four non-zero field components. This is expected since the projection of the electric polarization onto the propagation direction is smaller than the transverse projections because of the initial choice of scalings. These scalings dictate that the fast propagation variation is along z and the transverse variation (i.e. diffraction) is described by the slow variables X and Y.

Taking the z derivative of equation 3.94b and substituting equation 3.95a, the x-polarized electric field equation is written

$$\frac{\partial^2 \overline{A}_{1x}}{\partial z^2} = -\varepsilon_0\mu_0\omega_0^2\varepsilon^{\mathrm{L}}_{\mathcal{R}}(\omega_0)\overline{A}_{1x}$$
$$\Rightarrow \overline{A}_{1x} = A_{1x}e^{ik_0 z} \qquad (3.98)$$

where A_{1x} is a slowly-varying envelope, $\varepsilon_0\mu_0 = 1/c^2$ and c is the speed of light in vacuum. The "+" sign is chosen here for forward-going waves, and backward-going wave are neglected by the assumption of weak nonlinearity, which forces wave propagation to be linear to this order. The same relation holds for $\overline{A}_{1y}$, $\overline{B}_{1x}$ and $\overline{B}_{1y}$. The wavepackets travel in the z-direction with some mean wavenumber k_0, or propagation constant $k_0 = \pm\omega_0\sqrt{\varepsilon^{\mathrm{L}}_{\mathcal{R}}(\omega_0)}/c$, resulting in the mean phase velocity $v_p = \omega_0/k_0$ for the underlying carrier.

Using the expansion 3.84, the relevant equation at lowest order is

$$\frac{\partial^2\overline{A}_x}{\partial z^2} = -k_0^2\overline{A}_x + O(\varepsilon^2), \tag{3.99}$$

which determines the phase velocity. The order ε^2 term emphasizes the fact that this equation is only accurate to order ε. Equation 3.99 allows the removal of the fast phase variation such that subsequent analysis will reveal approximate evolution equations for just the slowly-varying field envelope. Note also that, since $A_{1z} = 0$, the total longitudinal field $A_z = O(\varepsilon^2)$, which will be determined in the following section.

Order ε^2 - Group Velocity

The previous order determined the phase velocity of the underlying wavepacket carrier, this order determines the group velocity of the wavepacket envelope. Faraday's Law (equation 3.88a) results in

$$\begin{aligned}
\hat{x}: \quad & \frac{\partial\overline{A}_{2y}}{\partial z} + \frac{\partial\overline{A}_{1y}}{\partial Z_1} = -i\mu_0\omega_0\overline{B}_{2x} + \mu_0\frac{\partial\overline{B}_{1x}}{\partial T} \\
\hat{y}: \quad & \frac{\partial\overline{A}_{2x}}{\partial z} + \frac{\partial\overline{A}_{1x}}{\partial Z_1} = i\mu_0\omega_0\overline{B}_{2y} - \mu_0\frac{\partial\overline{B}_{1y}}{\partial T},
\end{aligned} \tag{3.100a}$$

while Amperes Law (equation 3.89a) results in

$$\hat{x}: \quad \frac{\partial\overline{B}_{2y}}{\partial z} + \frac{\partial\overline{B}_{1y}}{\partial Z_1} = i\varepsilon_0\omega_0\varepsilon^{\mathrm{L}}_{\mathcal{R}}(\omega_0)\overline{A}_{2x} - \varepsilon_0\left[\varepsilon^{\mathrm{L}}_{\mathcal{R}}(\omega_0) + \omega_0\varepsilon^{\mathrm{L}'}_{\mathcal{R}}(\omega_0)\right]\frac{\partial\overline{A}_{1x}}{\partial T} \tag{3.101a}$$

$$\hat{y}: \quad \frac{\partial\overline{B}_{2x}}{\partial z} + \frac{\partial\overline{B}_{1x}}{\partial Z_1} = -i\varepsilon_0\omega_0\varepsilon^{\mathrm{L}}_{\mathcal{R}}(\omega_0)\overline{A}_{2y} + \varepsilon_0\left[\varepsilon^{\mathrm{L}}_{\mathcal{R}}(\omega_0) + \omega_0\varepsilon^{\mathrm{L}'}_{\mathcal{R}}(\omega_0)\right]\frac{\partial\overline{A}_{1y}}{\partial T}. \tag{3.101b}$$

Finally, in order to ensure divergence-free fields,

$$\frac{\partial\overline{A}_{1x}}{\partial X} + \frac{\partial\overline{A}_{1y}}{\partial Y} + \frac{\partial\overline{A}_{2z}}{\partial z} = 0 \tag{3.102}$$

$$\frac{\partial\overline{B}_{1x}}{\partial X} + \frac{\partial\overline{B}_{1y}}{\partial Y} + \frac{\partial\overline{B}_{2z}}{\partial z} = 0. \tag{3.103}$$

Here, the divergence equations are used instead of the z-component of the curl equations because the former provide direct relations for the longitudinal fields.

Performing the same steps used in the previous order, the equation governing A_x is

$$\frac{\partial^2\overline{A}_{2x}}{\partial z^2} + k_0^2\overline{A}_{2x} = -2ik_0\frac{\partial\overline{A}_{1x}}{\partial Z_1} - i\frac{\omega_0}{c^2}\left[2\varepsilon^{\mathrm{L}}_{\mathcal{R}}(\omega_0) + \omega_0\varepsilon^{\mathrm{L}'}_{\mathcal{R}}(\omega_0)\right]\frac{\partial\overline{A}_{1x}}{\partial T}. \tag{3.104}$$

The homogeneous solution to the left-hand side of equation 3.104 is

$$\overline{A}_{2x} = A_{2x}e^{ik_0z}, \tag{3.105}$$

such that the right-hand side, which has the same phase factor, is secular. In order to suppress unbounded growth of the particular solution for $\overline{A}_{2x}$ (which would be $\propto ze^{ik_0z}$), and therefore ensure that equation 3.84 is a uniform asymptotic expansion, this secular term must be set to zero, resulting in

$$2ik_0\frac{\partial A_{1x}}{\partial Z_1} = -i\frac{\omega_0}{c^2}\left[2\varepsilon^{\mathrm{L}}_{\mathcal{R}}(\omega_0) + \omega_0\varepsilon^{\mathrm{L}'}_{\mathcal{R}}(\omega_0)\right]\frac{\partial A_{1x}}{\partial T}. \tag{3.106}$$

Noting that

$$2k_0k_0' = 2\frac{\omega_0}{c}\sqrt{\varepsilon_{\mathcal{R}}^{\mathrm{L}}(\omega_0)}\left[\frac{1}{c}\sqrt{\varepsilon_{\mathcal{R}}^{\mathrm{L}}(\omega_0)} + \frac{\omega_0}{2c\sqrt{\varepsilon_{\mathcal{R}}^{\mathrm{L}}(\omega_0)}}\varepsilon_{\mathcal{R}}^{\mathrm{L}'}(\omega_0)\right] \tag{3.107}$$

$$= 2\frac{\omega_0}{c^2}\varepsilon_{\mathcal{R}}^{\mathrm{L}}(\omega_0) + \frac{\omega_0^2}{c^2}\varepsilon_{\mathcal{R}}^{\mathrm{L}'}(\omega_0), \tag{3.108}$$

equation 3.106 can be rewritten

$$\frac{\partial A_{1x}}{\partial Z_1} = -k_0'\frac{\partial A_{1x}}{\partial T} + O(\varepsilon), \tag{3.109}$$

which is the lowest-order evolution equation for the slowly-varying field envelope and has error of ε, which represents higher-order corrections that will be obtained in subsequent sections. Equation 3.109 well describes wavepacket propagation over distances short compared to the dispersion/diffraction/nonlinear lengths, and subsequent analysis will increase the accuracy of the approximate envelope wave equation by successive orders of ε.

Making the substitutions $A_x = \varepsilon A_{1x}$, $\partial/\partial z = \varepsilon\partial/\partial Z_1$, and $\partial/\partial t = \varepsilon\partial/\partial T$, the overall evolution equation for the x-polarized field envelope is currently

$$\frac{\partial A_x}{\partial z} + k_0'\frac{\partial A_x}{\partial t} = O(\varepsilon^3), \tag{3.110}$$

which is accurate to order ε^2. The error will be reduced to order ε^4 by deriving the NLS equations in the next section. Equation 3.110 has the traveling solution

$$A_x(x,y,z,t) = A_x(x,y,z,t-k_0'z) \tag{3.111}$$

where k_0' is the group delay coefficient and $v_g = 1/k_0'$ is the group velocity coefficient. The solution reveals that to this order, the envelope simply translates along the direction of propagation at the group velocity without change, which is clearly valid within the spatial and temporal confocal ranges of propagation.

Based on the derivation thus far, the fractional temporal bandwidth small parameter can be more formally defined. The group-velocity appears one order of ε later than the phase velocity, which implies the following relation

$$\left|k_0'\frac{\partial A}{\partial t}\right| \sim \varepsilon\,|k_0A|, \tag{3.112}$$

which, in the temporal frequency domain, is rewritten

$$\left|\Delta\omega k_0'\tilde{A}\right| \sim \varepsilon\left|k_0\tilde{A}\right| \Rightarrow \varepsilon \sim \left|\Delta\omega\frac{k_0'}{k_0}\right|. \tag{3.113}$$

Since the group delay is defined

$$k_0' = \frac{\sqrt{\varepsilon_{\mathcal{R}}^{\mathrm{L}}(\omega_0)}}{c} + \frac{\omega_0\varepsilon_{\mathcal{R}}^{\mathrm{L}'}(\omega_0)}{2c\sqrt{\varepsilon_{\mathcal{R}}^{\mathrm{L}}(\omega_0)}} \approx \frac{\sqrt{\varepsilon_{\mathcal{R}}^{\mathrm{L}}(\omega_0)}}{c}, \tag{3.114}$$

which is approximately the phase velocity, it is seen that $\varepsilon \sim |\Delta\omega/\omega_0|$ (more properly, $\eta \sim |\Delta\omega/\omega_0|$); therefore, the small temporal scaling parameter is the fractional bandwidth. For large fractional bandwidth approaching unity, more terms in the Taylor expansion of the dispersion need to be retained to properly describe dispersion over the pulse bandwidth.

Using equations 3.102 and 3.103, the longitudinal field envelopes are written

$$A_{2z} = \frac{i}{k_0}\left[\frac{\partial A_{1x}}{\partial X} + \frac{\partial A_{1y}}{\partial Y}\right] + O(\varepsilon) \tag{3.115}$$

$$B_{2z} = \frac{i}{k_0}\left[\frac{\partial B_{1x}}{\partial X} + \frac{\partial B_{1y}}{\partial Y}\right] + O(\varepsilon) \tag{3.116}$$

$$= \frac{i}{\mu_0\omega_0}\left[\frac{\partial A_{1x}}{\partial Y} - \frac{\partial A_{1y}}{\partial X}\right] + O(\varepsilon).$$

The over-bar is removed because all components travel with the same phase velocity v_p. Again, substituting the amplitude expansions, the total longitudinal electric field is

$$A_z = \frac{i}{k_0}\left[\frac{\partial A_x}{\partial x} + \frac{\partial A_y}{\partial y}\right] + O(\varepsilon^3). \tag{3.117}$$

The slowly-varying longitudinal electric field envelope is driven by transverse derivatives of A_x and A_y, and thus arises from the (paraxial) projection of the x and y polarizations onto the z axis.

Order ε^3 - The Multi-Dimensional NLS Equation

The multi-dimensional spatio-temporal nonlinear Schrödinger (NLS) equation shows up at this order in both the x and y polarization components of the electric field. The third-harmonic is also generated. The ε^3 terms from the quasi-monochromatic Maxwell's equations are

$$\hat{x}: \quad \frac{\partial \overline{A}_{2z}}{\partial Y} - \frac{\partial \overline{A}_{3y}}{\partial z} - \frac{\partial \overline{A}_{2y}}{\partial Z_1} - \frac{\partial \overline{A}_{1y}}{\partial Z_2} = i\mu_0\omega_0\overline{B}_{3x} - \mu_0\frac{\partial \overline{B}_{2x}}{\partial T} \tag{3.118a}$$

$$\mathrm{TH}: \quad \frac{\partial \overline{S}_{3y}}{\partial z} = -3i\mu_0\omega_0\overline{T}_{3x}$$

$$\hat{y}: \quad \frac{\partial \overline{A}_{3x}}{\partial z} + \frac{\partial \overline{A}_{2x}}{\partial Z_1} + \frac{\partial \overline{A}_{1x}}{\partial Z_2} - \frac{\partial \overline{A}_{2z}}{\partial X} = i\mu_0\omega_0\overline{B}_{3y} - \mu_0\frac{\partial \overline{B}_{2y}}{\partial T} \tag{3.118b}$$

$$\mathrm{TH}: \quad \frac{\partial \overline{S}_{3x}}{\partial z} = 3i\mu_0\omega_0\overline{T}_{3y},$$

for the electric field envelopes of the fundamental and third-harmonic, and

$$\hat{x}: \quad \frac{\partial \overline{B}_{2z}}{\partial Y} - \frac{\partial \overline{B}_{3y}}{\partial z} - \frac{\partial \overline{B}_{2y}}{\partial Z_1} - \frac{\partial \overline{B}_{1y}}{\partial Z_2} = \tag{3.119a}$$

$$-i\varepsilon_0\omega_0\left[\varepsilon^{\mathrm{L}}_{\mathcal{R}}(\omega_0)\overline{A}_{3x} + i\varepsilon^{\mathrm{L}'}_{\mathcal{R}}(\omega_0)\frac{\partial \overline{A}_{2x}}{\partial T} - \frac{\varepsilon^{\mathrm{L}''}_{\mathcal{R}}(\omega_0)}{2}\frac{\partial^2 \overline{A}_{1x}}{\partial T^2} + \frac{2}{\varepsilon_0}\overline{P}^{(3)}_x\right]$$

$$+\varepsilon_0\frac{\partial}{\partial T}\left[\varepsilon^{\mathrm{L}}_{\mathcal{R}}(\omega_0)\overline{A}_{2x} + i\varepsilon^{\mathrm{L}'}_{\mathcal{R}}(\omega_0)\frac{\partial \overline{A}_{1x}}{\partial T}\right]$$

$$\mathrm{TH}: \quad \frac{\partial \overline{T}_{3y}}{\partial z} = 3i\varepsilon_0\omega_0\varepsilon^{\mathrm{L}}_{\mathcal{R}}(3\omega_0)\overline{S}_{3x} + 6i\omega_0\overline{P}^{(3)}_{x,3}$$

$$\hat{y}: \quad \frac{\partial \overline{B}_{3x}}{\partial z} + \frac{\partial \overline{B}_{2x}}{\partial Z_1} + \frac{\partial \overline{B}_{1x}}{\partial Z_2} - \frac{\partial \overline{B}_{2z}}{\partial X} = \tag{3.119b}$$

$$-i\varepsilon_0\omega_0\left[\varepsilon^{\mathrm{L}}_{\mathcal{R}}(\omega_0)\overline{A}_{3y} + i\varepsilon^{\mathrm{L}'}_{\mathcal{R}}(\omega_0)\frac{\partial \overline{A}_{2y}}{\partial T} - \frac{\varepsilon^{\mathrm{L}''}_{\mathcal{R}}(\omega_0)}{2}\frac{\partial^2 \overline{A}_{1y}}{\partial T^2} + \frac{2}{\varepsilon_0}\overline{P}^{(3)}_y\right]$$

$$+\varepsilon_0\frac{\partial}{\partial T}\left[\varepsilon^{\mathrm{L}}_{\mathcal{R}}(\omega_0)\overline{A}_{2y} + i\varepsilon^{\mathrm{L}'}_{\mathcal{R}}(\omega_0)\frac{\partial \overline{A}_{1y}}{\partial T}\right]$$

$$\mathrm{TH}: \quad \frac{\partial \overline{T}_{3x}}{\partial z} = -3i\varepsilon_0\omega_0\varepsilon^{\mathrm{L}}_{\mathcal{R}}(3\omega_0)\overline{S}_{3x} - 6i\omega_0\overline{P}^{(3)}_{y,3},$$

for the magnetic field envelopes. The final equations from the divergence of the electric displacement and magnetic field are

$$\varepsilon^{\mathrm{L}}_{\mathcal{R}}(\omega_0)\left[\frac{\partial \overline{A}_{2x}}{\partial X} + \frac{\partial \overline{A}_{2y}}{\partial Y} + \frac{\partial \overline{A}_{3z}}{\partial z} + \frac{\partial \overline{A}_{2z}}{\partial Z_1}\right] \tag{3.120}$$

$$+i\varepsilon^{\mathrm{L}}_{\mathcal{R}}(\omega_0)'\frac{\partial}{\partial T}\left[\frac{\partial \overline{A}_{1x}}{\partial X} + \frac{\partial \overline{A}_{1y}}{\partial Y} + \frac{\partial \overline{A}_{2z}}{\partial z}\right] = 0$$

$$\mathrm{TH}: \quad \frac{\partial \overline{S}_{3z}}{\partial z} = 0$$

$$\frac{\partial \overline{B}_{2x}}{\partial X} + \frac{\partial \overline{B}_{2y}}{\partial Y} + \frac{\partial \overline{B}_{3z}}{\partial z} + \frac{\partial \overline{B}_{2z}}{\partial Z_1} = 0 \tag{3.121}$$

$$\mathrm{TH}: \quad \frac{\partial \overline{T}_{3z}}{\partial z} = 0,$$

where an immediate simplification of equation 3.120 results by substituting equation 3.102

$$(3): \quad \frac{\partial \overline{A}_{2x}}{\partial X} + \frac{\partial \overline{A}_{2y}}{\partial Y} + \frac{\partial \overline{A}_{3z}}{\partial z} + \frac{\partial \overline{A}_{2z}}{\partial Z_1} = 0. \tag{3.122}$$

The third-order polarizations are written

$$\overline{P}_x^{(3)} = \varepsilon_0 n_0 n_2 \left[|A_{1x}|^2 \overline{A}_{1x} + 2\Delta |A_{1y}|^2 \overline{A}_{1x} + \gamma \overline{A}_{1y}^2 \overline{A}_{1x}^* \right] \tag{3.123}$$

$$\overline{P}_y^{(3)} = \varepsilon_0 n_0 n_2 \left[|A_{1y}|^2 \overline{A}_{1y} + 2\Delta |A_{1x}|^2 \overline{A}_{1y} + \gamma \overline{A}_{1x}^2 \overline{A}_{1y}^* \right]$$

$$\overline{P}_{x,3}^{(3)} = \frac{\varepsilon_0}{8} \chi_{xxxx}(3\omega_0; \omega_0, \omega_0, \omega_0) \overline{A}_{1x}^3 + \frac{3\varepsilon_0}{8} \chi_{xyyx}(3\omega_0; \omega_0, \omega_0, \omega_0) \overline{A}_{1y}^2 \overline{A}_{1x} \tag{3.124}$$

$$\overline{P}_{y,3}^{(3)} = \frac{\varepsilon_0}{8} \chi_{xxxx}(3\omega_0; \omega_0, \omega_0, \omega_0) \overline{A}_{1y}^3 + \frac{3\varepsilon_0}{8} \chi_{xyyx}(3\omega_0; \omega_0, \omega_0, \omega_0) \overline{A}_{1x}^2 \overline{A}_{1y}.$$

Here, the nonlinear polarizations consist of third-order nonlinear refraction for the fundamental and the source terms for the third-harmonic driven by the fundamental.

As before, the equation governing A_x will be developed first. Taking the z derivative of equation 3.118b and substituting equation 3.119a results in

$$\frac{\partial^2 \overline{A}_{3x}}{\partial z^2} + ik_0 \frac{\partial \overline{A}_{2x}}{\partial Z_1} + ik_0 \frac{\partial \overline{A}_{1x}}{\partial Z_2} - ik_0 \frac{\partial \overline{A}_{2z}}{\partial X} = -ik_0 \mu_0 \frac{\partial \overline{B}_{2y}}{\partial T} \tag{3.125}$$

$$i\mu_0\omega_0 \left\{ \frac{\partial \overline{B}_{2z}}{\partial Y} - \frac{\partial \overline{B}_{2y}}{\partial Z_1} - \frac{\partial \overline{B}_{1y}}{\partial Z_2} - \varepsilon_0 \frac{\partial}{\partial T} \left[\varepsilon_{\mathcal{R}}^{\mathrm{L}}(\omega_0) \overline{A}_{2x} + i\varepsilon_{\mathcal{R}}^{\mathrm{L}'}(\omega_0) \frac{\partial \overline{A}_{1x}}{\partial T} \right] \right.$$

$$\left. + i\varepsilon_0\omega_0 \left[\varepsilon_{\mathcal{R}}^{\mathrm{L}}(\omega_0) \overline{A}_{3x} + i\varepsilon_{\mathcal{R}}^{\mathrm{L}'}(\omega_0) \frac{\partial \overline{A}_{2x}}{\partial T} - \frac{\varepsilon_{\mathcal{R}}^{\mathrm{L}''}(\omega_0)}{2} \frac{\partial^2 \overline{A}_{1x}}{\partial T^2} + \frac{2}{\varepsilon_0} \overline{P}_x^{(3)} \right] \right\},$$

which, after substitutions from order ε^2, can be rewritten

$$\frac{\partial^2 \overline{A}_{3x}}{\partial z^2} + k_0^2 \overline{A}_{3x} = -ik_0 \frac{\partial \overline{A}_{1x}}{\partial Z_2} - \frac{\partial^2 \overline{A}_{1x}}{\partial X^2} - \frac{\partial^2 \overline{A}_{1y}}{\partial X \partial Y} \tag{3.126}$$

$$-ik_0 \left[\frac{\partial \overline{A}_{2x}}{\partial Z_1} + \mu_0 \frac{\partial \overline{B}_{2y}}{\partial T} \right] + i\mu_0\omega_0 \left\{ \frac{i}{\mu_0\omega_0} \left[\frac{\partial^2 \overline{A}_{1x}}{\partial Y^2} - \frac{\partial^2 \overline{A}_{1y}}{\partial Y \partial X} \right] \right.$$

$$- \frac{\partial \overline{B}_{2y}}{\partial Z_1} - \frac{k_0}{\mu_0\omega_0} \frac{\partial \overline{A}_{1x}}{\partial Z_2} - \varepsilon_0 \left[\varepsilon_{\mathcal{R}}^{\mathrm{L}}(\omega_0) + \omega_0 \varepsilon_{\mathcal{R}}^{\mathrm{L}'}(\omega_0) \right] \frac{\partial \overline{A}_{2x}}{\partial T}$$

$$\left. - i\varepsilon_0 \left[\varepsilon_{\mathcal{R}}^{\mathrm{L}'}(\omega_0) + \frac{\omega_0}{2} \varepsilon_{\mathcal{R}}^{\mathrm{L}''}(\omega_0) \right] \frac{\partial^2 \overline{A}_{1x}}{\partial T^2} + 2i\omega_0 \overline{P}_x^{(3)} \right\}.$$

Setting the secular term to zero results in

$$2ik_0 \frac{\partial \overline{A}_{1x}}{\partial Z_2} + \frac{\partial^2 \overline{A}_{1x}}{\partial X^2} + \frac{\partial^2 \overline{A}_{1x}}{\partial Y^2} - \frac{\omega_0}{c^2} \left[\varepsilon_{\mathcal{R}}^{\mathrm{L}'}(\omega_0) + \frac{\omega_0}{2} \varepsilon_{\mathcal{R}}^{\mathrm{L}''}(\omega_0) \right] \frac{\partial^2 \overline{A}_{1x}}{\partial T^2} \tag{3.127}$$

$$+ 2\mu_0\omega_0^2 \overline{P}_x^{(3)} = -ik_0 \left[\frac{\partial \overline{A}_{2x}}{\partial Z_1} + \mu_0 \frac{\partial \overline{B}_{2y}}{\partial T} \right] - i\mu_0\omega_0 \frac{\partial \overline{B}_{2y}}{\partial Z_1}$$

$$- i\frac{\omega_0}{c^2} \left[\varepsilon_{\mathcal{R}}^{\mathrm{L}}(\omega_0) + \omega_0 \varepsilon_{\mathcal{R}}^{\mathrm{L}'}(\omega_0) \right] \frac{\partial \overline{A}_{2x}}{\partial T}.$$

Using the relation $\partial A_{1x}/\partial Z_1 = -k_0' \partial A_{1x}/\partial T$ and substituting from equation 3.100a, the right-hand side of equation 3.127 can be written

$$-2ik_0 \left[\frac{\partial \overline{A}_{2x}}{\partial Z_1} + k_0' \frac{\partial \overline{A}_{2x}}{\partial T} \right] - \frac{\omega_0^2 [\varepsilon_{\mathcal{R}}^{\mathrm{L}'}(\omega_0)]^2}{4c^2 \varepsilon_{\mathcal{R}}^{\mathrm{L}}(\omega_0)} \frac{\partial^2 \overline{A}_{1x}}{\partial T^2}. \tag{3.128}$$

Noting that

$$-k_0 k_0'' = -\frac{\omega_0}{c^2} \left\{ \varepsilon_{\mathcal{R}}^{\mathrm{L}'}(\omega_0) + \frac{\omega_0}{2} \varepsilon_{\mathcal{R}}^{\mathrm{L}''}(\omega_0) - \frac{\omega_0}{4\varepsilon_{\mathcal{R}}^{\mathrm{L}}(\omega_0)} \left[\varepsilon_{\mathcal{R}}^{\mathrm{L}'}(\omega_0) \right]^2 \right\}, \tag{3.129}$$

substituting equation 3.129 for the right-hand side, and writing the nonlinear coupling in full, equation 3.127 reduces to

$$2ik_0\left[\frac{\partial A_{2x}}{\partial Z_1}+k_0'\frac{\partial A_{2x}}{\partial T}+\frac{\partial A_{1x}}{\partial Z_2}\right]+\frac{\partial^2 A_{1x}}{\partial X^2}+\frac{\partial^2 A_{1x}}{\partial Y^2}-k_0k_0''\frac{\partial^2 A_{1x}}{\partial T^2} \tag{3.130}$$
$$+2k_0^2\frac{n_2}{n_0}\left[|A_{1x}|^2A_{1x}+2\Delta\left|A_{1y}\right|^2A_{1x}+\gamma A_{1y}^2A_{1x}^*\right]=O(\varepsilon).$$

Using the amplitude scaling relation $A_x=\varepsilon A_{1x}+\varepsilon^2A_{2x}$, and the substitution

$$\frac{\partial}{\partial z}=\varepsilon\frac{\partial}{\partial Z_1}+\varepsilon^2\frac{\partial}{\partial Z_2}, \tag{3.131}$$

the slowly-varying envelope equations 3.109 and 3.130 can be written in lab coordinates

$$2ik_0\left[\frac{\partial A_x}{\partial z}+k_0'\frac{\partial A_x}{\partial t}\right]+\frac{\partial^2 A_x}{\partial x^2}+\frac{\partial^2 A_x}{\partial y^2}-k_0k_0''\frac{\partial^2 A_x}{\partial t^2} \tag{3.132}$$
$$+2k_0^2\frac{n_2}{n_0}\left[|A_x|^2A_x+2\Delta|A_y|^2A_x+\gamma A_y^2A_x^*\right]=O(\varepsilon^4).$$

At this point in the analysis, the full evolution equation for the field envelope is valid to order ε^3. Equation 3.132 is easily verified by making the substitutions into the slow variables and amplitudes and comparing with the envelope equations obtained in this and the previous order. Note that there are extra terms containing A_{2x} and A_{2y} that have not been obtained in the analysis thus far. These terms, for example $\partial^2A_{2x}/\partial X^2$, $2\Delta|A_{1x}|^2A_{2x}$, and $\gamma A_{2y}^2A_{1x}^*$, are all of order ε^4 and higher and fall beyond the ε^3 accuracy of the current state of the derivation. These terms will present themselves in the next sections as the accuracy improves.

The leading-order distance evolution scale $Z_1\propto 1/\varepsilon$ of equation 3.132 represents the group delay, or group velocity. This scale can be easily removed with the Galilean transformation $T=t-k_0'z$, with the resulting leading-order scale ($Z_2\propto 1/\varepsilon^2$) representing diffraction/dispersion and self-focusing/self-phase modulation. This is a principal advantage of the first-order equation over the Helmholtz equation.

When the coordinate transformation $T=t-k_0'z$ is made and $A_y=0$, equation 3.132 is the (3+1)-D scalar NLS equation. Combined with the corresponding equation for A_y, equation 3.132 represents the coupled or vector NLS equations. The next section will determine the first-order corrections to the vector NLS equations. Since there is no coupling from A_z to A_x or A_y, or linear coupling from A_x directly to A_y to this order, the coupled NLS system is a fully vectorial one for isotropic and cubic media.

The transverse and nonlinear scales become apparent at this order. The terms obtained at this order are ε^2 smaller than the terms obtained at order ε. Therefore,

$$\left|\frac{\partial^2A_x}{\partial x^2}+\frac{\partial^2A_x}{\partial y^2}\right|\sim\varepsilon^2\left|k_0^2A_x\right|. \tag{3.133}$$

By transforming into the Fourier domain, the small parameter can be written

$$\kappa=\varepsilon\sim\frac{\sqrt{k_x^2+k_y^2}}{k_0}=\sin\theta. \tag{3.134}$$

This relation indicates that the transverse momenta must be less than the propagation constant k_0 in order that $\kappa<1$, as shown in Figure 2.2 for k_x. When $\kappa>1$, evanescent wave propagation must be considered. The transverse FWHM momenta are related to the width of the wavepacket by $k_x,k_y\sim 2\pi/w_0$, where circular symmetry is assumed. This relation gives the scaling $\kappa\sim\lambda/w_0$. Because $\sin\theta=k_x/k_0\ll 1$, the exact isotropic k-relation $k_z^2=k_0^2-k_x^2-k_y^2$ is reduced to the paraxial expression $k_z\approx k_0-k_x^2/2k_0-k_y^2/2k_0$, as given by the spatial Fourier transform of the linear part of equation 3.132.

By the same arguments, the nonlinear scale is written

$$\nu=\varepsilon\sim\sqrt{\frac{n_2}{n_0}}\,|A_x|, \tag{3.135}$$

which means that the nonlinear polarization expansion is well-ordered and converges when $\nu<1$. This occurs when the induced nonlinearity is weak compared to the linear index of refraction, as indicated.

Performing the same steps with the third-harmonic envelope results in

$$\frac{\partial^2\overline{S}_{3x}}{\partial z^2}=-k^2(3\omega_0)\overline{S}_{3x}-\frac{9\omega_0^2}{4c^2}\left[\chi_{xxxx}(3\omega_0)\overline{A}_{1x}^3+3\chi_{xyyx}(3\omega_0)\overline{A}_{1y}^2\overline{A}_{1x}\right], \tag{3.136}$$

which is recognized as a wave equation driven by a third-harmonic source term. The wavenumber for the third-harmonic is defined $k^2(3\omega_0) = 9\omega_0^2\varepsilon_{\mathcal{R}}^{\mathrm{L}}(3\omega_0)/c^2$. Because the driving polarization has the phase factor e^{3ik_0z}, so must the third harmonic in order for this equation to have a solution. The solution is then

$$S_{3x} = \frac{9\omega_0^2}{4c^2}\frac{\chi_{xxxx}(3\omega_0;\omega_0,\omega_0,\omega_0)\left[A_{1x}^3 + 3\Delta_K A_{1y}^2 A_{1x}\right]}{9k_0^2 - k^2(3\omega_0)}, \tag{3.137}$$

where Δ_K is the cross-phase modulation coefficient for the Kerr nonlinearity. The resonant denominator indicates that the strength of the third-harmonic grows near the phase-matching condition $k(3\omega_0) \approx 3k_0$ (or $n(3\omega_0) \approx n(\omega_0)$), but the unphysical pole is a manifestation of the fact that the derivation is not valid at the resonant condition, for which initially exponential growth of the third-harmonic would occur. The pole is not a problem in practice because the phase matching condition is difficult to achieve in condensed, linearly isotropic media. In fact, for useful nonlinear dielectrics with low loss, it is typically true that in the optical regime, $n(3\omega_0) > n(\omega_0)$, which has important ramifications to multi-dimensional stability.

Using equation 3.122, the longitudinal electric field envelope at this order is

$$A_{3z} = \frac{i}{k_0}\left[\frac{\partial A_{2z}}{\partial Z_1} + \frac{\partial A_{2x}}{\partial X} + \frac{\partial A_{2y}}{\partial Y}\right]. \tag{3.138}$$

Combining the equation for the longitudinal electric field envelope with equation 3.115, the total longitudinal field envelope is

$$A_z = \frac{i}{k_0}\left[\frac{\partial A_x}{\partial x} + \frac{\partial A_y}{\partial y}\right] + \frac{k_0'}{k_0^2}\frac{\partial}{\partial t}\left[\frac{\partial A_x}{\partial x} + \frac{\partial A_y}{\partial y}\right] + O(\varepsilon^4). \tag{3.139}$$

The form of the longitudinal field will be elaborated on in the next section.

Order ε^4 - The non-SVEA Corrections

In this section, the first set of higher-order corrections to the NLS envelope equation are obtained which allow for the description of the propagation of short pulses. These corrections are important in studies of propagation over distances greater than the dispersion/nonlinear lengths and are: linear and two-photon absorption, third-order linear dispersion, space-time focusing, optical shock, and Raman scattering. The evolution of the third-harmonic is not considered in this section because any corrections obtained here to the solution $\mathbf{S}_3$ of the previous order will not enter the final analysis. At ε^4 then, the terms from Maxwell's equations are

$$(1)\,\hat{x}: \quad \frac{\partial \overline{A}_{3z}}{\partial Y} - \frac{\partial \overline{A}_{4y}}{\partial z} - \frac{\partial \overline{A}_{3y}}{\partial Z_1} - \frac{\partial \overline{A}_{2y}}{\partial Z_2} - \frac{\partial \overline{A}_{1y}}{\partial Z_3} = i\mu_0\omega_0\overline{B}_{4x} - \mu_0\frac{\partial \overline{B}_{3x}}{\partial T} \tag{3.140a}$$

$$(1)\,\hat{y}: \quad \frac{\partial \overline{A}_{4x}}{\partial z} + \frac{\partial \overline{A}_{3x}}{\partial Z_1} + \frac{\partial \overline{A}_{2x}}{\partial Z_2} + \frac{\partial \overline{A}_{1x}}{\partial Z_3} - \frac{\partial \overline{A}_{3z}}{\partial X} = i\mu_0\omega_0\overline{B}_{4y} - \mu_0\frac{\partial \overline{B}_{3y}}{\partial T}, \tag{3.140b}$$

for the electric field envelope, and

$$\begin{aligned}(2)\,\hat{x}: \quad & \frac{\partial \overline{B}_{3z}}{\partial Y} - \frac{\partial \overline{B}_{4y}}{\partial z} - \frac{\partial \overline{B}_{3y}}{\partial Z_1} - \frac{\partial \overline{B}_{2y}}{\partial Z_2} - \frac{\partial \overline{B}_{1y}}{\partial Z_3} = \\ & -i\varepsilon_0\omega_0\left[\varepsilon_{\mathcal{R}}^{\mathrm{L}}(\omega_0)\overline{A}_{4x} + i\varepsilon_{\mathcal{R}}^{\mathrm{L}'}(\omega_0)\frac{\partial \overline{A}_{3x}}{\partial T} - \frac{\varepsilon_{\mathcal{R}}^{\mathrm{L}''}(\omega_0)}{2}\frac{\partial^2 \overline{A}_{2x}}{\partial T^2}\right. \\ & \left. -i\frac{\varepsilon_{\mathcal{R}}^{\mathrm{L}'''}(\omega_0)}{6}\frac{\partial^3 \overline{A}_{1x}}{\partial T^3} + i\varepsilon_I^{L}(\omega_0)\overline{A}_{1x} + \frac{2}{\varepsilon_0}\overline{P}_x^{(4)}\right] \\ & +\varepsilon_0\frac{\partial}{\partial T}\left[\varepsilon_{\mathcal{R}}^{\mathrm{L}}(\omega_0)\overline{A}_{3x} + i\varepsilon_{\mathcal{R}}^{\mathrm{L}'}(\omega_0)\frac{\partial \overline{A}_{2x}}{\partial T} - \frac{\varepsilon_{\mathcal{R}}^{\mathrm{L}''}(\omega_0)}{2}\frac{\partial^2 \overline{A}_{1x}}{\partial T^2} + \frac{2}{\varepsilon_0}\overline{P}_x^{(3)}\right]\end{aligned} \tag{3.141a}$$

$$(2)\,\hat{y}: \quad \frac{\partial \overline{B}_{4x}}{\partial z} + \frac{\partial \overline{B}_{3x}}{\partial Z_1} + \frac{\partial \overline{B}_{2x}}{\partial Z_2} + \frac{\partial \overline{B}_{1x}}{\partial Z_3} - \frac{\partial \overline{B}_{3z}}{\partial X} = \tag{3.141b}$$

$$-i\varepsilon_0\omega_0 \left[\varepsilon^{L}_{\mathcal{R}}(\omega_0)\overline{A}_{4y} + i\varepsilon^{L'}_{\mathcal{R}}(\omega_0)\frac{\partial \overline{A}_{3y}}{\partial T} - \frac{\varepsilon^{L''}_{\mathcal{R}}(\omega_0)}{2}\frac{\partial^2 \overline{A}_{2y}}{\partial T^2} \right.$$

$$\left. -i\frac{\varepsilon^{L'''}_{\mathcal{R}}(\omega_0)}{6}\frac{\partial^3 \overline{A}_{1y}}{\partial T^3} + i\varepsilon^{L}_{I}(\omega_0)\overline{A}_{1y} + \frac{2}{\varepsilon_0}\overline{P}^{(4)}_{y} \right]$$

$$+\varepsilon_0\frac{\partial}{\partial T}\left[\varepsilon^{L}_{\mathcal{R}}(\omega_0)\overline{A}_{3y} + i\varepsilon^{L'}_{\mathcal{R}}(\omega_0)\frac{\partial \overline{A}_{2y}}{\partial T} - \frac{\varepsilon^{L''}_{\mathcal{R}}(\omega_0)}{2}\frac{\partial^2 \overline{A}_{1y}}{\partial T^2} + \frac{2}{\varepsilon_0}\overline{P}^{(3)}_{y} \right],$$

for the magnetic field envelope. The final equations are from the divergence of the electric displacement and magnetic field

$$(3): \quad \frac{\partial \overline{A}_{3x}}{\partial X} + \frac{\partial \overline{A}_{3y}}{\partial Y} + \frac{\partial \overline{A}_{4z}}{\partial z} + \frac{\partial \overline{A}_{3z}}{\partial Z_1} + \frac{\partial \overline{A}_{2z}}{\partial Z_2} = \tag{3.142}$$

$$-\frac{2}{\varepsilon_0\varepsilon^{L}_{\mathcal{R}}(\omega_0)}\left[\frac{\partial \overline{P}^{(3)}_{x}}{\partial X} + \frac{\partial \overline{P}^{(3)}_{y}}{\partial Y} + \frac{\partial \overline{P}^{(3)}_{z}}{\partial z} \right]$$

$$(4): \quad \frac{\partial \overline{B}_{3x}}{\partial X} + \frac{\partial \overline{B}_{3y}}{\partial Y} + \frac{\partial \overline{B}_{4z}}{\partial z} + \frac{\partial \overline{B}_{3z}}{\partial Z_1} + \frac{\partial \overline{B}_{2z}}{\partial Z_2} = 0. \tag{3.143}$$

The third-order polarizations are written

$$\overline{P}^{(3)}_{z} = \varepsilon_0 n_0 n_2 \left\{ 2\Delta\left[|A_{1x}|^2 + |A_{1y}|^2 \right]\overline{A}_{2z} + \gamma\left[\overline{A}^2_{1x} + \overline{A}^2_{1y} \right]\overline{A}^*_{2z} \right\}, \tag{3.144}$$

which is the nonlinear polarization along the z-axis due to coupling between the transverse and longitudinal field, and

$$\overline{P}^{(4)}_{x} = \varepsilon_0 n_0 n_2 \left[2|A_{1x}|^2\overline{A}_{2x} + \overline{A}^2_{1x}\overline{A}^*_{2x} + 2\Delta|A_{1y}|^2\overline{A}_{2x} + \gamma\overline{A}^2_{1y}\overline{A}^*_{2x} \right. \tag{3.145}$$

$$\left. +2\Delta\overline{A}_{1y}\overline{A}^*_{2y}\overline{A}_{1x} + 2\Delta\overline{A}^*_{1y}\overline{A}_{2y}\overline{A}_{1x} + 2\gamma\overline{A}_{1y}\overline{A}_{2y}\overline{A}^*_{1x} \right]$$

$$+i\frac{\varepsilon_0\beta_2}{2k_f}\left[|A_{1x}|^2\overline{A}_{1x} + 2\Delta_K|A_{1y}|^2\overline{A}_{1x} + \gamma_K\overline{A}^2_{1y}\overline{A}^*_{1x} \right]$$

$$-\varepsilon_0 n_0 n_2 \tau_R \left\{ \left[\frac{\partial |A_{1x}|^2}{\partial T} + \Delta_R\frac{\partial |A_{1y}|^2}{\partial T} \right]\overline{A}_{1x} + \gamma_R\left[\frac{\partial \overline{A}^*_{1y}\overline{A}_{1x}}{\partial T} + \frac{\partial \overline{A}^*_{1x}\overline{A}_{1y}}{\partial T} \right]\overline{A}_{1y} \right\},$$

with a similar expression for $\overline{P}^{(4)}_{y}$. The first set of terms in the transverse nonlinear polarization consist of mixed field envelopes from different orders of the field amplitude expansion because A_{2x} can be substituted for one A_{1x} for example, giving an extra factor of ε. The second set of terms represents two-photon absorption while the last set represents the first-order approximation to Raman gain.

Following the same procedure used in the previous sections, the condition on the x polarization component at this order is

$$\frac{\partial^2 \overline{A}_{4x}}{\partial z^2} + k_0^2\overline{A}_{4x} = -2ik_0\left[\frac{\partial \overline{A}_{3x}}{\partial Z_1} + k_0'\frac{\partial \overline{A}_{3x}}{\partial T} \right] - 2ik_0\frac{\partial \overline{A}_{2x}}{\partial Z_2} - \frac{\partial^2 \overline{A}_{2x}}{\partial X^2} \tag{3.146}$$

$$-\frac{\partial^2 \overline{A}_{2x}}{\partial Y^2} - \frac{\partial^2 \overline{A}_{2x}}{\partial Z_1^2} + \frac{1}{c^2}\left[\varepsilon^{L}_{\mathcal{R}}(\omega_0) + 2\omega_0\varepsilon^{L'}_{\mathcal{R}}(\omega_0) + \frac{\omega_0^2}{2}\varepsilon^{L'}_{\mathcal{R}}(\omega_0) \right]\frac{\partial^2 \overline{A}_{2x}}{\partial T^2}$$

$$-2ik_0\frac{\partial \overline{A}_{1x}}{\partial Z_3} - 2\frac{\partial^2 \overline{A}_{1x}}{\partial Z_1\partial Z_2} + \frac{i}{c^2}\left[\varepsilon^{L'}_{\mathcal{R}}(\omega_0) + \omega_0\varepsilon^{L''}_{\mathcal{R}}(\omega_0) + \frac{\omega_0^2}{6}\varepsilon^{L'''}_{\mathcal{R}}(\omega_0) \right]\frac{\partial^3 \overline{A}_{1x}}{\partial T^3}$$

$$-ik_f^2\varepsilon^{L}_{I}(\omega_0)\overline{A}_{1x} - \frac{2}{\varepsilon_0}k_f^2\overline{P}^{(4)}_{x} - 4i\mu_0\omega_0\frac{\partial \overline{P}^{(3)}_{x}}{\partial T}.$$

Upon further manipulation and the use of equation 3.130, the secular term becomes

$$2ik_0\left[\frac{\partial A_{3x}}{\partial Z_1} + k_0'\frac{\partial A_{3x}}{\partial T} \right] + 2ik_0\frac{\partial A_{2x}}{\partial Z_2} + \frac{\partial^2 A_{2x}}{\partial X^2} + \frac{\partial^2 A_{2x}}{\partial Y^2} - k_0k_0''\frac{\partial^2 A_{2x}}{\partial T^2} \tag{3.147}$$

$$+2ik_0\frac{\partial A_{1x}}{\partial Z_3}+ik_f^2\varepsilon_I^L(\omega_0)A_{1x}-i\frac{k_0'}{k_0}\frac{\partial}{\partial T}\left[\frac{\partial^2 A_{1x}}{\partial X^2}+\frac{\partial^2 A_{1x}}{\partial Y^2}\right]$$
$$-\frac{i}{3}k_0k_0'''\frac{\partial^3 A_{1x}}{\partial T^3}+\frac{2}{\varepsilon_0}k_f^2P_x^{(4)}+i\frac{4k_f}{\varepsilon_0 n_0}\left[\frac{n_0}{c}-\frac{k_0'}{2}\right]\frac{\partial P_x^{(3)}}{\partial T}=O(\varepsilon),$$

where the third-order group-delay dispersion coefficient k_0''' is

$$\frac{1}{3}k_0k_0'''=\frac{1}{c^2}\left[\varepsilon_{\mathcal{R}}^{L'}(\omega_0)+\omega_0\varepsilon_{\mathcal{R}}^{L''}(\omega_0)+\frac{\omega_0^2}{6}\varepsilon_{\mathcal{R}}^{L'''}(\omega_0)\right]-k_0'k_0''. \tag{3.148}$$

Once again using the amplitude scaling relation

$$A_x=\varepsilon A_{1x}+\varepsilon^2A_{2x}+\varepsilon^3A_{3x}, \tag{3.149}$$

and the z scale relation

$$\frac{\partial}{\partial z}=\varepsilon\frac{\partial}{\partial Z_1}+\varepsilon^2\frac{\partial}{\partial Z_2}+\varepsilon^3\frac{\partial}{\partial Z_3}, \tag{3.150}$$

the full slowly-varying envelope equation to this order is written

$$\begin{aligned}
&2ik_0\left[\frac{\partial A_x}{\partial z}+k_0'\frac{\partial A_x}{\partial t}\right]+ik_0\alpha_0A_x+\frac{\partial^2A_x}{\partial x^2}+\frac{\partial^2A_x}{\partial y^2}-k_0k_0''\frac{\partial^2A_x}{\partial t^2}\\
&-\frac{i}{3}k_0k_0'''\frac{\partial^3A_x}{\partial t^3}-i\frac{k_0'}{k_0}\frac{\partial}{\partial t}\left[\frac{\partial^2A_x}{\partial x^2}+\frac{\partial^2A_x}{\partial y^2}\right]\\
&+2k_0^2\frac{n_2}{n_0}\left[|A_x|^2A_x+2\Delta|A_y|^2A_x+\gamma A_y^2A_x^*\right]\\
&+2ik_0^2\frac{n_2}{n_0}K\left[|A_x|^2A_x+2\Delta_K|A_y|^2A_x+\gamma_KA_y^2A_x^*\right]\\
&+4ik_fn_2\left[\frac{n_0}{c}-\frac{k_0'}{2}\right]\frac{\partial}{\partial t}\left[|A_x|^2A_x+2\Delta|A_y|^2A_x+\gamma A_y^2A_x^*\right]\\
&-2k_0^2\frac{n_2}{n_0}\tau_R\left\{\left[\frac{\partial|A_x|^2}{\partial T}+\Delta_R\frac{\partial|A_y|^2}{\partial T}\right]A_x+\gamma_R\left[\frac{\partial A_y^*A_x}{\partial T}+\frac{\partial A_x^*A_y}{\partial T}\right]A_y\right\}=O(\varepsilon^5),
\end{aligned} \tag{3.151}$$

where $\alpha_0=k_f^2\varepsilon_I^L(\omega_0)/k_0=k_f\varepsilon_I^L(\omega_0)/\sqrt{\varepsilon_{\mathcal{R}}^L(\omega_0)}$ is the linear absorption coefficient and $K=\beta_2/2k_0n_2$ is the normalized two-photon absorption coefficient [119]. The other additional terms to NLS are third-order dispersion, with coefficient k_0''', and the so-called space-time focusing [144] term. The space-time focusing term is one of a more general class of terms denoted here the space-time dispersion terms, and describes the (paraxial) curvature of the energy front due to spatio-temporal diffraction. Following nonlinear refraction and two-photon absorption, optical shock is the first-order time derivative of the (vectorial) nonlinearity and gives rise to an intensity-dependent group delay. The optical shock expression obtained here has two contributions, one directly from Maxwell's equation in the time derivative of the nonlinear polarization (proportional to phase delay), and one due to the removal of the SVEA by one order (proportional to group delay). The last term, proportional to the time derivative of the (vectorial) intensity, is the first-order (linear) approximation to the Raman gain/loss function, with time constant τ_R defined by equation 3.56, and results in amplification of low frequencies at the expense of high frequencies.

Solving equation 3.142 for A_{4z} using the fact that $\overline{A}_{4z}$ has the same propagation phase as all other field components, the contribution to the longitudinal field at this order is written

$$\begin{aligned}
A_{4z}=&\frac{i}{k_0}\left[\frac{\partial A_{3z}}{\partial Z_1}+\frac{\partial A_{2z}}{\partial Z_2}+\frac{\partial A_{3x}}{\partial X}+\frac{\partial A_{3y}}{\partial Y}\right]\\
&+\frac{2i}{k_0\varepsilon_0\varepsilon_{\mathcal{R}}^L(\omega_0)}\left[\frac{\partial P_x^{(3)}}{\partial X}+\frac{\partial P_y^{(3)}}{\partial Y}+\frac{\partial P_z^{(3)}}{\partial z}\right].
\end{aligned} \tag{3.152}$$

Combining this equation with A_{2z} and A_{3z}, the total longitudinal field is

$$A_z=\left[\frac{i}{k_0}+\frac{k_0'}{k_0^2}\frac{\partial}{\partial t}-\frac{i}{k_0^3}\left\{[k_0']^2-\frac{1}{2}k_0k_0''\right\}\frac{\partial^2}{\partial t^2}\right]\left[\frac{\partial A_x}{\partial x}+\frac{\partial A_y}{\partial y}\right] \tag{3.153}$$

$$-\frac{i}{2k_0^3}\left[\frac{\partial^3 A_x}{\partial x^3}+\frac{\partial^3 A_x}{\partial x\partial y^2}+\frac{\partial^3 A_y}{\partial y^3}+\frac{\partial^3 A_y}{\partial y\partial x^2}\right]+\frac{i}{k_0 n_0}\left[\frac{\partial \mathrm{NL}_x^{(3)}}{\partial x}+\frac{\partial \mathrm{NL}_y^{(3)}}{\partial y}\right]$$
$$-\frac{2in_2}{k_0 n_0}\left\{2\Delta\left[|A_x|^2+|A_y|^2\right]\left[\frac{\partial A_x}{\partial x}+\frac{\partial A_y}{\partial y}\right]+\gamma\left[A_x^2+A_y^2\right]\left[\frac{\partial A_x^*}{\partial x}+\frac{\partial A_y^*}{\partial y}\right]\right\},$$

where the nonlinear terms are defined

$$\mathrm{NL}_x^{(3)}=n_2\left[|A_x|^2A_x+2\Delta|A_y|^2A_x+\gamma A_y^2A_x^*\right] \tag{3.154}$$
$$\mathrm{NL}_y^{(3)}=n_2\left[|A_y|^2A_y+2\Delta|A_x|^2A_y+\gamma A_x^2A_y^*\right]. \tag{3.155}$$

There is a simple geometrical interpretation for the origin of the longitudinal field. Considering only linear propagation for the moment, Figure 3.2 illustrates the relationship between the projections of the polarization onto the x and z directions given an angle of propagation θ with the z axis. In the Fourier domain, the ratio between the transverse and longitudinal components

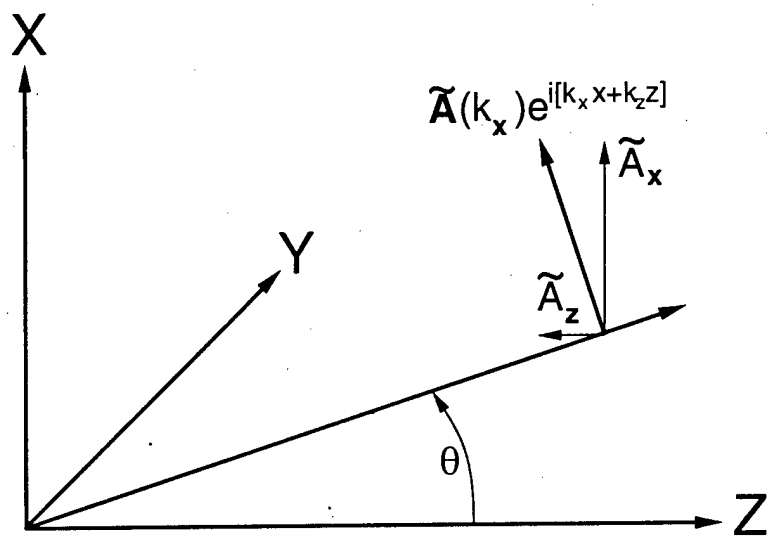

Figure 3.2 Origin of the longitudinal field projection. The field envelope $\mathbf{A}$ is decomposed into a plane-wave spectrum $\tilde{\mathbf{A}}$, with one member of that spectrum illustrated, propagating with angle θ, where $\sin\theta = k_x/k_0$. The direction of polarization is orthogonal to the direction of propagation, and is decomposed into transverse ($\tilde{A}_x$) and longitudinal ($\tilde{A}_z$) components. For simplicity, tilt in the y direction is not illustrated, but is a straightforward extension of the present geometry.

is given by

$$\tilde{A}_z=-\tan\theta\tilde{A}_x=-\frac{k_x}{k_z}\tilde{A}_x. \tag{3.156}$$

This geometry is easily extended to include the y transverse direction, with the result

$$\tilde{A}_z=-\frac{1}{k_z}\left[k_x\tilde{A}_x+k_y\tilde{A}_y\right]=-\frac{k_x\tilde{A}_x+k_y\tilde{A}_y}{\sqrt{k^2(\omega_0+\Delta\omega)-k_x^2-k_y^2}}. \tag{3.157}$$

The truncated Taylor's expansion, when transformed back to the real space domain, recovers the linear terms of equation 3.153.

Analogous to the projections of the transverse electric fields, the longitudinal field is also driven by the projections of the transverse nonlinear polarizations onto the z-axis. The paraxial projections appear in the nonlinear terms of equation 3.153, with additional contributions from the nonlinear coupling between the longitudinal and transverse fields.

Order ε^5 - The non-Paraxial Corrections

The results of this section are derived mainly for the purpose of obtaining the form of the propagation equation, including all commensurate terms through the fifth-order (or quintic) nonlinearity, which will be used later in the thesis as an ultrafast

saturation mechanism to stabilize multi-dimensional solitary-wave propagation. The fifth-order nonlinearity obtained here consists of three distinct contributions: directly from the fifth-order polarization, from the product of the third-order polarization with itself, and a "cascaded" contribution. The second contribution is a result of the reduction to a first-order equation and the cascaded contribution arises from the interaction between the fundamental and third-harmonic.

This derivation also illustrates the non-paraxial and analogous higher-order non-SVEA terms. The terms additional to the quintic nonlinearity which show up are then: dispersion of linear absorption, fourth-order linear dispersion and the non-paraxial spatial diffraction analog, second-order space-time dispersion, second-order shock (intensity-dependent group-delay dispersion) and the spatial analog intensity-dependent diffraction, Raman index dispersion, and nonlinear coupling with the longitudinal field. Some of these terms will be used in the remaining chapters of this thesis as well.

The two Maxwell's equations that are necessary at this order are:

$$(1)\ \hat{y}:\ \frac{\partial \overline{A}_{5x}}{\partial z}+\frac{\partial \overline{A}_{4x}}{\partial Z_1}+\frac{\partial \overline{A}_{3x}}{\partial Z_2}+\frac{\partial \overline{A}_{2x}}{\partial Z_3}+\frac{\partial \overline{A}_{1x}}{\partial Z_4}-\frac{\partial \overline{A}_{4z}}{\partial X}= i\mu_0\omega_0\overline{B}_{5y}-\mu_0\frac{\partial \overline{B}_{4y}}{\partial T} \tag{3.158}$$

$$\begin{aligned}(2)\ \hat{x}:\ &\frac{\partial \overline{B}_{4z}}{\partial Y}-\frac{\partial \overline{B}_{5y}}{\partial z}-\frac{\partial \overline{B}_{4y}}{\partial Z_1}-\frac{\partial \overline{B}_{3y}}{\partial Z_2}-\frac{\partial \overline{B}_{2y}}{\partial Z_3}-\frac{\partial \overline{B}_{1y}}{\partial Z_4}= \\ &-i\varepsilon_0\omega_0\left[\varepsilon^{L}_{\mathcal{R}}(\omega_0)\overline{A}_{5x}+i\varepsilon^{L'}_{\mathcal{R}}(\omega_0)\frac{\partial \overline{A}_{4x}}{\partial T}-\frac{\varepsilon^{L''}_{\mathcal{R}}(\omega_0)}{2}\frac{\partial^2\overline{A}_{3x}}{\partial T^2}-i\frac{\varepsilon^{L'''}_{\mathcal{R}}(\omega_0)}{6}\frac{\partial^3\overline{A}_{2x}}{\partial T^3}\right. \\ &\left.+\frac{\varepsilon^{L''''}_{\mathcal{R}}(\omega_0)}{24}\frac{\partial^4\overline{A}_{1x}}{\partial T^4}+i\varepsilon^{L}_{I}(\omega_0)\overline{A}_{2x}-\varepsilon^{L'}_{I}(\omega_0)\frac{\partial \overline{A}_{1x}}{\partial T}+\frac{2}{\varepsilon_0}\overline{P}^{(5)}_{x}\right] \\ &+\varepsilon_0\frac{\partial}{\partial T}\left[\varepsilon^{L}_{\mathcal{R}}(\omega_0)\overline{A}_{4x}+i\varepsilon^{L'}_{\mathcal{R}}(\omega_0)\frac{\partial \overline{A}_{3x}}{\partial T}-\frac{\varepsilon^{L''}_{\mathcal{R}}(\omega_0)}{2}\frac{\partial^2\overline{A}_{2x}}{\partial T^2}-\frac{\varepsilon^{L'''}_{\mathcal{R}}(\omega_0)}{6}\frac{\partial^3\overline{A}_{1x}}{\partial T^3}\right. \\ &\left.+i\varepsilon^{L}_{I}(\omega_0)\overline{A}_{1x}+\frac{2}{\varepsilon_0}\overline{P}^{(4)}_{x}\right].\end{aligned} \tag{3.159}$$

where the additional nonlinear polarization term is defined

$$\begin{aligned}\overline{P}^{(5)}_{x}=\ &\varepsilon_0\left[n_0n_4+i\frac{\beta_3}{2k_f}\right]\left\{\left[|A_{1x}|^4+\frac{3}{5}|A_{1y}|^4+\frac{6}{5}|A_{1x}|^2|A_{1y}|^2\right]\overline{A}_{1x}\right. \\ &\left.+\left[\frac{3}{5}\overline{A}^{*2}_{1x}\overline{A}^{2}_{1x}+\frac{1}{5}\overline{A}^{2}_{1x}\overline{A}^{*2}_{1y}\right]\overline{A}_{1x}+\frac{2}{5}|A_{1y}|^2\overline{A}^{2}_{1y}\overline{A}^{*}_{1x}\right\} \\ &+\frac{3\varepsilon_0}{8}\chi_{xxxx}(\omega_0;3\omega_0,-\omega_0,-\omega_0)\left\{\overline{S}_{3x}\left[\overline{A}^{*2}_{1x}+\gamma_K\overline{A}^{*2}_{1y}\right]+2\Delta_K\overline{S}_{3y}\overline{A}^{*}_{1y}\overline{A}^{*}_{1x}\right\} \\ &+\varepsilon_0n_0n_2\left[2\Delta|A_{2z}|^2\overline{A}_{1x}+\gamma\overline{A}^{2}_{2z}\overline{A}^{*}_{1x}\right] \\ &-\frac{\varepsilon_0n_0n''_R}{2}\left\{\left[\frac{\partial^2|A_{1x}|^2}{\partial T^2}+\Delta_R\frac{\partial^2|A_{1y}|^2}{\partial T^2}\right]\overline{A}_{1x}\right. \\ &\left.+\gamma_R\left[\frac{\partial^2\overline{A}^{*}_{1y}\overline{A}_{1x}}{\partial T^2}+\frac{\partial^2\overline{A}^{*}_{1x}\overline{A}_{1x}}{\partial T^2}\right]\overline{A}_{1y}\right\} \\ &+\text{mixed terms},\end{aligned} \tag{3.160}$$

which are the fifth-order terms from equation 3.82. The first set of terms in the nonlinear polarization is the direct contribution from $\chi^{(5)}$, while the second set of terms is the cascaded contribution from the interaction between the fundamental and third-harmonic. The third group of terms is the third-order nonlinear coupling with the z component of the electric field, the fourth is the Raman index dispersion and the last represents the mixed terms involving A_{1x}, A_{2x}, etc, which are not specified for convenience.

Using the same method employed before, the following secular equation for the evolution of the slowly-varying x-component of the electric field envelope is obtained:

$$2ik_0\left[\frac{\partial A_{4x}}{\partial Z_1}+k'_0\frac{\partial A_{4x}}{\partial T}\right]+2ik_0\frac{\partial A_{3x}}{\partial Z_2}+\frac{\partial^2 A_{3x}}{\partial X^2}+\frac{\partial^2 A_{3x}}{\partial Y^2}-k_0k''_0\frac{\partial^2 A_{3x}}{\partial T^2} \tag{3.161}$$

$$
\begin{aligned}
&+2ik_0\frac{\partial A_{2x}}{\partial Z_3}+ik_0\alpha_0A_{2x}-i\frac{k_0'}{k_0}\frac{\partial}{\partial T}\left[\frac{\partial^2A_{2x}}{\partial X^2}+\frac{\partial^2A_{2x}}{\partial Y^2}\right]-\frac{i}{3}k_0k_0'''\frac{\partial^3A_{2x}}{\partial T^3}\\
&+2ik_0\frac{\partial A_{1x}}{\partial Z_4}-k_0\alpha_0'\frac{\partial A_{1x}}{\partial T}-\frac{1}{4k_0^2}\left[\frac{\partial^4A_{1x}}{\partial X^4}+2\frac{\partial^4A_{1x}}{\partial^2X\partial^2Y}+\frac{\partial^4A_{1x}}{\partial Y^4}\right]\\
&+\frac{1}{k_0}\left[\frac{k_0''}{2}-\frac{k_0'^2}{k_0}\right]\frac{\partial^2}{\partial T^2}\left[\frac{\partial^2A_{1x}}{\partial X^2}+\frac{\partial^2A_{1x}}{\partial Y^2}\right]+\frac{1}{12}k_0k_0''''\frac{\partial^4A_{1x}}{\partial T^4}\\
&+\frac{2}{\varepsilon_0n_0^2}\left[\frac{\partial^2P_x^{(3)}}{\partial X^2}+\frac{\partial^2P_y^{(3)}}{\partial X\partial Y}+ik_0\frac{\partial P_z^{(3)}}{\partial X}-\frac{1}{4}\frac{\partial^2P_x^{(3)}}{\partial X^2}-\frac{1}{4}\frac{\partial^2P_x^{(3)}}{\partial Y^2}\right]\\
&-i\frac{4k_f}{\varepsilon_0n_0}\left[\frac{k_0'}{2}-\frac{n_0}{c}\right]\frac{\partial P_x^{(4)}}{\partial T}+\frac{k_f}{2\varepsilon_0n_0}\left\{k_0''-\frac{4}{k_0}\left[k_0'-\frac{n_0}{c}\right]^2\right\}\frac{\partial^2P_x^{(3)}}{\partial T^2}\\
&+i\frac{k_f}{\varepsilon_0n_0}\frac{\partial P_x^{(3)}}{\partial Z_2}+\frac{2k_f^2}{\varepsilon_0}P_x^{(5)}.
\end{aligned}
$$

The third line from the end contains terms with spatial derivatives of the third-order nonlinear polarization. The first three of these terms are vectorial resulting from the divergence equation, while the next two terms result from the reduction to a first-order equation. All of these terms correct the curvature of k-space (which is now slightly anisotropic) due to nonlinearity, termed here intensity-dependent diffraction. The next line contains first-order shock terms associated with two-photon absorption and Raman scattering, and the second-order shock associated with nonlinear refraction. The last line contains an additional term which is the result of the reduction to a first-order equation (discussed next, which contains further non-SVEA and non-paraxial nonlinear contributions) and the cascaded and direct quintic nonlinearity.

Evaluating the remaining Z_2 derivative term results in

$$
\begin{aligned}
i\frac{k_f}{\varepsilon_0n_0}\frac{\partial P_x^{(3)}}{\partial Z_2}=ik_fn_2\Big[&2\left|A_{1x}\right|^2\frac{\partial A_{1x}}{\partial Z_2}+A_{1x}^2\frac{\partial A_{1x}^*}{\partial Z_2}+2\Delta A_{1x}A_{1y}^*\frac{\partial A_{1y}}{\partial Z_2}\\
&+2\Delta A_{1x}A_{1y}\frac{\partial A_{1y}^*}{\partial Z_2}+2\Delta\left|A_{1y}\right|^2\frac{\partial A_{1x}}{\partial Z_2}+2\gamma A_{1x}^*A_{1y}\frac{\partial A_{1y}}{\partial Z_2}+\gamma A_{1y}^2\frac{\partial A_{1x}^*}{\partial Z_2}\Big],
\end{aligned}
\tag{3.162}
$$

which contains effective quintic nonlinear terms from the product of the cubic nonlinearity with itself and additional intensity-dependent diffraction and second-order shock terms. Keeping only the effective quintic nonlinear refraction terms

$$
\begin{aligned}
i\frac{k_f}{\varepsilon_0n_0}\frac{\partial P_x^{(3)}}{\partial Z_2}=-k_0^2\left[\frac{n_2}{n_0}\right]^2\Big\{&\left|A_{1x}\right|^4A_{1x}+\left[4\Delta^2-\gamma^2\right]\left|A_{1y}\right|^4A_{1x}\\
&+2\left[2\Delta+\gamma^2\right]\left|A_{1x}\right|^2\left|A_{1y}\right|^2A_{1x}+\gamma[2\Delta+1]A_{1x}^{*2}A_{1y}^2A_{1x}\\
&+\gamma[2\Delta-1]A_{1x}^2A_{1y}^{*2}A_{1x}+2\gamma\left|A_{1y}\right|^2A_{1y}^2A_{1x}^*\Big\},
\end{aligned}
\tag{3.163}
$$

which is similar in form to the direct contribution from $\chi^{(5)}$.

This contribution can be more easily understood intuitively by considering the total scalar relative dielectric constant

$$
\varepsilon\left(\left|A\right|^2\right)=n^2\left(\left|A\right|^2\right)=n_0^2+2n_0n_2\left|A\right|^2+2n_0n_4\left|A\right|^4,
\tag{3.164}
$$

keeping terms only up to fourth-order in field. In a second-order equation, such as Maxwell's equations or the Helmholtz equation, n^2 is the relevant quantity for wave propagation, while in a first-order equation, n is the relevant quantity. Using the appropriate Taylor's expansions,

$$
n\left(\left|A\right|^2\right)\approx n_0+n_2\left|A\right|^2+\left[n_4-\frac{n_2^2}{2n_0}\right]\left|A\right|^4,
\tag{3.165}
$$

which has the direct n_4 contribution from $\chi^{(5)}$ and an indirect contribution manifested by the expansion of the square-root as required in the first-order equation.

The cascaded interaction between the fundamental and third-harmonic produces another effective fifth-order nonlinear interaction. Evaluating the third-harmonic down-conversion terms of the fifth-order polarization given by equation 3.161

$$
\begin{aligned}
2k_0^2\frac{n_4^{\text{casc}}}{n_0}\Big[&\left|A_{1x}\right|^4A_{1x}+3\Delta_K\gamma_K\left|A_{1y}\right|^4A_{1x}+6\Delta_K^2\left|A_{1x}\right|^2\left|A_{1y}\right|^2A_{1x}\\
&+3\Delta_KA_{1x}^{*2}A_{1y}^2A_{1x}+\gamma_KA_{1x}^2A_{1y}^{*2}A_{1x}+2\Delta_K\left|A_{1y}\right|^2A_{1y}^2A_{1x}^*\Big],
\end{aligned}
\tag{3.166}
$$

where Δ_K and γ_K are the cross-phase modulation and vector four-wave mixing coefficients for the Kerr nonlinearity (the third-order Raman susceptibility cannot produce a third-harmonic) and the cascaded quintic nonlinear index is defined

$$n_4^{\text{casc}} = \frac{3}{32n_0}\frac{\chi_{xxxx}(3\omega_0;\omega_0,\omega_0,\omega_0)\chi_{xxxx}(\omega_0;3\omega_0,-\omega_0,-\omega_0)}{n_0^2-n^2(3\omega_0)}. \tag{3.167}$$

This is the same form as the effective n_2 produced by the nonresonant interaction between the fundamental and second-harmonic [194] mediated by $\chi^{(2)}$, which has received recent interest [196]. Resonant third-harmonic cascading has also recently been studied [211], with results away from the phase-matching condition similar to that derived here.

Writing out all three contributions to the vectorial quintic nonlinearity results in

$$\begin{aligned}
&2k_0^2\frac{n_4}{n_0}\left\{1+\frac{n_4^{\text{casc}}}{n_4}-\frac{1}{2}\frac{n_2^2}{n_0n_4}\right\}|A_{1x}|^4A_{1x} \\
&+2k_0^2\frac{n_4}{n_0}\left\{\frac{3}{5}+3\Delta_K\gamma_K\frac{n_4^{\text{casc}}}{n_4}-\frac{1}{2}\left[4\Delta^2-\gamma^2\right]\frac{n_2^2}{n_0n_4}\right\}|A_{1y}|^4A_{1x} \\
&+2k_0^2\frac{n_4}{n_0}\left\{\frac{6}{5}+6\Delta_K^2\frac{n_4^{\text{casc}}}{n_4}-\left[2\Delta+\gamma^2\right]\frac{n_2^2}{n_0n_4}\right\}|A_{1x}|^2|A_{1y}|^2A_{1x} \\
&+2k_0^2\frac{n_4}{n_0}\left\{\frac{3}{5}+3\Delta_K\frac{n_4^{\text{casc}}}{n_4}-\frac{\gamma}{2}\left[2\Delta+1\right]\frac{n_2^2}{n_0n_4}\right\}A_{1x}^{*2}A_{1y}^2A_{1x} \\
&+2k_0^2\frac{n_4}{n_0}\left\{\frac{1}{5}+\gamma_K\frac{n_4^{\text{casc}}}{n_4}-\frac{\gamma}{2}\left[2\Delta-1\right]\frac{n_2^2}{n_0n_4}\right\}A_{1x}^2A_{1y}^{*2}A_{1x} \\
&+2k_0^2\frac{n_4}{n_0}\left\{\frac{2}{5}+2\Delta_K\frac{n_4^{\text{casc}}}{n_4}-\gamma\frac{n_2^2}{n_0n_4}\right\}|A_{1y}|^2A_{1y}^2A_{1x}^*,
\end{aligned} \tag{3.168}$$

which will be used in the final higher-order NLS equation. Note that the coefficients of the intrinsic quintic nonlinearity are only strictly valid for the isotropic symmetry class under Kleinman symmetry such that $\Delta_K = \gamma_K = 1/3$ must also be used for the cascaded contributions.

Three-photon absorption, with coefficient β_3, is included in this study for completeness and to allow for resonant enhancement of the the quintic nonlinear index. The use of three-photon enhancement would violate the Kleinman symmetry assumed in deriving the cross-phase modulation coefficients of the fifth-order susceptibility, however. In three-photon resonance, the third-order susceptibilities responsible for third-harmonic generation and down conversion will also be enhanced. The imaginary parts of these susceptibilities would need to be considered as well, and is a straightforward extension to the present derivation. In this situation, the third-harmonic cascading process would also produce an additional, effective, three-photon absorption coefficient β_3^{casc}. Three-photon resonance is not used in this thesis, but this discussion is provided as an illustration of one means of enhancing the saturation effects of quintic nonlinear refraction.

3.2.3 Reduction to (1+1)-D Spatial and (2+1)-D Spatio-Temporal Equations

As mentioned previously, the scalings used for the derivation of the (3+1)-D spatio-temporal nonlinear wave equation are not the same as those that are valid for the numerical simulations performed in this thesis. In fact, the result of the derivation is a far more general vector equation than necessary for the simulations. This section reduces the full equation to simplified equations that are more easily dealt with numerically while still describing the necessary physics.

In both cases, linear confinement in the y dimension is provided by a slab waveguide structure, as shown in Figure 1.20. A detailed analysis of the influence of the waveguide is presented in Appendix C up to the order of the NLS equation. For simplicity, these results are not used directly here, but some simplifications are used that are the result of the discussions in Appendix D, which makes direct use of the waveguide equations derived in Appendix C. The main simplification is that all phase-dependent terms in the nonlinear polarization are neglected under the assumption that the difference in phase velocity between the TE and TM modes results in a beat length much shorter than the wave interaction distance.

The (1+1)-D Vector Spatial Nonlinear Wave Equation

In this situation, which describes the propagation and interaction among purely spatial solitons, the temporal derivatives and the y transverse spatial derivatives can be neglected. Also, by setting $\varepsilon = 0.1$, the diffraction and nonlinear small parameters satisfy $\kappa = \varepsilon$, and $\nu = \varepsilon^2$. These scalings are appropriate for the numerical studies of Chapter 5. Note that in the (1+1)-D case

of spatial solitons, quintic index saturation is not necessary for stability and will not be included because the expected intrinsic value of n_4^{eff} for the example material is too small to produce any noticeable effect.

Using these scalings, the appropriate evolution equation is

$$2ik_0\frac{\partial A_x}{\partial z}+ik_0\alpha_0A_x+\frac{\partial^2A_x}{\partial x^2}-\frac{1}{4k_0^2}\frac{\partial^4A_x}{\partial x^4} + 2k_0^2\frac{n_2}{n_0}\left\{[1+iK]\,|A_x|^2A_x+2\,[\Delta+iK\Delta_K]\,|A_y|^2A_x\right\}=0, \tag{3.169}$$

with the corresponding coupled evolution equation for A_y. The first term in equation 3.169 is the first-order propagator. Linear absorption is next, followed by paraxial (second-order x derivatives) and non-paraxial (fourth-order x derivatives) diffraction. Third-order nonlinear refraction and two-photon absorption including scalar and vectorial contributions (neglecting the phase-dependent vector four-wave mixing terms) follow.

Stimulated Raman scattering is not present in the cw case (although the Raman contribution to the instantaneous nonlinear index is retained), and it is assumed that spontaneous Raman scattering, which has not been discussed, is negligible. Note that the linear non-paraxial term is retained, while the nonlinear non-paraxial terms are neglected. This is justified by the fact that $\nu=\varepsilon^2$, which places the nonlinear non-paraxial terms order ε^2 smaller than the linear non-paraxial term.

The (2+1)-D Vector Spatio-Temporal Nonlinear Wave Equation

Like the previous case, here one spatial dimension is neglected due to transverse confinement by a slab waveguide. Therefore, the terms with y derivatives are not included, but all temporal derivatives must be retained, subject to the small scaling parameters. Again, setting $\varepsilon=0.1$, the scaling of the small parameters appropriate for the simulations of Chapter 6 are: $\kappa=\varepsilon^2$, $\eta=\varepsilon$, $\nu_2=\varepsilon^2$, and $\nu_4=\varepsilon$, where $\nu_2\sim|n_2/n_0|^{1/2}|A|$, and $\nu_4\sim|n_4/n_0|^{1/4}|A|$. The first two scales indicate that the non-SVEA terms are more important than the non-paraxial terms. The temporal scaling parameter is larger than the spatial parameter because short pulses are necessitated in this thesis by the desire for short propagation distances combined with the small anomalous group-delay dispersion of available materials such as fused silica. The nonlinear scalings indicate that the cubic nonlinearity is proportionally weaker than the quintic nonlinearity. Therefore, the quintic nonlinear terms will dominate over the second-order non-SVEA nonlinear terms, and the latter can be neglected. Even though the strength of the Raman nonlinearity is about the same as the instantaneous cubic Kerr nonlinearity, the spectral bandwidth of the spatio-temporal waves used in the simulations exceeds the optical phonon resonance frequency. Therefore, a three-term approximation to the Raman response is insufficient to correctly describe intra-pulse stimulated Raman scattering over the entire spectral bandwidth. For the simulations, it is assumed that the full Raman response enters at order ε^3 with the Kerr nonlinearity, as discussed in Chapter 4.

Using the scalings appropriate for the simulations then, the higher-order terms included in the reduced equation are the quintic and Raman nonlinearities and those terms that are the result of the removal of the slowly-varying envelope approximation by one order: third-order dispersion (TOD), space-time focusing [144], and optical shock [183]. The fourth-order dispersion (FOD) term is also used, but the other second-order non-SVEA terms need not be included, as discussed above. In the reduced time coordinate frame, where $T=t-k_0'z$ and k_0' is the group delay at the center frequency ω_0, the (2+1)-D vector nonlinear evolution equation takes the form

$$\begin{aligned}
&2ik_0\frac{\partial A_x}{\partial z}+ik_0\alpha_0A_x+\frac{\partial^2A_x}{\partial x^2}-k_0k_0''\frac{\partial^2A_x}{\partial T^2}-\frac{i}{3}k_0k_0'''\frac{\partial^3A_x}{\partial T^3}-i\frac{k_0'}{k_0}\frac{\partial^3A_x}{\partial T\partial x^2}\\
&+\frac{1}{12}k_0k_0''''\frac{\partial^4A_x}{\partial T^4}+2k_0^2\frac{n_2}{n_0}\left\{[1+iK]\,|A_x|^2A_x+2\,[\Delta+iK\Delta_K]\,|A_y|^2A_x\right\}\\
&-2k_0^2\frac{n_2}{n_0}\tau_R\left[\frac{\partial|A_x|^2}{\partial T}A_x+\Delta_R\frac{\partial|A_y|^2}{\partial T}A_x+\gamma_R\frac{\partial A_y^*A_x}{\partial T}A_y\right]\\
&+4ik_fn_2[1+iK]\left[\frac{n_0}{c}-\frac{k_0'}{2}\right]\frac{\partial}{\partial T}\left[|A_x|^2A_x+\Delta\,|A_y|^2A_x\right]\\
&-4ik_fn_2\tau_R\left[\frac{n_0}{c}-\frac{k_0'}{2}\right]\frac{\partial}{\partial T}\left[\frac{\partial|A_x|^2}{\partial T}A_x+\Delta_R\frac{\partial|A_y|^2}{\partial T}A_x+\gamma_R\frac{\partial A_y^*A_x}{\partial T}A_y\right]\\
&-k_0^2\frac{n_R''}{n_0}\left[\frac{\partial^2|A_x|^2}{\partial T^2}A_x+\Delta_R\frac{\partial^2|A_y|^2}{\partial T^2}A_x+\gamma_R\frac{\partial^2A_y^*A_x}{\partial T^2}A_y\right]\\
&+2k_0^2\frac{n_4}{n_0}\left\{1+\frac{n_4^{\text{casc}}}{n_4}-\frac{1}{2}\frac{n_2^2}{n_0n_4}\right\}|A_x|^4A_x
\end{aligned} \tag{3.170}$$

$$+2k_0^2\frac{n_4}{n_0}\left\{\frac{3}{5}+\gamma_K\left[2\Delta_K+\gamma_K\right]\frac{n_4^{\text{casc}}}{n_4}-\frac{1}{2}\left[4\Delta^2-\gamma^2\right]\frac{n_2^2}{n_0 n_4}\right\}|A_y|^4 A_x$$
$$+2k_0^2\frac{n_4}{n_0}\left\{\frac{6}{5}+2\Delta_K\left[2\Delta_K+\gamma_K\right]\frac{n_4^{\text{casc}}}{n_4}-\left[2\Delta+\gamma^2\right]\frac{n_2^2}{n_0 n_4}\right\}|A_x|^2|A_y|^2 A_x=0.$$

This equation is referred to simply as the higher-order, multi-dimensional vector NLS, or vector hNLS, equation.

The terms in equation 3.170 are, in order: propagation in the reduced-time coordinate frame, linear absorption, transverse paraxial diffraction, group-delay dispersion, third-order dispersion, space-time focusing, fourth-order dispersion, nonlinear self-/cross-phase modulation (SPM/CPM) and self-/cross-two-photon absorption, self-/cross-Raman amplification, vectorial optical shock (two lines including nonlinear phase modulation and Raman amplification), Raman index dispersion, and quintic nonlinear refraction (last three lines). The higher order non-SVEA terms of third- and fourth-order linear dispersion, optical shock and Raman scattering were described in more detail in section 2.4, while the spatio-temporal terms are discussed in section 4.1 and linear and two-photon absorption are discussed in section 5.3.

Chapter 4

Spatio-Temporal Diffraction and the Split-Step Numerical Method

The nonlinear evolution equation derived in the previous chapter can be solved with a variety of numerical techniques. In fact, the purpose of using the multiple-scales analysis was to remove the fast scales in order to reduce the complexity of the numerical method. This is in contrast to the vector nonlinear Helmholtz equation, which is second-order and possesses variations on the order of an optical wavelength and requires more complex methods for numerical solution.

The principal methods in use today to solve first-order partial differential equations are the finite-difference [212, 230] and split-step methods [231, 232]. The finite-difference method becomes cumbersome when dealing with multiple dimensions and higher-order derivatives, such as those required for third- and fourth-order dispersion and non-paraxial diffraction. This chapter examines the more aesthetic and intuitive split-step method. The split-step method solves, in alternating steps, the linear diffraction problem in it's natural Fourier domain and the nonlinear, or inhomogeneous, problem in the real-space domain.

The split-step method is illustrated schematically in Figure 4.1. The prototype problem to be solved is propagation of an initial field through a volume with inhomogeneous (spatially-varying) dielectric constant. The split-step method can be applied to quite general problems where the inhomogeneity is due to refractive, diffractive, or layered structures, but this thesis concentrates instead on inhomogeneity due to nonlinearity. Ignoring Fresnel reflections, the effect of an inhomogeneous dielectric constant on a propagating field is the accumulation of a spatially-varying complex phase. Instead of accumulating this phase continuously throughout propagation, the split-step method applies the phase (representing the inhomogeneity throughout a thin slab) at discrete points. Between these points, the field is propagated as if the medium were linear and homogeneous. The key characteristic of the split-step method is this alternation between linear diffraction and inhomogeneous phase accumulation, but it should be noted that the method, like the underlying first-order differential equation, is limited to unidirectional propagation and cannot be used when the longitudinal variation of the inhomogeneity is strong enough to produce significant backscattered radiation.

Section 4.1 describes the exact spatio-temporal linear diffraction problem for isotropic media and examines the linear spatio-temporal terms in the higher-order NLS equation. Section 4.2 derives the split-step method and discusses the application to (1+1)-D spatial and (2+1)-D spatio-temporal propagation. Finally, section 4.3 covers issues related to the implementation of the split-step method, with particular focus on the accuracy of the algorithm and how it scales with step size.

4.1 Linear Spatio-Temporal Diffraction

This section examines spatio-temporal propagation using the linear, scalar Helmholtz valid for homogeneous, isotropic media. Under these conditions, equation 3.44 can be written

$$\frac{\partial^2 \overline{A}}{\partial z^2} + \nabla_T^2 \overline{A} + k^2 \left(\omega_0 + i \frac{\partial}{\partial t} \right) \overline{A} = 0 \tag{4.1}$$

where the $\nabla \left[\nabla \cdot \overline{\mathbf{A}} \right]$ term is identically zero (because now $\nabla \cdot \mathbf{D} = 0$ implies that $\nabla \cdot \mathbf{E} = 0$) allowing for the consideration of a scalar equation, ∇_T is the transverse Laplacian, and $\overline{A}$ is defined

$$E(x,y,z,t) = \frac{1}{2} \left[\overline{A}(x,y,z,t) e^{-i\omega_0 t} + \overline{A}^*(x,y,z,t) e^{i\omega_0 t} \right], \tag{4.2}$$

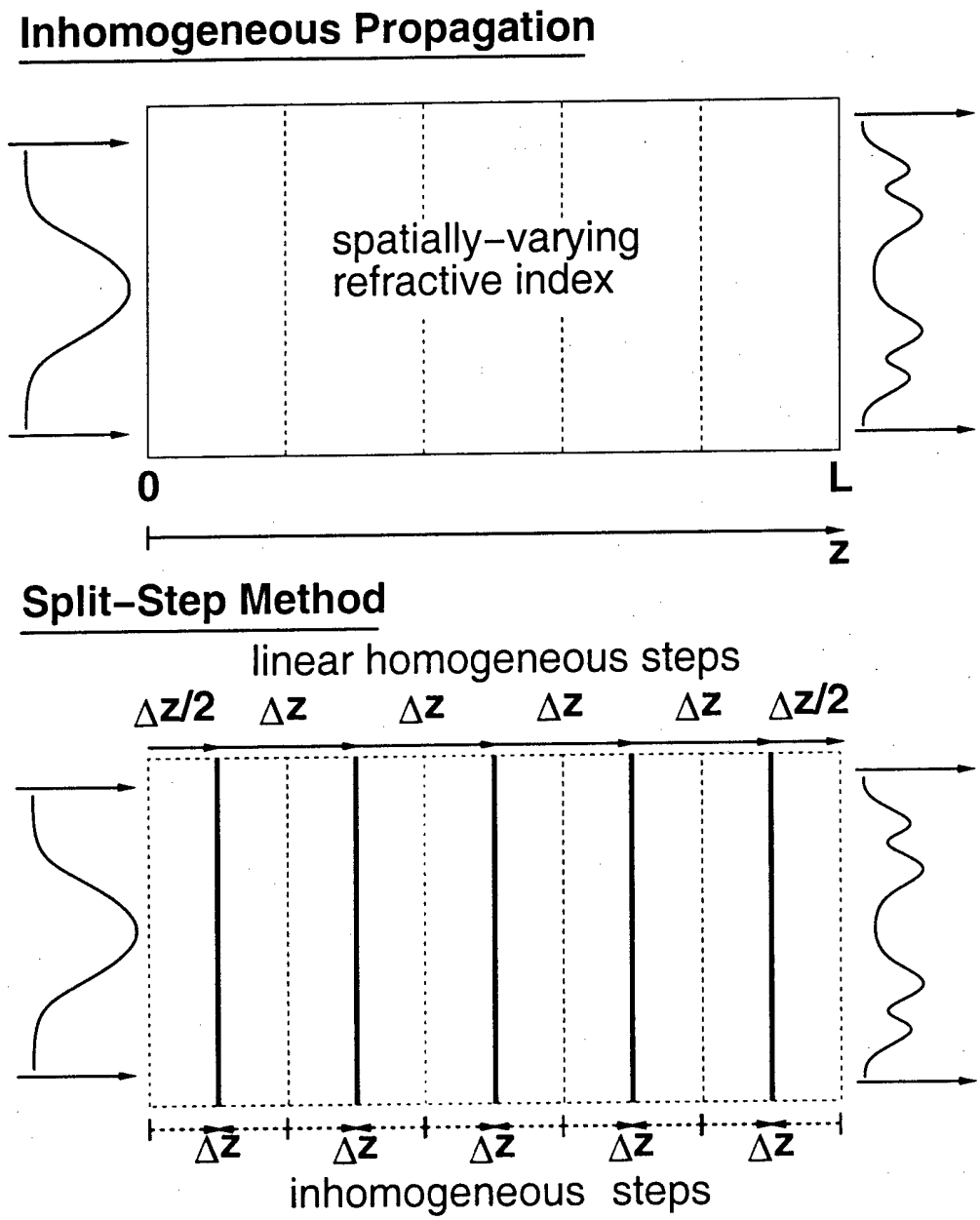

Figure 4.1: Representation of the split-step method. The top figure shows the desired propagation problem with index variation throughout the volume. The bottom figure shows the approximation used in the split-step method. The volume is divided into slabs of thickness $\Delta z \ll L$ with the inhomogeneous index in each slab reduced to a spatially-varying phase applied at the discrete positions along the mean propagation direction (represented by the heavy vertical lines) located at the midpoint of each slab. The field is propagated between these midpoints as if the medium were homogeneous.

using the quasi-monochromatic representation as before.

The spatio-temporal Fourier transform pair is defined

$$E(x,y,z,t) = \left[\frac{1}{2\pi}\right]^3 \int\int \tilde{E}(k_x,k_y,z,\omega)e^{i[\mathbf{k}_T\cdot\mathbf{r}_T-\omega t]}d\mathbf{k}_T d\omega \tag{4.3}$$

$$\tilde{E}(k_x,k_y,z,\omega) = \int\int E(x,y,z,t)e^{-i[\mathbf{k}_T\cdot\mathbf{r}_T-\omega t]}d\mathbf{r}_T dt \tag{4.4}$$

where $\mathbf{k}_T = k_x\hat{x} + k_y\hat{y}$ represents the transverse spatial frequencies and $\mathbf{r}_T = x\hat{x} + y\hat{y}$ is the transverse position vector. The spatio-temporal Fourier transform of the electric field becomes

$$\tilde{E}(k_x,k_y,z,\omega) = \frac{1}{2}\left[\tilde{A}(k_x,k_y,z,\omega-\omega_0) + \tilde{A}^*(k_x,k_y,z,\omega+\omega_0)\right]. \tag{4.5}$$

An equation will be developed that describes the evolution of the Fourier components with propagation distance, using the transverse spatio-temporal Fourier transform of equation 4.1.

In chapter 3, the two leading-order temporal scales were removed from the evolution equation. The carrier oscillation is removed by the use of the quasi-monochromatic representation, while forward-going propagation at the group velocity is removed by the coordinate transformation $T = t - k_0'z$. Using this transformation to the reduced-time coordinates, the wavepacket becomes

$$\overline{A}(x,y,z,t) \rightarrow \overline{A}(x,y,z,T-k_0'z). \tag{4.6}$$

Then, by the Fourier shift theorem, $\tilde{\overline{A}} \rightarrow \tilde{\overline{A}}e^{i\Delta\omega k_0'z}$. The evolution of the Fourier components of the wavepacket in reduced coordinates is then

$$\frac{\partial^2\tilde{\overline{A}}e^{i\Delta\omega k_0'z}}{\partial z^2} - \left[k_x^2+k_y^2\right]\tilde{\overline{A}}e^{i\Delta\omega k_0'z} + k^2(\Delta\omega+\omega_0)\tilde{\overline{A}}e^{i\Delta\omega k_0'z} = 0, \tag{4.7}$$

which, upon application of the second derivative with z, becomes

$$\frac{\partial^2\tilde{\overline{A}}}{\partial z^2} + 2i\Delta\omega k_0'\frac{\partial\tilde{\overline{A}}}{\partial z} + \left[k^2(\Delta\omega+\omega_0) - k_x^2 - k_y^2 - \Delta\omega^2 k_0'^2\right]\tilde{\overline{A}} = 0. \tag{4.8}$$

Equation 4.8 can be solved by assuming a solution of the form $\tilde{\overline{A}}(z) = \tilde{A}(0)\exp(\gamma z)$, thereby removing the fast propagation phase and producing a quadratic equation in γ

$$\gamma^2 + 2i\Delta\omega k_0'\gamma + \left[k^2(\Delta\omega+\omega_0) - k_T^2 - \Delta\omega^2 k_0'^2\right] = 0. \tag{4.9}$$

with the familiar solution

$$\begin{aligned}\gamma &= \frac{1}{2}\left\{-2i\Delta\omega k_0' \pm \sqrt{\left[2i\Delta\omega k_0'\right]^2 - 4\left[k^2(\Delta\omega+\omega_0) - k_x^2 - k_y^2 - \Delta\omega^2 k_0'^2\right]}\right\} \\ &= \pm i\sqrt{k^2(\Delta\omega+\omega_0) - k_x^2 - k_y^2} - i\Delta\omega k_0'.\end{aligned} \tag{4.10}$$

This solution includes both forward and backward going waves (with the backward going wave traveling at twice the group velocity with respect to the reduced frame), but since it was assumed there is no inhomogeneity, these waves are uncoupled. Therefore, the initial conditions can be chosen such that only a forward going wave (the "+" sign) need be considered. This is the crucial step in reducing the second-order differential equation into a first-order one and can be done exactly for linear homogeneous problems.

The forward-going solution is written

$$\tilde{\overline{A}}(k_x,k_y,z,\Delta\omega) = e^{ik_{rz}z}\tilde{A}(k_x,k_y,0,\Delta\omega), \tag{4.11}$$

where $\tilde{A}(0)$ is the transform of the initial field distribution in the transverse coordinates and time and

$$k_{rz} = \sqrt{k^2(\Delta\omega+\omega_0) - k_x^2 - k_y^2} - \Delta\omega k_0' \tag{4.12}$$

is the z-directed momentum of a particular Fourier component in the reduced coordinate frame. In equation 4.12, the full linear phase is accounted for in dispersive, non-paraxial propagation.

Equation 4.11 shows that linear propagation can be described by appropriately evolving the phase of each spatio-temporal frequency component of the wavepacket. The complex amplitude $\tilde{A}(k_x, k_y, 0, \Delta\omega)$ of the wavepacket for each transverse spatial and temporal frequency is known by specifying the initial field distribution for all time on a plane orthogonal to the direction of propagation. Each point in the three-dimensional Fourier space $(k_x, k_y, \Delta\omega)$ has an associated longitudinal wavenumber as prescribed by equation 4.12, which is multiplied by propagation distance to determine the proper phase for each spectral component.

A plot of the z-directed wavenumber is shown in Figure 4.2, where

$$k_z = \sqrt{k^2(\Delta\omega + \omega_0) - k_x^2} \tag{4.13}$$

in laboratory coordinates for one transverse spatial frequency, k_x. When k_z becomes imaginary, i.e. when $k_x > k(\Delta\omega + \omega_0)$,

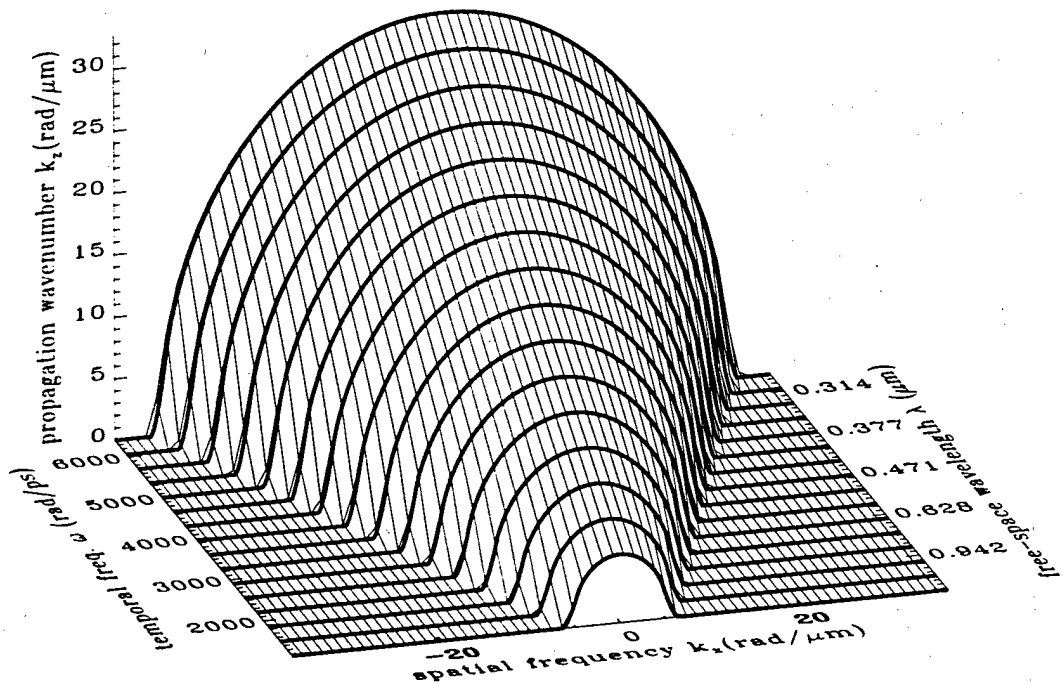

Figure 4.2: Spatio-temporal momentum space. This surface is calculated using the parameters of fused silica. The center frequency of 3770 rad/ps corresponds to a free-space wavelength of 0.5 μm.

the associated Fourier component propagates with large attenuation. Here, k_z is set to zero for these evanescent waves for clarity. As shown in the figure, the radius of curvature of the momentum surface increases with frequency. The transformation to reduced-time coordinates removes the first-order slope of the surface, $k_0' = k'(\omega_0)$, where

$$k'(\omega_0) = \left.\frac{\partial k(\omega)}{\partial \omega}\right|_{\omega=\omega_0}, \tag{4.14}$$

and results in the removal of a constant group delay, as shown in equation 4.12.

4.1.1 Spatio-Temporal Group-Velocity Space

The momentum surface given by k_z can be approximated about the carrier frequency ω_0 by

$$k_z(k_x, \Delta\omega) \approx k_z(k_x, 0) + \Delta\omega k_z'(k_x, 0) + \frac{\Delta\omega^2}{2} k_z''(k_x, 0), \tag{4.15}$$

where

$$k_z'(k_x, 0) = \left.\frac{\partial k_z(k_x, \omega)}{\partial \omega}\right|_{\omega=\omega_0} \quad \text{and} \quad k_z''(k_x, 0) = \left.\frac{\partial^2 k_z(k_x, \omega)}{\partial \omega^2}\right|_{\omega=\omega_0}, \tag{4.16}$$

thereby giving the z-directed group-delay and group-delay dispersion as a function of transverse spatial frequency. Taking the first and second derivatives of equation 4.13 with respect to frequency results in

$$k_z'(k_x,0) = \frac{k_0 k_0'}{\sqrt{k_0^2 - k_x^2}} = \frac{k_0 k_0'}{k_z(k_x,0)} \tag{4.17}$$

$$k_z''(k_x,0) = \frac{k_0^3 k_0'' - k_x^2 k_0 k_0'' - k_x^2 k_0'^2}{k_z^3(k_x,0)}. \tag{4.18}$$

Noting that $k_z = k_0 \cos\theta = k_x/\tan\theta$, the approximate momentum space can be written

$$k_z(k_x,\Delta\omega) \approx k_0\cos\theta + \frac{\Delta\omega k_0'}{\cos\theta} + \frac{\Delta\omega^2}{2}\left[\frac{k_0''}{\cos\theta} - \frac{\sin^2\theta}{\cos^3\theta}\frac{k_0'^2}{k_0}\right]. \tag{4.19}$$

This approximate expression yields some important insight into phenomena (termed here space-time dispersion effects) observed in the numerical simulations of Chapter 6, as now discussed.

Since the group velocity $v_g = 1/k_0'$, from equation 4.19, the z component of the group velocity is

$$v_{gz}(k_x,0) = v_g\cos\theta \tag{4.20}$$

which is also known as space-time focusing [144]. Space-time focusing refers to the change in the z-projected group velocity with the tilt angle of an off-axis plane wave component within the angular spectrum of the pulse and describes the natural curvature of the energy front in the spatio-temporal diffraction of a narrow pulse. The z component of the group velocity is plotted in Figure 4.3 versus transverse spatial frequency and wavelength ($\lambda = 2\pi c/\omega$). The group velocity as a function of

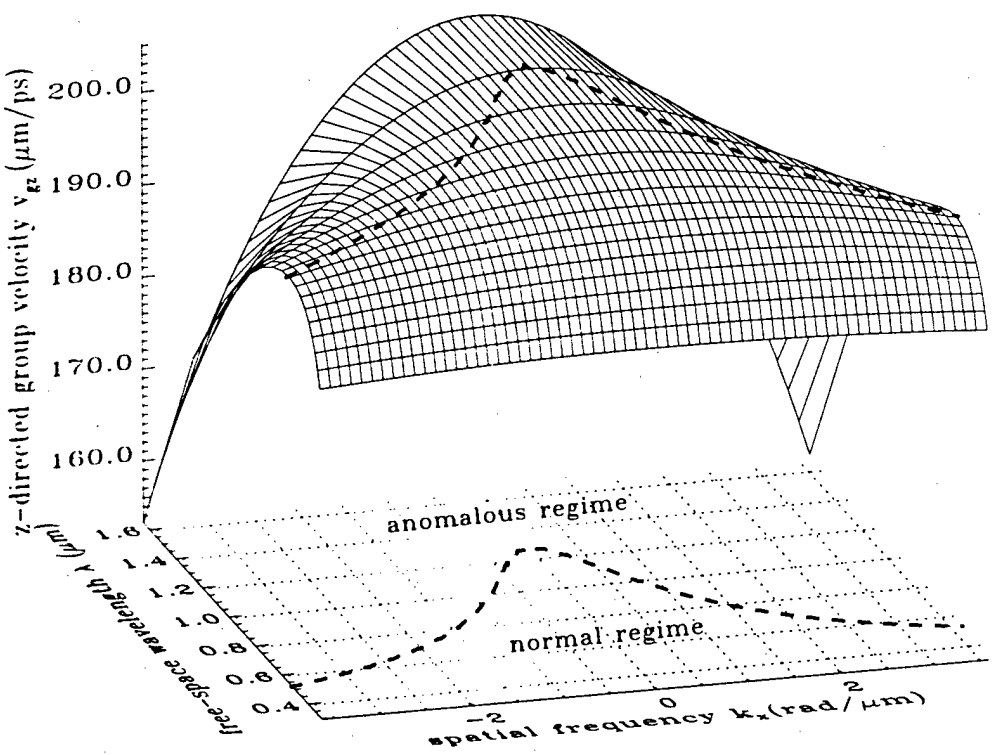

Figure 4.3: Spatio-temporal group velocity. This surface is calculated using the parameters of fused silica. The dashed curve separates the regions of anomalous and normal group-delay dispersion.

spatial and temporal frequency is given by the expression

$$v_{gz}(k_x,\omega) = \frac{k_z(k_x,\omega)}{k(\omega)k'(\omega)}, \tag{4.21}$$

where $\omega = \Delta\omega + \omega_0$. This expression is the inverse of the generalization of equation 4.17, which gives the group-delay at the central frequency ω_0. Note that in Figure 4.3, the group velocity is plotted versus wavelength instead of frequency.

Off-axis, the z-projected group delay dispersion coefficient k_z'' can be negative even when material dispersion dictates that $k''(\omega) > 0$. This occurs when

$$\tan\theta = \frac{k_x}{k_z} > \begin{cases} 0 & \text{for} \quad k''(\omega) <= 0 \\ \sqrt{k(\omega)k''(\omega)}/k'(\omega) & \text{for} \quad k''(\omega) > 0 \end{cases} . \tag{4.22}$$

The boundary between the normal ($k'' > 0$) and anomalous ($k'' < 0$) regimes is shown in Figure 4.3. An effective anomalous regime occurs because the curvature of the group velocity surface in the spatial-frequency direction varies along the temporal frequency direction. When the spatial frequency curvature is large for small temporal frequencies and small for large temporal frequencies, as is typically the case, a region of effective anomalous dispersion can exist, as illustrated in Figure 4.3. This effect may have ramifications for spatio-temporal solitary waves, such that a region where $k'' < 0$ may not be necessary for pulses with sufficient angular bandwidth, but will not be explored in this thesis. Note that this is a spatio-temporal effect and does not occur for purely temporal propagation.

For completeness, Figure 4.4 shows the z-projected group-delay dispersion surface $k_z''(k_x, \omega)$, where

$$k_z''(k_z, \omega) = \frac{k^3(\omega)k''(\omega) - k_x^2 k(\omega)k''(\omega) - k_x^2 k'^2(\omega)}{k_z^3(k_x, \omega)}, \tag{4.23}$$

is plotted as a function of wavelength. Figure 4.4 clearly shows the enlargement of the anomalous dispersion regime due to the

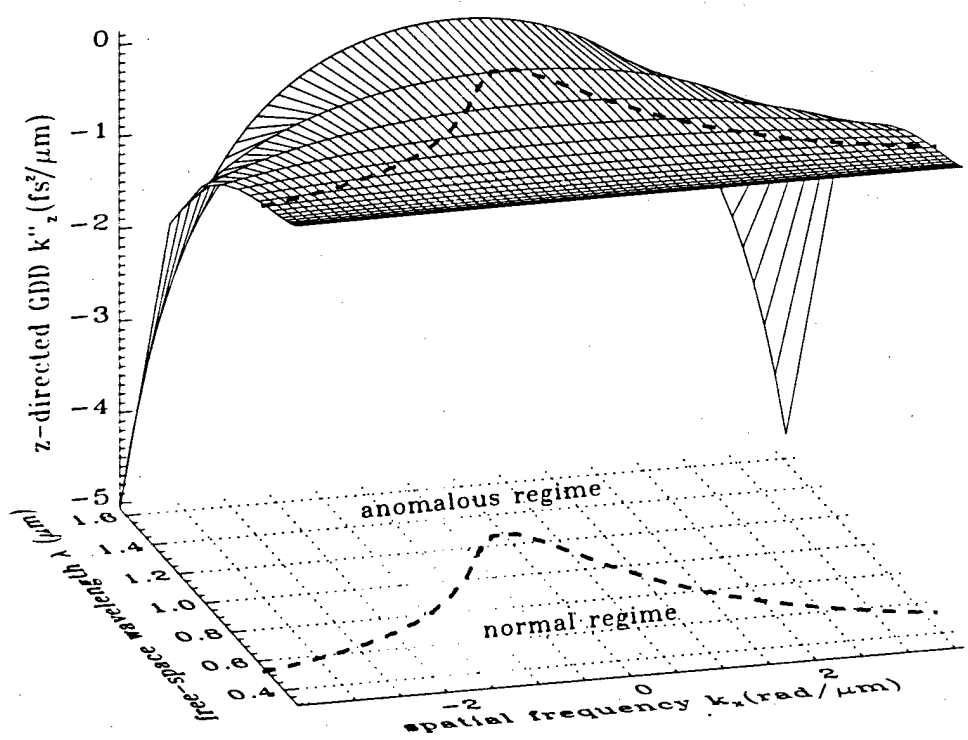

Figure 4.4: Spatio-temporal group-delay dispersion. This surface is calculated using the parameters of fused silica. The dashed curve separates the regions of anomalous and normal group-delay dispersion. Note that GDD is in units $fs^2/\mu m$ rather than $ps^2/\mu m$.

angular curvature of the momentum space. It is also evident that temporal broadening, which to first order is determined by the group-delay dispersion, varies off-axis. This is in large part due to the second-order space-time dispersion term obtained in the multiple-scales analysis, which is perhaps more appropriately referred to as the true space-time focusing term. In the anomalous regime, the projection of the wave onto the z-direction will broaden more with increasing angle, while in the normal

regime, the broadening will first decrease and then increase as the group-delay dispersion passes through zero with increasing angle. As a final note, the magnitude of z-projected third-order dispersion also changes dramatically with spatial frequency, as evident from the steepness of the group-delay dispersion surface at high spatial frequencies in the anomalous regime.

4.1.2 Linear Spatio-Temporal Propagation

This section briefly examines (2+1)-D linear spatio-temporal propagation in order to provide a graphical representation of the effects of space-time focusing. More detailed analysis of linear propagation is presented in Chapter 6. The initial condition for propagation is a transform-limited spatio-temporal wave whose shape is calculated numerically as the lowest-order eigenmode of the (2+1)-D NLS equation, and corresponds to the $\sigma = 0$ solution obtained in section 2.5, with normalized peak amplitude $U_0 = 1.94$. Using the same parameters as the simulations in Chapter 6 (i.e. $w_0 = 39.6\,\mu$m), the spatio-temporal wave has spatial full-width at half-maximum (FWHM) of 40.7 μm and temporal FWHM of 16.5 fs with central wavelength 1.55 μm, leading to fractional bandwidths of $\kappa \sim 0.01$ (not to be confused with the normalized interaction angle) and $\eta \sim 0.1$, respectively, which indicate that temporal (non-SVEA) effects will dominate.

Figure 4.5 shows the result of propagation over 7.5 confocal distances under the paraxial and SVEA approximations, as given by the (2+1)-D linear NLS equation,

$$2ik_0\frac{\partial A}{\partial z} + \frac{\partial^2 A}{\partial x^2} - k_0 k_0''\frac{\partial^2 A}{\partial T^2} = 0, \tag{4.24}$$

which only describes paraxial diffraction and group-delay dispersion. The (2+1)-D propagation geometry is illustrated in Figure 1.20, in which two spatio-temporal waves initially overlap at $z = 0$, with one propagating at an angle (dashed contours) such that the spatio-temporal frequency spectra are separated by twice the angular FWHM. This condition leads to a normalized interaction angle $\kappa = 2$, where κ is defined in section 5.1.1, and translates to approximately twice the linear resolvability angle, but is not exact because the waves are not Gaussian. The waves broaden by a factor of about 6.1 in each dimension after a distance of 7.5 Z_0, where the confocal distance Z_0 is defined as twice the distance over which the FWHM increases by a factor $\sqrt{2}$ in linear propagation. Because there is no space-time focusing, the energy fronts have no curvature or tilt.

For comparison, Figure 4.6 shows propagation under the same initial conditions but with the exact Fourier phase given by equation 4.12. In this case, the spatial broadening factor is 6.0, while the temporal broadening factor is 5.9. This slight asymmetry is expected because the governing equation is not symmetric in space and time. First-order space-time focusing is clearly shown in the on-axis spatio-temporal wave by the dashed curve, where the energy front is delayed (positive reduced times) for off-axis rays. The steepening of the leading edge (negative times) is also evident. This effect is the result of the interaction between anomalous group-delay dispersion and positive third-order dispersion.

The off-axis wave exhibits more complicated structure. The mean tilt angle corresponds to a spatial-frequency shift of about 0.07 rad/μm, which, from the group velocity and group-delay dispersion surfaces, produces a noticeable change in propagation parameters as shown in Figure 4.6. In addition to curvature of the energy front, the nonzero tilt of the wave also causes a delay of the central portion relative to the on-axis wave. The increase in the magnitude of z-projected group-delay dispersion with increasing angle, or second-order space-time dispersion, is evident from the figure as well by the visible increase in temporal broadening.

Because the parameters are the same as used for the spatio-temporal solitary wave simulations presented in Chapter 6, the higher-order linear effects observed here will be present in the nonlinear simulations as well. The present section also shows that the paraxial, SVEA NLS equation will not adequately describe spatio-temporal solitary wave propagation for the regime of interest.

4.1.3 The Linear Terms in the Higher-Order NLS equation

This section uses the exact expression for forward-going linear spatio-temporal propagation given by equations 4.11 and 4.12 in the reduced time coordinate frame in order to obtain the linear terms in the evolution equations derived in the previous chapters. This shows the equivalence between the descriptions in the Fourier domains and in the real-space domains and leads into the discussion of the split-step numerical method.

Ignoring evanescent waves, i.e. $k_x^2 + k_y^2 = k_T^2 < k^2(\Delta\omega + \omega_0)$, the z-directed momentum given by equation 4.12 can be approximated about $k_T = 0$

$$k_{rz} \approx k(\Delta\omega + \omega_0) - \frac{k_T^2}{2k(\Delta\omega + \omega_0)} - \frac{k_T^4}{8k^3(\Delta\omega + \omega_0)} - \Delta\omega k_0' \tag{4.25}$$

where only the first three terms of the Taylor expansion of the square-root are kept. The standard paraxial approximation keeps only the first two terms in the expansion; this approximation is made in the NLS equation. Retaining more terms in the

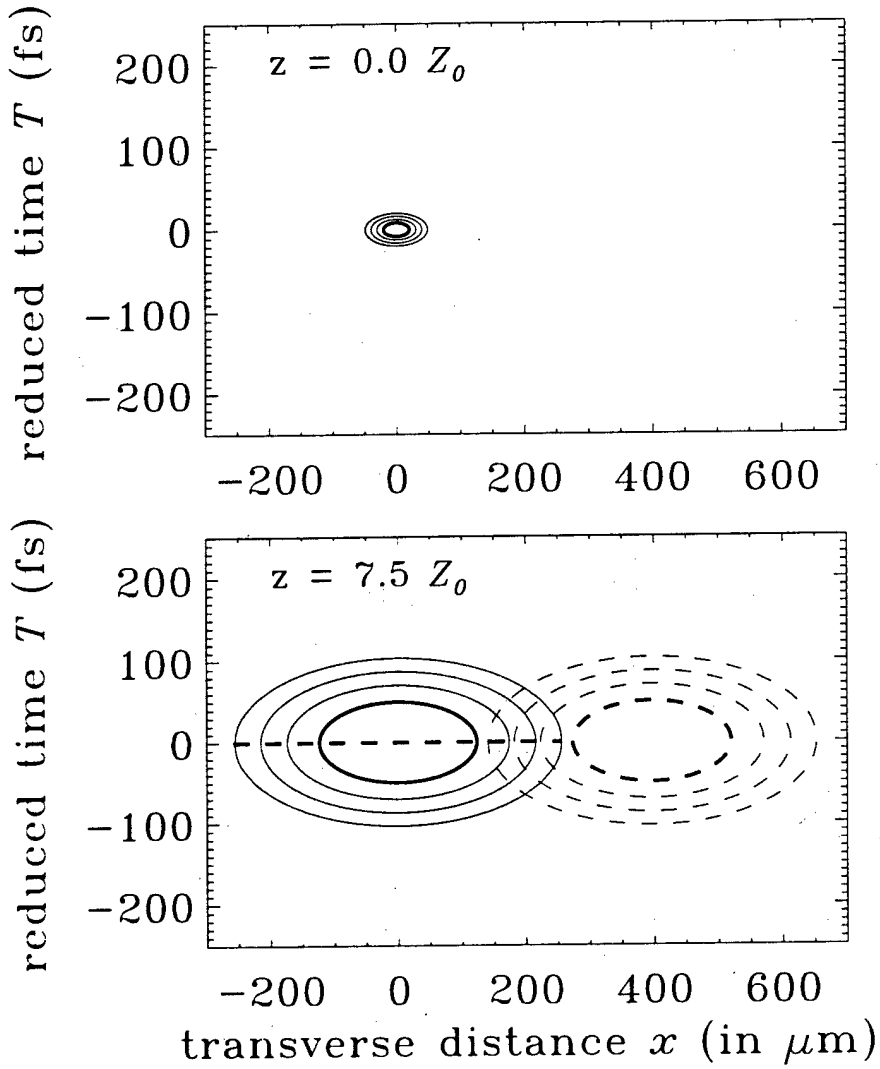

Figure 4.5: Linear diffraction under the paraxial and SVE approximations of initially overlapping spatio-temporal waves with tilted directions of propagation. The spatio-temporal waves of initial FWHM of 40.7 μm and 16.5 fs broaden to 247 μm and 99.8 fs after propagating 7.5 confocal distances. The dashed line indicates the position of the energy front (defined by the 1-D temporal centroid) across the spatial profile, and the contours are spaced by 3 dB intensity intervals.

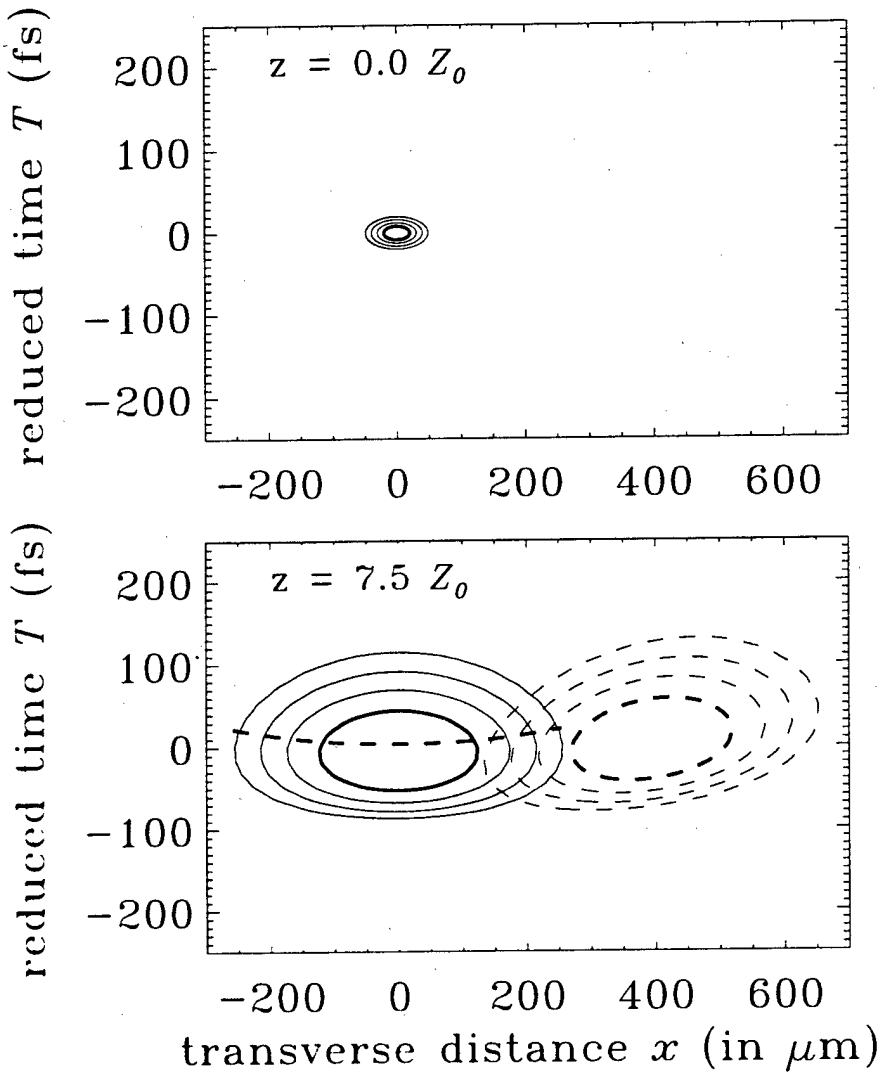

Figure 4.6: Fully non-paraxial and non-SVEA linear diffraction of two spatio-temporal waves, one tilted with respect to the axis of propagation. The on-axis spatio-temporal wave of initial FWHM of 40.7 μm and 16.5 fs broadens to 246 μm and 97.2 fs after propagating 7.5 confocal distances. The dashed curve indicates the position of the energy front (defined by the 1-D temporal centroid) across the spatial profile, and the contours are spaced by 3 dB intensity intervals.

expansion beyond the first two relaxes the paraxial approximation, but evanescent modes must be neglected in order for the expansion to converge. In this section, the first three terms will be kept in order to reproduce on a more intuitive basis the linear corrections to NLS that were obtained in Chapter 3.

Equation 4.25 still contains full linear dispersion. The slowly-varying envelope approximation (SVEA) assumes that the temporal variation of the envelope A is slow compared to the mean oscillation frequency ω_0. The frequency-domain interpretation is that the fractional bandwidth $\eta = \Delta\omega/\omega_0$, where $\Delta\omega$ is the FWHM of the spectral intensity envelope and ω_0 is the central frequency, is less than unity. These two measures are related by a factor called the time-bandwidth product. The dispersion relation only needs to be known over the frequency range in which the wavepacket spectrum $\tilde{A}$ is localized, implying that a Taylor expansion of the dispersion relation is sufficient. Thus the narrower the frequency width (or the longer the duration), the fewer terms in the Taylor expansion that need to be retained. The SVEA only keeps the first three terms in the dispersion relation, but the first five terms will be used in this analysis for comparison with the more complete derivation in Chapter 3:

$$k(\Delta\omega+\omega_0) \approx k_0 + \Delta\omega k_0' + \frac{1}{2}\Delta\omega^2 k_0'' + \frac{1}{6}\Delta\omega^3 k_0''' + \frac{1}{24}\Delta\omega^4 k_0'''', \tag{4.26}$$

which includes up to fourth-order dispersion. Using this expansion in equation 4.25 (which removes the mean group delay) and keeping terms only up to fourth power in k_T, $\Delta\omega$ and their products,

$$\begin{aligned} k_{rz} &\approx k_0 + \frac{1}{2}\Delta\omega^2 k_0'' + \frac{1}{6}\Delta\omega^3 k_0''' + \frac{1}{24}\Delta\omega^4 k_0'''' \\ &\quad - \frac{k_T^2}{2\left[k_0 + \Delta\omega k_0' + \frac{1}{2}\Delta\omega^2 k_0''\right]} - \frac{k_T^4}{8k_0^3} \\ &\approx k_0 + \frac{1}{2}\Delta\omega^2 k_0'' + \frac{1}{6}\Delta\omega^3 k_0''' + \frac{1}{24}\Delta\omega^4 k_0'''' \\ &\quad - \frac{k_T^2}{2k_0}\left[1 - \frac{\Delta\omega k_0'}{k_0} + \frac{\Delta\omega^2 k_0'^2}{k_0^2} - \frac{\Delta\omega^2 k_0''}{2k_0}\right] - \frac{k_T^4}{8k_0^3}. \end{aligned} \tag{4.27}$$

The terms obtained in addition to those present in standard NLS are third- and fourth-order dispersion, space-time dispersion and a non-paraxial correction.

The space-time dispersion terms from equation 4.27 can be written

$$\mathrm{STD} = \Delta\omega k_0'\left[1 + \frac{k_T^2}{2k_0^2}\right] - \Delta\omega k_0' + \frac{1}{2}\Delta\omega^2\left\{k_0'' + \frac{k_T^2}{2k_0^2}\left[k_0'' - 2\frac{k_0'^2}{k_0}\right]\right\}. \tag{4.28}$$

Noting that $k_T^2/k_0^2 = \sin^2\theta$ ($\approx \theta^2$ in the paraxial approximation) the terms are written

$$\mathrm{STD} = \Delta\omega\left[\frac{k_0'}{\cos\theta} - k_0'\right] + \frac{\Delta\omega^2}{2}\left[\frac{k_0''}{\cos\theta} - \sin^2\theta\frac{k_0'^2}{k_0}\right]. \tag{4.29}$$

To order θ^3, these terms are the same as the associated terms in equation 4.19. The first space-time dispersion term (called space-time focusing [144]) describes the off-axis variation in group delay in reduced coordinates while the second term describes the off-axis variation in group-delay dispersion. At this level of approximation, the region of anomalous group-delay dispersion is described by $\sin\theta \geq \sqrt{kk''}/k'$ when $k'' > 0$.

Concentrating for the moment only on the spatial-frequency terms in equation 4.27 results in,

$$k_z = k_0 - \frac{k_T^2}{2k_0} - \frac{k_T^4}{8k_0^3}. \tag{4.30}$$

Figure 4.7 shows a plot of the fully non-paraxial k-space, the paraxial approximation given by the first two terms of equation 4.30, and all three terms of equation 4.30. The figure clearly shows that the three-term expansion better approximates the exact k-surface than the two-term expansion given by the paraxial approximation, and is valid over much broader angular bandwidths.

In order to obtain the linear corrections to NLS in the real-space domain, equation 4.11 is written in differential form using the approximated k_{rz} from 4.27

$$\begin{aligned} \frac{\partial\bar{\bar{A}}}{\partial z} &= i\left\{k_0 + \frac{1}{2}\Delta\omega^2 k_0'' + \frac{1}{6}\Delta\omega^3 k_0''' + \frac{1}{24}\Delta\omega^4 k_0'''' \right. \\ &\quad \left. - \frac{k_T^2}{2k_0}\left[1 - \frac{\Delta\omega k_0'}{k_0} + \frac{\Delta\omega^2 k_0'^2}{k_0^2} - \frac{\Delta\omega^2 k_0''}{2k_0}\right] - \frac{k_T^4}{8k_0^3}\right\}\bar{\bar{A}}. \end{aligned} \tag{4.31}$$

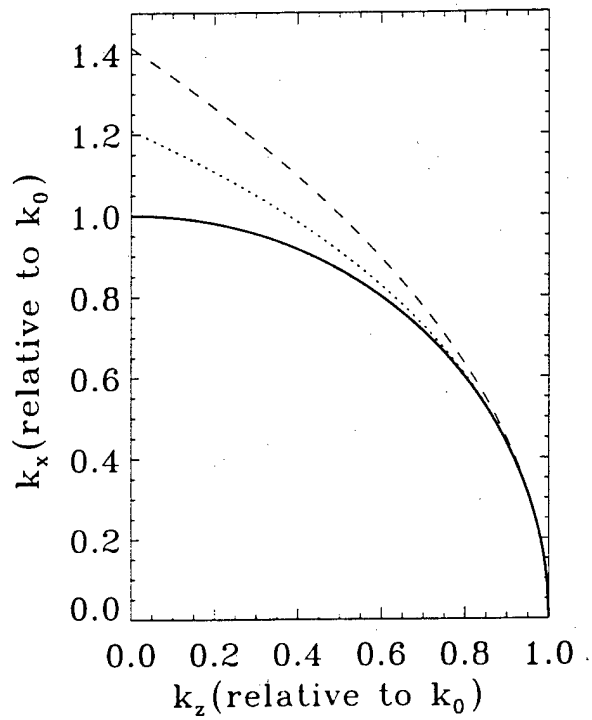

Figure 4.7: Illustration of the paraxial approximation. The solid curve is the exact k-space representation for isotropic media. The dashed curve is the paraxial approximation, while the dotted curve is the first-order correction to the paraxial approximation.

Inverse Fourier transforming leads to

$$\frac{\partial \overline{A}}{\partial z} = i\left\{k_0 - \frac{1}{2}k_0''\frac{\partial^2}{\partial T^2} - \frac{i}{6}k_0'''\frac{\partial^3}{\partial T^3} + \frac{1}{24}k_0''''\frac{\partial^4}{\partial T^4} + \frac{\nabla_T^2}{2k_0}\left[1 - i\frac{k_0'}{k_0}\frac{\partial}{\partial T} - \frac{k_0'^2}{k_0^2}\frac{\partial^2}{\partial T^2} + \frac{1}{2}\frac{k_0''}{k_0}\frac{\partial^2}{\partial T^2}\right] - \frac{\nabla_T^4}{8k_0^3}\right\}\overline{A}, \tag{4.32}$$

which is rewritten in more familiar form by making the transformation $\overline{A} \rightarrow A\exp(ik_0 z)$ to remove the fast propagation phase

$$2ik_0\frac{\partial A}{\partial z} + \nabla_T^2 A - k_0 k_0''\frac{\partial^2 A}{\partial T^2} - \frac{i}{3}k_0 k_0'''\frac{\partial^3 A}{\partial T^3} + \frac{1}{12}k_0 k_0''''\frac{\partial^4 A}{\partial T^4} + \nabla_T^2\left[-i\frac{k_0'}{k_0}\frac{\partial A}{\partial T} - \frac{k_0'^2}{k_0^2}\frac{\partial^2}{\partial T^2} + \frac{k_0''}{2k_0}\frac{\partial^2 A}{\partial T^2}\right] - \frac{\nabla_T^4 A}{4k_0^2} = 0 \tag{4.33}$$

which is the same as the linear part of equation 3.170 derived in Chapter 3.

4.2 Derivation of the Split-Step Method

The vector, higher-order nonlinear spatial 3.169 and spatio-temporal 3.170 wave equations can be written in the following notational form

$$\frac{\partial A_x}{\partial z} = i\hat{Q}A_x, \tag{4.34}$$

with a corresponding equation for A_y. Here, all linear and nonlinear effects are lumped into the operator $\hat{Q}$. The forward-going solution to equation 4.34 as a function of propagation distance z is written

$$A_x(z) = e^{i\int_0^z \hat{Q}(z')dz'}A_x(0), \tag{4.35}$$

where $A_x(0)$ is the initial value in space and time of the x-polarized envelope at $z = 0$.

Equation 4.35 can be examined more closely by writing the operator in terms of linear homogeneous and inhomogeneous parts $\hat{Q} = \hat{Q}^{\mathrm{L}} + \hat{Q}^{\mathrm{IH}}$. Choosing a small propagation distance Δz, and noting that $\hat{Q}^{\mathrm{L}}$ can be integrated directly, equation 4.35 reduces to

$$A_x(\Delta z) = e^{i\left[\Delta z \hat{Q}^{L} + \int_0^{\Delta z} \hat{Q}^{\mathrm{IH}}(z')dz'\right]} A_x(0). \tag{4.36}$$

The integral can be approximated to second-order accuracy in Δz

$$\begin{aligned}\int_0^{\Delta z} \hat{Q}^{\mathrm{IH}}(z')dz' &= \int_0^{\Delta z} \left\{ \hat{Q}^{\mathrm{IH}}(\Delta z/2) + \left[z' - \Delta z/2\right] \frac{\partial}{\partial z} \hat{Q}^{\mathrm{IH}}(\Delta z/2) + O(\Delta z^2) \right\} dz' \\ &= \hat{Q}^{\mathrm{IH}}(\Delta z/2)\Delta z + \frac{1}{2}\left[z' - \Delta z/2\right]^2 \Big|_0^{\Delta z} \frac{\partial}{\partial z} \hat{Q}^{\mathrm{IH}} + O(\Delta z^3) \\ &= \hat{Q}^{\mathrm{IH}}(\Delta z/2)\Delta z + O(\Delta z^3),\end{aligned} \tag{4.37}$$

so that the propagation equation becomes

$$A_x(\Delta z) = e^{i\Delta z\left[\hat{Q}^{L} + \hat{Q}^{\mathrm{IH}}(\Delta z/2)\right]} A_x(0). \tag{4.38}$$

Even though equation 4.37 is a second-order approximation to the integral of the nonlinear operator, there is no guarantee that the actual implementation is second-order accurate, since self-consistent envelopes at $\Delta z/2$ are unknown. The approximation used in the split-step method is that these values are determined by a $\Delta z/2$ linear propagation step, thus neglecting the nonlinear contribution. The result is that the nonlinear step is nominally first-order accurate, as shown in section 4.3.

The exponential can be rewritten in the well-known symmetrized form [232]

$$A_x(\Delta z) = e^{i\frac{\Delta z}{2}\hat{Q}^{L}} e^{i\Delta z \hat{Q}^{\mathrm{IH}}} e^{i\frac{\Delta z}{2}\hat{Q}^{L}} A_x(0), \tag{4.39}$$

which is second-order accurate in Δz and requires three operations for one longitudinal propagation step. This separation into linear and inhomogeneous steps is the main characteristic of the split-step method.

In order to verify the second-order accuracy of the splitting, the Taylor expansion of equation 4.39 is compared to that of equation 4.38. First Taylor-expanding equation 4.38 results in

$$\begin{aligned}e^{i\Delta z\left[\hat{Q}^{L} + \hat{Q}^{\mathrm{IH}}(\Delta z/2)\right]} = 1 + i\Delta z \left[\hat{Q}^{L} + \hat{Q}^{\mathrm{IH}}\left(\frac{\Delta z}{2}\right)\right] - \frac{\Delta z^2}{2}\Bigg[\hat{Q}^{L}\hat{Q}^{L} + \hat{Q}^{L}\hat{Q}^{\mathrm{IH}}\left(\frac{\Delta z}{2}\right) \\ + \hat{Q}^{\mathrm{IH}}\left(\frac{\Delta z}{2}\right)\hat{Q}^{L} + \hat{Q}^{\mathrm{IH}}\left(\frac{\Delta z}{2}\right)\hat{Q}^{\mathrm{IH}}\left(\frac{\Delta z}{2}\right)\Bigg] + O(\Delta z^3).\end{aligned} \tag{4.40}$$

The Taylor-expansion of the exponential operators in equation 4.39 to second-order is

$$\begin{aligned}e^{i\frac{\Delta z}{2}\hat{Q}^{L}} e^{i\Delta z \hat{Q}^{\mathrm{IH}}} e^{i\frac{\Delta z}{2}\hat{Q}^{L}} &= \left[1 + i\frac{\Delta z}{2}\hat{Q}^{L} - \frac{\Delta z^2}{8}\hat{Q}^{L}\hat{Q}^{L} + O(\Delta z^3)\right] \times \\ &\quad \left[1 + i\Delta z \hat{Q}^{\mathrm{IH}}\left(\frac{\Delta z}{2}\right) - \frac{\Delta z^2}{2}\hat{Q}^{\mathrm{IH}}\left(\frac{\Delta z}{2}\right)\hat{Q}^{\mathrm{IH}}\left(\frac{\Delta z}{2}\right) + O(\Delta z^3)\right] \times \\ &\quad \left[1 + i\frac{\Delta z}{2}\hat{Q}^{L} - \frac{\Delta z^2}{8}\hat{Q}^{L}\hat{Q}^{L} + O(\Delta z^3)\right] \\ &= 1 + i\Delta z\left[\hat{Q}^{L} + \hat{Q}^{\mathrm{IH}}\left(\frac{\Delta z}{2}\right)\right] - \frac{\Delta z^2}{2}\Bigg[\hat{Q}^{L}\hat{Q}^{L} + \hat{Q}^{L}\hat{Q}^{\mathrm{IH}}\left(\frac{\Delta z}{2}\right) \\ &\quad + \hat{Q}^{\mathrm{IH}}\left(\frac{\Delta z}{2}\right)\hat{Q}^{L} + \hat{Q}^{\mathrm{IH}}\left(\frac{\Delta z}{2}\right)\hat{Q}^{\mathrm{IH}}\left(\frac{\Delta z}{2}\right)\Bigg] + O(\Delta z^3).\end{aligned} \tag{4.41}$$

Since both of these expansions are the same to order Δz^2, the symmetrized representation 4.39 retains the second-order accuracy of equation 4.38.

It is clear from the discussion of section 4.1 that the linear operator is most naturally applied in the Fourier domain, where time derivatives are converted into temporal frequency and space derivatives are converted into spatial frequencies. As a result, the linear propagation steps are evaluated in the Fourier domain as follows,

$$e^{i\frac{\Delta z}{2}\hat{Q}^{L}} A_x(0) = \mathcal{F}^{-1}\left\{e^{i\frac{\Delta z}{2}\tilde{Q}^{L}} \tilde{A}_x(0)\right\}, \tag{4.42}$$

where $\mathcal{F}^{-1}$ is the inverse-Fourier transform operation, and $\tilde{Q}^{\mathrm{L}}$ is the Fourier phase function as given by equation 4.12 or 4.27 for example.

Now that the symmetrized representation is established, one further point needs to be addressed at this time. Propagation over some distance occurs in steps of size Δz. From equation 4.39, propagation over $2\Delta z$ is described by

$$\begin{aligned} A_x(2\Delta z) &= e^{i\frac{\Delta z}{2}\hat{Q}^{\mathrm{L}}} e^{i\Delta z\hat{Q}^{\mathrm{IH}}} e^{i\frac{\Delta z}{2}\hat{Q}^{\mathrm{L}}} e^{i\frac{\Delta z}{2}\hat{Q}^{\mathrm{L}}} e^{i\Delta z\hat{Q}^{\mathrm{IH}}} e^{i\frac{\Delta z}{2}\hat{Q}^{\mathrm{L}}} A_x(0) \\ &= e^{i\frac{\Delta z}{2}\hat{Q}^{\mathrm{L}}} e^{i\Delta z\hat{Q}^{\mathrm{IH}}} e^{i\Delta z\hat{Q}^{\mathrm{L}}} e^{i\Delta z\hat{Q}^{\mathrm{IH}}} e^{i\frac{\Delta z}{2}\hat{Q}^{\mathrm{L}}} A_x(0), \end{aligned} \tag{4.43}$$

which only requires five operations instead of six, because the two adjacent half-step linear operations coalesce into one full-step linear operation, as shown in Figure 4.1. In general then, for N steps of size Δz, the total number of operations is $2N+1$, instead of $3N$ as suggested by equation 4.39.

The following section will examine the special case of spatial propagation appropriate for (1+1)-D spatial solitons in slab waveguides with the split-step method. The generalization to the (2+1)-D spatio-temporal method is considered in section 4.2.2.

4.2.1 Nonlinear Spatial Propagation

The (1+1)-D nonlinear evolution equation appropriate for the spatial soliton studies presented in Chapter 5 is given by equation 3.169, repeated here for convenience:

$$\begin{aligned} 2ik_0\frac{\partial A_x}{\partial z} + ik_0\alpha_0 A_x + \frac{\partial^2 A_x}{\partial x^2} - \frac{1}{4k_0^2}\frac{\partial^4 A_x}{\partial x^4} \\ + 2k_0^2\frac{n_2}{n_0}\left\{[1+iK]\,|A_x|^2 A_x + 2\,[\Delta + iK\Delta_K]\,|A_y|^2 A_x\right\} = 0, \end{aligned} \tag{4.44}$$

where the non-paraxial nonlinear terms have been neglected due to weak nonlinearity, and the vector four-wave mixing term neglected under the assumption of short waveguide birefringence beat length. The transverse y dimension is not considered due to linear confinement by a slab waveguide. For simplicity, this equation does not include the modal-averaged coefficients due to lateral confinement as derived in Appendix C.

Using equation 4.34, the linear and inhomogeneous split-step operators can be written

$$\begin{aligned} \hat{Q}^{\mathrm{L}} &= \frac{1}{2k_0}\frac{\partial^2}{\partial x^2} - \frac{1}{8k_0^3}\frac{\partial^4}{\partial x^4} + i\frac{\alpha_0}{2} \approx \sqrt{k_0\left[k_0 + i\alpha_0\right] + \frac{\partial^2}{\partial x^2}} - k_0 \\ \tilde{Q}^{\mathrm{L}} &= k_z = \sqrt{k_0\left[k_0 + i\alpha_0\right] - k_x^2} - k_0. \end{aligned} \tag{4.45}$$

$$\hat{Q}^{\mathrm{IH}} = k_f n_2\left\{[1+iK]\,|A_x|^2 + 2\,[\Delta + iK\Delta_K]\,|A_y|^2\right\}. \tag{4.46}$$

Here, the expressions within the square-root are the exact (assuming weak absorption) operator and Fourier phase representations of linear spatial diffraction. A similar result was obtained previously [233], with a different, but equivalent, form of the linear non-paraxial operator. That work did not consider the nonlinear, non-paraxial terms that were derived in Chapter 3, but subsequent extensions [234] did consider those terms for a purely linear, spatially-varying refractive index. As mentioned before, the nonlinearly-induced index for the present studies is small enough that these terms can be neglected.

For correctness with off-axis plane wave components, the linear absorption term must be applied in the Fourier domain; however, these effects occur well beyond the order of the multiple-scales analysis in Chapter 3 due to the assumed order ε^3 smallness of the coefficient α_0. A constant (with respect to angle) absorption, which can be brought outside the square-root, can be applied in either the Fourier or real-space domain because of Parseval's theorem. It is more convenient (and more correct in terms of the precise behavior in the attenuation of off-axis energy flow) in the numerics to apply this term in the Fourier domain, because, if applied in the real-space domain along with nonlinearity, there is an ambiguity whether to attenuate the envelope before or after calculating the nonlinear effect. Two-photon absorption must be applied in the real-space domain along with nonlinear refraction.

4.2.2 Nonlinear Spatio-Temporal Propagation

The (2+1)-D spatio-temporal nonlinear evolution equation used in the simulations of Chapter 6 was derived in Chapter 3. Using the full Raman response in equation 3.170 results in:

$$2ik_0\frac{\partial A_x}{\partial z} + ik_0\alpha_0 A_x + \frac{\partial^2 A_x}{\partial x^2} - k_0 k_0''\frac{\partial^2 A_x}{\partial T^2} - \frac{i}{3}k_0 k_0'''\frac{\partial^3 A_x}{\partial T^3} - i\frac{k_0'}{k_0}\frac{\partial^3 A_x}{\partial T\partial x^2} \tag{4.47}$$

$$
\begin{aligned}
&+\frac{1}{12}k_0k_0''''\frac{\partial^4 A_x}{\partial T^4}+2k_0^2\frac{n_K}{n_0}\left[1+i\frac{n_2}{n_K}K\right]\left[|A_x|^2+2\Delta_K|A_y|^2\right]A_x\\
&+4ik_fn_K\left[1+i\frac{n_2}{n_K}K\right]\left[\frac{n_0}{c}-\frac{k_0'}{2}\right]\frac{\partial}{\partial T}\left[|A_x|^2A_x+2\Delta_K|A_y|^2A_x\right]\\
&+\frac{k_f}{2}\left\{k_f+i\frac{2}{n_0}\left[\frac{n_0}{c}-\frac{k_0'}{2}\right]\frac{\partial}{\partial T}\right\}\left[\int_0^\infty R_R(\tau)\,|A_x(T-\tau)|^2A_xd\tau\right.\\
&\qquad\qquad+\Delta_R\int_0^\infty R_R(\tau)\,|A_y(T-\tau)|^2A_xd\tau\\
&\qquad\qquad\left.+\gamma_R\int_0^\infty R_R(\tau)A_y^*(T-\tau)A_x(T-\tau)A_yd\tau\right]\\
&+2k_0^2\frac{n_4}{n_0}\left\{1+\frac{n_4^{\text{casc}}}{n_4}-\frac{1}{2}\frac{n_2^2}{n_0n_4}\right\}|A_x|^4A_x\\
&+2k_0^2\frac{n_4}{n_0}\left\{\frac{3}{5}+\gamma_K\left[2\Delta_K+\gamma_K\right]\frac{n_4^{\text{casc}}}{n_4}-\frac{1}{2}\left[4\Delta^2-\gamma^2\right]\frac{n_2^2}{n_0n_4}\right\}|A_y|^4A_x\\
&+2k_0^2\frac{n_4}{n_0}\left\{\frac{6}{5}+2\Delta_K\left[2\Delta_K+\gamma_K\right]\frac{n_4^{\text{casc}}}{n_4}-\left[2\Delta+\gamma^2\right]\frac{n_2^2}{n_0n_4}\right\}|A_x|^2|A_y|^2A_x=0.
\end{aligned}
$$

The full Raman response is used in the numerics because the spectral bandwidth of the spatio-temporal waves used in the simulations exceeds the bandwidth of the Raman gain spectrum.

The linear operator is written

$$
\begin{aligned}
\hat{Q}^{\text{L}}&=\frac{1}{2k_0}\frac{\partial^2}{\partial x^2}-\frac{k_0''}{2}\frac{\partial^2}{\partial T^2}-i\frac{k_0'''}{6}\frac{\partial^3}{\partial T^3}-i\frac{k_0'}{2k_0^2}\frac{\partial^3}{\partial T\partial x^2}+\frac{k_0''''}{24}\frac{\partial^4}{\partial T^4}+i\frac{\alpha_0}{2}\\
&\approx\sqrt{k\left(\omega_0+i\frac{\partial}{\partial T}\right)\left[k\left(\omega_0+i\frac{\partial}{\partial T}\right)+i\alpha\left(\omega_0+i\frac{\partial}{\partial T}\right)\right]+\frac{\partial^2}{\partial x^2}}-ik_0'\frac{\partial}{\partial T}-k_0.
\end{aligned}
\tag{4.48}
$$

Since the linear exponential operator is applied in the Fourier domain, resulting in an exponential phase function, the linear propagation phase is written

$$
\tilde{Q}^{\text{L}}=\sqrt{k(\Delta\omega+\omega_0)\left[k(\Delta\omega+\omega_0)+i\alpha(\Delta\omega+\omega_0)\right]-k_x^2}-\Delta\omega k_0'-k_0,
\tag{4.49}
$$

which is the exact linear phase k_{rz} as discussed in section 4.1 with the inclusion of weak linear absorption, but only strictly valid here when $k_x < k(\Delta\omega+\omega_0)$ because of the addition of the nonlinear terms.

The argument of the nonlinear exponential operator is defined

$$
\hat{Q}^{\text{NL}}=\frac{1}{A_x}\left\{k_f\text{NL}_2+k_f\text{NL}_4+i\frac{2}{n_0}\left[\frac{n_0}{c}-\frac{k_0'}{2}\right]\frac{\partial\text{NL}_2}{\partial T}\right\},
\tag{4.50}
$$

and is applied in the real-space domain. The factor $1/A_x$ is used to handle those nonlinear terms which cannot otherwise be written in the form of equation 4.34, such as the last Raman term and the Kerr cross-phase modulation and all Raman terms in the first-order shock. This factor serves to remove any fast phase variation (due to nonlinear refraction) from the nonlinear terms, which are grouped as follows:

$$
\begin{aligned}
\text{NL}_2=&\,n_K\left[1+i\frac{n_2}{n_K}K\right]\left[|A_x|^2+2\Delta_K|A_y|^2\right]A_x\\
&+\frac{1}{4n_0}\int_0^\infty R_R(\tau)\,|A_x(T-\tau)|^2A_xd\tau\\
&+\frac{\Delta_R}{4n_0}\int_0^\infty R_R(\tau)\,|A_y(T-\tau)|^2A_xd\tau\\
&+\frac{\gamma_R}{4n_0}\int_0^\infty R_R(\tau)A_y^*(T-\tau)A_x(T-\tau)A_yd\tau,
\end{aligned}
\tag{4.51}
$$

$$
\text{NL}_4=n_4\left\{1+\frac{n_4^{\text{casc}}}{n_4}-\frac{1}{2}\frac{n_2^2}{n_0n_4}\right\}|A_x|^4A_x
\tag{4.52}
$$

$$+ n_4 \left\{ \frac{3}{5} + \gamma_K \left[2\Delta_K + \gamma_K \right] \frac{n_4^{\text{casc}}}{n_4} - \frac{1}{2} \left[4\Delta^2 - \gamma^2 \right] \frac{n_2^2}{n_0 n_4} \right\} |A_y|^4 A_x$$
$$+ n_4 \left\{ \frac{6}{5} + 2\Delta_K \left[2\Delta_K + \gamma_K \right] \frac{n_4^{\text{casc}}}{n_4} - \left[2\Delta + \gamma^2 \right] \frac{n_2^2}{n_0 n_4} \right\} |A_x|^2 |A_y|^2 A_x.$$

Note that the factor $1/A_x$ cancels out from some of the terms in NL_2 and all of the terms in NL_4.

The nonlinear "index" produced by the last Raman term is proportional to the factor

$$\frac{A_y}{A_x} = \frac{|A_y|}{|A_x|} e^{i[\phi_y - \phi_x]}. \tag{4.53}$$

Since all fast variations, such as the propagation phase, have been removed, ϕ_y and ϕ_x (and thus their difference) have at most order ε^2 variation. The amplitude ratio serves as a normalizing factor to properly scale the size of the third Raman term in proportion to the first and second.

The convolutional Raman response integrals of the intensity are evaluated using an equivalent Fourier identity, but it should be noted that the resultant Fourier domain is different than the conventional temporal Fourier domain of the fields since it is defined as the transform of the intensity. For example,

$$\int_0^\infty R_R(\tau) \, |A_x(T-\tau)|^2 A_x d\tau = \mathcal{F}^{-1} \left\{ \chi_R(\Omega) \mathcal{F} \left\{ |A_x|^2 \right\} \right\} A_x, \tag{4.54}$$

where $\chi_R(\Omega)$ is the Raman susceptibility, approximated by a single Lorentzian resonance

$$\chi_R(\Omega) = \frac{R_0}{\Omega_f^2 - \Omega^2 - i\Omega\gamma}. \tag{4.55}$$

Stimulated Raman scattering is discussed in Appendix B.

4.3 Implementation and Accuracy of the Split-Step Method

The derivation of the split-step method indicated that the operator splitting given by equation 4.39 was second-order accurate in step-size Δz. In addition, the midpoint method used to evaluate the longitudinal integral of the nonlinear operator, as given by equation 4.37, is also second-order accurate, but relies on the knowledge of the field at the midpoint position, which is only approximately provided by the half-step of linear propagation. As a result, when the magnitude of the field changes sufficiently rapidly due to absorption, diffraction, etc., the accuracy of the entire method may scale with step-size worse than quadratically. The reason for this is that self-consistency is not strictly maintained since linear and nonlinear propagation are handled separately, meaning that the nonlinear phase accumulated over the interval Δz may not be properly accounted for.

A simple, intuitive explanation is provided by the consideration of the propagation of a spatial soliton using the split-step method. Starting with an initially transform-limited beam, the first half-step of linear diffraction results in broadening, or defocusing. The subsequent full nonlinear step, based on a slightly erroneous field value, imparts a focusing quadratic phase that over-compensates the phase curvature accumulated during the half step. The next full linear step first results in focusing to a waist (close to the original soliton form), and then broadening. This process is repeated over the entire propagation distance. It is clear that the beam approximately returns to its original soliton form only at distances which are multiples of the step size, and defocuses and refocuses in between. The actual error arises from the fact that the nonlinear phase is applied based on an approximate value for the field determined by linear propagation. The result is that the nonlinear phase may be no more accurate than a simple, first-order, forward Euler scheme.

The easiest way to numerically determine the order of accuracy of an algorithm is to compare the results of simulation with varying step size with that of "the best" simulation (i.e. using a very small step size). Another approach is to compare the results of simulation with an analytic solution, from which additional information can be gleaned, such as the absolute accuracy of the simulation, including the algorithm and model. This is a straightforward procedure when using solitons because the exact solution (in 1-D) is known and doesn't change (except for the usually unimportant nonlinearly-induced phase) with propagation. Both methods are used here.

In the following sections, numerical accuracy will be determined for various situations for both (1+1)-D spatial and (2+1)-D spatio-temporal propagation. For each case, the normalized root-mean square, or RMS, error is calculated between the test simulation and the reference:

$$\varepsilon = \frac{\sqrt{\Sigma \left| |A^{\text{test}}| - |A^{\text{ref}}| \right|^2}}{\Sigma |A^{\text{ref}}|}, \tag{4.56}$$

where the field amplitude A^{test} is calculated as a function of longitudinal step size.

4.3.1 (1+1)-D Spatial

Figure 4.8 shows how the numerical accuracy scales with step size for a single soliton propagating without absorption. The

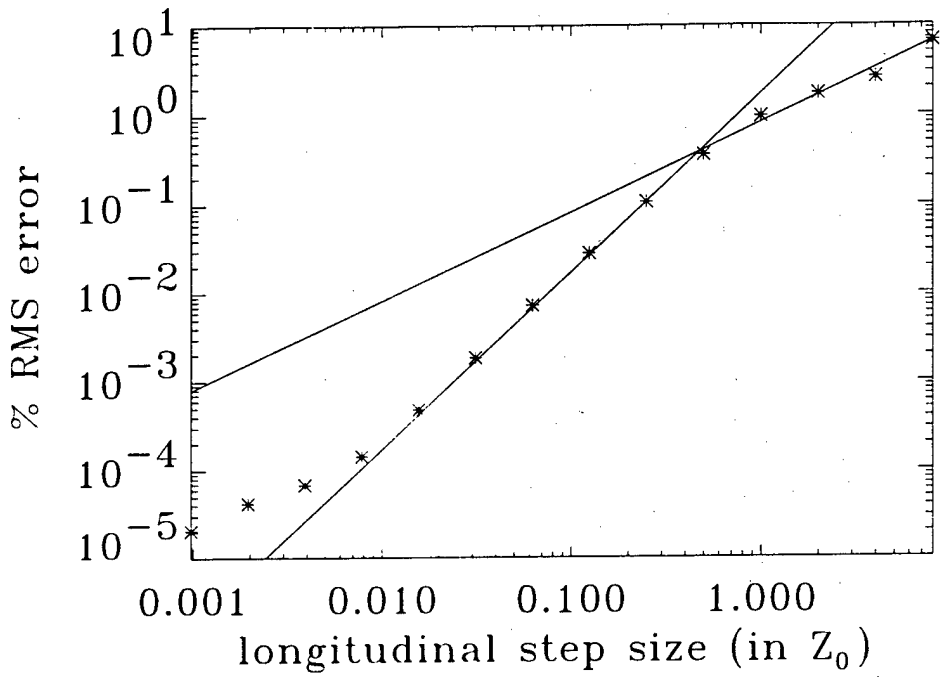

Figure 4.8: Plot of percentage RMS error as a function of step size for the propagation of a single spatial soliton without absorption using the split-step method. The data points represent results from the simulations while the lines represent error scalings of first and second order.

smallest step-size plotted in the figure is $\Delta z = Z_0/1024$, and the "exact" solution to which the others are compared is the result obtained when $\Delta z = Z_0/2048$. The longitudinal step size is written in terms of the confocal distance Z_0 because the Raleigh range $Z_0/2$ is generally considered as the distance over which noticeable changes of the wave appear in linear propagation. Therefore, the linear longitudinal steps in the split-step method must occur over distances much shorter than Z_0.

The simulation is performed using the initial field profile $\mathrm{sech}(x/w_0)$, where $w_0 = 17.3\ \mu$m, resulting in a spatial full-width at half-maximum (FWHM) of 30.5 μm, meaning that the paraxial approximation is valid because the fractional angular bandwidth $\kappa = 0.01$. The propagation distance is 10 Z_0. As shown in the figure, for large step sizes, the error decreases linearly with decreasing step size. In addition, as step size decreases phase this linear region, there is a large region over which the error scales quadratically, as naively expected. Finally, at the smallest step sizes, the scaling approaches linear again. The important point to note is that there is a large region over which second-order accuracy is obtained. This result thus verifies the order of the numerical method when stationary propagation is considered, but does not address the absolute accuracy when compared to the exact analytical solution or the order of the method for non-stationary propagation, which may be different.

The comparison between the numerical method with the theoretical soliton solution without absorption is shown in Figure 4.9. This figure illustrates the same behavior as shown in Figure 4.8, except for the presence of a distinct error floor beyond which the simulation can be no more accurate. It therefore makes no sense to decrease the longitudinal step-size below that which reaches the error floor.

The error floor is the result of discretization in the transverse dimension. Like the continuous NLS equation, the discretized NLS equation used in the numerics possesses a set of eigenmode solutions, which are different than their continuous counterparts. The numerical simulation is started with an eigenmode of the continuous NLS equation, which then evolves to an eigenmode of the discretized equation during propagation, leading to the absolute error shown. For the results of Figure 4.9, the 1024 element computational grid allows for 55 samples under the transverse spatial full-width at half-maximum (FWHM), and 6 samples under the spatial-frequency FWHM, resulting in an error floor of $4 \times 10^{-4}\%$, as shown in the figure. Increasing the computational grid to 8192 elements and simultaneously decreasing the transverse sampling interval by a factor of 4,

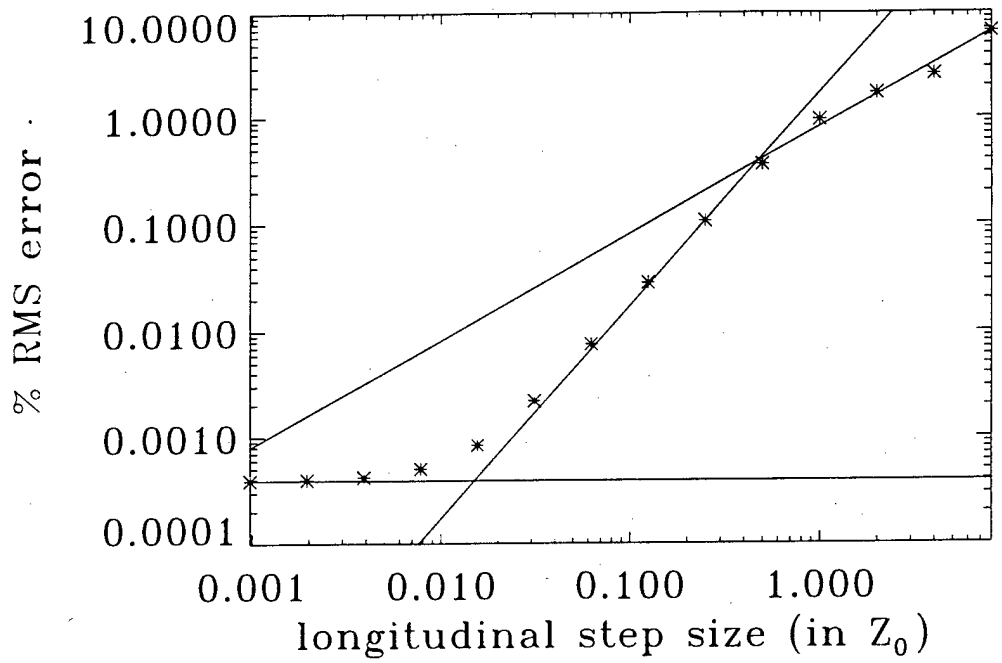

Figure 4.9: Plot of percentage RMS error between split-step simulation and the exact analytic form in the propagation of a single spatial soliton. The error decreases quadratically with step size, then reaches a floor at about $4 \times 10^{-4}\%$. The lines represent zeroth, first, and second order scalings.

with 221 samples under the spatial FWHM and 12 samples under the spatial-frequency FWHM, decreases the error floor to $2 \times 10^{-4}\%$. As the number of transverse samples becomes larger, the eigenmode of the discretized equations approaches that of the continuous equation, resulting in a decrease of the error. It is also found that increasing the number of samples under the spatial-frequency FWHM has little effect on the error.

In Chapter 5, simulations are performed in which the interaction between two spatial solitons of different widths is studied. It is therefore necessary to evaluate the error as the soliton width decreases, such that propagation no longer satisfies the paraxial approximation. Figure 4.10 plots error as a function of step-size for a pump soliton width $w_p = 2.16\ \mu$m, or FWHM 3.81 μm, with fractional angular bandwidth $\kappa = 0.1$. In addition, the induced third-order nonlinear fractional index $\nu_2 \sim 0.1$, and the propagation distance is 10 Z_0, where Z_0 is the confocal distance of the signal soliton of width $w_0 = 17.3\ \mu$m. Now, the step size is written in terms of the confocal distance of the pump, or Z_p, where $Z_0 = [w_0/w_p]^2 Z_p = 64\ Z_p$. Again, as shown in the figure, there is a region where the error decreases quadratically with step size, but now the error floor is significantly greater at 0.04%, but is still acceptable for most situations. The simulation is performed on a 2048 element grid with 14 samples under the spatial FWHM and 47 samples under the spatial frequency FWHM. Increasing the grid size to 8192 elements (with 55 and 47 samples respectively), reduces the error floor to 0.02%, a significant decrease, but still two-orders of magnitude higher than the fully paraxial case.

In this case, the transverse sampling is not the limiting factor. The main limitation is the fact that the simulation was performed with a soliton width that leads to non-paraxial propagation. Even though the linear non-paraxial corrections are included in the simulation, the scalings for κ and ν indicate that the nonlinear, non-paraxial terms are of about the same size as the first linear non-paraxial correction, and should be included as well. As shown in section 2.3.1, the fully non-paraxial, but also non-vectorial, spatial soliton solution is the same as the paraxial soliton, except for an unimportant nonlinear phase factor, and is only valid when all relevant non-paraxial terms in the evolution equation are retained, which is not the case here for simplicity.

These results indicate that the accuracy of the slit-step method scales second-order with longitudinal step size for stationary propagation. The accuracy must also be determined when attenuation due to linear and two-photon absorption is considered. In this case, absorption causes broadening of the soliton, as discussed in Chapter 5. Linear absorption is applied in the Fourier domain along with diffraction and is not expected to alter the order of the algorithm. Two-photon absorption, on the other hand,

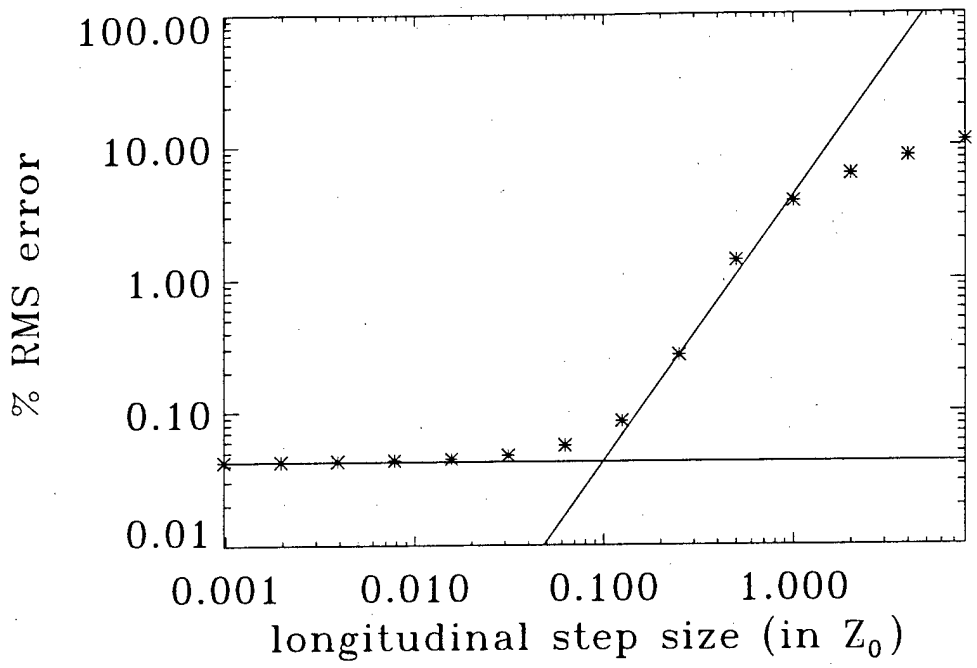

Figure 4.10: Plot of percentage RMS error between split-step simulation and the exact analytic form in the propagation of a single spatial soliton in violation of the paraxial approximation. The error decreases quadratically with step size, then reaches a floor at about 0.04%. The lines represent zeroth and second order scalings.

is applied in the real-space domain along with nonlinear refraction. Since two-photon absorption alters the amplitude based upon the approximate field, it is possible that the accuracy of the split-step method scales less than quadratically. Aside from absorption, the parameters of these simulations are the same as those used in generating the data of Figure 4.10.

Figure 4.11 shows that the error in fact decreases quadratically until the floor is reached, the same scaling as before. The analytic solution used as the reference is obtained in section 5.3, but is only approximate. The small error floor (some of which is due to non-paraxial propagation before broadening occurs) verifies that the analytic approximation is a good one. For all single soliton simulations, at most 256 steps per Z_p are sufficient to reach the error floor.

The final simulations to consider are those of the spatial soliton dragging interaction. During interaction, the soliton shapes can change considerably, therefore it is not expected that the accuracy will scale second-order with step size. This is confirmed in Figure 4.12, which shows that the accuracy is approximately order one-half, although there are small regions over which the error scales linearly with step size. Absolute accuracy can no longer be obtained because no analytic solutions exist to the vectorial NLS equations for non-unity cross-phase modulation coefficient. The reference solution is obtained numerically with longitudinal step size $\Delta z = Z_0/2048$, as before. Because the simulation is paraxial, with $w_0 = 17.3\ \mu$m for each soliton, only 1024 transverse samples are used, with 55 samples across the spatial FWHM.

Figure 4.13 shows the accuracy when the pump soliton propagates in the non-paraxial regime. Here, $w_p = 2.16\ \mu$m, the transverse grid is of size 2048, and the propagation distance is 10 Z_0, as before. Even though the overall accuracy scales approximately as order one-half, there is a region over which the scaling is order three-halves. There are similar regions in the paraxial simulation of Figure 4.13 as noted, but these region are less pronounced.

The most important data obtained in the soliton interaction simulations of Chapters 5 and 6 is the contrast ratio of the logic gate under various input conditions. The contrast ratio is not strongly sensitive to small variations in the fields at the output of the gate, so it will depend weakly on the accuracy of the simulation. The contrast of a gate is generally considered acceptable when it exceeds a given threshold. By how much it exceeds a given threshold is not important, therefore, some inaccuracy in the calculation of the contrast can be tolerated. As a result, the spatial soliton interaction simulations of Chapter 5 use a longitudinal step-size of $\Delta z = Z_p/256$, as mentioned in the single soliton results.

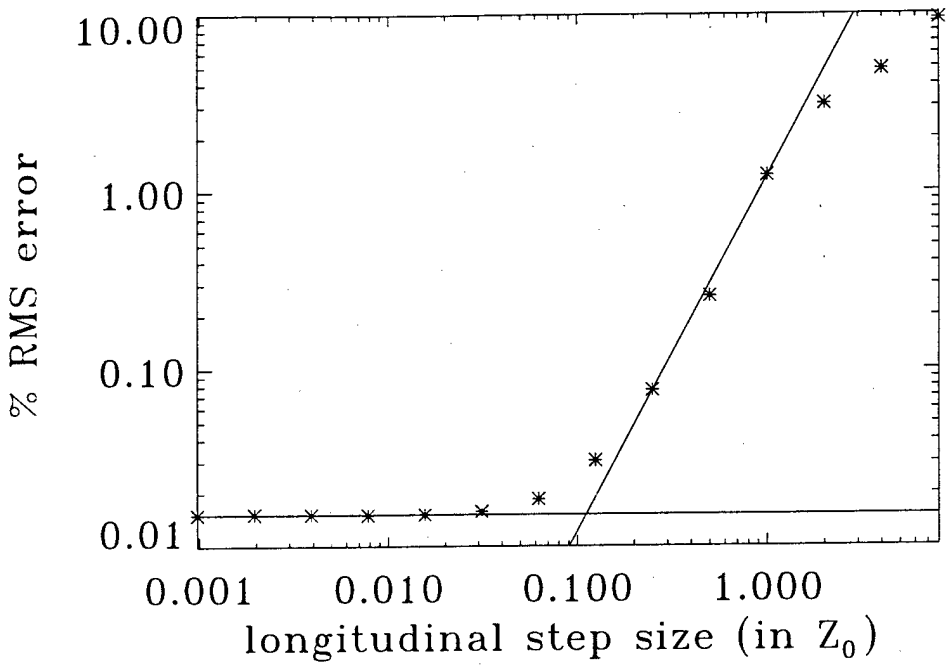

Figure 4.11: Plot of percentage RMS error between split-step simulation and the approximate analytic form in the propagation of a single spatial soliton with linear and two-photon absorption. The error decreases quadratically until it reaches a floor at about 0.02%. The lines represent zeroth and second order scalings.

4.3.2 (2+1)-D Spatio-Temporal

It is expected that the accuracy of the split-step method for (2+1)-D spatio-temporal propagation is similar to that for (1+1)-D spatial propagation. Because of the time-consuming nature of multi-dimensional simulations, this behavior is illustrated in this section using the results of two simulations. The grid size for both simulations is 1024 by 1024, with 20 samples across the spatial FWHM and 14 samples across the temporal FWHM. Most of the computational grid is unused, but the size and sampling are set to be consistent for the more general simulations of Chapter 6. The effect of this is to reduce the absolute deviation between simulation and exact results, but the order of accuracy will not be affected.

Figure 4.14 plots error as a function of step-size for spatio-temporal propagation using the (2+1)-D cubic-quintic NLS equation, which has stationary solitary-wave solutions, as discussed in section 2.5. For this simulation, $w_0 = 39.6\ \mu$m as before and the propagation distance is 2 Z_0, reduced mainly because of the computational time required for multi-dimensional simulation. The results of the simulation are compared with the exact eigenmode which is computed numerically. As in the (1+1)-D case, the error scales second-order with step-size until an error floor is reached. Since comparison is made to an exact numerical solution, the relative error would increase for longer propagation distances, thus requiring smaller Δz to reach the error floor.

The final numerical result, shown in Figure 4.15, indicates that the accuracy is slightly better than first order when the full numerical scheme discussed in section 4.2.2 is implemented for a scalar field. The error is computed using the numerical result obtained with the step size $\Delta z = Z_0/2048$ as the reference. Again, due to computation considerations, the propagation distance is 2 Z_0. Even though the simulations of Chapter 6 use much longer distances, the short distance used here is not a limitation because the accuracy scaling is independent of propagation distance. As before in the (1+1)-D spatial case, for most purposes, 256 steps per Z_0 is sufficient, although in some cases shorter step sizes are used in Chapter 6 because of the longer distances involved and the desire for quantitative information.

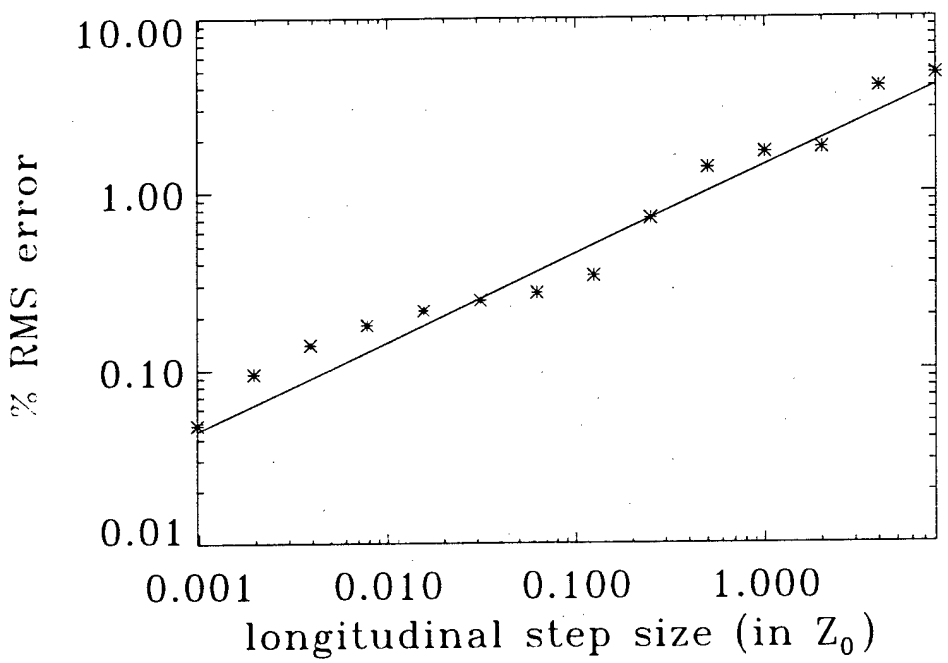

Figure 4.12: Plot of percentage RMS error as a function of step size for the interaction between two (paraxial) spatial solitons of the same size, including the effects of linear and two-photon absorption. The error decreases approximately as the square-root of step-size. The line represents one-half order scaling.

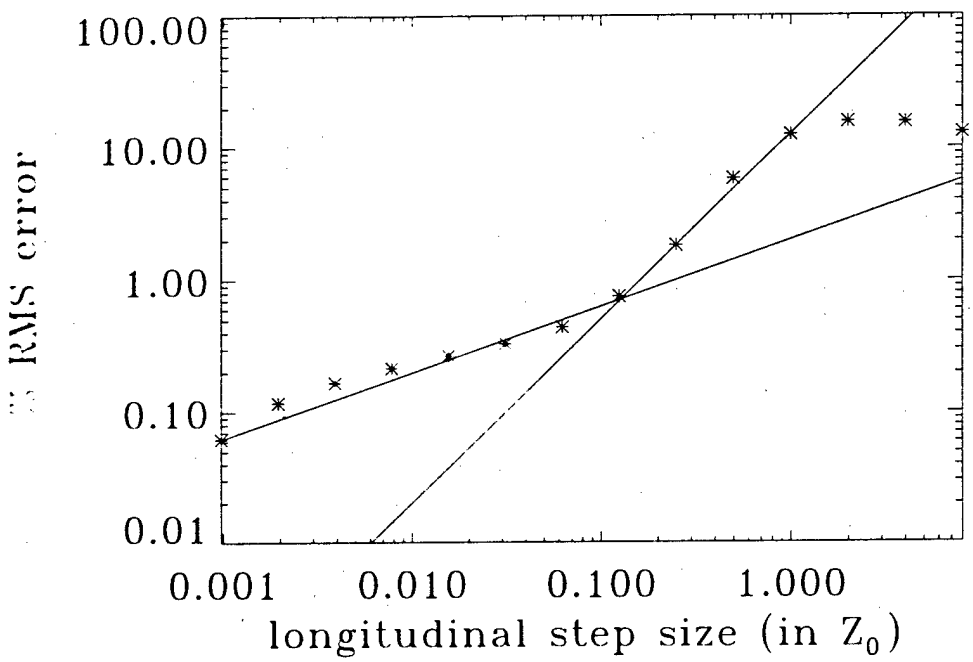

Figure 4.13: Plot of percentage RMS error as a function of step size for the interaction between two spatial solitons of different widths, including the effects of linear and two-photon absorption. The error decreases approximately as the square-root of step-size. The lines represents three-halves and one-half order scalings.

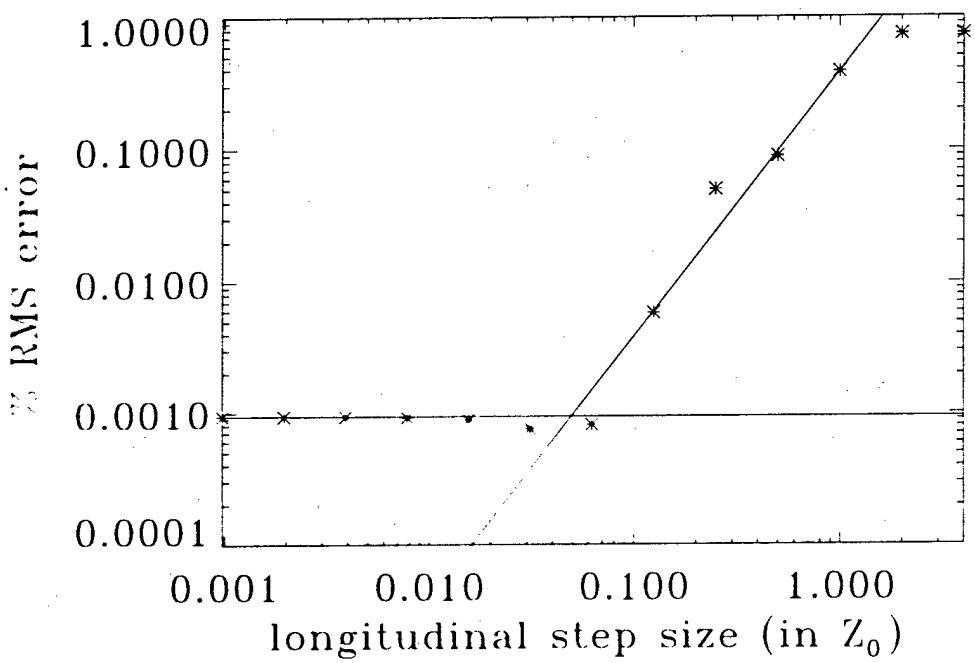

Figure 4.14: Plot of percentage RMS error between the split-step simulation and the exact numerical solution for stable spatio-temporal solitary wave propagation. Only the effects of paraxial diffraction, group-delay dispersion, and third- and fifth-order nonlinear refraction are included. The error decreases approximately second-order with step-size until a floor at about $9 \times 10^{-4}\%$ is reached. The lines represent zero and second order scalings.

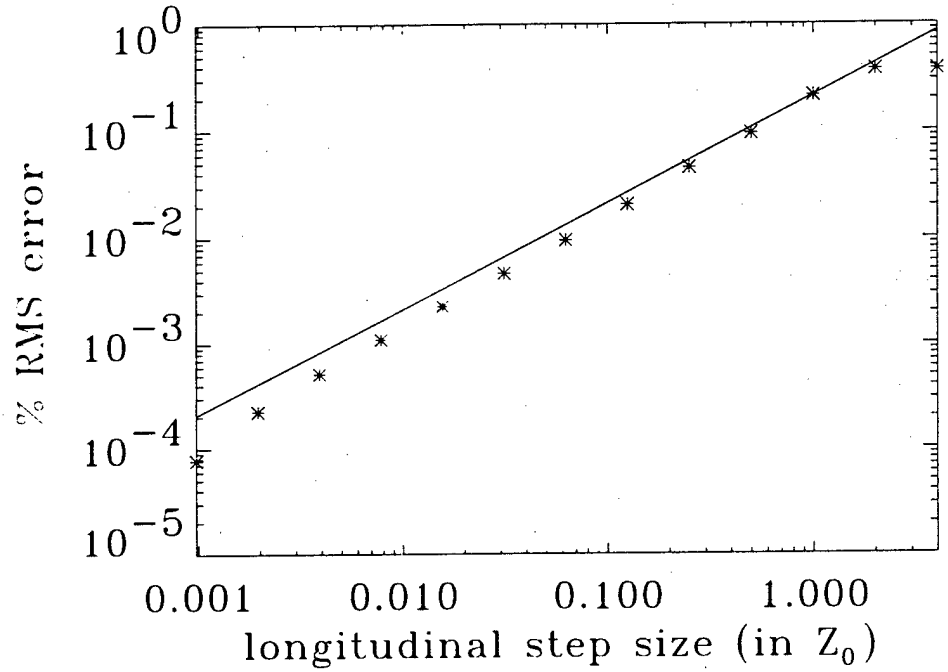

Figure 4.15. Plot of percentage RMS error as a function of step size for stabilized spatio-temporal solitary wave propagation, including all relevant higher-order effects. The error decreases slightly better than first-order with step-size. The line represents first order scaling.

Chapter 5

Conclusions

This thesis has developed the necessary framework for the study of general nonlinear, vectorial, spatio-temporal phenomena with large spatial and temporal bandwidths. This framework was applied to the study of novel optical logic devices based on the spatial interaction between 1-D spatial solitons and 2-D spatio-temporal solitary waves. These logic gates were found to have the properties of full level restoration, fanout with large noise margin, and cascadability to implement arbitrary logic functionality.

Chapter 1 provided motivation for the study of all-optical switching and logic devices, and covered the basic requirements for these devices as well. The main differences between switching and logic devices is that an optical logic device regenerates degraded data (given sufficient noise margins), has logic-level restoration, provides fanout, and is cascadable. Many contemporary switching devices, which do not intrinsically possess these properties, were then discussed: the nonlinear directional coupler, the Kerr gate, the nonlinear optical loop mirror, and the terahertz optical asymmetric demultiplexor. It was then shown that the intrinsic limitations of these devices could be overcome through the use of optical solitons, which propagate without dispersing and/or diffracting. In particular, the temporal and spatial soliton dragging interactions possess the necessary requirements of a three-terminal logic gate, and form the basis for the class of angular deflection logic gate studies of the later chapters, for which a nonlinear phase shift less than π can produce a resolvable change in the output state of the device.

A detailed discussion of optical solitons was given in Chapter 2. Following the historical development of solitary wave and soliton phenomena, 1-D spatial, 1-D temporal, and 2-D spatio-temporal solitons were discussed. In the 1-D cases, soliton solutions were obtained for higher-order equations beyond the traditional (1+1)-D nonlinear Schrödinger equation. For the spatial soliton, this corresponds to the scalar non-paraxial solution, while for the temporal soliton, solutions were shown for equations that contained higher-order dispersive terms one or two orders beyond the slowly-varying envelope approximation (but without Raman scattering). In the temporal soliton section, the effects of third- and fourth-order dispersion, optical shock, and Raman scattering were discussed as well, which have ramifications for the spatio-temporal simulations of Chapter 6. Finally, in the discussion on 2-D spatio-temporal solitary waves, fundamental eigenmode solutions to the (2+1)-D cubic-quintic nonlinear Schrödinger equation were presented, and the stability of these eigenmodes was shown due to the ultrafast saturation effect of a negative quintic nonlinearity. The effects of higher-order perturbations on these eigenmodes were discussed in Chapter 6.

The derivation of the fundamental nonlinear wave equations was presented in Chapter 3. First, the integral representation of the material polarization expansion up to fifth order was transformed into compact differential operator forms suitable for the quasi-monochromatic wave representation. Then, the fully vectorial, nonlinear Helmholtz equation was derived for optical wavepackets centered about a single fundamental frequency. Because of the difficulties this second-order equation presents to analytical and numerical solution, the following section derived via the multiple-scales perturbative technique, a fully vectorial, first-order nonlinear wave equation that consistently includes terms two-orders beyond the slowly-varying amplitude, slowly-varying envelope, and paraxial approximations, in addition to terms that describe the vectorial nonlinear coupling with the weak longitudinally-projected field and nonlinear coupling with a weak third-harmonic wave which produces an effective saturating quintic nonlinearity. This was the fundamental theoretical result of the thesis, and has application not only to the numerical studies of later chapters, but to other areas of study as well. For example, considerable attention has been paid recently to (3+1)-D nonlinear spatio-temporal propagation in the context of pulse splitting in the normal dispersion regime [152,153]. Simplified NLS-type models [154] have predicted pulse splitting, but it was also recognized that higher-order terms needed to be included in order to follow the subsequent evolution of the split pulses, which have significant angular and spectral bandwidths. More recent work has included scalar space-time non-paraxiality with shock [155], and NLS modified with Raman scattering [153]. These studies are able to qualitatively reproduce the asymmetric splitting behavior observed experimentally [153], but neglect additional physical effects that were derived in this chapter that can also lead to asymmetry.

Chapter 4 discussed linear spatio-temporal diffraction and the split-step numerical method used for the simulations in the remaining chapters. Diffraction in linear homogeneous media can be performed exactly given the correct initial conditions. The diffraction process can be viewed intuitively using the momentum space representation, which is generalized to include spatio-temporal diffraction in dispersive media. The split-step numerical method treats inhomogeneous propagation in two separate steps. The first step is linear homogeneous propagation over a distance short compared to the diffraction length and inhomogeneous length. The second step treats the refractive effect of inhomogeneity due to changes in the linear and/or nonlinear properties of the medium over the same distance. Using the symmetrized representation, the split-step method is expected to be second-order accurate in step-size. However, in the presence of strong nonlinear effects, the accuracy can drop to first-order or less. Even though the scaling can be worse than desirable, comparison of the numerical results to exact analytical and numerical solutions show that sufficient absolute accuracy can be obtained in the simulations.

The heart of the soliton interaction studies for optical logic gates is Chapter 5, which considered logic gates based on spatial soliton interactions. Specifically, the spatial collision and dragging interaction between orthogonally-polarized spatial solitons were found to provide the best performance for logic gates. These interaction were then studied in detail using the threshold contrast metric to find optimal operating parameters, where the dragging interaction generally produced better results. Then, the effects of linear and two-photon absorption on the propagation of a single soliton were studied. Figures-of-merit were derived to evaluate the suitability of a particular nonlinear material for soliton logic applications. The spatial collision and dragging interactions were then evaluated in the presence of absorption with the conclusion that, due to shorter effective interaction distances, the dragging interaction again provided better performance. Finally, using the metrics of small-signal gain, large-signal gain, fanout, and noise margin common in electronics, logic gates based on these interactions were examined. Subsequent cascaded studies show that a sequence of controlled inverters, in which the pump output of one stage divided by the fanout factor serves as the signal input to the next stage, which in the asymptotic limit forms a stable ring oscillator, results in complete logic level restoration and fanouts of two or greater with large noise margin. An additional cascaded geometry, in which the pump output of one stage serves as the pump input to a second stage, implements a two-input NOR gate. This gate was shown to possess complete logic-level restoration as well, with fanouts of two or greater and logic levels compatible with the single-stage inverter. These studies form the second major, systems-level, contribution of this thesis, and are perhaps the first time that such studies have been undertaken for all-optical devices.

The final results chapter, Chapter 6, studied logic gates based on 2-D spatio-temporal solitary waves. Stabilized propagation against the higher-order effects of third- and fourth-order dispersion, space-time focusing, optical shock, and intra-pulse stimulated Raman scattering, was demonstrated due to quintic index saturation. However, it was found that downshifting due to Raman scattering was the most detrimental effect to asymptotically stable propagation. Using this stabilized spatio-temporal wave as the pump, logic gates based on the spatial dragging interaction were studied. The single-stage inverter was shown to provide large-signal gains of two or greater, but cascaded operation proved more difficult due to the strong Raman downshift of the pump which serves as signal inputs to subsequent gates. After equalizing the group velocities of the interacting waves in the cascaded stages, the cross-Raman downshift caused strong energy depletion of the pump, which resulted in spatial broadening and dispersive wave generation, and reduced contrast. Using a weaker proportion of Raman to Kerr nonlinearity (more appropriate for a material such as AlGaAs), fanouts of two or greater were obtained in cascaded operation of inverter and two-input NOR gates with complete logic-level restoration.

The studies of this thesis pave the way for the experimental implementation of low-energy, ultrafast, all-optical logic gates for a variety of applications such as communications switching, routing, and coding, and special-purpose digital computing. The results show that, even though materials issues pose a great challenge for ultrafast systems with low average power, experimental studies using existing materials are warranted and could lead to new capability not possible with current or future electronics.

Bibliography

[1] J. W. Goodman, F. I. Leonberger, S.-Y. Kung, and R. A. Athale, "Optical interconnections for VLSI systems," *Proceedings of the IEEE*, vol. 72, pp. 850–866, 1984.

[2] R. McLeod, K. Wagner, and S. Blair, "(3+1)-dimensional optical soliton dragging logic," *Physical Review A*, vol. 52, pp. 3254–3278, October 1995.

[3] M. N. Islam, *Ultrafast fiber switching devices and systems*. Cambridge University Press, 1992.

[4] A. E. Willner, "Mining the optical bandwidth for a terabit per second," *IEEE Spectrum*, vol. 34, pp. 32–41, April 1997.

[5] R. W. Keyes, *The Physics of VLSI Systems*. New York: Addison-Wesley Publishing Co., 1987.

[6] S. Suzuki, *Photonics in Switching Volume II: Systems*, ch. Time- and wavelength-division switching systems. Academic Press, Inc., 1993.

[7] H. Takara, S. Kawanishi, M. Saruwatari, and T. Kitoh, "Nearly-penalty-free, fully TDM 100-gbit/s optical transmission by using two tunable mode-locked Er-doped fiber lasers," in *Conference on Optical Fiber Communications, OSA Technical Digest Series*, vol. 4, 1994. paper TuD5.

[8] L. F. Mollenauer, P. V. Mamyshev, and M. J. Neubelt, "Demonstration of soliton WDM transmission at up to 8×10 gbit/s error-free over transoceanic distances," in *Optical Fiber Communications*, 1996. Paper PD22.

[9] M. Nakazawa, K. Suzuki, H. Kubota, and K. Suzuki, "100 gbit/s WDM (20 gbit/s $\times$ 5 channels) soliton transmission over 1000 km using in-line synchronous modulation and optical filtering," *Electronics Letters*, vol. 33, 1997.

[10] P. R. Prucnal, "Time-division optical micro-area networks," in *International Conference on Advances in Interconnection and Packaging*, vol. SPIE 1389, 1990.

[11] K. L. Hall, J. P. Donnelly, S. H. Groves, C. I. Fennelly, R. J. Bailey, and A. Napoleon, "40-Gbit/s all-optical circulating shift register with an inverter," *Optics Letters*, vol. 22, pp. 1479–1481, October 1997.

[12] P. R. Prucnal, *Photonics in Switching Volume II: Systems*, ch. Photonic fast packet switching. Academic Press, Inc., 1993.

[13] I. Glesk, K. I. Kang, and P. R. Prucnal, "Ultrafast photonic packet switching with optical control," *Optics Express*, vol. 1, pp. 126–132, September 1997.

[14] S. D. Smith, I. Janossy, H. A. MacKenzie, J. G. H. Mathew, J. J. E. Reid, M. R. Taghizadeh, F. A. P. Tooley, and A. C. Walker, "Nonlinear optical circuit elements as logic gates for optical computers: the first digital optical circuits," *Optical Engineering*, vol. 24, pp. 569–574, July/August 1985.

[15] S. D. Smith, "Optical bistability, photonic logic, and optical computation," *Applied Optics*, vol. 25, pp. 1550–1564, May 1986.

[16] A. Huang, N. Whitaker, H. Avramopoulos, P. French, H. Hough, and I. Chuang, "Sagnac fiber logic gates and their possible applications: a system perspective," *Applied Optics*, vol. 33, pp. 6254–6267, September 1994.

[17] H. M. Gibbs, S. L. McCall, and T. N. C. Venkatesan, "Differential gain and bistability using a sodium-filled Fabry-Perot interferometer," *Physical Review Letters*, vol. 36, pp. 1135–1138, 1976.

[18] P. Denyer and D. Renshaw, *VLSI signal processing: a bit-serial approach*. Addison-Wesley Publishing Co., 1985.

[19] J.-P. Goedgebuer, N. Butterlin, and H. Porte, "Electro-optic systolic processor with a pipeline architecture," *Optics Letters*, vol. 20, pp. 1719–1721, August 1995.

[20] V. P. Heuring, H. F. Jordan, and J. R. Sauer, "Bit-serial architecture for optical computing," *Applied Optics*, vol. 31, p. 3213, June 1992.

[21] H. m Lu, "Computational origami: A geometric approach to regular multiprocessing," Master's thesis, Massachusetts Institute of Technology, 1988.

[22] B. K. Jenkins, P. Chavel, R. Forchheimer, A. A. Sachuck, and T. C. Strand, "Architectural implications of a digital optical processor," *Applied Optics*, vol. 23, pp. 3465–3474, October 1984.

[23] R. W. Keyes, "Physical limits in digital electronics," *Proceedings of the IEEE*, vol. 63, pp. 740–767, May 1975.

[24] R. W. Keyes, "What makes a good computer device?," *Science*, vol. 230, pp. 138–144, October 1985.

[25] D. A. B. Miller, "Device requirements for digital optical processing," *SPIE Critical Reviews: Digital Optical Computing*, vol. CR35, pp. 68–76, 1990.

[26] L. A. Glasser and D. W. Dobberpuhl, *VLSI Circuits*. Addison-Wesley, 1985.

[27] P. W. Milonni and J. H. Eberly, *Lasers*. John Wiley & Sons, 1988.

[28] S. D. Smith, A. C. Walker, F. A. P. Tooley, and B. S. Wherrett, "The demonstration of restoring digital optical logic," *Nature*, vol. 325, pp. 27–31, January 1987.

[29] P. D. Maker and R. W. Terhune, "Study of optical effects due to an induced polarization third-order in the electric field," *Physical Review A*, vol. 137, p. 801, February 1965.

[30] G. P. Agrawal, *Nonlinear Fiber Optics*. Academic Press, 1989.

[31] S. M. Jensen, "The nonlinear coherent coupler," *IEEE Journal of Quantum Electronics*, vol. QE-18, pp. 1580–1583, October 1982.

[32] G. I. Stegeman and E. M. Wright, "All-optical waveguide switching," *Optical and Quantum Electronics*, vol. 22, March 1990.

[33] A. Villeneuve, P. Mamyshev, J. U. Kang, G. I. Stegeman, J. S. Aitchison, and C. N. Ironside, "Efficient time-domain demultiplexing with spearate signal and control wavelengths in an algaas nonlinear directional coupler," *IEEE Journal of Quantum Electronics*, vol. 31, pp. 2165–2172, December 1995.

[34] A. M. Weiner, Y. Silberberg, H. Fouckhardt, D. E. Leaird, M. A. Saifi, M. J. Andrejco, and P. W. Smith, "Use of femtosecond square pulses to avoid pulse breakup in all-optical switching," *IEEE Journal of Quantum Electronics*, vol. 25, pp. 2648–2655, December 1989.

[35] S. Trillo, S. Wabnitz, E. M. Wright, and G. I. Stegeman, "Soliton switching in fiber nonlinear directional couplers," *Optics Letters*, vol. 13, pp. 672–674, August 1988.

[36] P. Dumais, A. Villeneuve, and J. S. Aitchison, "Bright temporal solitonlike pulses in self-defocusing AlGaAs waveguides near 800 nm," *Optics Letters*, vol. 21, pp. 260–262, February 1996.

[37] C. J. Hamilton, B. Vögele, J. S. Aitchison, G. T. Kennedy, W. Sibbett, W. Biehlig, U. Peschel, T. Peschel, and F. Lederer, "Bright solitary pulses in AlGaAs waveguides at half the band gap," *Optics Letters*, vol. 21, pp. 1226–1228, August 1996.

[38] N. J. Doran and D. Wood, "Nonlinear-optical loop mirror," *Optics Letters*, vol. 13, pp. 311–313, January 1988.

[39] J. S. Aitchison, A. Villeneuve, and G. I. Stegeman, "All-optical switching in two cascaded nonlinear directional couplers," *Optics Letters*, vol. 20, pp. 698–670, April 1995.

[40] S. Wabnitz, E. M. Wright, C. T. Seaton, and G. I. Stegeman, "Instabilities and all-optical phase-controlled switching in a nonlinear directional coupler," *Applied Physics Letters*, vol. 49, pp. 838–840, October 1986.

[41] M. A. Duguay and J. W. Hansen, "An ultrafast light gate," *Applied Physics Letters*, vol. 15, pp. 192–194, 1969.

[42] F. L. Pedrotti and L. S. Pedrotti, *Introduction to Optics*. Prentice Hall, 1987.

[43] T. Morioka, M. Saruwatari, and A. Takada, "Ultrafast optical multi/demultiplexer utilising optical Kerr effect in polarisation-maintaining single-mode fibers," *Electronics Letters*, vol. 23, pp. 453–454, April 1987.

[44] O. Dühr, F. Seifert, and V. Petrov, "Ultrafast kerr demultiplexing up to 460 Gbits/s in short optical fibers," *Applied Optics*, vol. 34, no. 24, pp. 5297–5300, 1995.

[45] M. Jinno and T. Matsumoto, "Nonlinear Sagnac interferometer switch and its applications," *IEEE Journal of Quantum Electronics*, vol. 28, pp. 875–882, April 1992.

[46] P. A. Andrekson, N. A. Olsson, D. J. Digiovanni, P. A. Morton, T. Tanbun-Ek, R. A. Logan, and K. W. Wecht, "64 Gbit/s all-optical demultiplexing with the nonlinear optical-loop mirror," *IEEE Photonics Technology Letters*, vol. 4, pp. 644–647, June 1992.

[47] H. Avramapoulos, P. M. W. French, M. C. Gabriel, H. H. Hough, J. N. A. Whitaker, and T. Morse, "Complete switching in a three-terminal Sagnac switch," *IEEE Photonics Technology Letters*, vol. 3, pp. 235–237, March 1991.

[48] K. Uchiyama, S. Kawanishi, H. Takara, T. Morioka, and M. Saruwatari, "100 Gbit/s to 6.3 Gbit/s demultiplexing experiment using polarization-independent nonlinear optical loop mirror," *Electronics Letters*, vol. 30, pp. 873–875, May 1994.

[49] X. D. Cao, B. C. Barnett, K. H. Ahn, Y. Liang, G. R. Williams, M. Vaziri, and M. N. Islam, "Experimental cascaded operation of low-birefringence nonliner-optical loop mirrors," *Optics Letters*, vol. 21, pp. 1211–1213, August 1996.

[50] J. P. Sokoloff, P. R. Prucnal, I. Glesk, and M. Kane, "A terahertz optical asymmetric demultiplexor (TOAD)," *IEEE Photonics Technology Letters*, vol. 5, pp. 787–790, July 1993.

[51] M. G. Kane, I. Glesk, J. P. Sokoloff, and P. R. Prucnal, "Asymmetric optical loop mirror: analysis of an all-optical switch," *Applied Optics*, vol. 33, pp. 6833–6842, October 1994.

[52] I. Glesk, J. P. Sokoloff, and P. R. Prucnal, "Demonstration of all-optical demultiplexing of TDM data at 250 Gbit/s," *Electronics Letters*, vol. 30, pp. 339–340, February 1994.

[53] K. I. Kang, T. G. Chang, I. Glesk, P. R. Prucnal, and R. K. Boncek, "Demonstration of ultrafast, all-optical, low control energy, single wavelength, polarization independent, cascadable, and integrable switch," *Applied Physics Letters*, vol. 67, pp. 605–607, July 1995.

[54] N. S. Patel, K. L. Hall, and K. A. Rauschenbach, "40-Gbit/s cascadable all-optical logic with an ultrafast nonlinear interferometer," *Optics Letters*, vol. 21, pp. 1466–1468, September 1996.

[55] R. J. Manning and G. Sherlock, "Recovery of a π phase shift in $\sim$ 12.5 ps in a semiconductor laser amplifier," *Electronics Letters*, vol. 31, pp. 307–308, February 1995.

[56] C. R. Menyuk, "Stability of solitons in birefringent optical fibers. I. Equal propagation amplitudes," *Optics Letters*, vol. 12, pp. 614–616, August 1987.

[57] C. R. Menyuk, "Stability of solitons in birefringent optical fibers. II. Arbitrary amplitudes," *Journal of the Optical Society of America B*, vol. 5, pp. 392–402, February 1988.

[58] S. Blair, K. Wagner, and R. McLeod, "Asymmetric spatial soliton dragging," *Optics Letters*, vol. 19, pp. 1943–1945, December 1994.

[59] M. N. Islam, "All-optical cascadable NOR gate with gain," *Optics Letters*, vol. 15, pp. 417–419, April 1990.

[60] G. Khitrova, H. M. Gibbs, Y. Kawamura, H. Iwamura, T. Ikegami, J. E. Sipe, and L. Ming, "Spatial solitons in a self-focusing semiconductor gain medium," *Physical Review Letters*, vol. 70, pp. 920–923, February 1993.

[61] F. Lederer and W. Biehlig, "Bright solitons and light bullets in semiconductor waveguides," *Electronics Letters*, vol. 30, pp. 1871–1872, October 1994.

[62] M. N. Islam, "Ultrafast all-optical logic gates based on soliton trapping in fibers," *Optics Letters*, vol. 14, pp. 1257–1259, November 1989.

[63] S. R. Friberg, "Soliton fusion and steering by the simultaneous launch of two different-color solitons," *Optics Letters*, vol. 16, pp. 1484–1486, October 1991.

[64] Y. Kodama and A. Hasegawa, "Effects of initial overlap on the propagation of optical solitons at different wavelengths," *Optics Letters*, vol. 16, pp. 208–210, February 1991.

[65] M. N. Islam, C. D. Poole, and J. P. Gordon, "Soliton trapping in birefringent optical fibers," *Optics Letters*, vol. 14, pp. 1011–1013, September 1989.

[66] M. N. Islam, C. E. Soccolich, and D. A. B. Miller, "Low-energy ultrafast fiber soliton logic gates," *Optics Letters*, vol. 15, pp. 909–911, August 1990.

[67] C. R. Menyuk, "Nonlinear pulse propagation in birefringent fibers," *IEEE Journal of Quantum Electronics*, vol. QE-23, pp. 174–176, February 1987.

[68] M. Shalaby and A. Barthelemy, "Experimental spatial soliton trapping and switching," *Optics Letters*, vol. 16, pp. 1472–1474, October 1991.

[69] K. Wagner and R. McLeod, "Spatial soliton dragging gates and light bullets," in *OSA Topical Meeting on Optical Computing*, March 1993. Palm Spings, CA.

[70] S. Blair, K. Wagner, and R. McLeod, "Material figures-of-merit for spatial soliton interactions in the presence of absorption," *Journal of the Optical Society of America B*, vol. 13, pp. 2141–2153, October 1996.

[71] Q. Wang, P. K. A. Wai, C.-J. Chen, and C. R. Menyuk, "Soliton shadows in birefringent optical fibers," *Optics Letters*, vol. 17, pp. 1265–1267, September 1992.

[72] J. P. Robinson and D. R. Anderson, "Soliton logic," *Optical Computing and Processing*, vol. 2, pp. 57–61, January 1992.

[73] V. E. Zakharov and A. B. Shabat, "Exact theory of two-dimensional self-focusing and one- dimensional self-modulation of waves in nonlinear media," *Soviet Physics JETP*, vol. 34, pp. 62–69, January 1972.

[74] V. I. Karpmann and V. V. Solov'ev, "A perturbational approach to the two-soliton system," *Physica D*, vol. 3, pp. 487–502, 1981.

[75] J. P. Gordon, "Interaction forces among solitons in optical fibers," *Optics Letters*, vol. 8, pp. 596–598, November 1983.

[76] K. J. Blow and N. J. Doran, "Bandwidth limits of nonlinear (soliton) optical communications systems," *Electronics Letters*, vol. 19, pp. 429–430, May 1983.

[77] D. Anderson and M. Lisak, "Bandwidth limits due to mututal pulse interaction in optical soliton communications systems," *Optics Letters*, vol. 11, pp. 174–176, 1986.

[78] L. F. Mollenauer, S. G. Evangelides, and J. P. Gordon, "Wavelength division multiplexing with solitons in ultra-long distance transmission using lumped amplifiers," *Journal of Lightwave Technology*, vol. 9, pp. 362–367, March 1991.

[79] E. Hecht, *Optics*. Addison-Wesley, second ed., 1987.

[80] M. Fogiel, ed., *Handbook of Mathematical, Scientific, and Engineering Formulas, Tables, Functions, Graphs, Transforms*. Research and Education Association, 1986.

[81] S. Chakravarty, M. J. Ablowitz, J. R. Sauer, and R. B. Jenkins, "Multisoliton interactions and wavelength-division multiplexing," *Optics Letters*, vol. 20, pp. 136–138, January 1995.

[82] S. Chi and S. Wen, "Optical soliton near zero-dispersion regine in Raman pump fiber," *Optics Communications*, vol. 69, January 1989.

[83] P. A. Andrekson, N. A. Olsson, P. C. Becker, J. R. Simpson, T. Tanbun-Ek, R. A. Logan, and K. W. Wecht, "Observation of multiple wavelength soliton collisions in optical systems with fiber amplifiers," *Applied Physics Letters*, vol. 57, pp. 1715–1717, October 1990.

[84] D. R. Andersen, D. E. Hooten, J. G. A. Swartzlander, and A. E. Kaplan, "Direct measurement of the transverse velocity of dark spatial solitons," *Optics Letters*, vol. 15, pp. 783–785, July 1990.

[85] S. R. Skinner, G. R. Allan, D. R. Anderson, and A. L. Smirl, "Dark spatial soliton propagation in bulk ZnSe," *IEEE Journal of Quantum Electronics*, vol. 27, pp. 2211–2219, September 1991.

[86] T.-T. Shi and S. Chi, "Nonlinear photonic switching by using the spatial soliton collision," *Optics Letters*, vol. 15, pp. 1123–1125, October 1990.

[87] F. M. Mitschke and L. F. Mollenauer, "Experimental observation of the interaction forces between solitons in optical fibers," *Optics Letters*, vol. 12, pp. 355–357, May 1987.

[88] F. Reynaud and A. Barthelemy, "Optically controlled interaction between two fundamental soliton beams," *Europhysics Letters*, vol. 12, pp. 401–405, July 1990.

[89] J. S. Aitchison, A. M. Weiner, Y. Silberberg, D. E. Leaird, M. K. Oliver, J. L. Jackel, and P. W. E. Smith, "Experimental observation of spatial soliton interactions," *Optics Letters*, vol. 16, pp. 15–17, January 1991.

[90] J.-R. Bian and A. K. Chan, "A nonlinear all-optical switch using spatial soliton interactions," *Microwave and Optical Technology Letters*, vol. 4, pp. 575–580, December 1991.

[91] M. Shalaby, F. Reynaud, and A. Barthelemy, "Experimental observation of spatial soliton interactions with a $\pi/2$ phase difference," *Optics Letters*, vol. 17, pp. 778–780, June 1992.

[92] P. L. Chu and C. Desem, "Mutual interaction between solitons of unequal amplitudes in optical fibre," *Electronics Letters*, vol. 21, pp. 1133–1134, November 1985.

[93] C. Desem and P. L. Chu, "Reducing soliton interaction in single-mode optical fibres," *IEE Proceedings, Part J*, vol. 134, pp. 145–151, June 1987.

[94] P. A. Andrekson, N. A. Olsson, J. R. Simpson, T. Tanbun-Ek, R. A. Logan, P. C. Becker, and K. W. Wecht, "Soliton collision interaction force dependence on wavelength separation in fibre amplifier based systems," *Electronics Letters*, vol. 26, pp. 1499–1501, August 1990.

[95] T. Aakjer, J. H. Povlsen, and K. Rottwitt, "Effects of initial overlap in a wavelength-division-multiplexed soliton transmission system," *Optics Letters*, vol. 18, pp. 1908–1910, November 1993.

[96] R. B. Jenkins, J. R. Sauer, S. Chakravarty, and M. J. Ablowitz, "Data-dependent timing jitter in wavelength-division-multiplexing soliton systems," *Optics Letters*, vol. 20, pp. 1964–1966, October 1995.

[97] L. Lefort and A. Barthelemy, "All-optical demultiplexing of a signal using collision and waveguiding of spatial solitons," *IEEE Photonics Technology Letters*, vol. 9, pp. 1364–1366, October 1997.

[98] A. Barthelemy, C. Froehly, S. Maneuf, and F. Reynaud, "Experimental observation of beams' self-deflection appearing with two-dimensional spatial soliton propagation in bulk Kerr material," *Optics Letters*, vol. 17, pp. 844–846, June 1992.

[99] B. Crosignani, A. Cutolo, and P. DiPorto, "Coupled-mode theory of nonlinear propagation in multimode and single-mode fibers: envelope solitons and self-confinement," *Journal of the Optical Society of America*, vol. 72, pp. 1136–1141, September 1982.

[100] S. V. Manakov, "On the theory of two-dimensional stationary self-focusing of electromagnetic waves," *Soviet Physics - JETP*, vol. 38, pp. 248–253, February 1974.

[101] B. A. Malomed and S. Wabnitz, "Soliton annihilation and fusion from resonant inelastic collisions in birefringent optical fibers," *Optics Letters*, vol. 16, pp. 1388–1390, September 1991.

[102] A. Villeneuve, J. U. Kang, J. S. Aitchison, and G. I. Stegeman, "Unity ratio of cross- to self-phase modulation in bulk AlGaAs and AlGaAs/GaAs MQW waveguides at half the band gap," *Applied Phycics Letters*, vol. 67, p. 760, August 1995.

[103] Q. Wang, P. Wai, C.-J. Chen, and C. R. Menyuk, "Numerical modeling of soliton-dragging logic gates," *Journal of the Optical Society of America B*, vol. 10, pp. 2030–2039, November 1993.

[104] R. McLeod, K. Wagner, and S. Blair, "Variational approach to orthogonally-polarized optical soliton interaction with cubic and quintic nonlinearities," *submited to Physica Scripta*, 1998.

[105] Y. Kodama *Physics Letters A*, vol. 123, p. 276, 1987.

[106] X. D. Cao and D. D. Meyerhofer, "Soliton collisions in optical birefringent fibers," *Journal of the Optical Society of America B*, vol. 11, pp. 380–385, February 1994.

[107] X. D. Cao and D. D. Meyerhofer, "All-optical switching by means of collisions of spatial vector solitons," *Optics Letters*, vol. 19, pp. 1711–1713, November 1994.

[108] J. U. Kang, G. I. Stegeman, and J. S. Aitchison, "One-dimensional spatial soliton dragging, trapping, and all-optical switching in AlGaAs waveguides," *Optics Letters*, vol. 21, pp. 189–191, February 1996.

[109] J. Millman and A. Grabel, *Microelectronics*. McGrall-Hill, second ed., 1987.

[110] D. A. B. Miller, "Refractive Fabry-Perot bistability with linear absorption: theory of operation and cavity optimization," *IEEE Journal of Quantum Electronics*, vol. QE-17, pp. 306–311, March 1981.

[111] E. Caglioti, S. Trillo, S. Wabnitz, and G. I. Stegeman, "Limitations to all-optical switching using nonlinear couplers in the presence of linear and nonlinear absorption and saturation," *Journal of the Optical Society of America B*, vol. 5, pp. 472–482, February 1988.

[112] G. I. Stegeman, E. M. Wright, N. Finlayson, R. Zanoni, and C. T. Seaton, "Third order nonlinear integrated optics," *Journal of Lightwave Technology*, vol. 6, pp. 953–970, June 1988.

[113] S. T. Ho, C. E. Soccolich, M. N. Islam, W. S. Hobson, A. F. J. Levi, and R. E. Slusher, "Nonlinear spectroscopy near half-gap in bulk and quantum well GaAs/AlGaAs waveguides," *Applied Physics Letters*, vol. 59, pp. 2558–2560, November 1991.

[114] K. W. DeLong, K. B. Rochford, and G. I. Stegeman, "Effect of two-photon absorption on all-optical guided-wave devices," *Applied Physics Letters*, vol. 55, pp. 1823–1825, October 1989.

[115] V. Mizrahi, K. W. DeLong, G. I. Stegeman, M. A. Saifi, and M. J. Andrejco, "Two-photon absorption as a limitation to all-optical switching," *Optics Letters*, vol. 14, pp. 1140–1142, October 1989.

[116] K. W. DeLong and G. I. Stegeman, "Two-photon absorption as a limitation to all-optical waveguide switching in semiconductors," *Applied Physics Letters*, vol. 57, p. 2063, November 1990.

[117] A. Hasegawa and Y. Kodama, "Signal transmission by optical solitons in monomode fiber," *Proceedings of the IEEE*, vol. 69, pp. 1145–1150, September 1981.

[118] J. S. Aitchison, A. M. Weiner, Y. Silberberg, M. K. Oliver, J. L. Jackel, D. E. Leaird, E. M. Vogel, and P. W. E. Smith, "Observation of spatial optical solitons in a nonlinear glass waveguide," *Optics Letters*, vol. 15, pp. 471–473, May 1990.

[119] Y. Silberberg, "Solitons and two-photon absorption," *Optics Letters*, vol. 15, pp. 1005–1007, September 1990.

[120] J. S. Aitchison, Y. Silberberg, A. M. Weiner, D. E. Leaird, M. K. Oliver, J. L. Jackel, E. M. Vogel, and P. W. E. Smith, "Spatial optical solitons in planar glass waveguides," *Journal of the Optical Soceity of America B*, vol. 8, pp. 1290–1297, June 1991.

[121] Y. Chen and J. Atai, "Absorption and amplification of dark solitons," *Optics Letters*, vol. 16, pp. 1933–1935, December 1991.

[122] A. B. Aceves and J. V. Moloney, "Effect of two-photon absorption on bright spatial soliton switches," *Optics Letters*, vol. 17, pp. 1488–1490, November 1992.

[123] X. Yang, Y. S. Kivshar, and B. Luther-Davies, "Is two-photon absorption a limitation to dark soliton switching?," *Optics Letters*, vol. 19, pp. 344–346, March 1994.

[124] D. L. Lee, *Electromagnetic Principals of Integrated Optics*. John Wiley & Sons, 1986. Chapter 7.

[125] B. L. Lawrence, M. Cha, J. U. Kang, W. Toruellas, G. Stegeman, G. Baker, J. Meth, and S. Etemad, "Large purely refractive nonlinear index of single crystal p-toluene sulfonate (PTS) at 1600 nm," *Electronics Letters*, vol. 30, p. 447, March 1994.

[126] A. Villeneuve, C. C. Yang, P. G. J. Wigley, G. I. Stegeman, J. S. Aitchison, and C. N. Ironside, "Ultrafast all-optical switching in semiconductor nonlinear directional couplers at half the band gap," *Applied Physics Letters*, vol. 61, p. 147, July 1992.

[127] K. Al-hemyari, A. Villeneuve, J. U. Kang, J. S. Aitchison, C. N. Ironside, and G. I. Stegeman, "Ultrafast all-optical switching in GaAlAs directional couplers at 1.55 μm without multiphoton absorption," *Applied Physics Letters*, vol. 63, pp. 3562–3564, December 1993.

[128] C. C. Yang, A. Villeneuve, G. I. Stegeman, and J. S. Aitchison, "Effects of three-photon absorption on nonlinear directional coupling," *Optics Letters*, vol. 17, pp. 710–712, May 1992.

[129] M. D. Dvorak, W. A. Schroeder, D. R. Anderson, A. L. Smirl, and B. S. Wherrett, "Measurement of the anisotropy of two-photon absorption coefficients in zincblende semiconductors," *IEEE Journal of Quantum Electronics*, vol. 30, pp. 256–268, February 1994.

[130] B. J. VanZeghbroeck, 1998. ECEN 4375 Class Notes, University of Colorado.

[131] M. J. Ablowitz and H. Segur, *Solitons and the inverse-scattering transform*, vol. 4. SIAM Studies in Applied Mathematics, 1981.

[132] A. Hasegawa and F. Tappert, "Transmission of stationary nonlinear optical pulses in dispersive dielectric fiber," *Applied Physics Letters*, vol. 23, 1973.

[133] P. M. Goorjian and Y. Silberberg, "Numerical simulation of light bullets using the full-vector time-dependent nonlinear Maxwell equations," *Journal of the Optical Society of America B*, vol. 14, pp. 3253–3260, November 1997.

[134] S. Blair and K. Wagner, "(2+1)-D propagation of spatio-temporal solitary waves including higher-order corrections," *accepted Optical and Quantum Electronics*, 1998.

[135] Y. Silberberg, "Collapse of optical pulses," *Optics Letters*, vol. 15, pp. 1282–1284, November 1990.

[136] A. B. Blagoeva, S. G. Dinev, A. A. Dreischuh, and A. Naidenov, "Light bullets formation in bulk media," *IEEE Journal of Quantum Electronics*, vol. 27, pp. 2060–2065, August 1991.

[137] P. W. Smith, "On the physical limits of digital optical switching and logic elements," *The Bell Systems Technical Journal*, vol. 61, pp. 1975–1993, October 1982.

[138] D. Shenoy and A. Puri, "Compensation for the soliton self-frequency shift and the third-order dispersion using bandwidth-limited optical gain," *Optics Communications*, vol. 113, pp. 401–406, January 1995.

[139] K. Hayata, H. Higaki, and M. Koshiba, "Stable light-bullet formation in a Kerr medium: A route to multidimensional solitons in the femtosecond regime," *IEICE Transactions on Electronics*, vol. E78-C, pp. 38–42, January 1995.

[140] D. N. Christodoulides and R. I. Joseph, "Femtosecond solitary waves in optical fibres," *Electronics Letters*, vol. 20, pp. 659–660, August 1984.

[141] R. H. Stolen, C. Lee, and R. K. Jain, "Development of the stimulated Raman spectrum in single-mode silica fibers," *Journal of the Optical Society of America B*, vol. 1, pp. 652–657, August 1984.

[142] J. U. Kang, A. Villeneuve, M. Sheik-Bahae, G. I. Stegeman, K. Al-hemyari, J. S. Aitchison, and C. N. Ironside, "Limitation due to three-photon absorption on the useful spectral range for nonlinear optics in AlGaAs below half bandgap," *Applied Physics Letters*, vol. 65, pp. 147–149, July 1994.

[143] G. I. Stegeman, A. Villeneuve, J. S. Aitchison, and C. N. Ironside, *Nonlinear Integrated Optics and All-Optical Waveguide Switching in Semiconductors*, p. p. 415. NATO ASI Series **3**, 1995.

[144] J. E. Rothenberg, "Space-time focusing: breakdown of the slowly varying envelope approximation in the self-focusing of femtosecond pulses," *Optics Letters*, vol. 17, pp. 1340–1342, 1992.

[145] J. P. Gordon, "Theory of the soliton self-frequency shift," *Optics Letters*, vol. 11, pp. 662–664, October 1986.

[146] A. T. Ryan and G. P. Agrawal, "Spatiotemporal coupling in dispersive nonlinear planar waveguides," *Journal of the Optical Society of America B*, vol. 12, pp. 2382–2389, December 1995.

[147] B. L. Lawrence, M. Cha, W. E. Toruellas, G. I. Stegeman, S. Etemad, G. Baker, and F. Kajzar, "Measurement of the complex nonlinear refractive index of single crystal p-toluene sulfonate at 1064 nm," *Aplied Physics Letters*, vol. 64, p. 2273, May 1994.

[148] P. B. Corkum, C. Rolland, and T. Srinivasan-Rao, "Supercontinuum generation in gases," *Physical Review Letters*, vol. 57, pp. 2268–2271, November 1986.

[149] C. R. Menyuk, M. N. Islam, and J. P. Gordon, "Raman effect in birefringent optical fibers," *Optics Letters*, vol. 16, pp. 566–568, April 1991.

[150] R. H. Stolen, J. P. Gordon, W. J. Tomlinson, and H. A. Haus, "Raman response function of silica-core fibers," *Journal of the Optical Society of America B*, vol. 6, pp. 1159–1166, June 1989.

[151] Y.-H. Kao, M. N. Islam, J. M. Saylor, R. E. Slusher, and W. S. Hobson, "Raman effect in AlGaAs waveguides for subpicosecond pulses," *Journal of Applied Physics*, vol. 78, pp. 2198–2203, August 1995.

[152] J. K. Ranka, R. W. Schirmer, and A. L. Gaeta, "Observation of pulse splitting in nonlinear dispersive media," *Physical Review Letters*, vol. 77, pp. 3783–3786, October 1996.

[153] S. A. Diddams, H. K. Eaton, A. A. Zozulya, and T. S. Clement, "Characterizing the nonlinear propagation of femtosecond pulses in bulk media," *submitted to IEEE Journal of Selected Topics in Quantum Electronics*, 1997.

[154] J. E. Rothenberg, "Pulse splitting during self-focusing in normally dispersive media," *Optics Letters*, vol. 17, pp. 583–585, April 1992.

[155] G. Fibich and G. C. Papanicolaou, "Self-focusing in the presence of small time dispersion and nonparaxiality," *Optics Letters*, vol. 22, pp. 1379–1381, September 1997.

[156] M. A. Newhouse, D. L. Weidman, and D. W. Hall, "Enhanced-nonlinearity single-mode lead silicate optical fiber," *Optics Letters*, vol. 15, pp. 1185–1187, November 1990.

[157] M. Asobe, K. Naganuma, T. Kaino, T. Kanamori, S. Tomaru, and T. Kurihara, "Switching energy limitation in all-optical switching due to group-velocity dispersion in highly nonlinear waveguides," *Applied Physics Letters*, vol. 64, pp. 2922–2924, May 1994.

[158] M. Thakur, R. C. Frye, and B. I. Greene, "Nonresonant absorption of single-crystal films of polydiacetylene measured by photothermal deflection spectroscopy," *Applied Physics Letters*, vol. 56, pp. 1187–1188, March 1990.

[159] F. Wijnands, T. Rasmussen, H. J. W. M. Hoekstra, J. Povlsen, A. Bjarklev, and R. M. D. Ridder, "Efficient interface conditions for the semi-vectorial finite-difference beam propagation method," *Optical and Quantum Electronics*, vol. 27, pp. 961–975, 1995.

[160] J. W. Fleming, "Material dispersion in lightguide glasses," *Electronics Letters*, vol. 14, pp. 326–328, May 1978.

[161] C. S. Gardner, J. M. Greene, M. J. Kruskal, and R. M. Miura, "Method for solving the Korteweg-deVries equation," *Physical Review Letters*, vol. 19, pp. 1095–1097, November 1967.

[162] M. J. Ablowitz, M. D. Kruskal, A. C. Newell, and H. Segur, "The inverse scattering transform - Fourier analysis for nonlinear problems," *Studies in Applied Mathematics*, vol. 53, pp. 249–315, 1974.

[163] M. J. Ablowitz and P. A. Clarkson, *Solitons, Nonlinear Evolution Equations, and the Inverse-Scattering Transform*, vol. London Mathematical Society Lecture Note Series 149. Cambridge University Press, 1991.

[164] J. S. Russell, "Report on waves," in *Rep. 14th Meet. Brit. Assoc. Adv. Sci.*, pp. 311–390, 1844.

[165] P. G. Drazin and R. S. Johnson, *Solitons: an introduction*. Cambridge University Press, 1989.

[166] N. J. Zabusky and M. D. Kruskal, "Interactions of 'solitons' in a collisionless plasma and the recurrence of initial states," *Physical Review Letters*, vol. 15, pp. 240–243, August 1965.

[167] D. J. Korteweg and G. deVries, "On the change of form of long waves advancing in a rectangular canal, and on a new type of long stationay waves," *Philos. Mag.*, vol. 39, no. 5, pp. 422–423, 1895.

[168] E. Fermi, J. Pasta, and S. M. Ulam, "Studies in nonlinear problems," *Technical Report, Los Alamos Scientific Laboratory*, vol. LA-1940, 1955.

[169] R. Y. Chiao, E. Garmire, and C. H. Townes, "Self-trapping of optical beams," *Physical Review Letters*, vol. 13, pp. 479–482, October 1964.

[170] N. F. Pilipetskii and A. R. Rustamov, "Observation of self-focusing of light in liquids," *JETP Letters*, vol. 2, pp. 55–56, 1965.

[171] M. Hercher, "Laser-induced damage in transparent media," *Journal of the Optical Society of America*, vol. 54, April 1964.

[172] C. R. Giuliano and J. H. Marburger, "Observation of moving self-foci in sapphire," *Physical Review Letters*, vol. 27, pp. 905–908, October 1971.

[173] J. E. Bjorkholm and A. Ashkin, "cw self-focusing and self-trapping of light in sodium vapor," *Physical Review Letters*, vol. 32, pp. 129–132, January 1974.

[174] P. Lallemand and N. Bloembergen, "Self-focusing of laser beams and stimulated Raman gain in liquids," *Physical Review Letters*, vol. 15, pp. 1010–1012, December 1965.

[175] P. L. Kelley, "Self-focusing of optical beams," *Physical Review Letters*, vol. 15, pp. 1005–1008, December 1965.

[176] J. J. Rasmussen and K. Rypdal, "Blow-up in Nonlinear Schrödinger Equations - I: A general review," *Physica Scripta*, vol. 33, pp. 481–497, 1986.

[177] W. G. Wagner, H. A. Haus, and J. H. Marburger, "Large-scale self-trapping of optical beams in the paraxial ray approximation," *Physical Review*, vol. 175, pp. 256–266, November 1968.

[178] V. I. Bespalov and V. I. Talanov, "Filamantary structure of light beams in nonlinear liquids," *JETP Letters*, vol. 3, pp. 307–310, June 1966.

[179] J. H. Marburger and E. Dawes, "Dynamical formation of a small-scale filament," *Physical Review Letters*, vol. 21, no. 8, pp. 556–558, 1968.

[180] H. A. Haus, "Higher order trapped light beam solutions," *Applied Physics Letters*, vol. 8, pp. 128–129, March 1966.

[181] T. K. Gustafson, P. L. Kelley, R. Y. Chiao, and R. G. Brewer, "Self-trapping in media with saturation of the nonlinear index," *Applied Physics Letters*, vol. 12, pp. 165–168, March 1968.

[182] L. F. Mollenauer, R. H. Stolen, and J. P. Gordon, "Experimental observation of picosecond pulse narrowing and solitons in optical fibers," *Physical Review Letters*, vol. 45, pp. 1095–1098, September 1980.

[183] T. K. Gustafson, J. P. Taran, H. A. Haus, J. R. Lifsitz, and P. L. Kelley, "Self-modulation, self-steepening, and spectral development of light in small-scale trapped filaments," *Physical Review*, vol. 177, pp. 306–313, January 1969.

[184] D. Andersen and M. Lisak, "Nonlinear asymmetric self-phase modulation and self-steepening of pulses in long optical waveguides," *Physical Review A*, vol. 27, pp. 1393–1398, March 1983.

[185] Y. R. Shen and N. Bloembergen, "Theory of stimulated Brillouin and Raman scattering," *Physical Review*, vol. 137, pp. 1787–1805, March 1965.

[186] K. J. Blow and D. Wood, "Theoretical description of transient stimulated Raman scattering in optical fibers," *IEEE Journal of Quantum Electronics*, vol. 25, pp. 2665–2673, December 1989.

[187] F. M. Mitschke and L. F. Mollenauer, "Discovery of the soliton self-frequency shift," *Optics Letters*, vol. 11, pp. 659–661, October 1986.

[188] A. Barthelemy, S. Maneuf, and C. Froehly, "Propagation soliton et auto-confinement de faisceaux laser par nonlinearite optique de Kerr," *Optics Communications*, vol. 55, no. 3, pp. 201–206, 1985.

[189] S. Maneuf, R. Desailly, and C. Froehly, "Stable self-trapping of laser beams: Observation in a nonlinear planar waveguide," *Optics Communications*, vol. 65, no. 3, pp. 193–198, 1988.

[190] J. S. Aitchison, K. Al-Hemyari, C. N. Ironside, R. S. Grant, and W. Sibbett, "Observation of spatial solitons in AlGaAs waveguides," *Electronics Letters*, vol. 28, pp. 1879–1880, September 1992.

[191] A. Barthelemy, B. Colombeau, C. Froehly, and M. Vampouille, "Stable soliton and nonsoliton three-dimensional propagation of intense light by multiple beams interference in Kerr matrials," in *Technical Digest of the OSA 1990 Annual Meeting*, 1990.

[192] T. K. Gustafson, J. P. E. Taran, P. L. Kelley, and R. Y. Chiao, "Self-modulation of picosecond pulses in electro-optic crystals," *Optics Communications*, vol. 2, pp. 17–21, May 1970.

[193] J.-M. R. Thomas and J.-P. E. Taran, "Pulse distortions in mismatched second harmonic generation," *Optics Communicatins*, vol. 4, pp. 329–334, January 1972.

[194] A. C. Newell and J. V. Moloney, *Nonlinear Optics*. Addison-Wesley, 1992.

[195] M. J. Ablowitz, G. Biondini, and S. Blair, "Multi-dimensional pulse propagation in non-resonant $\chi^{(2)}$ materials," *Physics Letters A*, vol. 236, pp. 520–524, December 1997.

[196] R. DeSalvo, D. J. Hagan, M. Sheik-Bahae, G. Stegeman, and E. W. V. Stryland, "Self-focusing and self-defocusing by cascaded second-order effects in KTP," *Optics Letters*, vol. 17, pp. 28–30, January 1992.

[197] L. Torner, C. R. Menyuk, and G. I. Stegeman, "Excitation of solitons with cascaded $\chi^{(2)}$ nonlinearities," *Optics Letters*, vol. 19, pp. 1615–1617, October 1994.

[198] A. V. Buryak and Y. S. Kivshar, "Spatial optical solitons governed by quadratic nonlinearity," *Optics Letters*, vol. 19, pp. 1612–1614, October 1994.

[199] R. Schiek, Y. Baek, and G. I. Stegeman, "One-dimensional spatial solitary waves due to cascaded second order nonlinearities in planar waveguides," *Physical Review E*, vol. 53, January 1996.

[200] R. G. Wenzel, J. L. Carlsten, and K. J. Drühl, "Soliton experiments in stimulated Raman scattering," *Journal of Statistical Physics*, vol. 39, no. 5/6, pp. 621–632, 1985.

[201] A. S. Gouveia-Neto, A. S. L. Gomes, and J. R. Taylor, "Femtosecond soliton Raman generation," *IEEE Journal of Quantum Electronics*, vol. 24, pp. 332–340, February 1988.

[202] J. G. A. Swartzlander and C. T. Law, "Optical vortex solitons observed in Kerr nonlinear media," *Physical Review Letters*, vol. 69, pp. 2503–2506, October 1992.

[203] A. Braun, G. Korn, X. Liu, D. Du, J. Squier, and G. Mourou, "Self-channeling of high-peak-power femtosecond laser pulses in air," *Optics Letters*, vol. 20, pp. 73–75, January 1995.

[204] M. Segev, B. Crosignani, A. Yariv, and B. Fischer, "Spatial solitons in photorefractive media," *Physical Review Letters*, vol. 68, pp. 923–926, February 1992.

[205] N. Belanger, A. Villeneuve, and J. S. Aitchison, "Solitonlike pulses in self-defocusing AlGaAs waveguides," *Journal of the Optical Society of America B*, vol. 14, pp. 3003–3012, November 1997.

[206] D. N. Christodoulides and R. I. Joseph, "Femtosecond solitary waves in optical fibres - beyond the slowly varying envelope approximation," *Applied Physics Letters*, vol. 47, pp. 76–78, July 1985.

[207] P. L. Francois, J. F. Bayon, and F. Alard, "Design of monomode quadruple-clad fibres," *Electronics Letters*, vol. 20, pp. 688–689, August 1984.

[208] Y. Kodama, "On integrable systems with higher order corrections," *Physics Letters*, vol. 107A, pp. 245–249, February 1985.

[209] A. A. Kolokolov, "Stability of the dominant mode of the nonlinear wave equation in cubic media," *Journal of Applied Mechanics and Technical Physics*, vol. 3, p. 426, 1973.

[210] D. E. Edmundson and R. H. Enns, "Fully three-dimensional collisions of bistable light bullets," *Optics Letters*, vol. 18, pp. 1609–1611, October 1993.

[211] S. Saltiel, S. Tanev, and A. D. Boardman, "High-order nonlinear phase shift caused by cascaded third-order processes," *Optics Letters*, vol. 22, pp. 148–150, February 1997.

[212] W. H. Press, S. A. Teukolsky, W. T. Vetterling, and B. P. Flannery, *Numerical Recipes in C*. Cambridge University Press, second ed., 1992.

[213] J. M. Soto-Crespo, D. R. Heatley, and E. M. Wright, "Stability of the higher-bound states in a saturable self-focusing medium," *Physical Review A*, vol. 44, no. 1, 1991.

[214] L. Allen and J. H. Eberly, *Optical resonance and two-level atoms*. Dover, 1987.

[215] R. W. Boyd, *Nonlinear Optics*. Academic Press, 1992.

[216] R. W. Equall, Y. Sun, R. L. Cone, and R. M. Macfarlane, "Ultraslow optical dephasing in Eu^{3+}:Y_2SiO_5," *Physical Review Letters*, vol. 72, pp. 2179–2182, April 1994.

[217] T. W. Mossberg, "Time-domain frequency-selective optical data storage," *Optics Letters*, vol. 7, pp. 77–79, February 1982.

[218] P. Saari, R. Kaarli, and A. Rebane, "Picosecond time- and space-domain holography by photochemical hole burning," *Journal of the Optical Society of America B*, vol. 3, pp. 527–534, April 1986.

[219] A. Renn and U. P. Wild, "Spectral hole burning and hologram storage," *Applied Optics*, vol. 26, pp. 4040–4041, 1987.

[220] P. N. Butcher and D. Cotter, *The Elements of Nonlinear Optics*. Cambridge University Press, 1990.

[221] Y. R. Shen, *The Principles of Nonlinear Optics*. John Wiley and Sons, 1984.

[222] R. W. Hellwarth, A. Owyoung, and N. George, "Origin of the nonlinear refractive index of liquid CCl_4," *Physical Review A*, vol. 4, pp. 2342–2347, December 1971.

[223] T. Brabec and F. Krausz, "Nonlinear optical pulse propagation in the single-cycle regime," *Physical Review Letters*, vol. 78, pp. 3282–3285, April 1997.

[224] C. N. Ironside, "Ultra-fast all-optical switching," *Contemporary Physics*, vol. 34, no. 1, pp. 1–18, 1993.

[225] A. Yariv and P. Yeh, *Optical Waves in Crystals*. John Wiley & Sons, 1984.

[226] R. McLeod, *Spectral-Domain Analysis and Design of Three-Dimensional Optical Switching and Computing Systems*. PhD thesis, University of Colorado, 1995.

[227] E. Hairer, S. P. Norsett, and G. Wanner, *Solving Ordinary Differential Equations I*. Springer series in computational mathematics, Springer-Verlag, 1987.

[228] K. S. Yee, "Numerical solution of initial boundary value problems involving Maxwell's equations in isotropic media," *IEEE Transactions on Antennas and Propagation*, vol. AP-14, pp. 302–307, May 1966.

[229] R. W. Ziolkowski and J. B. Judkins, "Applications of the nonlinear finite difference time domain (NL-FDTD) method to pulse propagation in nonlinear media: self-focusing the linear-nonlinear interfaces," *Radio Science*, vol. 28, pp. 901–911, September-October 1993.

[230] D. U. von Rosenberg, *Methods for the Numerical Solution of Partial Differential Equations*. American Elsevier Publishing Company, Inc., 1969.

[231] F. Tappert, "Numerical solutions of the Korteweg-de Vries equation and its generalizations by the split-step Fourier method," in *Lectures in Applied Mathematics*, vol. 15, pp. 215–216, American Mathematical Society, 1974.

[232] J. A. Fleck, J. R. Morris, and M. D. Feit, "Time-dependent propagation of high energy laser beams through the atmosphere," *Applied Physics*, vol. 10, pp. 129–160, 1976.

[233] M. D. Feit and J. J. A. Fleck, "Beam nonparaxiality, filament formation, and beam breakup in the self-focusing of optical beams," *Journal of the Optical Society of America B*, vol. 5, pp. 633–640, March 1988.

[234] D. Yevick and M. Glasner, "Foward wide-angle light propagation in semiconductor rib waveguides," *Optics Letters*, vol. 15, pp. 174–176, February 1990.

[235] J. Arabat and J. Etchepare, "Nonresonant fifth-order nonlinearities induced by ultrashort intense pulses," *Journal of the Optical Society of America B*, vol. 10, pp. 2377–2382, December 1993.

[236] F. W. Sears, M. W. Zemansky, and H. D. Young, *University Physics*. Addison-Wesley, seventh ed., 1987.

[237] A. Yariv, *Quantum Electronics*. John-Wiley & Sons, third ed., 1989.

[238] A. Höök, "Influence of stimulated raman scattering on cross-phase modulation between waves in optical fibers," *Optics Letters*, vol. 17, pp. 115–117, January 1992.

[239] A. R. Mickelson, *Guided Wave Optics*. Van Nostrand Reinhold, 1993.

[240] D. Marcuse, *Theory of dielectric optical waveguides*. Academic Press, 1991.

Appendix A

Symmetry Properties of the Nonlinear Susceptibility Tensors

The symmetry properties derived in this appendix are the intrinsic index/frequency permutation symmetry and spatial symmetry. The intrinsic symmetry is a fundamental property of the susceptibility tensors, while the spatial symmetry depends on the particular choice of material class. The two triclinic classes are the only ones in which the number of independent elements cannot be reduced. This thesis deals mainly with the isotropic symmetry class (i.e. glasses, liquids, gases), but the results are valid for cubic 432 (i.e. $LiFe_5O_8$), $\bar{4}3m$ (GaAs, CdTe) and m3m (Ge, Si, GaP, ZnSe, ZnTe) as well with minor modifications.

First, the intrinsic index/frequency permutation symmetry property is discussed in the general case of nth-order nonlinear polarization. Then, the spatial symmetries are discussed for the specific cases of the third-order and fifth-order polarizations.

A.1 The Intrinsic Permutation Symmetry

In order to present a general proof of the intrinsic permutation symmetry property, the fully dispersive n^{th}-order nonlinear convolution integral is used:

$$P_j^{(n)}(t) = \varepsilon_0 \int_0^\infty \int_0^\infty \cdots \int_0^\infty R_{j\alpha_1\alpha_2\ \ \alpha_n}(\tau_1, \tau_2, \ldots, \tau_n) E_{\alpha_1}(t-\tau_1) \\ E_{\alpha_2}(t-\tau_2)\ldots E_{\alpha_n}(t-\tau_n) d\tau_1 d\tau_2 \cdots d\tau_n. \tag{A.1}$$

The spatial dependence is dropped for convenience. The form of equation A.1 is a result of the application of time-invariance [220], which, when combined with the causal nature of the response function, leads to the intrinsic permutation symmetry property, as discussed later in this section.

Following the same steps used for transforming the linear response integral in section 3.1.1, the nonlinear polarization A.1 is written in the temporal frequency domain as

$$\tilde{P}_j^{(n)}(\omega) = \varepsilon_0 \int \cdots \int \chi^{(n)}_{j\alpha_1\ \ \alpha_n}(\omega; \omega_1, \ldots, \omega_n) \tilde{E}_{\alpha_1}(\omega_1) \ldots \times \\ \tilde{E}_{\alpha_n}(\omega_n) \delta(\omega - \omega_1 - \ldots - \omega_n) d\omega_1 \ldots d\omega_n, \tag{A.2}$$

where the nth order nonlinear susceptibility tensor is defined

$$\chi^{(n)}_{j\alpha_1\ldots\alpha_n}(\omega; \omega_1, \ldots, \omega_n) \equiv \int \cdots \int \Theta(\tau_1) \ldots \Theta(\tau_n) \times \\ R^{(n)}_{j\alpha_1\ \ \alpha_n}(\tau_1, \ldots, \tau_n) e^{i[\omega_1\tau_1 + \ldots + \omega_n\tau_n]} d\tau_1 \ldots d\tau_n.$$

Here, Θ is the Heaviside step function that explicitly enforces causality. Note that all factors of $1/2\pi$, due to the definition of the Fourier transform pair (given by equations 3.20a and 3.20b) in terms of the radial frequency ω, are neglected for simplicity. These factors cancel upon return to the time-domain representation.

In the non-degenerate frequency case of equation A.2, the n fields in the product can be arranged in any order with the corresponding rearrangement of the indices and frequency arguments of the susceptibility tensor. There are $n!$ such equivalent

arrangements

$$\begin{aligned}
&\chi^{(n)}_{j\alpha_1\alpha_2\ldots\alpha_n}(\omega;\omega_1,\omega_2,\ldots,\omega_n)\tilde{E}_{\alpha_1}(\omega_1)\tilde{E}_{\alpha_2}(\omega_2)\ldots\tilde{E}_{\alpha_n}(\omega_n) = \\
&\chi^{(n)}_{j\alpha_n\alpha_2\ldots\alpha_1}(\omega;\omega_n,\omega_2,\ldots,\omega_1)\tilde{E}_{\alpha_n}(\omega_n)\tilde{E}_{\alpha_2}(\omega_2)\ldots\tilde{E}_{\alpha_1}(\omega_1) = \\
&\ldots = \\
&\chi^{(n)}_{j\alpha_n\alpha_{n-1}\ldots\alpha_1}(\omega;\omega_n,\omega_{n-1},\ldots,\omega_1)\tilde{E}_{\alpha_n}(\omega_n)\tilde{E}_{\alpha_{n-1}}(\omega_{n-1})\ldots\tilde{E}_{\alpha_1}(\omega_1).
\end{aligned} \tag{A.3}$$

The field products in equation A.3 can appear in any order by the commutation of the multiplication operator (there are $n!$ equivalent arrangements of the fields) and results in the intrinsic index-frequency permutation symmetry of the χ tensors:

$$\begin{aligned}
\chi^{(n)}_{j\alpha_1\alpha_2\ldots\alpha_n}(\omega;\omega_1,\omega_2,\ldots,\omega_n) &= \chi^{(n)}_{j\alpha_n\alpha_2\ldots\alpha_1}(\omega;\omega_n,\omega_2,\ldots,\omega_1) = \\
&\ldots = \chi^{(n)}_{j\alpha_n\alpha_{n-1}\ldots\alpha_1}(\omega;\omega_n,\omega_{n-1},\ldots,\omega_1).
\end{aligned} \tag{A.4}$$

For $\chi^{(3)}$, the intrinsic permutation symmetry property states that

$$\begin{aligned}
\chi_{jklm}(\omega;\omega_1,\omega_2,\omega_3) &= \chi_{jkml}(\omega;\omega_1,\omega_3,\omega_2) = \\
\chi_{jlkm}(\omega;\omega_2,\omega_1,\omega_3) &= \chi_{jlmk}(\omega;\omega_2,\omega_3,\omega_1) = \\
\chi_{jmkl}(\omega;\omega_3,\omega_1,\omega_2) &= \chi_{jmlk}(\omega;\omega_3,\omega_2,\omega_1),
\end{aligned} \tag{A.5}$$

for example.

Full index-frequency permutation symmetry, or Kleinman symmetry, results when the nth-order interaction is non-resonant, meaning that $\chi^{(n)}$ is real [215]. In the case of general $\chi^{(3)}$ phenomena for example, Kleinman symmetry requires that all one-, two-, and three-photon transitions are virtual (i.e. the medium is transparent to all frequencies involved), but in the case of nonlinear refraction, the requirement applies to just the one- and two-photon transitions. It is apparent that the Manley-Rowe relations hold under these conditions. Kleinman symmetry means that the first index/frequency pair takes part in the permutation, with a total of $(n+1)!$ arrangements. In addition, under Kleinman symmetry, the $(n+1)$ frequency arguments can be permuted independently from the indices [220]. For generality and to include the effects of one- and two-photon absorption, Kleinman symmetry is not invoked for the third-order susceptibility in this appendix, although it is invoked for the fifth-order susceptibility in order to simplify the derivation, without loss of validity, as explained later.

A.2 Symmetries of $\chi^{(3)}$

In the case of the third-order polarization, equation A.2 reduces to

$$\begin{aligned}
\tilde{P}^{(3)}_j(\omega) = \varepsilon_0 \int\int\int \chi_{jklm}(\omega;\omega_1,\omega_2,\omega_3)\tilde{E}_k(\omega_1)\tilde{E}_l(\omega_2)\tilde{E}_m(\omega_3) \times \\
\delta(\omega-\omega_1-\omega_2-\omega_3)d\omega_1 d\omega_2 d\omega_3.
\end{aligned} \tag{A.6}$$

The $\chi^{(3)}$ tensor has 81 elements. The intrinsic permutation symmetry property is used in combination with the spatial symmetry reductions to reduce the number of independent and nonzero elements for a given nonlinear process. The reductions due to spatial symmetry are considered next.

For the more general case of the cubic crystal symmetry classes 432, $\bar{4}3$m or m3m, there are 21 nonzero elements of the $\chi^{(3)}$ tensor of which only 4 are independent [220]:

$$\begin{aligned}
\chi^{(3)}_{jjjj}: &\quad \chi^{(3)}_{xxxx} = \chi^{(3)}_{yyyy} = \chi^{(3)}_{zzzz} \\
\chi^{(3)}_{jjkk}: &\quad \chi^{(3)}_{xxyy} = \chi^{(3)}_{xxzz} = \chi^{(3)}_{yyxx} = \chi^{(3)}_{yyzz} = \chi^{(3)}_{zzxx} = \chi^{(3)}_{zzyy} \\
\chi^{(3)}_{jkjk}: &\quad \chi^{(3)}_{xyxy} = \chi^{(3)}_{xzxz} = \chi^{(3)}_{yxyx} = \chi^{(3)}_{yzyz} = \chi^{(3)}_{zxzx} = \chi^{(3)}_{zyzy} \\
\chi^{(3)}_{jkkj}: &\quad \chi^{(3)}_{xyyx} = \chi^{(3)}_{xzzx} = \chi^{(3)}_{yxxy} = \chi^{(3)}_{yzzy} = \chi^{(3)}_{zxxz} = \chi^{(3)}_{zyyz},
\end{aligned} \tag{A.7}$$

where $j \neq k$. For the isotropic symmetry class, only three elements are independent because of the additional requirement [220]

$$\chi^{(3)}_{jjjj} = \chi^{(3)}_{jjkk} + \chi^{(3)}_{jkjk} + \chi^{(3)}_{jkkj}. \tag{A.8}$$

Aside from using the spatial symmetries, equation A.6 cannot be further simplified until the nonlinear mixing process is specified. In this thesis, the third-order processes of interest are the frequency-degenerate case of nonlinear refraction, third-harmonic generation and third-harmonic downconversion. The latter two processes, in cascade, result in effective fifth-order nonlinear refraction at the fundamental frequency. These three processes are now discussed separately.

A.2.1 Nonlinear Refraction

Using the quasi-monochromatic approximation 3.21, equation A.6 can be written for nonlinear refraction

$$\begin{aligned}\tilde{P}_j^{(3)+}(\omega) = \frac{\varepsilon_0}{8}\int\int\int \chi_{jklm}(\omega;\omega_1,\omega_2,\omega_3)\times \\ \big[\tilde{A}_k^*(\omega_1+\omega_0)\tilde{A}_l(\omega_2-\omega_0)\tilde{A}_m(\omega_3-\omega_0) \\ +\tilde{A}_k(\omega_1-\omega_0)\tilde{A}_l^*(\omega_2+\omega_0)\tilde{A}_m(\omega_3-\omega_0) \\ +\tilde{A}_k(\omega_1-\omega_0)\tilde{A}_l(\omega_2-\omega_0)\tilde{A}_m^*(\omega_3+\omega_0)\big]\times \\ \delta(\omega-\omega_1-\omega_2-\omega_3)d\omega_1 d\omega_2 d\omega_3,\end{aligned} \tag{A.9}$$

with corresponding equation for the conjugate third-order nonlinear polarization with time dependence centered about $-\omega_0$. Now, the third-order susceptibility tensor is Taylor-expanded about the center frequencies ω_0 and $-\omega_0$. Taking the first term in equation A.9 for example

$$\begin{aligned}&\chi_{jklm}(\omega;\omega_1,\omega_2,\omega_3)\tilde{A}_k^*(\omega_1+\omega_0)\tilde{A}_l(\omega_2-\omega_0)\tilde{A}_m(\omega_3-\omega_0) = \\ &\Bigg[\chi_{jklm}(\omega_0;-\omega_0,\omega_0,\omega_0) + [\omega_1+\omega_0]\left.\frac{\partial\chi_{jklm}(\omega_0;\omega_1,\omega_0,\omega_0)}{\partial\omega_1}\right|_{\omega_1=-\omega_0} + \cdots \\ &\qquad + [\omega_2-\omega_0]\left.\frac{\partial\chi_{jklm}(\omega_0;-\omega_0,\omega_2,\omega_0)}{\partial\omega_2}\right|_{\omega_2=\omega_0} + \cdots \\ &\qquad + [\omega_3-\omega_0]\left.\frac{\partial\chi_{jklm}(\omega_0;-\omega_0,\omega_0,\omega_3)}{\partial\omega_3}\right|_{\omega_3=\omega_0} + \cdots\Bigg]\times \\ &\tilde{A}_k^*(\omega_1+\omega_0)\tilde{A}_l(\omega_2-\omega_0)\tilde{A}_m(\omega_3-\omega_0).\end{aligned}$$

It is evident that each term in the susceptibility expansion is subject to the spatial symmetry reductions, but the fact that the derivative terms are subject to the intrinsic index-frequency permutation symmetry is less obvious. In order to see this, the proper Taylor expansions are used in equation A.9 which is subsequently transformed back into the time domain, using a procedure similar to that outlined in section 3.1.1. The result is

$$\begin{aligned}P_j^{(3)+}(t) = \frac{\varepsilon_0}{8}\Bigg[&\chi_{jklm}\left(\omega_0;-\omega_0+i\frac{\partial}{\partial t},\omega_0+i\frac{\partial}{\partial t},\omega_0+i\frac{\partial}{\partial t}\right)A_k^*(t)A_l(t)A_m(t) \\ &+\chi_{jklm}\left(\omega_0;\omega_0+i\frac{\partial}{\partial t},-\omega_0+i\frac{\partial}{\partial t},\omega_0+i\frac{\partial}{\partial t}\right)A_k(t)A_l^*(t)A_m(t) \\ &+\chi_{jklm}\left(\omega_0;\omega_0+i\frac{\partial}{\partial t},\omega_0+i\frac{\partial}{\partial t},-\omega_0+i\frac{\partial}{\partial t}\right)A_k(t)A_l(t)A_m^*(t)\Bigg]e^{-i\omega_0 t}.\end{aligned} \tag{A.10}$$

where the operator arguments are interpreted as the Taylor expansion about the frequency variable and the derivative operations are only performed on the corresponding field envelopes; thus, ordering of the field envelopes is important. After the derivative operators have been applied to the appropriate envelopes, the ordering of the envelopes is no longer important, and the arguments of the susceptibility (with the corresponding indices) can be permuted. It is now evident that index-frequency permutation symmetry holds.

The combination of the spatial symmetry reductions with the intrinsic permutation symmetry property is now used to reduce the general, fully-dispersive case of nonlinear refraction and the special case of the Raman susceptibility.

Fully Dispersive Nonlinear Refraction

Applying first the spatial symmetry reductions of the more general cubic classes to equation A.10 results in the following tabulation of terms

$$1)\qquad \chi_{jjjj}\left(\omega_0;-\omega_0+i\frac{\partial}{\partial t},\omega_0+i\frac{\partial}{\partial t},\omega_0+i\frac{\partial}{\partial t}\right)A_j^*(t)A_j(t)A_j(t)$$

$$1)\qquad \chi_{jjjj}\left(\omega_0;\omega_0+i\frac{\partial}{\partial t},-\omega_0+i\frac{\partial}{\partial t},\omega_0+i\frac{\partial}{\partial t}\right)A_j(t)A_j^*(t)A_j(t)$$

$$
\begin{aligned}
&1) \quad \chi_{jjjj}\left(\omega_0;\omega_0+i\frac{\partial}{\partial t},\omega_0+i\frac{\partial}{\partial t},-\omega_0+i\frac{\partial}{\partial t}\right)A_j(t)A_j(t)A_j^*(t)\\
&2) \quad \chi_{jjkk}\left(\omega_0;-\omega_0+i\frac{\partial}{\partial t},\omega_0+i\frac{\partial}{\partial t},\omega_0+i\frac{\partial}{\partial t}\right)A_j^*(t)A_k(t)A_k(t)\\
&3) \quad \chi_{jjkk}\left(\omega_0;\omega_0+i\frac{\partial}{\partial t},-\omega_0+i\frac{\partial}{\partial t},\omega_0+i\frac{\partial}{\partial t}\right)A_j(t)A_k^*(t)A_k(t)\\
&3) \quad \chi_{jjkk}\left(\omega_0;\omega_0+i\frac{\partial}{\partial t},\omega_0+i\frac{\partial}{\partial t},-\omega_0+i\frac{\partial}{\partial t}\right)A_j(t)A_k(t)A_k^*(t)\\
&3) \quad \chi_{jkjk}\left(\omega_0;-\omega_0+i\frac{\partial}{\partial t},\omega_0+i\frac{\partial}{\partial t},\omega_0+i\frac{\partial}{\partial t}\right)A_k^*(t)A_j(t)A_k(t)\\
&2) \quad \chi_{jkjk}\left(\omega_0;\omega_0+i\frac{\partial}{\partial t},-\omega_0+i\frac{\partial}{\partial t},\omega_0+i\frac{\partial}{\partial t}\right)A_k(t)A_j^*(t)A_k(t)\\
&3) \quad \chi_{jkjk}\left(\omega_0;\omega_0+i\frac{\partial}{\partial t},\omega_0+i\frac{\partial}{\partial t},-\omega_0+i\frac{\partial}{\partial t}\right)A_k(t)A_j(t)A_k^*(t)\\
&3) \quad \chi_{jkkj}\left(\omega_0;-\omega_0+i\frac{\partial}{\partial t},\omega_0+i\frac{\partial}{\partial t},\omega_0+i\frac{\partial}{\partial t}\right)A_k^*(t)A_k(t)A_j(t)\\
&3) \quad \chi_{jkkj}\left(\omega_0;\omega_0+i\frac{\partial}{\partial t},-\omega_0+i\frac{\partial}{\partial t},\omega_0+i\frac{\partial}{\partial t}\right)A_k(t)A_k^*(t)A_j(t)\\
&2) \quad \chi_{jkkj}\left(\omega_0;\omega_0+i\frac{\partial}{\partial t},\omega_0+i\frac{\partial}{\partial t},-\omega_0+i\frac{\partial}{\partial t}\right)A_k(t)A_k(t)A_j^*(t).
\end{aligned}
$$

The same numbered terms are identical by the use of the intrinsic index-frequency permutation symmetry property, thus reducing equation A.10 to

$$
\begin{aligned}
P_j^{(3)+}(t) = \frac{3\varepsilon_0}{8}\Bigg[&\chi_{jjjj}\left(\omega_0;-\omega_0+i\frac{\partial}{\partial t},\omega_0+i\frac{\partial}{\partial t},\omega_0+i\frac{\partial}{\partial t}\right)A_j^*(t)A_j(t)A_j(t)\\
&+2\chi_{jkkj}\left(\omega_0;-\omega_0+i\frac{\partial}{\partial t},\omega_0+i\frac{\partial}{\partial t},\omega_0+i\frac{\partial}{\partial t}\right)A_k^*(t)A_k(t)A_j(t)\\
&+\chi_{jjkk}\left(\omega_0;-\omega_0+i\frac{\partial}{\partial t},\omega_0+i\frac{\partial}{\partial t},\omega_0+i\frac{\partial}{\partial t}\right)A_j^*(t)A_k(t)A_k(t)\Bigg]e^{-i\omega_0 t},
\end{aligned}
\tag{A.11}
$$

where $j \neq k$. It is evident that equation A.11 is also valid for instantaneous nonlinear refraction by simply removing the time derivatives from the arguments of the susceptibilities.

For the isotropic symmetry class, the following relationship holds

$$
\begin{aligned}
\chi_{jjjj}(\omega_0;-\omega_0,\omega_0,\omega_0) &= 2\chi_{jkkj}(\omega_0;-\omega_0,\omega_0,\omega_0)\\
&\quad+\chi_{jjkk}(\omega_0;-\omega_0,\omega_0,\omega_0),
\end{aligned}
$$

and, under Kleinman symmetry, $\chi_{jkkj}(\omega_0;-\omega_0,\omega_0,\omega_0) = \chi_{jjkk}(\omega_0;-\omega_0,\omega_0,\omega_0)$. These relationships are valid in both the fully dispersive and instantaneous cases. The instantaneous case is shown for brevity.

The Raman Susceptibility

Now, considering the special case of stimulated Raman scattering as discussed in Appendix B, equation A.10 reduces to

$$
\begin{aligned}
P_{Rj}^{(3)+}(t) = \frac{\varepsilon_0}{8}\Bigg\{&\chi^{\mathrm{R}}_{jklm}\left(\omega_0;i\frac{\partial}{\partial t}\right)\Big[A_k^*(t)A_l(t)\Big]A_m(t)\\
&+\chi^{\mathrm{R}}_{jklm}\left(\omega_0;i\frac{\partial}{\partial t}\right)\Big[A_k(t)A_l^*(t)\Big]A_m(t)\Bigg\}e^{-i\omega_0 t}.
\end{aligned}
\tag{A.12}
$$

Now, the derivative operator argument operates on the product between two envelopes enclosed in brackets. Notice that since the Raman susceptibility is a function of one frequency argument, the intrinsic permutation symmetry only applies to the two

envelopes inside the brackets. Applying the spatial symmetries results in

$$
\begin{aligned}
&1) \quad \chi^{R}_{jjjj}\left(\omega_0; i\frac{\partial}{\partial t}\right)\left[A_j^*(t)A_j(t)\right]A_j(t)\\
&1) \quad \chi^{R}_{jjjj}\left(\omega_0; i\frac{\partial}{\partial t}\right)\left[A_j(t)A_j^*(t)\right]A_j(t)\\
&2) \quad \chi^{R}_{jjkk}\left(\omega_0; i\frac{\partial}{\partial t}\right)\left[A_j^*(t)A_k(t)\right]A_k(t)\\
&3) \quad \chi^{R}_{jjkk}\left(\omega_0; i\frac{\partial}{\partial t}\right)\left[A_j(t)A_k^*(t)\right]A_k(t)\\
&3) \quad \chi^{R}_{jkjk}\left(\omega_0; i\frac{\partial}{\partial t}\right)\left[A_k^*(t)A_j(t)\right]A_k(t)\\
&2) \quad \chi^{R}_{jkjk}\left(\omega_0; i\frac{\partial}{\partial t}\right)\left[A_k(t)A_j^*(t)\right]A_k(t)\\
&4) \quad \chi^{R}_{jkkj}\left(\omega_0; i\frac{\partial}{\partial t}\right)\left[A_k^*(t)A_k(t)\right]A_j(t)\\
&4) \quad \chi^{R}_{jkkj}\left(\omega_0; i\frac{\partial}{\partial t}\right)\left[A_k(t)A_k^*(t)\right]A_j(t).
\end{aligned}
$$

Again, the same numbered terms are identical by the intrinsic index-frequency permutation symmetry. With these reductions, equation A.12 can be written

$$
\begin{aligned}
P^{(3)+}_{Rj}(t) = \frac{\varepsilon_0}{4}\Bigg\{&\chi^{R}_{jjjj}\left(\omega_0; i\frac{\partial}{\partial t}\right)\left[A_j^*(t)A_j(t)\right]A_j(t)\\
&+\chi^{R}_{jkkj}\left(\omega_0; i\frac{\partial}{\partial t}\right)\left[A_k^*(t)A_k(t)\right]A_j(t)\\
&+\chi^{R}_{jjkk}\left(\omega_0; i\frac{\partial}{\partial t}\right)\left[A_k^*(t)A_j(t)\right]A_k(t)\\
&+\chi^{R}_{jjkk}\left(\omega_0; i\frac{\partial}{\partial t}\right)\left[A_j^*(t)A_k(t)\right]A_k(t)\Bigg\}e^{-i\omega_0 t}.
\end{aligned}
\tag{A.13}
$$

This expression is the generalization to higher-order terms of the result obtained for the study of the Raman effect in AlGaAs waveguides [151]. Note that, for the isotropic class

$$
\chi^{R}_{jjjj} = 2\chi^{R}_{jjkk} + \chi^{R}_{jkkj}, \tag{A.14}
$$

and, invoking Kleinman symmetry, $\chi^{R}_{jjkk} = \chi^{R}_{jkkj}$.

A.2.2 Third-Harmonic Generation

The general form of the instantaneous polarization at the third harmonic driven by the fundamental at ω_0 is

$$
P^{(3)+}_{THGj}(t) = \frac{\varepsilon_0}{8}\chi_{jklm}(3\omega_0;\omega_0,\omega_0,\omega_0)A_k(t)A_l(t)A_m(t)e^{-3i\omega_0 t}, \tag{A.15}
$$

where the frequency dependence is neglected for simplicity. This is not an approximation as such because in the multiple-scales analysis of Chapter 3, the frequency dependence of the third-harmonic susceptibility plays no role to the order of the derivation.

Using the spatial symmetry properties, the terms in the third-harmonic polarization are

$$
\begin{aligned}
&1) \quad \chi_{jjjj}(3\omega_0;\omega_0,\omega_0,\omega_0)A_j(t)A_j(t)A_j(t)\\
&2) \quad \chi_{jjkk}(3\omega_0;\omega_0,\omega_0,\omega_0)A_j(t)A_k(t)A_k(t)\\
&2) \quad \chi_{jkjk}(3\omega_0;\omega_0,\omega_0,\omega_0)A_k(t)A_j(t)A_k(t)\\
&2) \quad \chi_{jkkj}(3\omega_0;\omega_0,\omega_0,\omega_0)A_k(t)A_k(t)A_j(t).
\end{aligned}
$$

The intrinsic permutation symmetry property forces the last three terms to be equal. The polarization is then

$$P^{(3)+}_{THGj}(t) = \frac{\varepsilon_0}{8}\Big[\chi_{jjjj}(3\omega_0;\omega_0,\omega_0,\omega_0)A_j(t)A_j(t)A_j(t) + 3\chi_{jkkj}(3\omega_0;\omega_0,\omega_0,\omega_0)A_k(t)A_k(t)A_j(t)\Big]e^{-3i\omega_0 t}, \tag{A.16}$$

where, for the isotropic symmetry class,

$$\chi_{jjjj}(3\omega_0;\omega_0,\omega_0,\omega_0) = 3\chi_{jkkj}(3\omega_0;\omega_0,\omega_0,\omega_0)\,. \tag{A.17}$$

Note that these expressions are generally valid even under the conditions of three-photon resonance, neglecting frequency dispersion.

A.2.3 Third-Harmonic Downconversion

Again neglecting frequency dependence, the form for the polarization at the fundamental due to mixing between the third-harmonic and the fundamental is

$$P^{(3)+}_{THDj}(t) = \frac{\varepsilon_0}{8}\Big[\chi_{jklm}(\omega_0;3\omega_0,-\omega_0,-\omega_0)S_k(t)A^*_l(t)A^*_m(t) + \chi_{jklm}(\omega_0;-\omega_0,3\omega_0,-\omega_0)A^*_k(t)S_l(t)A^*_m(t) + \chi_{jklm}(\omega_0;-\omega_0,-\omega_0,3\omega_0)A^*_k(t)A^*_l(t)S_m(t)\Big]e^{-i\omega_0 t}, \tag{A.18}$$

where S is the envelope of the third-harmonic. Using the spatial symmetries, the terms in the polarization are

$$\begin{array}{ll}
1) & \chi_{jjjj}(\omega_0;3\omega_0,-\omega_0,-\omega_0)S_j(t)A^*_j(t)A^*_j(t)\\
1) & \chi_{jjjj}(\omega_0;-\omega_0,3\omega_0,-\omega_0)A^*_j(t)S_j(t)A^*_j(t)\\
1) & \chi_{jjjj}(\omega_0;-\omega_0,-\omega_0,3\omega_0)A^*_j(t)A^*_j(t)S_j(t)\\
 & \\
2) & \chi_{jjkk}(\omega_0;3\omega_0,-\omega_0,-\omega_0)S_j(t)A^*_k(t)A^*_k(t)\\
3) & \chi_{jjkk}(\omega_0;-\omega_0,3\omega_0,-\omega_0)A^*_j(t)S_k(t)A^*_k(t)\\
3) & \chi_{jjkk}(\omega_0;-\omega_0,-\omega_0,3\omega_0)A^*_j(t)A^*_k(t)S_k(t)\\
 & \\
3) & \chi_{jkjk}(\omega_0;3\omega_0,-\omega_0,-\omega_0)S_k(t)A^*_j(t)A^*_k(t)\\
2) & \chi_{jkjk}(\omega_0;-\omega_0,3\omega_0,-\omega_0)A^*_k(t)S_j(t)A^*_k(t)\\
3) & \chi_{jkjk}(\omega_0;-\omega_0,-\omega_0,3\omega_0)A^*_k(t)A^*_j(t)S_k(t)\\
 & \\
3) & \chi_{jkkj}(\omega_0;3\omega_0,-\omega_0,-\omega_0)S_k(t)A^*_k(t)A^*_j(t)\\
3) & \chi_{jkkj}(\omega_0;-\omega_0,3\omega_0,-\omega_0)A^*_k(t)S_k(t)A^*_j(t)\\
2) & \chi_{jkkj}(\omega_0;-\omega_0,-\omega_0,3\omega_0)A^*_k(t)A^*_k(t)S_j(t),
\end{array}$$

which is in the same form as nonlinear refraction. This is expected because in both cases, there are only two non-degenerate frequencies.

The nonlinear polarization for third-harmonic downconversion is

$$P^{(3)+}_{THDj}(t) = \frac{3\varepsilon_0}{8}\Big[\chi_{jjjj}(\omega_0;3\omega_0,-\omega_0,-\omega_0)S_j(t)A^*_j(t)A^*_j(t) + 2\chi_{jkkj}(\omega_0;3\omega_0,-\omega_0,-\omega_0)S_k(t)A^*_k(t)A^*_j(t) + \chi_{jjkk}(\omega_0;3\omega_0,-\omega_0,-\omega_0)S_j(t)A^*_k(t)A^*_k(t)\Big]e^{-i\omega_0 t}. \tag{A.19}$$

For the isotropic symmetry class,

$$\chi_{jjjj}(\omega_0;3\omega_0,-\omega_0,-\omega_0) = 2\chi_{jkkj}(\omega_0;3\omega_0,-\omega_0,-\omega_0) + \chi_{jjkk}(\omega_0;3\omega_0,-\omega_0,-\omega_0)\,,$$

as before.

A.3 Symmetries of $\chi^{(5)}$ - Quintic Nonlinear Refraction and Three-Photon Absorption

In the case of the fifth-order polarization, equation A.2 reduces to

$$\tilde{P}_j^{(5)}(\omega) = \varepsilon_0 \int \cdots \int \chi_{jklmno}(\omega;\omega_1,\ldots,\omega_5)\tilde{E}_k(\omega_1)\tilde{E}_l(\omega_2)\tilde{E}_m(\omega_3)\tilde{E}_n(\omega_4)\times \tilde{E}_o(\omega_5)\delta(\omega-\omega_1-\omega_2-\omega_3-\omega_4-\omega_5)d\omega_1 d\omega_2 d\omega_3 d\omega_4 d\omega_5. \tag{A.20}$$

The $\chi^{(5)}$ tensor has 729 elements. Even though the development of the third-order polarization is valid for both the isotropic and cubic 432, $\bar{4}$3m and m3m symmetry classes and processes other than nonlinear refraction, the fifth-order polarization is developed only for isotropic symmetry and instantaneous response. This is a simplification that has no consequences in the multiple-scales analysis. Any frequency dependence will appear one order later than the instantaneous response. In addition, fifth-harmonic generation is also not described because the influence of the fifth-harmonic on the fundamental occurs well beyond the order of the multiple-scales derivation.

In the time-domain then, the fifth-order instantaneous polarization for nonlinear refraction is written

$$\begin{aligned}
&P_j^{(5)+}(t) = \\
&\frac{\varepsilon_0}{32}\Big[\chi_{jklmno}(\omega_0;-\omega_0,-\omega_0,\omega_0,\omega_0,\omega_0)A_k^*(t)A_l^*(t)A_m(t)A_n(t)A_o(t) \\
&+\chi_{jklmno}(\omega_0;-\omega_0,\omega_0,-\omega_0,\omega_0,\omega_0)A_k^*(t)A_l(t)A_m^*(t)A_n(t)A_o(t) \\
&+\chi_{jklmno}(\omega_0;-\omega_0,\omega_0,\omega_0,-\omega_0,\omega_0)A_k^*(t)A_l(t)A_m(t)A_n^*(t)A_o(t) \\
&+\chi_{jklmno}(\omega_0;-\omega_0,\omega_0,\omega_0,\omega_0,-\omega_0)A_k^*(t)A_l(t)A_m(t)A_n(t)A_o^*(t) \\
&+\chi_{jklmno}(\omega_0;\omega_0,-\omega_0,-\omega_0,\omega_0,\omega_0)A_k(t)A_l^*(t)A_m^*(t)A_n(t)A_o(t) \\
&+\chi_{jklmno}(\omega_0;\omega_0,-\omega_0,\omega_0,-\omega_0,\omega_0)A_k(t)A_l^*(t)A_m(t)A_n^*(t)A_o(t) \\
&+\chi_{jklmno}(\omega_0;\omega_0,-\omega_0,\omega_0,\omega_0,-\omega_0)A_k(t)A_l^*(t)A_m(t)A_n(t)A_o^*(t) \\
&+\chi_{jklmno}(\omega_0;\omega_0,\omega_0,-\omega_0,-\omega_0,\omega_0)A_k(t)A_l(t)A_m^*(t)A_n^*(t)A_o(t) \\
&+\chi_{jklmno}(\omega_0;\omega_0,\omega_0,-\omega_0,\omega_0,-\omega_0)A_k(t)A_l(t)A_m^*(t)A_n(t)A_o^*(t) \\
&+\chi_{jklmno}(\omega_0;\omega_0,\omega_0,\omega_0,-\omega_0,-\omega_0)A_k(t)A_l(t)A_m(t)A_n^*(t)A_o^*(t)\Big]e^{-i\omega_0 t}.
\end{aligned} \tag{A.21}$$

Spatial symmetry of the isotropic class results in 183 nonzero terms of the sixth-order tensor, with 30 independent:

$$\begin{array}{ccccccc}
\chi_{jjjjjj} & \chi_{jjjjkk} & \chi_{jjkkkk} & \chi_{jjkkjj} & \chi_{jjjkjk} & \chi_{jjkjkj} & \chi_{jjjkkj} \\
\chi_{jjkjjk} & \chi_{jkjkjj} & \chi_{jkjkkk} & \chi_{jkjjkj} & \chi_{jkjjjk} & \chi_{jkkjkk} & \chi_{jkkjjj} \\
\chi_{jkkkjk} & \chi_{jkkkkj} & \chi_{jjkkll} & \chi_{jjklkl} & \chi_{jjkllk} & \chi_{jkjkll} & \chi_{jkjlkl} \\
\chi_{jkjllk} & \chi_{jkkjll} & \chi_{jkljkl} & \chi_{jklllk} & \chi_{jkkljl} & \chi_{jklkjl} & \chi_{jklljk} \\
\chi_{jkkllj} & \chi_{jkllkj} & & & & &
\end{array}$$

where $j \neq k \neq l$. Using Kleinman symmetry (which is not strictly valid near three-photon resonance), the fifth-order polarization responsible for nonlinear refraction and three-photon absorption can be written

$$\begin{aligned}
P_j^{(5)+}(t) = \frac{\varepsilon_0}{32}\Big\{&\chi_{jjjjjj}(\omega_0;-\omega_0,-\omega_0,\omega_0,\omega_0,\omega_0)\left[10\left|A_j(t)\right|^4 A_j(t)\right] \\
&+5\chi_{jjkkkk}(\omega_0;-\omega_0,-\omega_0,\omega_0,\omega_0,\omega_0)\times \\
&\quad\left[4\left|A_k(t)\right|^2 A_k^2(t)A_j^*(t)+6\left|A_k(t)\right|^4 A_j(t)\right] \\
&+10\chi_{jjjjkk}(\omega_0;-\omega_0,-\omega_0,\omega_0,\omega_0,\omega_0)\times \\
&\quad\left[3A_j^{*2}(t)A_k^2(t)+A_j^2(t)A_k^{*2}(t)+6\left|A_j(t)\right|^2\left|A_k(t)\right|^2\right]A_j(t) \\
&+15\chi_{jjkkll}(\omega_0,-\omega_0,-\omega_0,\omega_0,\omega_0,\omega_0)\times \\
&\quad\Big[4\left|A_k(t)\right|^2 A_l^2(t)A_j^*(t)+2A_k^{*2}(t)A_l^2(t)A_j(t)+ \\
&\quad 4\left|A_k(t)\right|^2\left|A_l(t)\right|^2 A_j(t)\Big]\Big\},
\end{aligned}$$

where $\chi_{jjkkk} = \chi_{jjjjk}$. In this case, Kleinman symmetry means that there are no one-, two-, three-, four-, or five-photon resonances. As mentioned previously, these processes (except for the possibility of three-photon absorption) are assumed weak at the very least for materials of interest.

Now, using the relationship [235]

$$\chi_{jjjjj} = 5\chi_{jjkkk} = 15\chi_{jjkkll}, \tag{A.22}$$

the fifth-order polarization is finally written

$$\begin{aligned} P_j^{(5)+}(t) = \frac{5\varepsilon_0}{16}\chi_{jjjjj}(\omega_0; -\omega_0, -\omega_0, \omega_0, \omega_0, \omega_0)\, e^{-i\omega_0 t} \times \\ \Big[|A_j(t)|^4 A_j(t) + \frac{3}{5}|A_k(t)|^4 A_j(t) + \frac{6}{5}|A_j(t)|^2 |A_k(t)|^2 A_j(t) \\ + \frac{2}{5}|A_k(t)|^2 A_k^2(t) A_j^*(t) + \frac{3}{5}A_j^{*2}(t) A_k^2(t) A_j(t) + + \frac{1}{5}A_j^2(t) A_k^{*2}(t) A_j(t) \\ + \frac{2}{5}|A_k(t)|^2 A_l^2(t) A_j^*(t) + \frac{1}{5}A_k^{*2}(t) A_l^2(t) A_j(t) + \frac{2}{5}|A_k(t)|^2 |A_l(t)|^2 A_j(t) \Big]. \end{aligned} \tag{A.23}$$

A similar result has been obtained previously [226]. The first three and last terms are phase-independent and give rise to fifth-order self- and cross-nonlinear refraction. The second line contains phase-dependent couplings between two polarizations. These terms are rigorously absent for the orthogonal circular polarization basis set [226], and are neglected here under the assumption of differing phase velocities between the orthogonally-polarized linear eigenmodes of a slab waveguide. The last three terms contain all three field components and can be neglected. This is justified in the multiple-scales analysis where it is shown that, in the paraxial approximation, the projection of the field onto the direction of propagation is one order smaller than the transverse projections and therefore, in the fifth-order polarization, all three components do not enter to the order of the derivation.

Appendix B

The Raman Response Function and Raman Susceptibility

This appendix examines the third-order nonlinear response given by

$$P_j^{(3)}(\mathbf{r},t) = \varepsilon_0 R^{\mathrm{K}}_{jklm}(\mathbf{r})E_k(\mathbf{r},t)E_l(\mathbf{r},t)E_m(\mathbf{r},t) + \varepsilon_0 \int_0^\infty R^{\mathrm{R}}_{jklm}(\mathbf{r},\tau)E_k(\mathbf{r},t-\tau)E_l(\mathbf{r},t-\tau)E_m(\mathbf{r},t)d\tau, \tag{B.1}$$

which consists of instantaneous (Kerr) and delayed (Raman) parts. Specifically, the second term, or the Raman response, is examined in detail here. The spatial dependence will be dropped in what follows.

The first section presents a classical derivation of the Raman susceptibility based upon a simple spring-mass model for molecular vibration. The second section derives the Raman gain coefficient which is the quantity measured experimentally. The final section takes the third-order polarization given by equation B.1 and approximates the convolution integral for finite-bandwidth excitation. The resulting form is more suitable for analytic representation.

B.1 Origin of The Raman Response

The Raman response typically arises from the motion of a molecule in response to a driving electromagnetic field. This is in contrast to the electronic response which involves oscillation of the electron cloud relative to the nucleus, producing a radiating dipole. A molecule can undergo rotational or vibrational motion, but since this thesis is mainly concerned with nonlinear media in the solid-state, it is assumed that the vibrational motion dominates.

In order to derive the Raman response function, assume that there are N identical harmonic oscillators per unit volume, where each oscillator represents one molecule. For simplicity, only the 1-D scalar case is considered so that the vibrational coordinate is represented by $X(t)$. Newton's second law [236] states that

$$m\frac{d^2X(t)}{dt^2} = F^{\mathrm{tot}}(t), \tag{B.2}$$

where m is the mass and, in the case of the harmonic oscillator (or simple spring-mass system), $F^{\mathrm{tot}}(t)$ represents the total force on the molecule and includes the force of the driving field and the natural restoring force via Hook's Law.

The electrical driving force on the molecule can be derived by first considering the electrostatic stored energy density [237]

$$\mathcal{E} = \frac{1}{2}\varepsilon\left[E(t)\cdot E(t)\right], \tag{B.3}$$

where ε is the total material dielectric constant. For simplicity, keeping only the contribution from molecular vibration, the dielectric constant can be written

$$\varepsilon = \varepsilon_0\left[1 + N\alpha(X)\right], \tag{B.4}$$

where ε_0 is the free-space dielectric constant, and α represents the molecular polarizability (not the linear absorption coefficient which is not considered in this Appendix), which is necessarily a function of the normal coordinate of vibration X, i.e. the

driving force is a function of the offset from the rest position. Taking a two-term Taylor expansion of the polarizability results in

$$\alpha(X) \approx \alpha_0 + X \left.\frac{\partial \alpha}{\partial X}\right|_{X=0}, \tag{B.5}$$

where α_0 is the polarizability at the rest position and the first derivative is the differential polarizability.

Now, the electrostatic stored energy can be written

$$\mathcal{E} = \frac{\varepsilon_0}{2}\left\{1 + N\left[\alpha_0 + X\left.\frac{\partial \alpha}{\partial X}\right|_{X=0}\right]\right\}[E(t)\cdot E(t)]. \tag{B.6}$$

The force exerted on a unit volume of polarizable material is then

$$F(t) = \frac{\partial \mathcal{E}}{\partial X} = \frac{\varepsilon_0}{2}\left.\frac{\partial \alpha}{\partial X}\right|_{X=0}[E(t)\cdot E(t)], \tag{B.7}$$

where the force is divided by N to represent the force per molecule. The total force can now be written

$$F^{\text{tot}}(t) = \frac{\varepsilon_0}{2}\left.\frac{\partial \alpha}{\partial X}\right|_{X=0}[E(t)\cdot E(t)] - kX(t). \tag{B.8}$$

Here, k is the spring constant representing the restoring force of the molecule.

The equation of motion for the oscillator is then

$$\frac{d^2X(t)}{dt^2} + \Omega_f^2 X(t) = \frac{\varepsilon_0\left[\frac{\partial \alpha}{\partial X}\right]_0[E(t)\cdot E(t)]}{2m}, \tag{B.9}$$

where the natural oscillation frequency $\Omega_f = \sqrt{k/m}$. With the inclusion of a phenomenological damping term proportional to the velocity of vibration, the equation of motion becomes

$$\frac{d^2X(t)}{dt^2} + \gamma\frac{dX(t)}{dt} + \Omega_f^2 X(z,t) = \frac{\varepsilon_0\left[\frac{\partial \alpha}{\partial X}\right]_0[E(t)\cdot E(t)]}{2m}. \tag{B.10}$$

which is the equation of motion for a damped harmonic oscillator. Transforming into the temporal frequency domain results in the solution

$$\left[-\Omega^2 - i\Omega\gamma + \Omega_f^2\right]\tilde{X}(\Omega) = \frac{\varepsilon_0\left[\frac{\partial \alpha}{\partial X}\right]_0}{2m}\mathcal{F}\{E(t)\cdot E(t)\}(\Omega)$$

$$\Rightarrow \tilde{X}(\Omega) = \frac{\varepsilon_0\left[\frac{\partial \alpha}{\partial X}\right]_0}{2m}\left\{\frac{\mathcal{F}\{E(t)\cdot E(t)\}(\Omega)}{\Omega_f^2 - \Omega^2 - i\Omega\gamma}\right\}, \tag{B.11}$$

which gives the expression for the molecular vibration spectrum.

Now, the material polarization is defined

$$P(t) = N\mu(t) \tag{B.12}$$

where the induced dipole moment of the molecule is

$$\begin{aligned}\mu(t) = \varepsilon_0\alpha(X)E(t) &\approx \varepsilon_0\left[\alpha_0 + X(t)\left.\frac{\partial \alpha}{\partial X}\right|_{X=0}\right]E(t)\\ &= \varepsilon_0\left[\alpha_0 + \mathcal{F}^{-1}\{\tilde{X}(\Omega)\}\left.\frac{\partial \alpha}{\partial X}\right|_{X=0}\right]E(t).\end{aligned} \tag{B.13}$$

The nonlinear part of the material polarization due to Raman scattering can be written

$$P_R^{(3)}(t) = \varepsilon_0\mathcal{F}^{-1}\{\chi^{\text{R}}(\Omega)\mathcal{F}\{E(t)\cdot E(t)\}(\Omega)\}E(t). \tag{B.14}$$

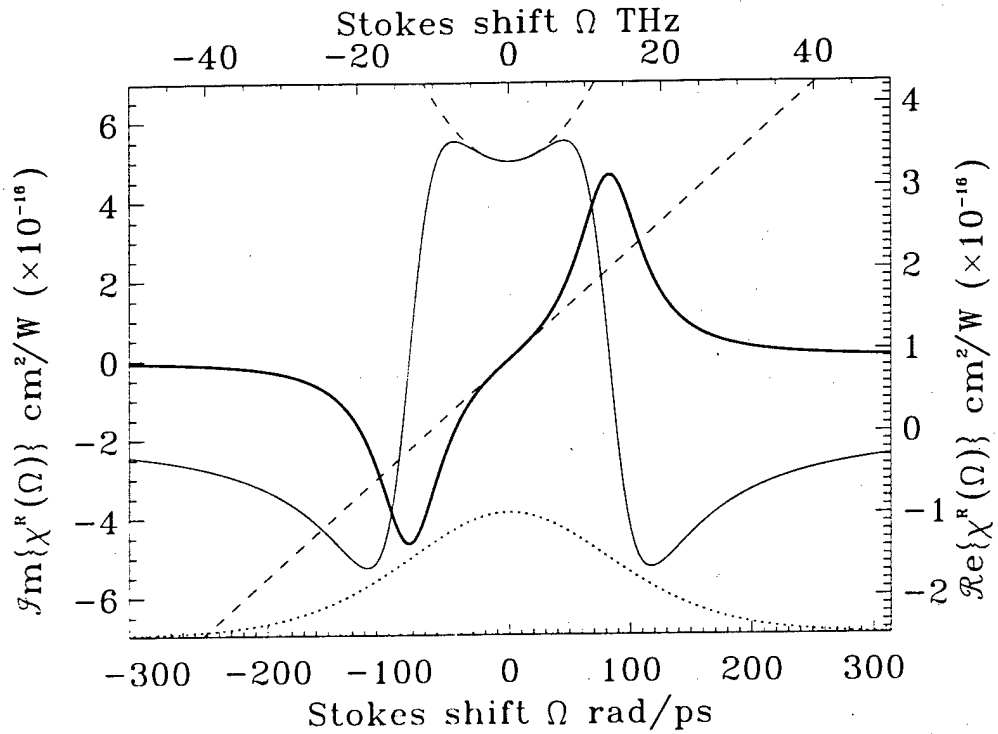

Figure B.1: Real and imaginary parts of the Raman susceptibility for fused silica. Here, γ = 10.4 THz = 65.6 rad/ps, Ω_f = 14.2 THz = 89.0 rad/ps, and, at $\lambda_f = 1.55\ \mu$m, $R_0 = 2.62 \times 10^{-12}$ cm^2/W · ps^2. The heavy solid curve is the imaginary part and the thin solid curve is the real part. For positive Stokes shift Ω, the imaginary part leads to gain, while for negative Stokes shift, the imaginary part leads to loss. The dashed curves indicate the three-term Taylor approximation which is valid within the range ± 5 THz. The dotted curve is the frequency-domain convolution of a 16.5 fs sech() pulse.

where the Raman susceptibility takes the form

$$\chi^R(\Omega) = \frac{\varepsilon_0 N}{2m}\left[\frac{\partial\alpha}{\partial X}\right]_0^2 \left\{\frac{1}{\Omega_f^2 - \Omega^2 - i\Omega\gamma}\right\} = \frac{R_0}{\Omega_f^2 - \Omega^2 - i\Omega\gamma}. \tag{B.15}$$

The real and imaginary parts of the Raman susceptibility appropriate for silica [141] are shown in Figure B.1. Note that for $\Omega \gg \Omega_f, \gamma$, the susceptibility $\chi^R(\Omega) \to 0$ because the time-scale of the driving field is too short for the molecule to respond.

Transforming back into the time domain

$$P_R^{(3)}(t) = \varepsilon_0 \left\{R^R(t) * [E(t)\cdot E(t)]\right\} E(t). \tag{B.16}$$

where the Raman response function is defined

$$R^R(t) = \mathcal{F}^{-1}\left\{\frac{R_0}{\Omega_f^2 - \Omega^2 - i\Omega\gamma}\right\} = \frac{R_0 e^{-\gamma t/2}\sin(\Omega_R t)\Theta(t)}{\Omega_R}, \tag{B.17}$$

and $\Omega_R = \sqrt{\Omega_f^2 - \gamma^2/4}$. Written in integral form

$$P_R^{(3)}(t) = \varepsilon_0 \int_0^\infty R^R(\tau)E(t-\tau)\cdot E(t-\tau)E(t)d\tau. \tag{B.18}$$

The Raman response function for silica is shown in Figure B.2.

B.2 The Raman Gain Spectrum

The previous section derived the form of the Raman susceptibility and Raman response functions for a single Lorentzian line. In typical experimental situations, the Raman susceptibility is mapped out by measuring the Raman gain versus the difference

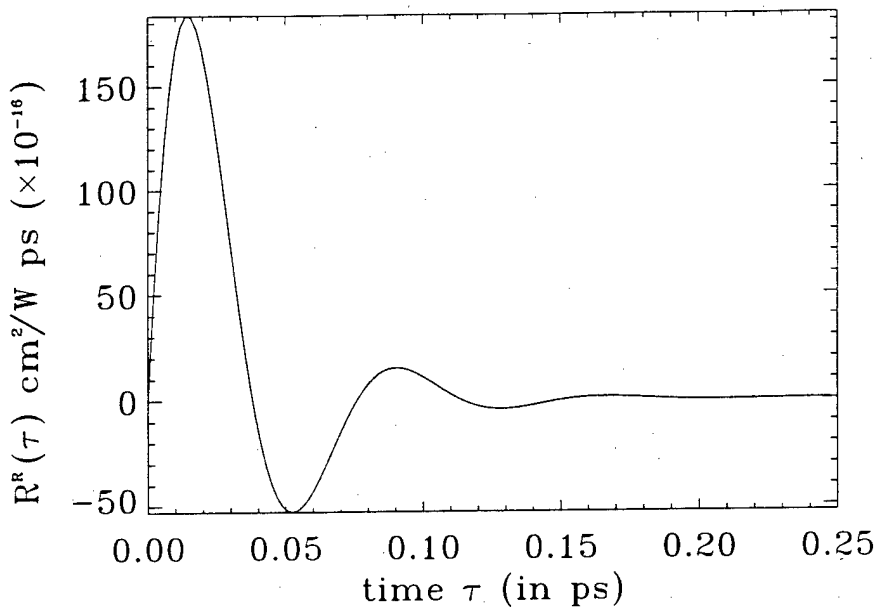

Figure B.2: Raman response function for fused silica: $\gamma = 65.6$ rad/ps, $\Omega_R = 13.2$ THz $= 82.7$ rad/ps, and, at $\lambda_f = 1.55\ \mu$m, $R_0 = 2.62 \times 10^{-12}\ \mathrm{cm^2/W \cdot ps^2}$.

frequency between two monochromatic beams: the pump beam and the probe (Stokes or anti-Stokes) beam. The probe beam experiences exponential gain or loss at the expense of the pump.

This theoretical treatment of Raman gain begins with the scalar nonlinear coupling between two monochromatic plane waves for simplicity

$$E(z,t) = \frac{1}{2}A_p(z)e^{i[k_p z - \omega_p t]} + \frac{1}{2}A_s(z)e^{i[k_s z - \omega_s t]} + \mathrm{cc}, \tag{B.19}$$

such that only the inter-pulse effects of stimulated Raman scattering are treated.

Since this analysis deals with monochromatic beams, the temporal frequency domain is the natural space in which to derive the Raman gain coefficient. Transforming the electric field then

$$\begin{aligned}\tilde{E}(z,\omega) = &\frac{1}{2}A_p(z)e^{ik_p z}\delta(\omega-\omega_p) + \frac{1}{2}A_p^*(z)e^{-ik_p z}\delta(\omega+\omega_p)\\ &+ \frac{1}{2}A_s(z)e^{ik_s z}\delta(\omega-\omega_s) + \frac{1}{2}A_s^*(z)e^{-ik_s z}\delta(\omega+\omega_s),\end{aligned} \tag{B.20}$$

and ignoring linear absorption and diffraction, the scalar nonlinear wave equation in the temporal frequency domain is

$$\begin{aligned}&\frac{\partial^2\tilde{E}(\omega)}{\partial z^2} + k^2(\omega)\tilde{E}(\omega) + \frac{\omega^2}{c^2}\chi^{\mathrm{K}}(\omega;\omega,\omega,\omega)\tilde{E}(\omega)\tilde{E}(\omega)\tilde{E}(\omega)\\ &+ \frac{\omega^2}{c^2}\int\int\chi^{\mathrm{R}}(\omega;\Omega)\tilde{E}(\omega_1)\tilde{E}(\omega_2)\tilde{E}(\omega-\Omega)d\omega_1 d\omega_2 = 0,\end{aligned} \tag{B.21}$$

where $\Omega = \omega_1 + \omega_2$ and initially both the electronic Kerr and Raman susceptibilities are considered.

The nonlinear polarizations of interest are those that drive the wave equation at ω_p or ω_s. These polarizations are

$$\begin{aligned}\tilde{P}_K(\omega_p) = \frac{3\varepsilon_0}{8}\Big[&\chi^{\mathrm{K}}(\omega_p;-\omega_p,\omega_p,\omega_p)\,|A_p|^2\\ &+2\chi^{\mathrm{K}}(\omega_p;-\omega_s,\omega_s,\omega_p)\,|A_s|^2\Big]A_p e^{ik_p z}\end{aligned} \tag{B.22}$$

$$\tilde{P}_K(\omega_s) = \frac{3\varepsilon_0}{8}\Big[\chi^{\mathrm{K}}(\omega_s;-\omega_s,\omega_s,\omega_s)\,|A_s|^2 \tag{B.23}$$

$$+2\chi^{K}(\omega_s;-\omega_p,\omega_p,\omega_s)\,|A_p|^2\Big]\,A_s e^{ik_s z}$$

$$\begin{aligned}\tilde{P}_R(\omega_p) = \frac{\varepsilon_0}{8}\int\int \chi^{R}(\omega;\Omega)\,\big[&A_p^* A_p\delta(\omega_1+\omega_p)\delta(\omega_2-\omega_p)\\ &+A_p A_p^*\delta(\omega_1-\omega_p)\delta(\omega_2+\omega_p)\big]\,A_p\delta(\omega-\Omega-\omega_p)e^{ik_p z}d\omega_1 d\omega_2\\ +\frac{\varepsilon_0}{8}\int\int \chi^{R}(\omega;\Omega)\,\big[&A_s^* A_s\delta(\omega_1+\omega_s)\delta(\omega_2-\omega_s)\\ &+A_s A_s^*\delta(\omega_1-\omega_s)\delta(\omega_2+\omega_s)\big]\,A_p\delta(\omega-\Omega-\omega_p)e^{ik_p z}d\omega_1 d\omega_2\\ +\frac{\varepsilon_0}{8}\int\int \chi^{R}(\omega;\Omega)\,\big[&A_p A_s^*\delta(\omega_1-\omega_p)\delta(\omega_2+\omega_s)\\ &+A_s^* A_p\delta(\omega_1+\omega_s)\delta(\omega_2-\omega_p)\big]\,A_s\delta(\omega-\Omega-\omega_s)e^{ik_p z}d\omega_1 d\omega_2\end{aligned} \tag{B.24}$$

$$\begin{aligned}\tilde{P}_R(\omega_s) = \frac{\varepsilon_0}{8}\int\int \chi^{R}(\omega;\Omega)\,\big[&A_s^* A_s\delta(\omega_1+\omega_s)\delta(\omega_2-\omega_s)\\ &+A_s A_s^*\delta(\omega_1-\omega_s)\delta(\omega_2+\omega_s)\big]\,A_s\delta(\omega-\Omega-\omega_s)e^{ik_s z}d\omega_1 d\omega_2\\ +\frac{\varepsilon_0}{8}\int\int \chi^{R}(\omega;\Omega)\,\big[&A_p^* A_p\delta(\omega_1+\omega_p)\delta(\omega_2-\omega_p)\\ &+A_p A_p^*\delta(\omega_1-\omega_p)\delta(\omega_2+\omega_p)\big]\,A_s\delta(\omega-\Omega-\omega_s)e^{ik_s z}d\omega_1 d\omega_2\\ +\frac{\varepsilon_0}{8}\int\int \chi^{R}(\omega;\Omega)\,\big[&A_s A_p^*\delta(\omega_1-\omega_s)\delta(\omega_2+\omega_p)\\ &+A_p^* A_s\delta(\omega_1+\omega_p)\delta(\omega_2-\omega_s)\big]\,A_p\delta(\omega-\Omega-\omega_p)e^{ik_s z}d\omega_1 d\omega_2,\end{aligned} \tag{B.25}$$

where the intrinsic symmetry property was used in the instantaneous polarization and the four-wave mixing terms ($2\omega_p-\omega_s$, etc) are neglected. Evaluation of the Raman susceptibility integrals results in

$$\tilde{P}_R(\omega_p) = \frac{\varepsilon_0}{4}\Big\{\chi^{R}(\omega_p;0)\,|A_p|^2+\big[\chi^{R}(\omega_p;0)+\chi^{R}(\omega_p;\omega_p-\omega_s)\big]\,|A_s|^2\Big\}A_p e^{ik_p z} \tag{B.26}$$

$$\tilde{P}_R(\omega_s) = \frac{\varepsilon_0}{4}\Big\{\chi^{R}(\omega_s;0)\,|A_s|^2+\big[\chi^{R}(\omega_s;0)+\chi^{R}(\omega_s;\omega_s-\omega_p)\big]\,|A_p|^2\Big\}A_s e^{ik_s z}. \tag{B.27}$$

Defining the nonlinear indices

$$n_K(\omega) = \frac{3}{8n(\omega)}\mathcal{R}e\left\{\chi^{K}(\omega;-\omega,\omega,\omega)\right\} \tag{B.28}$$

$$n_R(\omega,\Omega) = \frac{1}{4n(\omega)}\mathcal{R}e\left\{\chi^{R}(\omega;\Omega)\right\}, \tag{B.29}$$

where $\Omega=\omega_p-\omega_s$, and making the slowly-varying amplitude approximation (SVAA)

$$\frac{\partial^2 A_{p,s}}{\partial z^2} \ll 2ik_{p,s}\frac{\partial A_{p,s}}{\partial z}, \tag{B.30}$$

the coupled nonlinear evolution equations become

$$\begin{aligned}2ik_p\frac{\partial A_p}{\partial z}+2k_p^2\frac{n_K(\omega_p)}{n(\omega_p)}\Bigg\{&\left[1+\frac{n_R(\omega_p,0)}{n_K(\omega_p)}\right]|A_p|^2\\ &+\left[2+\frac{n_R(\omega_p,0)+n_R(\omega_p,\Omega)}{n_K(\omega_p)}\right]|A_s|^2\Bigg\}A_p\\ +i\frac{3\omega_p^2}{4c^2}&Im\left\{\chi^{K}(\omega_p;-\omega_p,\omega_p,\omega_p)\right\}|A_p|^2A_p\\ +i\frac{3\omega_p^2}{4c^2}&\left[2\,Im\left\{\chi^{K}(\omega_p;-\omega_s,\omega_s,\omega_p)\right\}+\frac{2}{3}Im\left\{\chi^{R}(\omega_p;\Omega)\right\}\right]|A_s|^2A_p=0\end{aligned} \tag{B.31}$$

$$
\begin{aligned}
2ik_s\frac{\partial A_s}{\partial z} + 2k_s^2\frac{n_K(\omega_s)}{n(\omega_s)}\Bigg\{&\left[1+\frac{n_R(\omega_s,0)}{n_K(\omega_s)}\right]|A_s|^2 \\
&+\left[2+\frac{n_R(\omega_s,0)+n_R(\omega_s,-\Omega)}{n_K(\omega_s)}\right]|A_p|^2\Bigg\}A_s \\
&+ i\frac{3\omega_s^2}{4c^2}Im\left\{\chi^{\mathrm{K}}(\omega_s;-\omega_s,\omega_s,\omega_s)\right\}|A_s|^2A_s \\
&+ i\frac{3\omega_s^2}{4c^2}\left[2Im\left\{\chi^{\mathrm{K}}(\omega_s;-\omega_p,\omega_p,\omega_s)\right\}+\frac{2}{3}Im\left\{\chi^{\mathrm{R}}(\omega_s;-\Omega)\right\}\right]|A_p|^2A_s = 0,
\end{aligned}
\tag{B.32}
$$

where $Im\left\{\chi^K\right\}$ corresponds to self- and cross-two-photon absorption and is always negative, and the Raman gain/loss susceptibility component given by $Im\left\{\chi^{\mathrm{R}}(\omega;0)\right\} = 0$ by (anti) symmetry. Note that now the ratio between the cross- and self-phase modulation coefficients no longer equals 2 in general, a fact previously noted [238].

Considering only the imaginary part of the Raman susceptibility responsible for Raman gain for simplicity, the coupled equations can be rewritten

$$\frac{\partial A_p}{\partial z} = -\frac{k_p}{4n_p^2}Im\left\{\chi^{\mathrm{R}}(\omega_p;\Omega)\right\}|A_s|^2A_p \tag{B.33}$$

$$\frac{\partial A_s}{\partial z} = \frac{k_s}{4n_s^2}Im\left\{\chi^{\mathrm{R}}(\omega_s;\Omega)\right\}|A_p|^2A_s, \tag{B.34}$$

where $n_p = n(\omega_p)$, $n_s = n(\omega_s)$ and $Im\left\{\chi^{\mathrm{R}}(-\Omega)\right\} = -Im\left\{\chi^{\mathrm{R}}(\Omega)\right\}$ from equation B.60.

Multiplying equation B.33 by A_p^* and adding to the conjugate of equation B.33 multiplied by A_p results in

$$\frac{\partial|A_p|^2}{\partial z} = -\frac{k_p}{2n_p^2}Im\left\{\chi^{\mathrm{R}}(\omega_p;\Omega)\right\}|A_s|^2|A_p|^2. \tag{B.35}$$

Defining the optical intensity

$$I(\omega) = \frac{\varepsilon_0 cn(\omega)}{2}|A(\omega)|^2, \tag{B.36}$$

equation B.35 can be rewritten

$$\frac{\partial I_p}{\partial z} = -\frac{k_p}{\varepsilon_0 cn_p^2 n_s}Im\left\{\chi^{\mathrm{R}}(\omega_p;\Omega)\right\}I_sI_p. \tag{B.37}$$

Performing the same steps with equation B.34 results in

$$\frac{\partial I_s}{\partial z} = \frac{k_s}{\varepsilon_0 cn_s^2 n_p}Im\left\{\chi^{\mathrm{R}}(\omega_s;\Omega)\right\}I_pI_s. \tag{B.38}$$

Adding these two equations in order to obtain the evolution of the total optical intensity indicates that intensity is not conserved. Since the interacting fields are monochromatic plane waves, this directly implies that optical energy is not conserved, because energy is supplied to molecular oscillations, then dissipated through the damping term.

What is conserved by this system of equations is total photon number. Defining the photon flux

$$\Phi(\omega) = \frac{\varepsilon_0 cn(\omega)}{2\hbar\omega}|A(\omega)|^2, \tag{B.39}$$

the coupled equations for the evolution of the photon flux are

$$\frac{\partial\Phi_p}{\partial z} = -\frac{k_pk_s}{\varepsilon_0 n_p^2 n_s^2}Im\left\{\chi^{\mathrm{R}}(\omega_p;\Omega)\right\}\Phi_s\Phi_p \tag{B.40}$$

$$\frac{\partial\Phi_s}{\partial z} = \frac{k_sk_p}{\varepsilon_0 n_s^2 n_p^2}Im\left\{\chi^{\mathrm{R}}(\omega_s;\Omega)\right\}\Phi_p\Phi_s \tag{B.41}$$

where it is apparent that total photon number is conserved.

Now, back to the original purpose of defining the Raman gain coefficient. Typically, when $|A_p|^2 \gg |A_s|^2$, the depletion of the pump is negligible, reducing the coupled equations to just

$$\frac{\partial A_s(z)}{\partial z} = \frac{k_s}{4n_s^2}Im\left\{\chi^{\mathrm{R}}(\omega_s;\Omega)\right\}|A_p(0)|^2A_s(z), \tag{B.42}$$

where the z dependence has been restored. Now equation B.42 can be easily solved

$$A_s(z) = e^{\frac{1}{2}G_R z} A_s(0), \tag{B.43}$$

where the Raman gain is defined as

$$G_R \equiv \frac{k_s}{2n_s^2} Im\left\{\chi^{\mathrm{R}}(\omega_s;\Omega)\right\} |A_p|^2 = g_R I_p. \tag{B.44}$$

The quantity typically reported in the literature as the Raman gain constant is, from equation B.38,

$$g_R \equiv \frac{k_s}{\varepsilon_0 c n_s^2 n_p} Im\left\{\chi^{\mathrm{R}}(\omega_s;\Omega)\right\}, \tag{B.45}$$

and has units of cm/W. For example, in silica-core fiber, a gain constant of $g_R = 1.86 \times 10^{-11}$ cm/W was measured for the peak Stokes shift of 13.2 THz (440 cm^{-1}) with a pump wavelength of 532 nm [141], and in $Al_{0.24}Ga_{0.76}As$ slab waveguide, a gain constant of $g_R = 7 \times 10^{-8}$ cm/W was measured for a peak shift of 8.4 THz (280 cm^{-1}) with pump wavelength 515 nm [151].

For the Raman susceptibility given by equation B.15, the real and imaginary parts are

$$\mathcal{R}e\left\{\chi^{\mathrm{R}}(\Omega)\right\} = \frac{R_0\left[\Omega_f^2 - \Omega^2\right]}{\left[\Omega_f^2 - \Omega^2\right]^2 + \Omega^2\gamma^2} \tag{B.46}$$

$$Im\left\{\chi^{\mathrm{R}}(\Omega)\right\} = \frac{R_0\Omega\gamma}{\left[\Omega_f^2 - \Omega^2\right]^2 + \Omega^2\gamma^2}, \tag{B.47}$$

so that the Raman gain constant can be written

$$g_R = \frac{R_0 k_p}{\varepsilon_0 c n_s n_p^2} \cdot \frac{\Omega\gamma}{\left[\Omega_f^2 - \Omega^2\right]^2 + \Omega^2\gamma^2}. \tag{B.48}$$

The peak of the imaginary part occurs at the frequency

$$\Omega_{\max} = \sqrt{\frac{2\Omega_f^2 - \gamma^2 + \left[\gamma^4 - 4\gamma^2\Omega_f^2 + 16\Omega_f^4\right]^{1/2}}{6}}. \tag{B.49}$$

For weak damping $\gamma \ll \Omega_{\max}$, the frequency at peak gain $\Omega_{\max} \approx \Omega_R \approx \Omega_f$, and the line width of the gain $\approx \gamma$. It is useful to obtain an expression for Ω_f. Solving equation B.49 then,

$$\Omega_f^2 = \Omega_{\max}\sqrt{\gamma^2 + 4\Omega_{\max}^2} - \Omega_{\max}^2, \tag{B.50}$$

so that Ω_f can be determined when the line width γ and peak down-shift $\Omega_{\max}$ are known, which can be easily obtained from experimental data.

The resonance approximation to equation B.15 is common in the literature. Taking $\Omega \approx \Omega_f$ and after a series of straightforward manipulations, the susceptibility reduces to

$$\chi_R(\Omega) \approx \frac{R_0/\Omega}{2\left[\Omega_f - \Omega\right] - i\gamma}, \tag{B.51}$$

with real and imaginary parts

$$\mathcal{R}e\left\{\chi^{\mathrm{R}}(\Omega)\right\} \approx \frac{R_0\left[\Omega_f - \Omega\right]/\Omega}{4\left[\Omega_f - \Omega\right]^2 + \gamma^2} \tag{B.52}$$

$$Im\left\{\chi^{\mathrm{R}}(\Omega)\right\} \approx \frac{R_0\gamma/\Omega}{4\left[\Omega_f - \Omega\right]^2 + \gamma^2}. \tag{B.53}$$

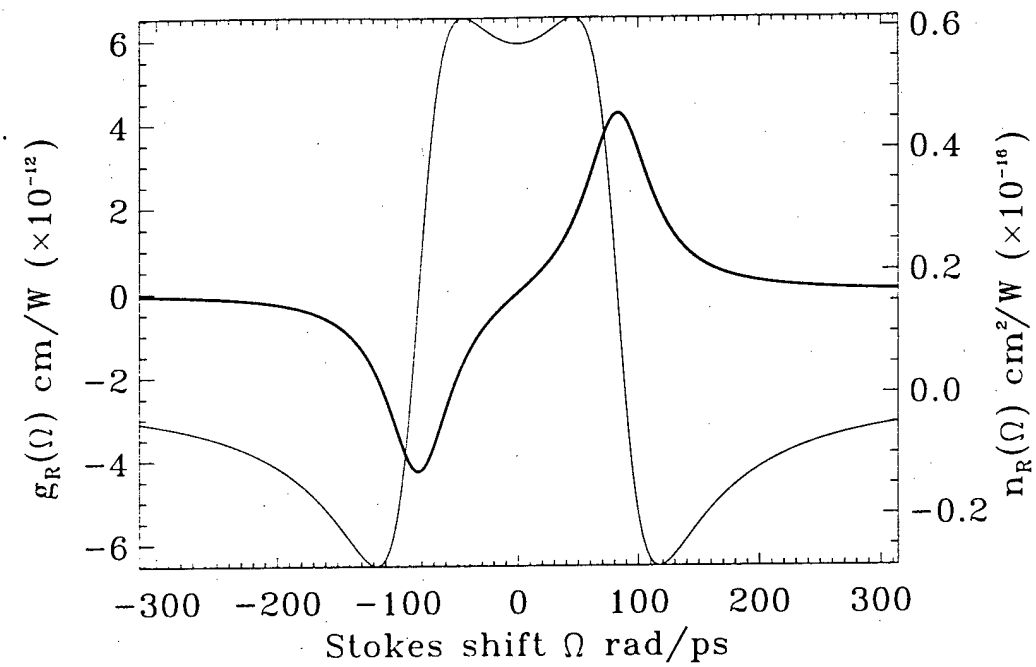

Figure B.3: Raman gain and index spectra for fused silica, calculated from the data in Figure B.1. The Raman index is defined by equation B.29, and the Raman gain constant is defined by equation B.45.

Now, the Raman gain coefficient for the Stokes beam becomes

$$g_R(\Omega) \approx \frac{R_0 \gamma k_p}{\varepsilon_0 c n_s n_p^2} \cdot \frac{1/\Omega}{\left[\Omega_f - \Omega\right]^2 + \gamma^2/4}. \tag{B.54}$$

The Stokes down-shift frequency that experiences maximum gain is then given by

$$\Omega_{\max} \approx \frac{4\Omega_f + \sqrt{4\Omega_f^2 - 3\gamma^2}}{6}. \tag{B.55}$$

Note from equation B.15 that R_0 has units of $m^2/V^2 \cdot s^2$. In the International System (SI) of units, the free-space dielectric constant has the value $\varepsilon_0 = 8.854 \times 10^{-12}$ $C^2/N{\cdot}m^2$, which also has units F/m, or $W{\cdot}s/V^2{\cdot}m$. For silica fiber, $R_0 = 5.03 \times 10^{-15}$ $cm^2 \cdot V^{-2} \cdot s^2$ which for $\lambda_f = 1.55\ \mu m$, equals 2.62×10^{-12} $cm^2/W \cdot ps^2$.

B.3 The Raman Susceptibility

Using the same steps as used for the linear material polarization in section 3.1.1, the Raman response integral is transformed into the temporal frequency domain. The frequency-domain representation is approximated for finite bandwidth excitation and transformed back into the time domain in a form that can be easily incorporated into the theory and numerics of subsequent chapters. This result is compared to that obtained directly from the Taylor-expansion of the time-domain form of equation B.1. Finally, using the results of Appendix A, the third-order polarization is reduced to a form suitable for the isotropic and cubic $\bar{4}3m$ symmetry classes. Section A.2 discusses the intrinsic permutation symmetry property of the fully dispersive case and the reduction to the Raman response, and the spatial symmetry properties of the chosen classes as they relate to $\chi^{(3)}$.

Writing the driving fields in their Fourier-domain representation, the Raman response of equation B.1 becomes

$$\begin{aligned} P_{Rj}^{(3)}(t) &= \varepsilon_0 \int_0^\infty R_{jklm}^{\mathrm{R}}(\tau) \int \tilde{E}_k(\omega_1) e^{-i\omega_1[t-\tau]} d\omega_1 \int \tilde{E}_l(\omega_2) e^{-i\omega_2[t-\tau]} d\omega_2 E_m(t) d\tau \\ &= \varepsilon_0 \int \int \chi_{jklm}^{\mathrm{R}}(\omega;\Omega) \tilde{E}_k(\omega_1) \tilde{E}_l(\omega_2) E_m(t) e^{-i\Omega t} d\omega_1 d\omega_2, \end{aligned} \tag{B.56}$$

where $\Omega = \omega_1 + \omega_2$ is the Stokes ($\Omega < 0$) or anti-Stokes ($\Omega > 0$) frequency and the third-order Raman nonlinear susceptibility is defined

$$\chi^{\mathrm{R}}_{jklm}(\omega;\Omega) \equiv \int \Theta(\tau) R^{\mathrm{R}}_{jklm}(\tau) e^{i\Omega\tau} d\tau \tag{B.57}$$

and $\chi^{\mathrm{R}}_{jklm}(-\Omega) = \chi^{\mathrm{R}*}_{jklm}(\Omega)$ because the Raman response function is real. It is evident that the Raman susceptibility is subject to the Kramers-Kronig relation discussed in the context of the linear susceptibility.

The imaginary part of the susceptibility $Im\left\{\chi^{\mathrm{R}}(\Omega)\right\}$, where $\chi_R(\Omega) = \mathcal{R}e\left\{\chi^{\mathrm{R}}(\Omega)\right\} + iIm\left\{\chi^{\mathrm{R}}(\Omega)\right\}$, is proportional to the Raman gain, which is typically the quantity measured in experiments, as discussed in the previous section. Therefore, it is useful to have a relationship between the imaginary part of the Raman susceptibility and the Raman response function. The inverse Fourier transform of equation B.57 results in

$$R^{\mathrm{R}}(\tau)\Theta(\tau) = \int \chi^{\mathrm{R}}(\omega;\Omega) e^{-i\Omega\tau} d\Omega. \tag{B.58}$$

Through the Kramers-Kronig relation, the real part of the Raman susceptibility can be determined from the imaginary part and the response function evaluated by relation B.58. Alternatively, the Raman response function can be determined directly from $Im\left\{\chi^{\mathrm{R}}(\Omega)\right\}$. Since the Raman response function is real, by equation B.57, the real part of the Raman susceptibility is symmetric and the imaginary part anti-symmetric. Note that equation B.58 can be rewritten

$$\begin{aligned} R^{\mathrm{R}}(\tau)\Theta(\tau) &= \int \left[\mathcal{R}e\left\{\chi^{\mathrm{R}}(\omega;\Omega)\right\} + iIm\left\{\chi^{\mathrm{R}}(\omega;\Omega)\right\}\right]\left[\cos(\Omega\tau) - i\sin(\Omega\tau)\right] d\Omega \\ &= \int \mathcal{R}e\left\{\chi^{\mathrm{R}}(\omega;\Omega)\right\}\cos(\Omega\tau) d\Omega + \int Im\left\{\chi^{\mathrm{R}}(\omega;\Omega)\right\}\sin(\Omega\tau) d\Omega, \end{aligned} \tag{B.59}$$

where the anti-symmetric terms integrate to zero. Because the left-hand side of the equation is zero when $\tau < 0$, it must be true that the two integrals on the right-hand side are equal and opposite when $\tau < 0$, leading to the relation

$$\begin{aligned} R^{\mathrm{R}}(\tau)\Theta(\tau) &= 2\int \mathcal{R}e\left\{\chi^{\mathrm{R}}(\omega;\Omega)\right\}\cos(\Omega\tau) d\Omega \\ &= 2\int Im\left\{\chi^{\mathrm{R}}(\omega;\Omega)\right\}\sin(\Omega\tau) d\Omega, \end{aligned} \tag{B.60}$$

when $\tau > 0$.

The nonlinear polarization is now written in the temporal frequency domain

$$\begin{aligned} \tilde{P}^{(3)}_{Rj}(\omega) &= \varepsilon_0 \int\int\int \chi^{\mathrm{R}}_{jklm}(\omega;\Omega)\tilde{E}_k(\omega_1)\tilde{E}_l(\omega_2)E_m(t)e^{-i\Omega t} d\omega_1 d\omega_2 e^{i\omega t} dt \\ &= \varepsilon_0 \int\int \chi^{\mathrm{R}}_{jklm}(\omega;\Omega)\tilde{E}_k(\omega_1)\tilde{E}_l(\omega_2)\left\{\int E_m(t)e^{i[\omega-\Omega]t} dt\right\} d\omega_1 d\omega_2 \\ &= \varepsilon_0 \int\int \chi^{\mathrm{R}}_{jklm}(\omega;\Omega)\tilde{E}_k(\omega_1)\tilde{E}_l(\omega_2)\tilde{E}_m(\omega-\Omega) d\omega_1 d\omega_2. \end{aligned} \tag{B.61}$$

Using the Fourier-domain wavepacket representation and keeping only the terms producing a polarization near ω_0, e.g. the terms responsible for nonlinear refraction and nonlinear gain/absorption, the polarization becomes

$$\begin{aligned} \tilde{P}^{(3)+}_{Rj}(\omega) = \frac{\varepsilon_0}{8}\int\int \chi^{\mathrm{R}}_{jklm}(\omega;\Omega) \times \\ \left[\tilde{A}^*_k(\omega_1+\omega_0)\tilde{A}_l(\omega_2-\omega_0)\tilde{A}_m(\omega-\Omega-\omega_0) + \right. \\ \tilde{A}_k(\omega_1-\omega_0)\tilde{A}^*_l(\omega_2+\omega_0)\tilde{A}_m(\omega-\Omega-\omega_0) + \\ \left.\tilde{A}_k(\omega_1-\omega_0)\tilde{A}_l(\omega_2-\omega_0)\tilde{A}^*_m(\omega-\Omega+\omega_0)\right] d\omega_1 d\omega_2, \end{aligned} \tag{B.62}$$

where $j,k,l,m \in \{x,y,z\}$. The Raman response is typically at low frequencies (when compared to optical frequencies), for example, the peak of the Raman gain in fused silica is at 13.2 THz. Therefore the strongest response will occur when Ω is near that peak. For the last term of equation B.62, $\Omega \approx 2\omega_0$ and $\chi_R(2\omega_0) \approx 0$ from section B.1.

In order to arrive at a simpler time-domain representation, the Raman susceptibility tensor of equation B.62 is Taylor-expanded about $\Omega = 0$. The Taylor expansion is

$$\chi^{\mathrm{R}}_{jklm}(\omega_0;\Omega) = \chi^{\mathrm{R}}_{jklm}(\omega_0;0) \tag{B.63}$$

$$+[\omega_1 \pm \omega_0] \left.\frac{\partial \chi^{\mathrm{R}}_{jklm}(\omega_0;\omega_1 \pm \omega_0)}{\partial \omega_1}\right|_{\omega_1=\mp\omega_0}$$

$$+[\omega_2 \mp \omega_0] \left.\frac{\partial \chi^{\mathrm{R}}_{jklm}(\omega_0;\mp\omega_0 + \omega_2)}{\partial \omega_2}\right|_{\omega_2=\pm\omega_0} + \cdots.$$

Using these expansions, the integral of the Raman susceptibility is approximated as

$$\begin{aligned}\tilde{P}^{(3)+}_{Rj}(\omega) = \frac{\varepsilon_0}{8}\int\int\left\{\chi^{\mathrm{R}} + [\omega_1+\omega_0]\chi^{\mathrm{R}'}_2 + [\omega_2-\omega_0]\chi^{\mathrm{R}'}_1 + \cdots\right\}\times \\ \tilde{A}^*_k(\omega_1+\omega_0)\tilde{A}_l(\omega_2-\omega_0)\tilde{A}_m(\mathbf{r},\omega-\Omega-\omega_0)d\omega_1 d\omega_2 \\ + \frac{\varepsilon_0}{8}\int\int\left\{\chi^{\mathrm{R}} + [\omega_1-\omega_0]\chi^{\mathrm{R}'}_1 + [\omega_2+\omega_0]\chi^{\mathrm{R}'}_2 + \cdots\right\}\times \\ \tilde{A}_k(\omega_1-\omega_0)\tilde{A}^*_l(\omega_2+\omega_0)\tilde{A}_m(\omega-\Omega-\omega_0)d\omega_1 d\omega_2\end{aligned} \tag{B.64}$$

where the following shorthand notation is used

$$\chi^{\mathrm{R}} = \chi^{\mathrm{R}}_{jklm}(\omega_0;0) \tag{B.65}$$

$$\chi^{\mathrm{R}'}_1 = \left.\frac{\partial \chi^{\mathrm{R}}_{jklm}(\omega_0;\omega_1-\omega_0)}{\partial \omega_1}\right|_{\omega_1=\omega_0} = \left.\frac{\partial \chi^{\mathrm{R}}_{jklm}(\omega_0;-\omega_0+\omega_2)}{\partial \omega_2}\right|_{\omega_2=\omega_0} \tag{B.66}$$

$$\chi^{\mathrm{R}'}_2 = \left.\frac{\partial \chi^{\mathrm{R}}_{jklm}(\omega_0;\omega_1+\omega_0)}{\partial \omega_1}\right|_{\omega_1=-\omega_0} = \left.\frac{\partial \chi^{\mathrm{R}}_{jklm}(\omega_0;\omega_0+\omega_2)}{\partial \omega_2}\right|_{\omega_2=-\omega_0}. \tag{B.67}$$

Now equation B.64 can be written in the time-domain. For example, inverse-transforming the first integral of equation B.64

$$\begin{aligned}P^{(3)+}_{Rj}(t) &= \frac{\varepsilon_0}{8}\chi^{\mathrm{R}}\int\int\int \tilde{A}^*_k(\omega_1+\omega_0)\tilde{A}_l(\omega_2-\omega_0)\times \\ &\qquad \tilde{A}_m(\omega-\omega_1-\omega_2-\omega_0)d\omega_1 d\omega_2 e^{-i\omega t}d\omega \\ &+ \frac{\varepsilon_0}{8}\chi^{\mathrm{R}'}_2\int\int\int [\omega_1+\omega_0]\tilde{A}^*_k(\omega_1+\omega_0)\tilde{A}_l(\omega_2-\omega_0)\times \\ &\qquad \tilde{A}_m(\omega-\omega_1-\omega_2-\omega_0)d\omega_1 d\omega_2 e^{-i\omega t}d\omega + \cdots \\ &= \frac{\varepsilon_0}{8}\chi^{\mathrm{R}}\int\int\int \tilde{A}_m(\omega')e^{-i\omega' t}d\omega'\tilde{A}^*_k(\omega_1+\omega_0)e^{-i\omega_1 t}d\omega_1\times \\ &\qquad \tilde{A}_l(\omega_2-\omega_0)e^{-i\omega_2 t}d\omega_2 e^{-i\omega_0 t} \\ &+ \frac{\varepsilon_0}{8}\chi^{\mathrm{R}'}_2\int\int\int \tilde{A}_m(\omega')e^{-i\omega' t}d\omega'[\omega_1+\omega_0]\tilde{A}^*_k(\omega_1+\omega_0)e^{-i\omega_1 t}d\omega_1\times \\ &\qquad \tilde{A}_l(\omega_2-\omega_0)e^{-i\omega_2 t}d\omega_2 e^{-i\omega_0 t} + \cdots \\ &= \frac{\varepsilon_0}{8}\left[\chi^{\mathrm{R}}A^*_k(t)A_l(t) + i\chi^{\mathrm{R}'}_2\frac{\partial A^*_k(t)}{\partial t}A_l(t) + \right. \\ &\qquad \left. i\chi^{\mathrm{R}'}_1 A^*_k(t)\frac{\partial A_l(t)}{\partial t} + \cdots\right]A_m(t)\,e^{-i\omega_0 t}.\end{aligned} \tag{B.68}$$

Using equation B.57, the coefficients

$$\chi^{\mathrm{R}'}_1 = \chi^{\mathrm{R}'}_2 = i\int \tau\Theta(\tau)R^{\mathrm{R}}_{jklm}(\tau)d\tau \equiv \chi^{\mathrm{R}'}. \tag{B.69}$$

Note that $\chi^{\mathrm{R}'}$ is purely imaginary because it is proportional to the slope of the Raman gain at zero frequency. Now the first term of the Raman polarization can be written

$$\begin{aligned}P^{(3)+}_{Rj} &= \frac{\varepsilon_0}{8}\left[\chi^{\mathrm{R}}A^*_k(t)A_l(t) + i\chi^{\mathrm{R}'}\frac{\partial A^*_k(t)A_l(t)}{\partial t} + \cdots\right]A_m(t)e^{-i\omega_0 t} \\ &= \frac{\varepsilon_0}{8}\chi^{\mathrm{R}}_{jklm}\left(\omega_0; i\frac{\partial}{\partial t}\right)[A^*_k(t)A_l(t)]A_m(t)e^{-i\omega_0 t},\end{aligned} \tag{B.70}$$

where the derivative argument acts on the quantity in brackets. Combining this expression with that obtained for the second integral in equation B.64 results in

$$P_{Rj}^{(3)+}(t) = \frac{\varepsilon_0}{8}\left\{\chi^{\mathrm{R}}_{jklm}\left(\omega_0; i\frac{\partial}{\partial t}\right)\left[A_k^*(t)A_l(t) + A_k(t)A_l^*(t)\right]\right\}A_m(t)e^{-i\omega_0 t}. \tag{B.71}$$

Here, the function of the operator is interpreted by a Taylor expansion about zero frequency.

An alternative approach is to start with the time-domain convolutional representation given by equation 3.18, rewritten here in component form

$$\begin{aligned} P_{Rj}^{(3)+}(t) &= \frac{\varepsilon_0}{8}\int_0^\infty R^{\mathrm{R}}_{jklm}(\tau)A_k^*(t-\tau)A_l(t-\tau)A_m(t)e^{-i\omega_0 t}d\tau \\ &+ \frac{\varepsilon_0}{8}\int_0^\infty R^{\mathrm{R}}_{jklm}(\tau)A_k(t-\tau)A_l^*(t-\tau)A_m(t)e^{-i\omega_0 t}d\tau. \end{aligned} \tag{B.72}$$

Defining $s = t - \tau$, the delayed fields can be Taylor-expanded about t

$$\begin{aligned} A(s) &= A(t) + [s-t]\left.\frac{\partial A(s)}{\partial s}\right|_{s=t} + \frac{[s-t]^2}{2}\left.\frac{\partial^2 A(s)}{\partial s^2}\right|_{s=t} + \cdots \\ &= A(t) - \tau\frac{\partial A(t)}{\partial t} + \frac{\tau^2}{2}\frac{\partial^2 A(t)}{\partial t^2} + \cdots. \end{aligned} \tag{B.73}$$

Substituting into the convolution integral results in

$$\begin{aligned} P_{Rj}^{(3)+}(t) &= \frac{\varepsilon_0}{8}\left[A_k^*(t)A_l(t) + A_k(t)A_l^*(t)\right]A_m(t)e^{-i\omega_0 t}\int_0^\infty R^{\mathrm{R}}_{jklm}(\tau)d\tau \\ &- \frac{\varepsilon_0}{8}\left[\frac{\partial A_k^*(t)A_l(t)}{\partial t} + \frac{\partial A_k(t)A_l^*(t)}{\partial t}\right]A_m(t)e^{-i\omega_0 t}\int_0^\infty \tau R^{\mathrm{R}}_{jklm}(\tau)d\tau \\ &+ \cdots. \end{aligned} \tag{B.74}$$

Using equation B.57, it is clear that equations B.71 and B.74 are the same. Defining the constant

$$T^{\mathrm{R}}_{jklm} \equiv -i\chi^{\mathrm{R}'} = \int_0^\infty \tau R^{\mathrm{R}}_{jklm}(\tau)d\tau, \tag{B.75}$$

equations B.71 and B.74 can be simplified to

$$\begin{aligned} P_{Rjklm}^{(3)+}(t) &= \frac{\varepsilon_0}{8}\chi^{\mathrm{R}}_{jklm}(\omega_0;0)\left[A_k^*(t)A_l(t) + A_k(t)A_l^*(t)\right]A_m(t)e^{-i\omega_0 t} \\ &- \frac{\varepsilon_0}{8}T^{\mathrm{R}}_{jklm}\left[\frac{\partial A_k^*(t)A_l(t)}{\partial t} + \frac{\partial A_k(t)A_l^*(t)}{\partial t}\right]A_m(t)e^{-i\omega_0 t} \\ &- \frac{\varepsilon_0}{16}\chi^{\mathrm{R}''}(\omega_0;0)\left[\frac{\partial^2 A_k^*(t)A_l(t)}{\partial t^2} + \frac{\partial^2 A_k(t)A_l^*(t)}{\partial t^2}\right]A_m(t)e^{-i\omega_0 t} + \cdots. \end{aligned} \tag{B.76}$$

The first-order term in the Raman expansion is a linear approximation to the Raman gain/loss curve. The second-order term is a parabolic approximation to the dispersion of the Raman nonlinear refractive index. The next correction for the Raman gain is third-order cubic as evident by the fact that the imaginary part of the susceptibility is anti-symmetric.

The total induced third-order polarization including the instantaneous and Raman contributions can then be written

$$\begin{aligned} P_{jklm}^{(3)+}(t) = \frac{\varepsilon_0}{8}\Big\{ & \chi^{\mathrm{K}}_{jklm}(\omega_0;-\omega_0,\omega_0,\omega_0)A_k^*(t)A_l(t)A_m(t) \\ & +\chi^{\mathrm{K}}_{jklm}(\omega_0;\omega_0,-\omega_0,\omega_0)A_k(t)A_l^*(t)A_m(t) \\ & +\chi^{\mathrm{K}}_{jklm}(\omega_0;\omega_0,\omega_0,-\omega_0)A_k(t)A_l(t)A_m^*(t) + \\ & +\chi^{\mathrm{R}}_{jklm}(\omega_0;0)\left[A_k^*(t)A_l(t) + A_k(t)A_l^*(t)\right]A_m(t)\Big\}e^{-i\omega_0 t} \\ & - \frac{\varepsilon_0}{8}T^{\mathrm{R}}_{jklm}\left[\frac{\partial A_k^*(t)A_l(t)}{\partial t} + \frac{\partial A_k(t)A_l^*(t)}{\partial t}\right]A_m(t)e^{-i\omega_0 t} \\ & - \frac{\varepsilon_0}{16}\chi^{\mathrm{R}''}_{jklm}(\omega_0;0)\left[\frac{\partial^2 A_k^*(t)A_l(t)}{\partial t^2} + \frac{\partial^2 A_k(t)A_l^*(t)}{\partial t^2}\right]A_m(t)e^{-i\omega_0 t}. \end{aligned} \tag{B.77}$$

Using the spatial and intrinsic symmetry reductions from section A.2, equation B.77 becomes

$$
\begin{aligned}
P_j^{(3)+}(t) = \frac{3\varepsilon_0}{8} \Big[& \chi^{\mathrm{K}}_{jjjj}(\omega_0; -\omega_0, \omega_0, \omega_0) A_j^*(t) A_j(t) A_j(t) \\
& + 2\chi^{\mathrm{K}}_{jkkj}(\omega_0; -\omega_0, \omega_0, \omega_0) A_k^*(t) A_k(t) A_j(t) \\
& + \chi^{\mathrm{K}}_{jjkk}(\omega_0; -\omega_0, \omega_0, \omega_0) A_j^*(t) A_k(t) A_k(t) \Big] e^{-i\omega_0 t} \\
+ \frac{\varepsilon_0}{4} \Big\{ & \Big[\chi^{\mathrm{R}}_{jjjj}(\omega_0; 0) A_j^*(t) A_j(t) + \chi^{\mathrm{R}}_{jkkj}(\omega_0; 0) A_k^*(t) A_k(t) \Big] A_j(t) \\
& + \chi^{\mathrm{R}}_{jjkk}(\omega_0; 0) \Big[A_k^*(t) A_j(t) + A_j^*(t) A_k(t) \Big] A_k(t) \Big\} e^{-i\omega_0 t} \\
- \frac{\varepsilon_0}{4} \Big\{ & \Big[T^{\mathrm{R}}_{jjjj} \frac{\partial A_j^*(t) A_j(t)}{\partial t} + T^{\mathrm{R}}_{jkkj} \frac{\partial A_k^*(t) A_k(t)}{\partial t} \Big] A_j(t) \\
& + T^{\mathrm{R}}_{jjkk} \Big[\frac{\partial A_k^*(t) A_j(t)}{\partial t} + \frac{\partial A_j^*(t) A_k(t)}{\partial t} \Big] A_k(t) \Big\} e^{-i\omega_0 t} \\
- \frac{\varepsilon_0}{8} \Big\{ & \Big[\chi^{\mathrm{R}''}_{jjjj} \frac{\partial^2 A_j^*(t) A_j(t)}{\partial t^2} + \chi^{\mathrm{R}''}_{jkkj} \frac{\partial^2 A_k^*(t) A_k(t)}{\partial t^2} \Big] A_j(t) \\
& + \chi^{\mathrm{R}''}_{jjkk} \Big[\frac{\partial^2 A_k^*(t) A_j(t)}{\partial t^2} + \frac{\partial^2 A_j^*(t) A_k(t)}{\partial t^2} \Big] A_k(t) \Big\} e^{-i\omega_0 t},
\end{aligned}
\tag{B.78}
$$

which is the form used in the multiple-scales analysis.

Appendix C

Derivation of the (2+1)-D Vector Nonlinear Schrödinger Equation for a Slab Waveguide

This appendix reduces the full (3+1)-D NLS evolution equation for nonlinear spatio-temporal propagation in homogeneous media to the (2+1)-D equation appropriate for propagation in a planar waveguide structure that supports TE and TM modes. The key to this derivation is the use of separation of variables in which the functional form of the one-dimensional linearly-guided profile is separated from the envelope in the unguided dimensions. To lowest order (sec. C.1), this separation of variables results in the well-known effective index approximation, which reduces the dimension of the problem. At higher orders, the concept of effective index is extended to the linear dispersive (secs. C.2 and C.3) and nonlinear terms (sec. C.3). The resulting nonlinear wave equation is the (2+1)-D reduced version of the (3+1)-D NLS equation (with the transverse dimension y removed), with effective values of the material parameters which represent the influence of the transversely guided modes.

Section D.2 of Appendix D evaluates the effective linear dispersion coefficients for a generic three-layer slab waveguide structure. The results of this analysis for typical waveguide parameters justify certain approximations made in this multiple-scales derivation in order to obtain an NLS equation for the waveguide modes.

The waveguide geometry is shown in Figure C.1. By symmetry, the waveguide supports two sets of modes, transverse electric (TE) and transverse magnetic (TM), which are of orthogonal linear polarizations. Thus, the use of the Cartesian polarization basis set is not arbitrary. The initial electric and magnetic field envelopes are written

$$\begin{aligned}\overline{\mathbf{A}}_1 = {} & \hat{x}\, U_x^{\mathrm{TE}}\left(y, \omega_0 + i\varepsilon\frac{\partial}{\partial T}\right) A_1^{\mathrm{TE}}(X, Z_i, T)e^{i\beta^{\mathrm{TE}}z} \\ & + \hat{y}\, V_y^{\mathrm{TM}}\left(y, \omega_0 + i\varepsilon\frac{\partial}{\partial T}\right) B_1^{\mathrm{TM}}(X, Z_i, T)e^{i\beta^{\mathrm{TM}}z} \\ & + \hat{z}\, V_z^{\mathrm{TM}}\left(y, \omega_0 + i\varepsilon\frac{\partial}{\partial T}\right) B_1^{\mathrm{TM}}(X, Z_i, T)e^{i\beta^{\mathrm{TM}}z}\end{aligned} \tag{C.1}$$

$$\begin{aligned}\overline{\mathbf{B}}_1 = {} & \frac{\hat{x}}{\eta^{\mathrm{TM}}} V_x^{\mathrm{TM}}\left(y, \omega_0 + i\varepsilon\frac{\partial}{\partial T}\right) B_1^{\mathrm{TM}}(X, Z_i, T)e^{i\beta^{\mathrm{TM}}z} \\ & + \frac{\hat{y}}{\eta^{\mathrm{TE}}} U_y^{\mathrm{TE}}\left(y, \omega_0 + i\varepsilon\frac{\partial}{\partial T}\right) A_1^{\mathrm{TE}}(X, Z_i, T)e^{i\beta^{\mathrm{TE}}z} \\ & + \frac{\hat{z}}{\eta^{\mathrm{TE}}} U_z^{\mathrm{TE}}\left(y, \omega_0 + i\varepsilon\frac{\partial}{\partial T}\right) A_1^{\mathrm{TE}}(X, Z_i, T)e^{i\beta^{\mathrm{TE}}z},\end{aligned} \tag{C.2}$$

such that the interaction between waveguide modes is handled explicitly by the choice of slowly-varying envelopes A_1^{TE} and B_1^{TM}. The waveguide mode profiles $\mathbf{U}^{\mathrm{TE}}$ and $\mathbf{V}^{\mathrm{TM}}$ are unitless with the components U_x^{TE} and V_x^{TM} normalized to unity. Therefore, the envelopes A_1^{TE} and B_1^{TM} have units V/m, while $A_1^{\mathrm{TE}}/\eta^{\mathrm{TE}}$ and $B_1^{\mathrm{TM}}/\eta^{\mathrm{TM}}$ have units of A/m. The constants $\eta^{\mathrm{TE}} = \mu_0\omega_0/\beta^{\mathrm{TE}}$ and $\eta^{\mathrm{TM}} = \mu_0\omega_0/\beta^{\mathrm{TM}}$ represent the material impedance seen by the TE and TM modes [239]. These impedances have units V/A = Ohms.

The frequency-dependence of $\mathbf{U}$ and $\mathbf{V}$ is included to describe the variation of guided profiles (and effective index) with wavelength, which simplifies the analysis [194]. Note that the waveguide modes do not have z variation. This approximation fixes the modes such that they cannot change with propagation and is valid when the induced nonlinear index is small compared to the linear index variation of the waveguide, which is the case assumed here. In fact, typical nonlinear index changes are on the

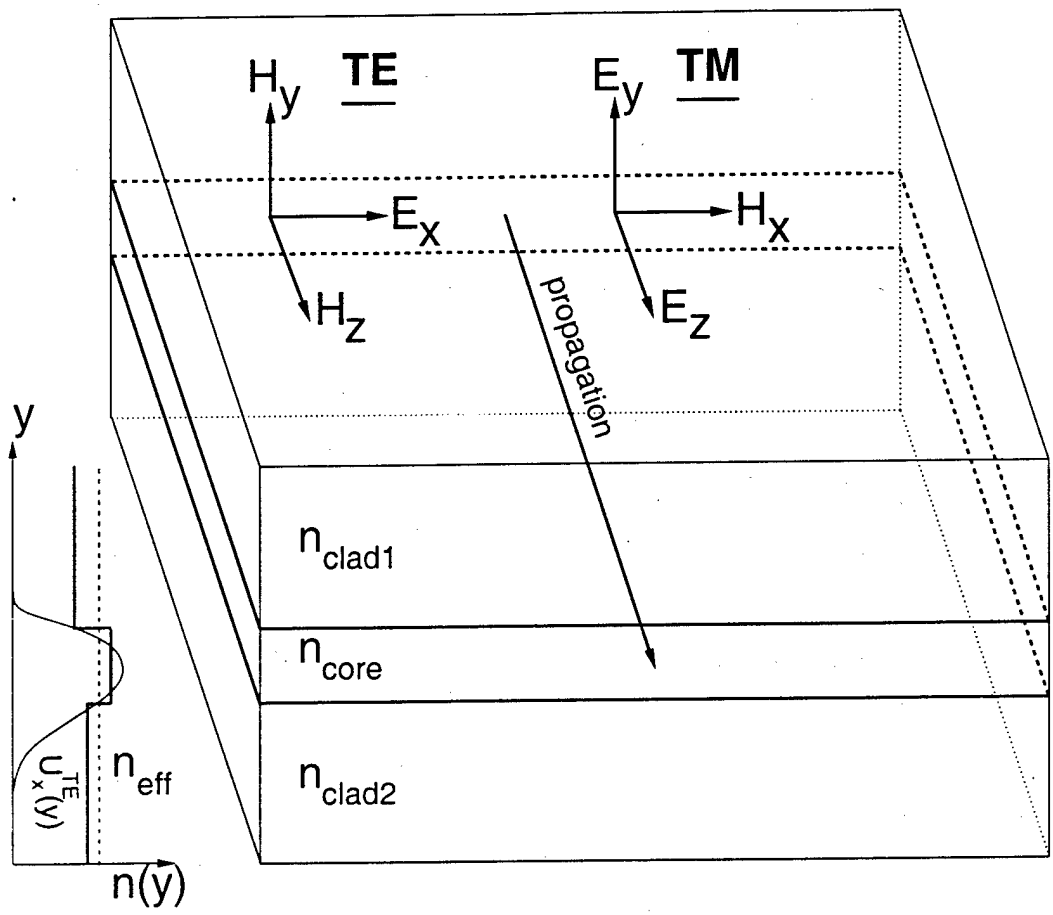

Figure C.1: Waveguide geometry used for (2+1)-D derivation. The linear refractive index varies along the y-direction, which gives rise to distinct sets of TE (electric field polarized along x) and TM (magnetic field polarized along x) modes.

order of $10^{-5} - 10^{-4}$, while weakly guiding waveguide structures have $\Delta n \sim 10^{-3} - 10^{-2}$. Only one TE and one TM mode are considered and are assumed to be fundamental modes (no zero crossings of the field), but this assumption is not a requirement for the general case derived here. Extension to multiple, higher-order modes, is straightforward [99], but not necessary in this thesis.

Guided modes typically have profile variations on the order of a few wavelengths, therefore y is taken to be a fast variable such that

$$\nabla = \hat{x}\varepsilon\frac{\partial}{\partial X} + \hat{y}\frac{\partial}{\partial y} + \hat{z}\left[\frac{\partial}{\partial z} + \varepsilon\frac{\partial}{\partial Z_1} + \varepsilon^2\frac{\partial}{\partial Z_2} + \cdots\right]. \tag{C.3}$$

Because of this change, Maxwell's equations need to be suitably modified. The modification of Faraday's and Ampere's Laws is straightforward:

$$\hat{x}: \quad \frac{\partial \overline{A}_z}{\partial y} - \left[\frac{\partial}{\partial z} + \varepsilon\frac{\partial}{\partial Z_1} + \cdots\right]\overline{A}_y = i\mu_0\left[\omega_0 + i\varepsilon\frac{\partial}{\partial T}\right]\overline{B}_x \tag{C.4}$$

$$\hat{y}: \quad \left[\frac{\partial}{\partial z} + \varepsilon\frac{\partial}{\partial Z_1} + \cdots\right]\overline{A}_x - \varepsilon\frac{\partial \overline{A}_z}{\partial X} = i\mu_0\left[\omega_0 + i\varepsilon\frac{\partial}{\partial T}\right]\overline{B}_y \tag{C.5}$$

$$\hat{z}: \quad \varepsilon\frac{\partial \overline{A}_y}{\partial X} - \frac{\partial \overline{A}_x}{\partial y} = i\mu_0\left[\omega_0 + i\varepsilon\frac{\partial}{\partial T}\right]\overline{B}_z, \tag{C.6}$$

$$\hat{x}: \quad \frac{\partial \overline{B}_z}{\partial y} - \left[\frac{\partial}{\partial z} + \varepsilon\frac{\partial}{\partial Z_1} + \cdots\right]\overline{B}_y = \tag{C.7}$$

$$-i\varepsilon_0\left[\omega_0 + i\varepsilon\frac{\partial}{\partial T}\right]\left[\varepsilon^L\left(y, \omega_0 + i\varepsilon\frac{\partial}{\partial T}\right)\overline{A}_x + \frac{2}{\varepsilon_0}\overline{P}_x^{(NL)+}\right]$$

$$\hat{y}: \left[\frac{\partial}{\partial z}+\varepsilon\frac{\partial}{\partial Z_1}+\cdots\right]\overline{B}_x-\varepsilon\frac{\partial\overline{B}_z}{\partial X}= \tag{C.8}$$
$$-i\varepsilon_0\left[\omega_0+i\varepsilon\frac{\partial}{\partial T}\right]\left[\varepsilon^{\mathrm{L}}\left(y,\omega_0+i\varepsilon\frac{\partial}{\partial T}\right)\overline{A}_y+\frac{2}{\varepsilon_0}\overline{P}_y^{(\mathrm{NL})+}\right]$$

$$\hat{z}: \varepsilon\frac{\partial\overline{B}_y}{\partial X}-\frac{\partial\overline{B}_x}{\partial y}= \tag{C.9}$$
$$-i\varepsilon_0\left[\omega_0+i\varepsilon\frac{\partial}{\partial T}\right]\left[\varepsilon^{\mathrm{L}}\left(y,\omega_0+i\varepsilon\frac{\partial}{\partial T}\right)\overline{A}_z+\frac{2}{\varepsilon_0}\overline{P}_z^{(\mathrm{NL})+}\right].$$

Gauss's Law, on the other hand, is not quite so straightforward because the dielectric constant now has variation in the y direction. This change is

$$\frac{\partial}{\partial y}\left[\varepsilon^{\mathrm{L}}\left(y,\omega_0+i\varepsilon\frac{\partial}{\partial T}\right)\overline{A}_y\right] \tag{C.10}$$
$$+\varepsilon^{\mathrm{L}}\left(y,\omega_0+i\varepsilon\frac{\partial}{\partial T}\right)\left\{\varepsilon\frac{\partial\overline{A}_x}{\partial X}+\left[\frac{\partial}{\partial z}+\varepsilon\frac{\partial}{\partial Z_1}+\cdots\right]\overline{A}_z\right\}=$$
$$-\frac{2}{\varepsilon_0}\left\{\varepsilon\frac{\partial\overline{P}_x^{(\mathrm{NL})+}}{\partial X}+\frac{\partial\overline{P}_y^{(\mathrm{NL})+}}{\partial y}+\left[\frac{\partial}{\partial z}+\varepsilon\frac{\partial}{\partial Z_1}+\cdots\right]\overline{P}_z^{(\mathrm{NL})+}\right\}.$$

Finally, the magnetic field divergence equation is

$$\varepsilon\frac{\partial\overline{B}_x}{\partial X}+\frac{\partial\overline{B}_y}{\partial y}+\left[\frac{\partial\overline{B}_z}{\partial z}+\varepsilon\frac{\partial\overline{B}_z}{\partial Z_1}+\cdots\right]=0. \tag{C.11}$$

With these changes from the (3+1)-D derivation noted, the waveguide derivation can begin.

C.1 Order ε - Effective Indices and Phase Velocity

At the lowest order, Maxwell's equations result in

$$(\mathrm{TM})\ \hat{x}: \frac{\partial\overline{A}_{1z}}{\partial y}-\frac{\partial\overline{A}_{1y}}{\partial z}=i\mu_0\omega_0\overline{B}_{1x} \tag{C.12}$$

$$(\mathrm{TE})\ \hat{y}: \frac{\partial\overline{A}_{1x}}{\partial z}=i\mu_0\omega_0\overline{B}_{1y} \tag{C.13}$$

$$(\mathrm{TE})\ \hat{z}: \frac{\partial\overline{A}_{1x}}{\partial y}=-i\mu_0\omega_0\overline{B}_{1z}, \tag{C.14}$$

which allows the electric fields to be determined from the magnetic fields,

$$(\mathrm{TE})\ \hat{x}: \frac{\partial\overline{B}_{1z}}{\partial y}-\frac{\partial\overline{B}_{1y}}{\partial z}=-i\varepsilon_0\omega_0\varepsilon^{\mathrm{L}}_{\mathcal{R}}(y,\omega_0)\overline{A}_{1x} \tag{C.15}$$

$$(\mathrm{TM})\ \hat{y}: \frac{\partial\overline{B}_{1x}}{\partial z}=-i\varepsilon_0\omega_0\varepsilon^{\mathrm{L}}_{\mathcal{R}}(y,\omega_0)\overline{A}_{1y} \tag{C.16}$$

$$(\mathrm{TM})\ \hat{z}: \frac{\partial\overline{B}_{1x}}{\partial y}=i\varepsilon_0\omega_0\varepsilon^{\mathrm{L}}_{\mathcal{R}}(y,\omega_0)\overline{A}_{1z}, \tag{C.17}$$

which allows the magnetic fields to be determined from the electric fields, and

$$(\mathrm{TM})\quad \frac{\partial\ln\varepsilon^{\mathrm{L}}_{\mathcal{R}}(y,\omega_0)}{\partial y}\overline{A}_{1y}+\frac{\partial\overline{A}_{1y}}{\partial y}+\frac{\partial\overline{A}_{1z}}{\partial z}=0 \tag{C.18}$$

$$(\mathrm{TE})\quad \frac{\partial\overline{B}_{1y}}{\partial y}+\frac{\partial\overline{B}_{1z}}{\partial z}=0, \tag{C.19}$$

which relate the y and z polarization components and offer no additional information. To this order, all six field components are nonzero. Equations C.12, C.16, C.17 and C.18 determine the TM mode and equations C.13, C.14, C.15, and C.19 determine the TE mode.

TE Mode

Working first with the TE mode, taking the z derivative of equation C.13 and substituting equation C.15 results in

$$\frac{\partial^2 \overline{A}_{1x}}{\partial z^2} = i\mu_0\omega_0 \left[\frac{\partial \overline{B}_{1z}}{\partial y} + i\varepsilon_0\omega_0\varepsilon^{\mathrm{L}}_{\mathcal{R}}(y,\omega_0)\overline{A}_{1y} \right]. \tag{C.20}$$

Substituting equation C.14 for $\overline{B}_{1z}$,

$$-\left[\beta^{\mathrm{TE}}\right]^2 A_{1x} = i\mu_0\omega_0 \left[-\frac{1}{i\mu_0\omega_0}\frac{\partial^2 A_{1x}}{\partial y^2} + i\varepsilon_0\omega_0\varepsilon^{\mathrm{L}}_{\mathcal{R}}(y,\omega_0)A_{1x} \right], \tag{C.21}$$

which, upon rearrangement, yields the eigenvalue equation

$$\frac{\partial^2 A_{1x}}{\partial y^2} = \left\{ \left[\beta^{\mathrm{TE}}\right]^2 - k^2(y,\omega_0) \right\} A_{1x}. \tag{C.22}$$

Equation C.22 is a function of only the fast variable y and determines the TE guided profile $U_x^{\mathrm{TE}}(y,\omega_0)$ and effective propagation constant β^{TE}. Since the envelope $A_1^{\mathrm{TE}}(X, Z_i, T)$ cancels, equation C.22 can be written as

$$\frac{\partial^2 U_x^{\mathrm{TE}}(y,\omega_0)}{\partial y^2} = \left\{ \left[\beta^{\mathrm{TE}}\right]^2 - k^2(y,\omega_0) \right\} U_x^{\mathrm{TE}}(y,\omega_0). \tag{C.23}$$

This equation is most appropriate for waveguide structures with continuous variation of the refractive index, but in general, is not sufficient to determine the guided profile [240]. The constraint provided by the finite one-dimensional power of the guided mode provides the necessary additional information.

For waveguide with discontinuous, or step, variations in refractive index, equation C.23 can be solved in each homogeneous region and linked through the appropriate boundary conditions. These boundary conditions are the continuity of the tangential electric and magnetic fields across the dielectric interfaces. For the TE mode, A_x and B_z are continuous, and by equation C.14, $\partial A_x/\partial y$ is continuous [239]. Therefore, the boundary conditions are given by the continuity of

$$U_x^{\mathrm{TE}}(y,\omega_0) \quad \text{and} \quad \frac{\partial U_x^{\mathrm{TE}}(y,\omega_0)}{\partial y}. \tag{C.24}$$

Determination of the magnetic field components of the TE mode, $U_y^{\mathrm{TE}}(y,\omega_0)$ and $U_z^{\mathrm{TE}}(y,\omega_0)$, is not necessary since the wave equations will be developed for the vector electric field.

For a known index and guided amplitude profile, the dispersion relation can be written as an overlap integral. This can be seen by multiplying equation C.23 by U_x^{TE} and integrating, resulting in

$$\left[\beta^{\mathrm{TE}}\right]^2 = \frac{\int k^2(y,\omega_0)\left[U_x^{\mathrm{TE}}\right]^2 dy - \int \left[\frac{\partial U_x^{\mathrm{TE}}}{\partial y}\right]^2 dy}{\int \left[U_x^{\mathrm{TE}}\right]^2 dy}. \tag{C.25}$$

TM Mode

The TM guided profile is most easily obtained using the magnetic field. Taking the z derivative of equation C.16 and substituting equation C.12 results in

$$\frac{\partial^2 \overline{B}_{1x}}{\partial z^2} = i\varepsilon_0\omega_0\varepsilon^{\mathrm{L}}_{\mathcal{R}}(y,\omega_0) \left[-\frac{\partial \overline{A}_{1z}}{\partial y} + i\mu_0\omega_0\overline{B}_{1x} \right]. \tag{C.26}$$

Substituting equation C.17 for $\overline{A}_{1z}$,

$$-\left[\beta^{\mathrm{TM}}\right]^2 B_{1x} = -\left[\frac{\partial^2 B_{1x}}{\partial y^2} - \frac{\partial \ln \varepsilon^{\mathrm{L}}_{\mathcal{R}}(y,\omega_0)}{\partial y}\frac{\partial B_{1x}}{\partial y} \right] - \varepsilon_0\mu_0\omega_0^2\varepsilon^{\mathrm{L}}_{\mathcal{R}}(y,\omega_0)B_{1x}, \tag{C.27}$$

which, upon rearrangement, yields the eigenvalue equation

$$\frac{\partial^2 V_x^{\mathrm{TM}}(y,\omega_0)}{\partial y^2} - \frac{\partial \ln \varepsilon^{\mathrm{L}}_{\mathcal{R}}(y,\omega_0)}{\partial y}\frac{\partial V_x^{\mathrm{TM}}(y,\omega_0)}{\partial y} = \left\{ \left[\beta^{\mathrm{TM}}\right]^2 - k^2(y,\omega_0) \right\} V_x^{\mathrm{TM}}(y,\omega_0), \tag{C.28}$$

which again is most appropriate for continuous index variation.

For step variations, the boundary conditions for the TM mode are the continuity of B_x and A_z across any dielectric interface. Using equation C.17 for A_z leads to the continuity of

$$V_x^{\mathrm{TM}}(y,\omega_0) \quad \text{and} \quad \frac{1}{\varepsilon_{\mathcal{R}}^{\mathrm{L}}(y,\omega_0)}\frac{\partial V_x^{\mathrm{TM}}(y,\omega_0)}{\partial y}. \tag{C.29}$$

In order to facilitate the derivation of the TE and TM nonlinear wave equations, the $\hat{y}$ and $\hat{z}$ components of the electric field associated with the TM mode must be obtained. From equation C.16

$$\begin{aligned} V_y^{\mathrm{TM}}(y,\omega_0) &= -\frac{\beta^{\mathrm{TM}}}{\eta^{\mathrm{TM}}\varepsilon_0\omega_0\varepsilon_{\mathcal{R}}^{\mathrm{L}}(y,\omega_0)}V_x^{\mathrm{TM}}(y,\omega_0) \\ &= -\left[\frac{\beta^{\mathrm{TM}}}{k(y,\omega_0)}\right]^2 V_x^{\mathrm{TM}}(y,\omega_0), \end{aligned} \tag{C.30}$$

which determines the y component, and from equation C.17

$$\begin{aligned} V_z^{\mathrm{TM}}(y,\omega_0) &= \frac{i}{\eta^{\mathrm{TM}}\varepsilon_0\omega_0\varepsilon_{\mathcal{R}}^{\mathrm{L}}(y,\omega_0)}\frac{\partial V_x^{\mathrm{TM}}(y,\omega_0)}{\partial y} \\ &= \frac{i\beta^{\mathrm{TM}}}{k^2(y,\omega_0)}\frac{\partial V_x^{\mathrm{TM}}(y,\omega_0)}{\partial y}, \end{aligned} \tag{C.31}$$

which determines the z component. These expressions are fully non-paraxial in the guided dimension because of the choice of y as a fast variable.

Note that the z profile of equation C.31 depends on a transverse derivative. The major contribution to this transverse derivative is the transverse wavenumber. When the transverse wavenumber is small (as is the case for low-order modes in a strongly-guiding structure, or for modes in a weakly-guiding structure), the mode angular spectrum remains close to the z-axis, meaning that $V_z^{\mathrm{TM}} \ll V_{x,y}^{\mathrm{TM}}$, which is the paraxial condition. Even though the paraxial condition is imposed on the unguided envelopes A and B by the choice of the slow transverse variable X, it does not need to be imposed on the guided profiles U and V which depend on the fast variable y. Later in the derivation (sec. C.3), though, this condition will be imposed in order to simplify the nonlinear polarization.

The dispersion relation for the TM mode can be obtained in a similar manner to that for the TE mode, with the result

$$[\beta^{\mathrm{TM}}]^2 = \frac{\int k^2(y,\omega_0)\left[V_x^{\mathrm{TM}}\right]^2 dy - \int\left[\frac{\partial V_x^{\mathrm{TM}}}{\partial y}\right]^2 dy + \frac{1}{2}\int\frac{\partial^2 \ln\varepsilon_{\mathcal{R}}^{\mathrm{L}}(y,\omega_0)}{\partial y^2}\left[V_x^{\mathrm{TM}}\right]^2 dy}{\int\left[V_x^{\mathrm{TM}}\right]^2 dy}. \tag{C.32}$$

The eigenvalue equation C.28 can be recast into a more familiar form in terms of the y-component of the electric field. Substituting $V_x^{\mathrm{TM}}(y,\omega_0) \propto \varepsilon_{\mathcal{R}}^{\mathrm{L}}(y,\omega_0)V_y^{\mathrm{TM}}(y,\omega_0)$ into C.28 results in [159]

$$\begin{aligned} &\frac{\partial^2 V_y^{\mathrm{TM}}(y,\omega_0)}{\partial y^2} + \frac{\partial \ln\varepsilon_{\mathcal{R}}^{\mathrm{L}}(y,\omega_0)}{\partial y}\frac{\partial V_y^{\mathrm{TM}}(y,\omega_0)}{\partial y} \\ &\qquad + \frac{\partial^2 \ln\varepsilon_{\mathcal{R}}^{\mathrm{L}}(y,\omega_0)}{\partial y^2}V_y^{\mathrm{TM}}(y,\omega_0) = \left\{[\beta^{\mathrm{TM}}]^2 - k^2(y,\omega_0)\right\}V_y^{\mathrm{TM}}(y,\omega_0). \end{aligned} \tag{C.33}$$

C.2 Order ε^2 - Group Velocity

Similar to the (3+1)-D derivation, this order determines the group delay of the TE and TM envelopes, except that now the group-delay has contributions from both the material and waveguide dispersions. The waveguide dispersion is responsible for the difference in TE and TM group delays, which can be tailored somewhat by the choice of waveguide parameters. In a weakly-guiding structure, the group delays will be nearly equal when the material is linearly isotropic as is the case here.

Another difference from the (3+1)-D derivation is the inclusion of the frequency-dependence of the waveguide mode [194]. The first-order dispersion of the waveguide mode is included as

$$\overline{A}_{2x} = \overline{A}_{2x}^{\dagger} + iU_x^{\mathrm{TE}'}(y,\omega_0)\frac{\partial A_1^{\mathrm{TE}}(X,Z_i,T)}{\partial T}e^{i\beta^{\mathrm{TE}}z}, \tag{C.34}$$

where $\overline{A}_{2x}$ is the second term in the electric field expansion and is composed of an unknown component $\overline{A}^{\dagger}_{2x}$ and the first term in the electric field expansion obtained at the previous order which now includes dispersion of the waveguide profile. The other components of the electric and magnetic fields are handled similarly.

From Maxwell's equations then, Faraday's Law results in

$$\text{(TM)}\ \hat{x}:\ \frac{\partial \overline{A}_{2z}}{\partial y} - \frac{\partial \overline{A}_{2y}}{\partial z} - \frac{\partial \overline{A}_{1y}}{\partial Z_1} = i\mu_0\omega_0\overline{B}_{2x} - \mu_0\frac{\partial \overline{B}_{1x}}{\partial T} \tag{C.35}$$

$$\text{(TE)}\ \hat{y}:\ \frac{\partial \overline{A}_{2x}}{\partial z} + \frac{\partial \overline{A}_{1x}}{\partial Z_1} - \frac{\partial \overline{A}_{1z}}{\partial X} = i\mu_0\omega_0\overline{B}_{2y} - \mu_0\frac{\partial \overline{B}_{1y}}{\partial T} \tag{C.36}$$

$$\text{(TE)}\ \hat{z}:\ \frac{\partial \overline{A}_{1y}}{\partial X} - \frac{\partial \overline{A}_{2x}}{\partial y} = i\mu_0\omega_0\overline{B}_{2z} - \mu_0\frac{\partial \overline{B}_{1z}}{\partial T}, \tag{C.37}$$

while the modified Ampere's Law gives

$$\text{(TE)}\ \hat{x}:\ \frac{\partial \overline{B}_{2z}}{\partial y} - \frac{\partial \overline{B}_{2y}}{\partial z} - \frac{\partial \overline{B}_{1y}}{\partial Z_1} = -i\varepsilon_0\omega_0\varepsilon^{\mathrm{L}}_{\mathcal{R}}(y,\omega_0)\overline{A}_{2x} + \varepsilon_0\left[\varepsilon^{\mathrm{L}}_{\mathcal{R}}(y,\omega_0) + \omega_0\varepsilon^{\mathrm{L}'}_{\mathcal{R}}(y,\omega_0)\right]\frac{\partial \overline{A}_{1x}}{\partial T} \tag{C.38}$$

$$\text{(TE)}\ \hat{y}:\ \frac{\partial \overline{B}_{2x}}{\partial z} + \frac{\partial \overline{B}_{1x}}{\partial Z_1} - \frac{\partial \overline{B}_{1z}}{\partial X} = -i\varepsilon_0\omega_0\varepsilon^{\mathrm{L}}_{\mathcal{R}}(y,\omega_0)\overline{A}_{2y} + \varepsilon_0\left[\varepsilon^{\mathrm{L}}_{\mathcal{R}}(y,\omega_0) + \omega_0\varepsilon^{\mathrm{L}'}_{\mathcal{R}}(y,\omega_0)\right]\frac{\partial \overline{A}_{1y}}{\partial T} \tag{C.39}$$

$$\text{(TM)}\ \hat{z}:\ \frac{\partial \overline{B}_{1y}}{\partial X} - \frac{\partial \overline{B}_{2x}}{\partial y} = -i\varepsilon_0\omega_0\varepsilon^{\mathrm{L}}_{\mathcal{R}}(y,\omega_0)\overline{A}_{2z} + \varepsilon_0\left[\varepsilon^{\mathrm{L}}_{\mathcal{R}}(y,\omega_0) + \omega_0\varepsilon^{\mathrm{L}'}_{\mathcal{R}}(y,\omega_0)\right]\frac{\partial \overline{A}_{1z}}{\partial T}. \tag{C.40}$$

Finally, the divergence laws give

$$\text{(TM)}\ \frac{\partial \varepsilon^{\mathrm{L}}_{\mathcal{R}}(y,\omega_0)}{\partial y}\overline{A}_{2y} + \varepsilon^{\mathrm{L}}_{\mathcal{R}}(y,\omega_0)\left[\frac{\partial \overline{A}_{1x}}{\partial X} + \frac{\partial \overline{A}_{2y}}{\partial y} + \frac{\partial \overline{A}_{2z}}{\partial z} + \frac{\partial \overline{A}_{1z}}{\partial Z_1}\right] + i\frac{\partial \varepsilon^{\mathrm{L}'}_{\mathcal{R}}(y,\omega_0)}{\partial y}\frac{\partial \overline{A}_{1y}}{\partial T} + i\varepsilon^{\mathrm{L}'}_{\mathcal{R}}(y,\omega_0)\frac{\partial}{\partial T}\left[\frac{\partial \overline{A}_{1y}}{\partial y} + \frac{\partial \overline{A}_{1z}}{\partial z}\right] = 0 \tag{C.41}$$

$$\text{(TE)}\ \frac{\partial \overline{B}_{1x}}{\partial X} + \frac{\partial \overline{B}_{2y}}{\partial y} + \frac{\partial \overline{B}_{2z}}{\partial z} + \frac{\partial \overline{B}_{1z}}{\partial Z_1} = 0. \tag{C.42}$$

TE Mode

Now the envelope equation for the TE mode is derived. Taking the z-derivative of equation C.36, and substituting equation C.38 and the y-derivative of equation C.37, results in

$$\begin{aligned}\frac{\partial^2 \overline{A}_{2x}}{\partial z^2} + \frac{\partial^2 \overline{A}_{2x}}{\partial y^2} + \frac{\omega_0^2}{c^2}\varepsilon^{\mathrm{L}}_{\mathcal{R}}(y,\omega_0)\overline{A}_{2x} &= \frac{\partial^2 \overline{A}_{1z}}{\partial z\partial X} + \frac{\partial^2 \overline{A}_{1y}}{\partial y\partial X} \\ &- i\beta_1^{\mathrm{TE}}\frac{\partial \overline{A}_{1x}}{\partial Z_1} - i\frac{\omega_0}{c^2}\left[\varepsilon^{\mathrm{L}}_{\mathcal{R}}(y,\omega_0) + \omega_0\varepsilon^{\mathrm{L}'}_{\mathcal{R}}(y,\omega_0)\right]\frac{\partial \overline{A}_{1x}}{\partial T} \\ &+ \mu_0\frac{\partial^2 \overline{B}_{1z}}{\partial y\partial T} - i\mu_0\omega_0\frac{\partial \overline{B}_{1y}}{\partial Z_1} - \mu_0\frac{\partial^2 \overline{B}_{1y}}{\partial z\partial T}.\end{aligned} \tag{C.43}$$

After substituting from order ε, the TE mode equation reduces to

$$\begin{aligned}\frac{\partial^2 \overline{A}_{2x}}{\partial z^2} + \frac{\partial^2 \overline{A}_{2x}}{\partial y^2} + \frac{\omega_0^2}{c^2}\varepsilon^{\mathrm{L}}_{\mathcal{R}}(y,\omega_0)\overline{A}_{2x} &= \\ -2i\left[\beta^{\mathrm{TE}}\frac{\partial \overline{A}_{1x}}{\partial Z_1} - k(y,\omega_0)k'(y,\omega_0)\frac{\partial \overline{A}_{1x}}{\partial T}\right] &- \frac{\partial \ln\varepsilon^{\mathrm{L}}_{\mathcal{R}}(y,\omega_0)}{\partial y}\frac{\partial \overline{A}_{1y}}{\partial X}.\end{aligned} \tag{C.44}$$

Using C.34, equation C.44 can be written

$$\frac{\partial^2 \overline{A}_{2x}^{\dagger}}{\partial z^2} + \frac{\partial^2 \overline{A}_{2x}^{\dagger}}{\partial y^2} + \frac{\omega_0^2}{c^2}\varepsilon_{\mathcal{R}}^{\mathrm{L}}(y,\omega_0)\overline{A}_{2x}^{\dagger} - i\left[\left\{\left[\beta^{\mathrm{TE}}\right]^2 - k^2(y,\omega_0)\right\}U_x^{\mathrm{TE}'}(y,\omega_0) - \frac{\partial^2 U_x^{\mathrm{TE}'}(y,\omega_0)}{\partial y^2}\right]\frac{\partial \overline{A}_1^{\mathrm{TE}}}{\partial T} = -2i\left[\beta^{\mathrm{TE}}\frac{\partial \overline{A}_{1x}}{\partial Z_1} + k(y,\omega_0)k'(y,\omega_0)\frac{\partial \overline{A}_{1x}}{\partial T}\right] - \frac{\partial \ln \varepsilon_{\mathcal{R}}^{\mathrm{L}}(y,\omega_0)}{\partial y}\frac{\partial \overline{A}_{1y}}{\partial X}. \tag{C.45}$$

The left-hand side can be reduced by taking a frequency derivative of equation C.23,

$$\left\{\left[\beta^{\mathrm{TE}}\right]^2 - k^2(y,\omega_0)\right\}U_x^{\mathrm{TE}'}(y,\omega_0) - \frac{\partial^2 U_x^{\mathrm{TE}'}(y,\omega_0)}{\partial y^2} = -\frac{\partial}{\partial \omega_0}\left\{\left[\beta^{\mathrm{TE}}\right]^2 - k^2(y,\omega_0)\right\}U_x^{\mathrm{TE}}(y,\omega_0), \tag{C.46}$$

which, upon substitution, results in

$$\frac{\partial^2 \overline{A}_{2x}^{\dagger}}{\partial z^2} + \frac{\partial^2 \overline{A}_{2x}^{\dagger}}{\partial y^2} + k^2(y,\omega_0)\overline{A}_{2x}^{\dagger} = -2i\left[\beta^{\mathrm{TE}}\frac{\partial \overline{A}_{1x}}{\partial Z_1} + k(y,\omega_0)k'(y,\omega_0)\frac{\partial \overline{A}_{1x}}{\partial T}\right] - \frac{\partial \ln \varepsilon_{\mathcal{R}}^{\mathrm{L}}(y,\omega_0)}{\partial y}\frac{\partial \overline{A}_{1y}}{\partial X} - i\frac{\partial}{\partial \omega_0}\left\{\left[\beta^{\mathrm{TE}}\right]^2 - k^2(y,\omega_0)\right\}U_x^{\mathrm{TE}}(y,\omega_0)\frac{\partial \overline{A}_1^{\mathrm{TE}}(y,\omega_0)}{\partial T} = -2i\,\beta^{\mathrm{TE}}\left[\frac{\partial \overline{A}_{1x}}{\partial Z_1} + \beta^{\mathrm{TE}'}\frac{\partial \overline{A}_{1x}}{\partial T}\right] - \frac{\partial \ln \varepsilon_{\mathcal{R}}^{\mathrm{L}}(y,\omega_0)}{\partial y}\frac{\partial \overline{A}_{1y}}{\partial X}. \tag{C.47}$$

Equation C.47 is in the form $Lu = f$ where L is an operator and f is the forcing function. By the Fredholm alternative theorem [194], this equation has a solution if and only if $(u_h^*, f) = 0$, where u_h is the homogeneous solution, i.e. $Lu_h = 0$. The homogeneous solution for $\overline{A}_{2x}^{\dagger}$ is just the TE mode so that $u_h \propto U_x^{\mathrm{TE}}(y,\omega_0)e^{i\beta^{\mathrm{TE}}z}$. In order to guarantee a unique solution then,

$$\beta^{\mathrm{TE}}\frac{\partial A_1^{\mathrm{TE}}}{\partial Z_1}\int\left[U_x^{\mathrm{TE}}(y,\omega_0)\right]^2 dy + \beta^{\mathrm{TE}}\beta^{\mathrm{TE}'}\frac{\partial A_1^{\mathrm{TE}}}{\partial T}\int\left[U_x^{\mathrm{TE}}(y,\omega_0)\right]^2 dy + \frac{1}{2i}\frac{\partial B_1^{\mathrm{TM}}}{\partial X}e^{i[\beta^{\mathrm{TM}}-\beta^{\mathrm{TE}}]z}\int V_x^{\mathrm{TM}}(y,\omega_0)U_x^{\mathrm{TE}}(y,\omega_0)\frac{\partial \ln \varepsilon_{\mathcal{R}}^{\mathrm{L}}(y,\omega_0)}{\partial y}dy = 0, \tag{C.48}$$

which can be written in the simpler form

$$\frac{\partial A_1^{\mathrm{TE}}}{\partial Z_1} = -\beta^{\mathrm{TE}'}\frac{\partial A_1^{\mathrm{TE}}}{\partial T} + i\frac{\partial B_1^{\mathrm{TM}}}{\partial X}e^{i[\beta^{\mathrm{TM}}-\beta^{\mathrm{TE}}]z}\frac{\int V_x^{\mathrm{TM}}(y,\omega_0)U_x^{\mathrm{TE}}(y,\omega_0)[\partial \ln \varepsilon_{\mathcal{R}}^{\mathrm{L}}(y,\omega_0)/\partial y]dy}{2\beta^{\mathrm{TE}}\int\left[U_x^{\mathrm{TE}}(y,\omega_0)\right]^2 dy}. \tag{C.49}$$

Note that the TE-mode group-delay is defined as

$$\beta^{\mathrm{TE}'} \equiv \frac{\partial \beta^{\mathrm{TE}}}{\partial \omega_0}, \tag{C.50}$$

which can be evaluated from the eigenvalue equation C.23 or the TE dispersion relation C.25. The TE-mode group velocity is defined as $v_g^{\mathrm{TE}} \equiv 1/\beta^{\mathrm{TE}'}$.

The extra term in equation C.49 indicates linear coupling between the TM and TE modes due to the variation of the TM mode along the x direction, thus serving as a source term for the TE mode. This effect arises because of the differing rates of diffraction on either side of a dielectric interface and does not occur in homogeneous regions; in the (3+1)-D case, the dielectric "interface" is due to nonlinearity, which occurs at order ε^3, and this term appears with the vectorial nonlinear couplings at order

ε^5. Since the TE mode travels with the natural phase delay β^{TE}, and the extra component generated by the TM mode is driven with the phase delay β^{TM}, there is a coherence length, $L_{coh} = [\beta^{TM} - \beta^{TE}]^{-1}$, over which the effects of this term are important. It is assumed that the propagation lengths of ultimate interest ($\sim Z_2$) are much longer than this coherence length ($\sim Z_1$) so that the generation of a new TE component averages to zero, and the term can be neglected.

TM Mode

Performing the same steps with the TM mode results in

$$\begin{aligned}\frac{\partial^2\overline{B}_{2x}}{\partial z^2} + \frac{\partial^2\overline{B}_{2x}}{\partial y^2} - \frac{\partial\varepsilon^L_{\mathcal{R}}(y,\omega_0)}{\partial y}\frac{\partial\overline{B}_{2x}}{\partial y} + k^2(y,\omega_0)\overline{B}_{2x} = \\ -2i\left[\beta^{TM}\frac{\partial\overline{B}_{1x}}{\partial Z_1} + k(y,\omega_0)k'(y,\omega_0)\frac{\partial\overline{B}_{1x}}{\partial T}\right] + \frac{\partial\ln\varepsilon^L_{\mathcal{R}}(y,\omega_0)}{\partial y}\frac{\partial\overline{B}_{1y}}{\partial X} \\ -i\frac{\partial}{\partial\omega_0}\left[\frac{\partial\ln\varepsilon^L_{\mathcal{R}}(y,\omega_0)}{\partial y}\right]\frac{\partial^2\overline{B}_{1x}}{\partial y\partial T}.\end{aligned} \tag{C.51}$$

Taking a frequency derivative of equation C.28 allows C.51 to be written

$$\begin{aligned}\frac{\partial^2\overline{B}^{\dagger}_{2x}}{\partial z^2} + \frac{\partial^2\overline{B}^{\dagger}_{2x}}{\partial y^2} - \frac{\partial\varepsilon^L_{\mathcal{R}}(y,\omega_0)}{\partial y}\frac{\partial\overline{B}^{\dagger}_{2x}}{\partial y} + k^2(y,\omega_0)\overline{B}^{\dagger}_{2x} = \\ -i\frac{\partial}{\partial\omega_0}\left\{[\beta^{TM}]^2 - k^2(y,\omega_0)\right\}\frac{\partial\overline{B}_{1x}}{\partial T} - i\frac{\partial}{\partial\omega_0}\left[\frac{\partial\ln\varepsilon^L_{\mathcal{R}}(y,\omega_0)}{\partial y}\right]\frac{\partial^2\overline{B}_{1x}}{\partial y\partial T} \\ -2i\left[\beta^{TM}\frac{\partial\overline{B}_{1x}}{\partial Z_1} + k(y,\omega_0)k'(y,\omega_0)\frac{\partial\overline{B}_{1x}}{\partial T}\right] - \frac{\partial\ln\varepsilon^L_{\mathcal{R}}(y,\omega_0)}{\partial y}\frac{\partial\overline{B}_{1y}}{\partial X} \\ +i\frac{\partial}{\partial\omega_0}\left[\frac{\partial\ln\varepsilon^L_{\mathcal{R}}(y,\omega_0)}{\partial y}\right]\frac{\partial^2\overline{B}_{1x}}{\partial y\partial T} \\ = -2i\beta^{TM}\left[\frac{\partial\overline{B}_{1x}}{\partial Z_1} + \beta^{TM\prime}\frac{\partial\overline{B}_{1x}}{\partial T}\right] - \frac{\partial\ln\varepsilon^L_{\mathcal{R}}(y,\omega_0)}{\partial y}\frac{\partial\overline{B}_{1y}}{\partial X}.\end{aligned} \tag{C.52}$$

Again using the Fredholm alternative theorem, equation C.52 is written in group-delay form

$$\begin{aligned}\frac{\partial B_1^{TM}}{\partial Z_1} = -\beta^{TM\prime}\frac{\partial B_1^{TM}}{\partial T} \\ + i\frac{\partial A_1^{TE}}{\partial X}e^{i[\beta^{TE}-\beta^{TM}]z}\frac{\int U_x^{TE}(y,\omega_0)V_x^{TM}(y,\omega_0)[\partial\ln\varepsilon^L_{\mathcal{R}}(y,\omega_0)/\partial y]dy}{2\beta^{TM}\int[V_x^{TM}(y,\omega_0)]^2dy}.\end{aligned} \tag{C.53}$$

The effective TM-mode group-delay coefficient is

$$\beta^{TM\prime} \equiv \frac{\partial\beta^{TM}}{\partial\omega_0}, \tag{C.54}$$

where β^{TM} is obtained from equation C.28 or the TM dispersion relation C.32.

C.3 Order ε^3 - Coupled Nonlinear Schrödinger Equations

The nonlinear Schrödinger equation appears at this order for both the TE and TM modes. The difference between the results obtained here and those obtained in the (3+1)-D derivation is the appearance of effective material constants representing diffraction and nonlinearity. Because of the linear coupling between the TE and TM modes due to transverse index variation, diffraction in the unguided transverse direction is modified slightly from the linear homogeneous case. Note that this effect does not show up in purely scalar analysis [194], but, except in the strongly-guided case, can be neglected nonetheless. The effective nonlinearity is given by modal overlap integrals of the material nonlinear coefficient with the appropriate waveguide profiles for self- and cross-phase modulation.

At this order, the second derivative with frequency of the mode profiles associated with A_1 and B_1 must be included, along with the first derivative with frequency of the mode profiles associated with A_2 and B_2:

$$\overline{A}_{3x} = \overline{A}_{3x}^{\dagger} + iU_x^{\mathrm{TE}'}(y,\omega_0)\frac{\partial A_2^{\mathrm{TE}}(X,Z_i,T)}{\partial T}e^{i\beta^{\mathrm{TE}}z} - \frac{1}{2}U_x^{\mathrm{TE}''}(y,\omega_0)\frac{\partial^2 A_1^{\mathrm{TE}}(X,Z_i,T)}{\partial T^2}e^{i\beta^{\mathrm{TE}}z}. \tag{C.55}$$

Again, $\overline{A}_{3x}^{\dagger}$ is the unknown component of the electric field.

Now, Maxwell's curl equations result in

$$\text{(TM)}\ \hat{x}:\ \frac{\partial \overline{A}_{3z}}{\partial y} - \frac{\partial \overline{A}_{3y}}{\partial z} - \frac{\partial \overline{A}_{2y}}{\partial Z_1} - \frac{\partial \overline{A}_{1y}}{\partial Z_2} = i\mu_0\omega_0\overline{B}_{3x} - \mu_0\frac{\partial \overline{B}_{2x}}{\partial T} \tag{C.56}$$

$$\text{(TE)}\ \hat{y}:\ \frac{\partial \overline{A}_{3x}}{\partial z} + \frac{\partial \overline{A}_{2x}}{\partial Z_1} + \frac{\partial \overline{A}_{1x}}{\partial Z_2} - \frac{\partial \overline{A}_{2z}}{\partial X} = i\mu_0\omega_0\overline{B}_{3y} - \mu_0\frac{\partial \overline{B}_{2y}}{\partial T} \tag{C.57}$$

$$\text{(TE)}\ \hat{z}:\ \frac{\partial \overline{A}_{2y}}{\partial X} - \frac{\partial \overline{A}_{3x}}{\partial y} = i\mu_0\omega_0\overline{B}_{3z} - \mu_0\frac{\partial \overline{B}_{2z}}{\partial T}, \tag{C.58}$$

and

$$\begin{aligned}\text{(TE)}\ \hat{x}:\ \frac{\partial \overline{B}_{3z}}{\partial y} - \frac{\partial \overline{B}_{3y}}{\partial z} - \frac{\partial \overline{B}_{2x}}{\partial Z_1} - \frac{\partial \overline{B}_{1y}}{\partial Z_2} &= -i\varepsilon_0\omega_0\varepsilon_{\mathcal{R}}^{\mathrm{L}}(y,\omega_0)\overline{A}_{3x} \\ &+\varepsilon_0\left[\varepsilon_{\mathcal{R}}^{\mathrm{L}}(y,\omega_0) + \omega_0\varepsilon_{\mathcal{R}}^{\mathrm{L}'}(y,\omega_0)\right]\frac{\partial \overline{A}_{2x}}{\partial T} - 2i\omega_0 P_{1x}^{(3)} \\ &+i\varepsilon_0\left[\varepsilon_{\mathcal{R}}^{\mathrm{L}'}(y,\omega_0) + \frac{\omega_0}{2}\varepsilon_{\mathcal{R}}^{\mathrm{L}''}(y,\omega_0)\right]\frac{\partial^2 \overline{A}_{1x}}{\partial T^2}\end{aligned} \tag{C.59}$$

$$\begin{aligned}\text{(TE)}\ \hat{y}:\ \frac{\partial \overline{B}_{3x}}{\partial z} + \frac{\partial \overline{B}_{2x}}{\partial Z_1} + \frac{\partial \overline{B}_{1x}}{\partial Z_2} - \frac{\partial \overline{B}_{2z}}{\partial X} &= -i\varepsilon_0\omega_0\varepsilon_{\mathcal{R}}^{\mathrm{L}}(y,\omega_0)\overline{A}_{3y} \\ &+\varepsilon_0\left[\varepsilon_{\mathcal{R}}^{\mathrm{L}}(y,\omega_0) + \omega_0\varepsilon_{\mathcal{R}}^{\mathrm{L}'}(y,\omega_0)\right]\frac{\partial \overline{A}_{2y}}{\partial T} - 2i\omega_0 P_{1y}^{(3)} \\ &+i\varepsilon_0\left[\varepsilon_{\mathcal{R}}^{\mathrm{L}'}(y,\omega_0) + \frac{\omega_0}{2}\varepsilon_{\mathcal{R}}^{\mathrm{L}''}(y,\omega_0)\right]\frac{\partial^2 \overline{A}_{1y}}{\partial T^2}\end{aligned} \tag{C.60}$$

$$\begin{aligned}\text{(TM)}\ \hat{z}:\ \frac{\partial \overline{B}_{2y}}{\partial X} - \frac{\partial \overline{B}_{3x}}{\partial y} &= -i\varepsilon_0\omega_0\varepsilon_{\mathcal{R}}^{\mathrm{L}}(y,\omega_0)\overline{A}_{3z} \\ &+\varepsilon_0\left[\varepsilon_{\mathcal{R}}^{\mathrm{L}}(y,\omega_0) + \omega_0\varepsilon_{\mathcal{R}}^{\mathrm{L}'}(y,\omega_0)\right]\frac{\partial \overline{A}_{2z}}{\partial T} - 2i\omega_0 P_{1z}^{(3)} \\ &+i\varepsilon_0\left[\varepsilon_{\mathcal{R}}^{\mathrm{L}'}(y,\omega_0) + \frac{\omega_0}{2}\varepsilon_{\mathcal{R}}^{\mathrm{L}''}(y,\omega_0)\right]\frac{\partial^2 \overline{A}_{1z}}{\partial T^2},\end{aligned} \tag{C.61}$$

where the third-order polarizations are written, for example,

$$\overline{P}_{1x}^{(3)} = \varepsilon_0 n_0 n_2(y)\left\{\left[|A_{1x}|^2 + 2\Delta|A_{1y}|^2 + 2\Delta|A_{1z}|^2\right]\overline{A}_{1x} + \gamma\left[\overline{A}_{1y}^2 + \overline{A}_{1z}^2\right]\overline{A}_{1x}^*\right\}. \tag{C.62}$$

The Maxwell divergence equations give

$$\begin{aligned}\text{(TM)}\quad &\frac{\partial\varepsilon_{\mathcal{R}}^{\mathrm{L}}(y,\omega_0)}{\partial y}\overline{A}_{3y} + \varepsilon_{\mathcal{R}}^{\mathrm{L}}(y,\omega_0)\left[\frac{\partial \overline{A}_{3y}}{\partial y} + \frac{\partial \overline{A}_{2x}}{\partial X} + \frac{\partial \overline{A}_{3z}}{\partial z} + \frac{\partial \overline{A}_{2z}}{\partial Z_1} + \frac{\partial \overline{A}_{1z}}{\partial Z_2}\right] \\ &+i\frac{\partial\varepsilon_{\mathcal{R}}^{\mathrm{L}'}(y,\omega_0)}{\partial y}\frac{\partial \overline{A}_{2y}}{\partial T} + i\varepsilon_{\mathcal{R}}^{\mathrm{L}'}(y,\omega_0)\frac{\partial}{\partial T}\left[\frac{\partial \overline{A}_{2y}}{\partial y} + \frac{\partial \overline{A}_{1x}}{\partial X} + \frac{\partial \overline{A}_{2z}}{\partial z} + \frac{\partial \overline{A}_{1z}}{\partial Z_1}\right] \\ &-\frac{1}{2}\frac{\partial\varepsilon_{\mathcal{R}}^{\mathrm{L}''}(y,\omega_0)}{\partial y}\frac{\partial^2 \overline{A}_{1y}}{\partial T^2} - \frac{1}{2}\varepsilon_{\mathcal{R}}^{\mathrm{L}''}(y,\omega_0)\frac{\partial^2}{\partial T^2}\left[\frac{\partial \overline{A}_{1y}}{\partial y} + \frac{\partial \overline{A}_{1z}}{\partial z}\right] =\end{aligned} \tag{C.63}$$

$$-\frac{2}{\varepsilon_0}\frac{\partial P_{1y}^{(3)}}{\partial y}-\frac{2}{\varepsilon_0}\frac{\partial P_{1z}^{(3)}}{\partial z}$$

$$\text{(TE)}\quad \frac{\partial \overline{B}_{2x}}{\partial X}+\frac{\partial \overline{B}_{3y}}{\partial y}+\frac{\partial \overline{B}_{3z}}{\partial z}+\frac{\partial \overline{B}_{2z}}{\partial Z_1}+\frac{\partial \overline{B}_{1z}}{\partial Z_2}=0. \tag{C.64}$$

TE Mode

As before, taking the z-derivative of equation C.57, and substituting equation C.59 and the y-derivative of equation C.58, results in

$$\begin{aligned}
&\frac{\partial^2\overline{A}_{3x}}{\partial z^2}+\frac{\partial^2\overline{A}_{3x}}{\partial y^2}+k^2(y,\omega_0)\overline{A}_{3x}=-\frac{\partial^2\overline{A}_{2x}}{\partial z\partial Z_1}-\frac{\partial^2\overline{A}_{1x}}{\partial z\partial Z_2}+\frac{\partial^2\overline{A}_{2y}}{\partial y\partial X}+\frac{\partial^2\overline{A}_{2z}}{\partial z\partial X}\\
&+\mu_0\frac{\partial^2\overline{B}_{2z}}{\partial y\partial T}-\mu_0\frac{\partial^2\overline{B}_{2y}}{\partial z\partial T}-i\mu_0\omega_0\frac{\partial\overline{B}_{2y}}{\partial Z_1}-i\mu_0\omega_0\frac{\partial\overline{B}_{1y}}{\partial Z_2}-2\omega_0^2\mu_0P_{1x}^{(3)}\\
&-i\frac{\omega_0}{c^2}\left[\varepsilon_{\mathcal{R}}^{\mathrm{L}}(y,\omega_0)+\omega_0\varepsilon_{\mathcal{R}}^{\mathrm{L}'}(y,\omega_0)\right]\frac{\partial\overline{A}_{2x}}{\partial T}+\frac{\omega_0}{c^2}\left[\varepsilon_{\mathcal{R}}^{\mathrm{L}'}(y,\omega_0)+\frac{\omega_0}{2}\varepsilon_{\mathcal{R}}^{\mathrm{L}''}(y,\omega_0)\right]\frac{\partial^2\overline{A}_{1x}}{\partial T^2}.
\end{aligned} \tag{C.65}$$

Using the appropriate substitutions from order ε^2 and order ε, this equation can be written

$$\begin{aligned}
&\frac{\partial^2\overline{A}_{3x}}{\partial z^2}+\frac{\partial^2\overline{A}_{3x}}{\partial y^2}+k^2(y,\omega_0)\overline{A}_{3x}=\\
&\quad-2\frac{\partial^2\overline{A}_{2x}}{\partial z\partial Z_1}-2ik(y,\omega_0)k'(y,\omega_0)\frac{\partial\overline{A}_{2x}}{\partial T}-2\frac{\partial^2\overline{A}_{1x}}{\partial z\partial Z_2}-\frac{\partial^2\overline{A}_{1x}}{\partial X^2}\\
&\quad-\frac{\partial^2\overline{A}_{1x}}{\partial Z_1^2}+\left\{\left[k'(y,\omega_0)\right]^2+k(y,\omega_0)k''(y,\omega_0)\right\}\frac{\partial^2\overline{A}_{1x}}{\partial T^2}-2\omega_0^2\mu_0P_{1x}^{(3)}\\
&\quad-i\frac{\partial}{\partial\omega_0}\left[\frac{\partial\ln\varepsilon_{\mathcal{R}}^{\mathrm{L}}(y,\omega_0)}{\partial y}\right]\frac{\partial^2\overline{A}_{1x}}{\partial X\partial T}-\frac{\partial\ln\varepsilon_{\mathcal{R}}^{\mathrm{L}}(y,\omega_0)}{\partial y}\frac{\partial\overline{A}_{2y}}{\partial X}.
\end{aligned} \tag{C.66}$$

With the substitution of C.55, the terms on the left-hand side of equation C.68 containing A_{3y} become

$$\begin{aligned}
&\frac{\partial^2\overline{A}_{3x}}{\partial z^2}+\frac{\partial^2\overline{A}_{3x}}{\partial y^2}+k^2(y,\omega_0)\overline{A}_{3x}=\\
&\quad+\frac{\partial^2\overline{A}_{3x}^{\dagger}}{\partial z^2}+\frac{\partial^2\overline{A}_{3x}^{\dagger}}{\partial y^2}+k^2(y,\omega_0)\overline{A}_{3x}^{\dagger}\\
&\quad+2i\left[\beta^{\mathrm{TE}}\beta^{\mathrm{TE}'}-k(y,\omega_0)k'(y,\omega_0)\right]\frac{\partial\overline{A}_{2x}^{\dagger}}{\partial T}\\
&\quad-\left\{\left[\beta^{\mathrm{TE}'}\right]^2+\beta^{\mathrm{TE}}\beta^{\mathrm{TE}''}-\left[k'(y,\omega_0)\right]^2-k(y,\omega_0)k''(y,\omega_0)\right\}\frac{\partial^2\overline{A}_{1x}}{\partial T^2}\\
&\quad-2\left[\beta^{\mathrm{TE}}\beta^{\mathrm{TE}'}-k(y,\omega_0)k'(y,\omega_0)\right]U_x^{\mathrm{TE}'}(y,\omega_0)\frac{\partial^2\overline{A}_1^{\mathrm{TE}}}{\partial T^2}.
\end{aligned} \tag{C.67}$$

Now, equation C.66 reduces to

$$\begin{aligned}
&\frac{\partial^2\overline{A}_{3x}^{\dagger}}{\partial z^2}+\frac{\partial^2\overline{A}_{3x}^{\dagger}}{\partial y^2}+k^2(y,\omega_0)\overline{A}_{3x}^{\dagger}=\\
&\quad-2i\beta^{\mathrm{TE}}\left[\frac{\partial\overline{A}_{2x}^{\dagger}}{\partial Z_1}+\beta^{\mathrm{TE}'}\frac{\partial\overline{A}_{2x}^{\dagger}}{\partial T}\right]-2i\beta^{\mathrm{TE}}\frac{\partial\overline{A}_{1x}}{\partial Z_2}-\frac{\partial^2\overline{A}_{1x}}{\partial X^2}-\frac{\partial^2\overline{A}_{1x}}{\partial Z_1^2}\\
&\quad+\left\{\left[\beta^{\mathrm{TE}'}\right]^2+\beta^{\mathrm{TE}}\beta^{\mathrm{TE}''}\right\}\frac{\partial^2\overline{A}_{1x}}{\partial T^2}+2\beta^{\mathrm{TE}}U_x^{\mathrm{TE}'}(y,\omega_0)\frac{\partial^2\overline{A}_1^{\mathrm{TE}}}{\partial T\partial Z_1}\\
&\quad+2\beta^{\mathrm{TE}}\beta^{\mathrm{TE}'}U_x^{\mathrm{TE}'}(y,\omega_0)\frac{\partial^2\overline{A}_1^{\mathrm{TE}}}{\partial T^2}-i\frac{\partial}{\partial\omega_0}\left[\frac{\partial\ln\varepsilon_{\mathcal{R}}^{\mathrm{L}}(y,\omega_0)}{\partial y}\right]\frac{\partial^2\overline{A}_{1y}}{\partial X\partial T}
\end{aligned} \tag{C.68}$$

$$
\begin{aligned}
&- i\frac{\partial \ln \varepsilon^{\mathrm{L}}_{\mathcal{R}}(y,\omega_0)}{\partial y} V_y^{\mathrm{TM}\prime} \frac{\partial^2 \overline{B}_1^{\mathrm{TM}}}{\partial X \partial T} - \frac{\partial \ln \varepsilon^{\mathrm{L}}_{\mathcal{R}}(y,\omega_0)}{\partial y} \frac{\partial \overline{A}^{\dagger}_{2y}}{\partial X} \\
&- 2\omega_0^2 \mu_0 P^{(3)}_{1x},
\end{aligned}
$$

which has homogeneous solution $\overline{A}^{\dagger}_{3x} \propto U_x^{\mathrm{TE}}(y,\omega_0) e^{i\beta^{\mathrm{TE}} z}$. Applying the Fredholm alternative theorem to the right-hand side of equation C.68 gives the following condition

$$
\begin{aligned}
&2i\beta^{\mathrm{TE}} \left[\frac{\partial A_2^{\mathrm{TE}}}{\partial Z_1} + \beta^{\mathrm{TE}\prime} \frac{\partial A_2^{\mathrm{TE}}}{\partial T} + \frac{\partial A_1^{\mathrm{TE}}}{\partial Z_2} \right] \int \left[U_x^{\mathrm{TE}}(y,\omega_0) \right]^2 dy \\
&+ \left[\frac{\partial^2 A_1^{\mathrm{TE}}}{\partial X^2} - \left\{ \left[\beta^{\mathrm{TE}\prime} \right]^2 + \beta^{\mathrm{TE}} \beta^{\mathrm{TE}\prime\prime} \right\} \frac{\partial^2 A_1^{\mathrm{TE}}}{\partial T^2} + \frac{\partial^2 A_1^{\mathrm{TE}}}{\partial Z_1^2} \right] \int \left[U_x^{\mathrm{TE}}(y,\omega_0) \right]^2 dy \\
&- 2\beta^{\mathrm{TE}} \left[\frac{\partial^2 A_1^{\mathrm{TE}}}{\partial Z_1 \partial T} + \beta^{\mathrm{TE}\prime} \frac{\partial^2 A_1^{\mathrm{TE}}}{\partial T^2} \right] \int U_x^{\mathrm{TE}\prime}(y,\omega_0) U_x^{\mathrm{TE}}(y,\omega_0) dy \\
&+ 2n_0 k_f^2 \left| A_1^{\mathrm{TE}} \right|^2 A_1^{\mathrm{TE}} \int n_2(y) \left[U_x^{\mathrm{TE}}(y,\omega_0) \right]^4 dy \\
&+ 2n_0 k_f^2 \left\{ 2\Delta \left| B_1^{\mathrm{TM}} \right|^2 A_1^{\mathrm{TE}} + \gamma \left[B_1^{\mathrm{TM}} \right]^2 A_1^{\mathrm{TE}*} e^{2i[\beta^{\mathrm{TM}} - \beta^{\mathrm{TE}}]z} \right\} \times \\
&\qquad \int n_2(y) \left\{ \left[V_y^{\mathrm{TM}}(y,\omega_0) U_x^{\mathrm{TE}}(y,\omega_0) \right]^2 + \left[V_z^{\mathrm{TM}}(y,\omega_0) U_x^{\mathrm{TE}}(y,\omega_0) \right]^2 \right\} dy \\
&+ i \frac{\partial^2 B_1^{\mathrm{TM}}}{\partial X \partial T} e^{i[\beta^{\mathrm{TM}} - \beta^{\mathrm{TE}}]z} \int \frac{\partial \ln \varepsilon^{\mathrm{L}}_{\mathcal{R}}(y,\omega_0)}{\partial y} V_y^{\mathrm{TM}\prime}(y,\omega_0) U_x^{\mathrm{TE}}(y,\omega_0) dy \\
&+ i \frac{\partial^2 B_1^{\mathrm{TM}}}{\partial X \partial T} e^{i[\beta^{\mathrm{TM}} - \beta^{\mathrm{TE}}]z} \int \frac{\partial}{\partial \omega_0} \left[\frac{\partial \ln \varepsilon^{\mathrm{L}}_{\mathcal{R}}(y,\omega_0)}{\partial y} \right] V_y^{\mathrm{TM}}(y,\omega_0) U_x^{\mathrm{TE}}(y,\omega_0) dy \\
&+ \frac{\partial B_2^{\mathrm{TM}}}{\partial X} e^{i[\beta^{\mathrm{TM}} - \beta^{\mathrm{TE}}]z} \int \frac{\partial \ln \varepsilon^{\mathrm{L}}_{\mathcal{R}}(y,\omega_0)}{\partial y} V_y^{\mathrm{TM}}(y,\omega_0) U_x^{\mathrm{TE}}(y,\omega_0) dy = 0.
\end{aligned}
\tag{C.69}
$$

Using equation C.49, the A_1^{TE} terms with Z_1 derivatives are written

$$
\begin{aligned}
-2\beta^{\mathrm{TE}} \frac{\partial^2 A_1^{\mathrm{TE}}}{\partial Z_1 \partial T} \int U_x^{\mathrm{TE}\prime} U_x^{\mathrm{TE}} dy &= 2\beta^{\mathrm{TE}} \beta^{\mathrm{TE}\prime} \frac{\partial^2 A_1^{\mathrm{TE}}}{\partial T^2} \int U_x^{\mathrm{TE}\prime} U_x^{\mathrm{TE}} dy \\
&- i \frac{\partial^2 B_1^{\mathrm{TM}}}{\partial X \partial T} e^{i[\beta^{\mathrm{TM}} - \beta^{\mathrm{TE}}]z} \frac{\int U_x^{\mathrm{TE}\prime} U_x^{\mathrm{TE}} dy \int V_y^{\mathrm{TM}} U_x^{\mathrm{TE}} [\partial \ln \varepsilon^{\mathrm{L}}_{\mathcal{R}}(y,\omega_0)/\partial y] dy}{\int \left[U_x^{\mathrm{TE}} \right]^2 dy}
\end{aligned}
\tag{C.70}
$$

$$
\begin{aligned}
\frac{\partial^2 A_1^{\mathrm{TE}}}{\partial Z_1^2} \int \left[U_x^{\mathrm{TE}} \right]^2 dy &= \left[\beta^{\mathrm{TE}\prime} \right]^2 \frac{\partial^2 A_1^{\mathrm{TE}}}{\partial T^2} \int \left[U_x^{\mathrm{TE}} \right]^2 dy \\
&- i \frac{\beta^{\mathrm{TE}\prime} + \beta^{\mathrm{TM}\prime}}{2\beta^{\mathrm{TE}}} \frac{\partial^2 B_1^{\mathrm{TM}}}{\partial X \partial T} e^{i[\beta^{\mathrm{TM}} - \beta^{\mathrm{TE}}]z} \int V_y^{\mathrm{TM}} U_x^{\mathrm{TE}} [\partial \ln \varepsilon^{\mathrm{L}}_{\mathcal{R}}(y,\omega_0)/\partial y] dy \\
&- \frac{\partial^2 A_1^{\mathrm{TE}}}{\partial X^2} \frac{\int V_y^{\mathrm{TM}} U_x^{\mathrm{TE}} \left[\frac{\partial \ln \varepsilon^{\mathrm{L}}_{\mathcal{R}}(y,\omega_0)}{\partial y} \right] dy \int V_x^{\mathrm{TM}} U_y^{\mathrm{TE}} \left[\frac{\partial \ln \varepsilon^{\mathrm{L}}_{\mathcal{R}}(y,\omega_0)}{\partial y} \right] dy}{4\beta^{\mathrm{TE}} \beta^{\mathrm{TM}} \int \left[V_x^{\mathrm{TM}} \right]^2 dy}.
\end{aligned}
\tag{C.71}
$$

Finally, using these expressions and defining the effective diffraction and nonlinear coefficients, the evolution equation becomes

$$
\begin{aligned}
2i\beta^{\mathrm{TE}} \left[\frac{\partial A_2^{\mathrm{TE}}}{\partial Z_1} + \beta^{\mathrm{TE}\prime} \frac{\partial A_2^{\mathrm{TE}}}{\partial T} + \frac{\partial A_1^{\mathrm{TE}}}{\partial Z_2} \right] + \sigma^{\mathrm{TE}} \frac{\partial^2 A_1^{\mathrm{TE}}}{\partial X^2} - \beta^{\mathrm{TE}} \beta^{\mathrm{TE}\prime\prime} \frac{\partial^2 A_1^{\mathrm{TE}}}{\partial T^2} \\
+ 2k_0^2 \frac{n_2^{\mathrm{TE-spm}}}{n_0} \left| A_1^{\mathrm{TE}} \right|^2 A_1^{\mathrm{TE}} + 4k_0^2 \frac{n_2^{\mathrm{TE-xpm}}}{n_0} \Delta \left| B_1^{\mathrm{TM}} \right|^2 A_1^{\mathrm{TE}} = 0,
\end{aligned}
\tag{C.72}
$$

where the phase-dependent terms arising from the x projections of the TM mode have been dropped. This is justified because the terms that show up at this order are significant over the distance scale Z_2 (and farther), and the phase dependent terms are assumed to have coherence length $L_{\mathrm{coh}} \sim Z_1$, and therefore average away for NLS propagation. For the same reasons, the

phase-dependent terms in the nonlinear polarization are also dropped, because they have a phase factor $e^{2i[\beta^{TM}-\beta^{TE}]}$ associated with them, and coherence length $L_{coh}/2$.

The diffraction coefficient is defined as

$$\sigma^{TE} = 1 - \frac{\int V_y^{TM} U_x^{TE} \left[\frac{\partial \varepsilon_{\mathcal{R}}^{L}(y,\omega_0)}{\partial y}\right] dy \int V_x^{TM} U_y^{TE} \left[\frac{\partial \varepsilon_{\mathcal{R}}^{L}(y,\omega_0)}{\partial y}\right] dy}{4\beta^{TE}\beta^{TM} \int [U_x^{TE}]^2 dy \int [V_x^{TM}]^2 dy} \tag{C.73}$$

which has primary contribution from linear homogeneous diffraction and an additional contribution arising from the linear coupling between the two waveguide modes. This latter contribution is assumed small and σ taken as unity. In the case of a step-index waveguide, this assumption is well justified by noting that the derivative of the dielectric function results in a delta function, which, in the integrals in the numerator, serves to sample the value of the product of the modal envelopes at each interface. With a finite number of interfaces, these contributions will be much smaller than the continuous summation given by the integrals in the denominator.

The effective self- and cross-phase modulation coefficients are defined

$$n_2^{TE-spm} \equiv \frac{\int n_2(y) \left[U_x^{TE}(y,\omega_0)\right]^4 dy}{\int [U_x^{TE}]^2 dy} \tag{C.74}$$

$$n_2^{TE-xpm} \equiv \frac{\int n_2(y) \left[U_x^{TE}(y,\omega_0) V_y^{TM}(y,\omega_0)\right]^2 dy}{\int [U_x^{TE}]^2 dy}. \tag{C.75}$$

Note that in writing the effective nonlinear coefficient for cross-phase modulation that it was assumed that $V_z^{TM} \ll V_y^{TM}, U_x^{TE}$, which is valid for weak guidance. Due to the overlap between the TE and TM modes, the effective ratio between the self-phase modulation and cross-phase modulation coefficients may not equal the intrinsic value 2Δ, because, in general, $n_2^{TE-spm} \neq n_2^{TE-xpm}$.

Taking the results from this and the previous order, the nonlinear wave equation for the TE mode in laboratory units is

$$\begin{aligned} 2i\beta^{TE}\left[\frac{\partial A^{TE}}{\partial z} + \beta^{TE\prime}\frac{\partial A^{TE}}{\partial t}\right] + \frac{\partial^2 A^{TE}}{\partial x^2} - \beta^{TE}\beta^{TE\prime\prime}\frac{\partial^2 A^{TE}}{\partial t^2} \\ + 2k_0^2 \frac{n_2^{TE-spm}}{n_0}\left|A^{TE}\right|^2 A^{TE} + 4k_0^2 \frac{n_2^{TE-xpm}}{n_0}\Delta\left|B^{TM}\right|^2 A^{TE} = 0. \end{aligned} \tag{C.76}$$

TM Mode

Performing the same steps with the x-component of the magnetic field results in

$$\begin{aligned} &\frac{\partial^2 \overline{B}_{3x}^{\dagger}}{\partial z^2} + k^2(y,\omega_0)\overline{B}_{3x}^{\dagger} + \frac{\partial^2 \overline{B}_{3x}^{\dagger}}{\partial y^2} - \frac{\partial \ln \varepsilon_{\mathcal{R}}^{L}(y,\omega_0)}{\partial y}\frac{\partial \overline{B}_{3x}^{\dagger}}{\partial y} = \\ &- 2i\beta^{TM}\left[\frac{\partial \overline{B}_{2x}^{\dagger}}{\partial Z_1} + \beta^{TM\prime}\frac{\partial \overline{B}_{2x}^{\dagger}}{\partial T}\right] - 2i\beta^{TM}\frac{\partial \overline{B}_{1x}}{\partial Z_2} - \frac{\partial^2 \overline{B}_{1x}}{\partial X^2} - \frac{\partial^2 \overline{B}_{1x}}{\partial Z_1^2} \\ &+ \left\{\left[\beta^{TM\prime}\right]^2 + \beta^{TM}\beta^{TM\prime\prime}\right\}\frac{\partial^2 \overline{B}_{1x}}{\partial T^2} + 2\beta^{TM}V_x^{TM\prime}(y,\omega_0)\frac{\partial^2 \overline{B}_1^{TM}}{\partial T \partial Z_1} \\ &+ 2\beta^{TM}\beta^{TM\prime}V_x^{TM\prime}(y,\omega_0)\frac{\partial^2 \overline{B}_1^{TM}}{\partial T^2} - i\frac{\eta^{TM}}{\eta^{TE}}\frac{\partial}{\partial \omega_0}\left[\frac{\partial \ln \varepsilon_{\mathcal{R}}^{L}(y,\omega_0)}{\partial y}\right]\frac{\partial^2 \overline{B}_{1y}}{\partial X \partial T} \\ &- i\frac{\eta^{TM}}{\eta^{TE}}\frac{\partial \ln \varepsilon_{\mathcal{R}}^{L}(y,\omega_0)}{\partial y}U_x^{TE\prime}(y,\omega_0)\frac{\partial^2 \overline{A}_1^{TE}}{\partial T \partial X} - \frac{\eta^{TM}}{\eta^{TE}}\frac{\partial \ln \varepsilon_{\mathcal{R}}^{L}(y,\omega_0)}{\partial y}\frac{\partial \overline{B}_{2y}^{\dagger}}{\partial X} \\ &+ 2i\eta^{TM}\omega_0\left[\frac{\partial \ln \varepsilon_{\mathcal{R}}^{L}(y,\omega_0)}{\partial y}P_{1z}^{(3)} - \frac{\partial P_{1z}^{(3)}}{\partial y} + \frac{\partial P_{1y}^{(3)}}{\partial z}\right], \end{aligned} \tag{C.77}$$

which has homogeneous solution $\overline{B}^{\dagger}_{3x} \propto V_x^{\mathrm{TM}}(y,\omega_0)e^{i\beta^{\mathrm{TM}}z}$. Applying the Fredholm alternative theorem to the right-hand side of equation C.77 gives the following condition

$$
\begin{aligned}
&2i\beta^{\mathrm{TM}}\left[\frac{\partial B_2^{\mathrm{TM}}}{\partial Z_1}+\beta^{\mathrm{TM}\prime}\frac{\partial B_2^{\mathrm{TM}}}{\partial T}+\frac{\partial B_1^{\mathrm{TM}}}{\partial Z_2}\right]\int\left[V_x^{\mathrm{TM}}(y,\omega_0)\right]^2dy \\
&+\left[\frac{\partial^2 B_1^{\mathrm{TM}}}{\partial X^2}-\left\{\left[\beta^{\mathrm{TM}\prime}\right]^2+\beta^{\mathrm{TM}}\beta^{\mathrm{TM}\prime\prime}\right\}\frac{\partial^2 B_1^{\mathrm{TM}}}{\partial T^2}+\frac{\partial^2 B_1^{\mathrm{TM}}}{\partial Z_1^2}\right]\int\left[V_x^{\mathrm{TM}}(y,\omega_0)\right]^2dy \\
&-2\beta^{\mathrm{TM}}\left[\frac{\partial^2 B_1^{\mathrm{TM}}}{\partial Z_1\partial T}+\beta^{\mathrm{TM}\prime}\frac{\partial^2 B_1^{\mathrm{TM}}}{\partial T^2}\right]\int V_x^{\mathrm{TM}\prime}(y,\omega_0)V_x^{\mathrm{TM}}(y,\omega_0)dy \\
&+2n_0k_f^2\left|B_1^{\mathrm{TM}}\right|^2B_1^{\mathrm{TM}}\int n_2(y)\left[V_y^{\mathrm{TM}}(y,\omega_0)\right]^3V_x^{\mathrm{TM}}(y,\omega_0)dy \\
&+\frac{2n_0k_f^2}{\beta^{\mathrm{TM}}}\left\{2\Delta\beta^{\mathrm{TM}}\left|A_1^{\mathrm{TE}}\right|^2B_1^{\mathrm{TM}}+\gamma\left[2\beta^{\mathrm{TE}}-\beta^{\mathrm{TM}}\right]\left[A_1^{\mathrm{TE}}\right]^2B_1^{\mathrm{TM}*}e^{2i[\beta^{\mathrm{TE}}-\beta^{\mathrm{TM}}]z}\right\}\times \\
&\qquad\int n_2(y)\left[U_x^{\mathrm{TE}}(y,\omega_0)\right]^2V_y^{\mathrm{TM}}(y,\omega_0)V_x^{\mathrm{TM}}(y,\omega_0)dy \\
&+i\frac{\eta^{\mathrm{TM}}}{\eta^{\mathrm{TE}}}\frac{\partial^2 A_1^{\mathrm{TE}}}{\partial X\partial T}e^{i[\beta^{\mathrm{TE}}-\beta^{\mathrm{TM}}]z}\int\left[\frac{\partial\ln\varepsilon_{\mathcal{R}}^{\mathrm{L}}(y,\omega_0)}{\partial y}\right]U_y^{\mathrm{TE}\prime}(y,\omega_0)V_x^{\mathrm{TM}}(y,\omega_0)dy \\
&+i\frac{\eta^{\mathrm{TM}}}{\eta^{\mathrm{TE}}}\frac{\partial^2 A_1^{\mathrm{TE}}}{\partial X\partial T}e^{i[\beta^{\mathrm{TE}}-\beta^{\mathrm{TM}}]z}\int\frac{\partial}{\partial\omega_0}\left[\frac{\partial\ln\varepsilon_{\mathcal{R}}^{\mathrm{L}}(y,\omega_0)}{\partial y}\right]U_y^{\mathrm{TE}}(y,\omega_0)V_x^{\mathrm{TM}}(y,\omega_0)dy \\
&+\frac{\eta^{\mathrm{TM}}}{\eta^{\mathrm{TE}}}\frac{\partial A_2^{\mathrm{TE}}}{\partial X}e^{i[\beta^{\mathrm{TE}}-\beta^{\mathrm{TM}}]z}\int\frac{\partial\ln\varepsilon_{\mathcal{R}}^{\mathrm{L}}(y,\omega_0)}{\partial y}U_y^{\mathrm{TE}}(y,\omega_0)V_x^{\mathrm{TM}}(y,\omega_0)dy\;=\;0,
\end{aligned}
\tag{C.78}
$$

where again it was assumed that $V_z^{\mathrm{TM}} \ll V_y^{\mathrm{TM}}, U_x^{\mathrm{TE}}$ such that the z component of the nonlinear polarization P_{1z} can be neglected.

As before, using equation C.53, the B_1^{TM} terms with Z_1 are rewritten, allowing the solvability condition to be reduced to

$$
\begin{aligned}
&2i\beta^{\mathrm{TM}}\left[\frac{\partial B_2^{\mathrm{TM}}}{\partial Z_1}+\beta^{\mathrm{TM}\prime}\frac{\partial B_2^{\mathrm{TM}}}{\partial T}+\frac{\partial B_1^{\mathrm{TM}}}{\partial Z_2}\right]+\sigma^{\mathrm{TM}}\frac{\partial^2 B_1^{\mathrm{TM}}}{\partial X^2}-\beta^{\mathrm{TM}}\beta^{\mathrm{TM}\prime\prime}\frac{\partial^2 B_1^{\mathrm{TM}}}{\partial T^2} \\
&\qquad+2k_0^2\frac{n_2^{\mathrm{TM-spm}}}{n_0}\left|B_1^{\mathrm{TM}}\right|^2B_1^{\mathrm{TM}}+4k_0^2\frac{n_2^{\mathrm{TM-xpm}}}{n_0}\Delta\left|A_1^{\mathrm{TE}}\right|^2B_1^{\mathrm{TM}}=0,
\end{aligned}
\tag{C.79}
$$

where the phase-dependent terms arising from the x projections of the TE mode have been dropped. The phase-dependent terms in the nonlinear polarization are also dropped. The diffraction coefficient is defined as

$$
\sigma^{\mathrm{TM}}=1-\frac{\int U_x^{\mathrm{TE}}V_x^{\mathrm{TM}}\left[\frac{\partial\varepsilon_{\mathcal{R}}^{\mathrm{L}}(y,\omega_0)}{\partial y}\right]dy\int U_x^{\mathrm{TE}}V_y^{\mathrm{TM}}\left[\frac{\partial\varepsilon_{\mathcal{R}}^{\mathrm{L}}(y,\omega_0)}{\partial y}\right]dy}{4\beta^{\mathrm{TM}}\beta^{\mathrm{TE}}\int\left[V_x^{\mathrm{TM}}\right]^2dy\int\left[U_x^{\mathrm{TE}}\right]^2dy},
\tag{C.80}
$$

which is again taken as unity, and the effective self- and cross-phase modulation coefficients are defined

$$
n_2^{\mathrm{TM-spm}}\equiv\frac{\int n_2(y)\left[V_y^{\mathrm{TM}}(y,\omega_0)\right]^3V_x^{\mathrm{TM}}(y,\omega_0)dy}{\int\left[V_x^{\mathrm{TM}}\right]^2dy}
\tag{C.81}
$$

$$
n_2^{\mathrm{TM-xpm}}\equiv\frac{\int n_2(y)\left[U_x^{\mathrm{TE}}(y,\omega_0)\right]^2V_y^{\mathrm{TM}}(y,\omega_0)V_x^{\mathrm{TM}}(y,\omega_0)dy}{\int\left[V_x^{\mathrm{TM}}\right]^2dy}.
\tag{C.82}
$$

Taking the results from this and the previous order, the nonlinear wave equation for the TM mode in laboratory units is

$$
\begin{aligned}
&2i\beta^{\mathrm{TM}}\left[\frac{\partial B^{\mathrm{TM}}}{\partial z}+\beta^{\mathrm{TM}\prime}\frac{\partial B^{\mathrm{TM}}}{\partial t}\right]+\frac{\partial^2 B^{\mathrm{TM}}}{\partial x^2}-\beta^{\mathrm{TM}}\beta^{\mathrm{TM}\prime\prime}\frac{\partial^2 B^{\mathrm{TM}}}{\partial t^2} \\
&\qquad+2k_0^2\frac{n_2^{\mathrm{TM-spm}}}{n_0}\left|B^{\mathrm{TM}}\right|^2B^{\mathrm{TM}}+4k_0^2\frac{n_2^{\mathrm{TM-xpm}}}{n_0}\Delta\left|A^{\mathrm{TE}}\right|^2B^{\mathrm{TM}}=0.
\end{aligned}
\tag{C.83}
$$

As mentioned previously, these results are obtained strictly for the purposes of illustration of the effects of transverse guidance, which, in the weak guidance approximation, results is effective linear and nonlinear coefficients. The modified NLS equations are not used for the simulations directly, but the effective linear coefficients are evaluated in Appendix D for the purposes of obtaining the birefringence beat length and the group-velocity walkoff length.

Appendix D

Optical Properties of Fused Silica

The numerical simulations presented in this thesis make use of the material parameters of fused silica. The reasons for this choice are numerous: fused silica is highly transparent in the visible and infrared with small linear and two-photon absorption and ultrafast non-resonant nonlinearity, has anomalous group-delay dispersion at the telecommunications wavelengths around $\lambda_f = 1.55\ \mu$m, has high damage threshold, is well characterized, and has well-developed technology for fabrication into slab and cylindrical waveguide devices. The main downside, though, is the relatively small nonlinear coefficient. Because of this fact, other nonresonant nonlinear materials, such as AlGaAs and PTS, will ultimately need to be studied, but fused silica serves as a useful material on which to base initial investigations and the results obtained should be generalizable to other materials.

The first section discusses the optical properties of fused silica in bulk, while the second section looks at glass slab waveguides, in which the linear properties are modified due to transverse confinement.

D.1 Properties of Bulk Fused Silica

For comparison, linear and nonlinear properties of fused silica and other candidate materials are shown in Table D.1. The other materials are presented here because optical properties are used in Chapter 5 to derive figures of merit for use in spatial soliton switching.

For the spatio-temporal simulations, the linear index dispersion and nonlinear Raman dispersion need to be discussed. Appendix B covers the Raman response function and Raman susceptibility spectrum for fused silica. The linear index dispersion is typically given by a Sellmeier-type relation of the form

$$n^2(\lambda) = 1 + \sum_{j=1}^{\ell} \frac{B_j \lambda^2}{\lambda^2 - \lambda_j^2}, \tag{D.1}$$

where λ_j are the resonance wavelengths and B_j are the associated oscillator strengths. Table D.2 lists the coefficients for fused silica [30].

Material	fused silica	39% Pb silicate	PTS	$Al_{.18}Ga_{.82}As$
reference	[30]	[156]	[125]	[127]
λ_0 (μm)	1.55	1.064	1.6	1.55
n_0	1.444	1.774	1.8	3.4
k_0'' (ps^2/μm)	-2.79×10^{-8}	1.17×10^{-7}	> 0?	1×10^{-6} [157]
α (cm^{-1})	0.1	0.1	0.3^a	0.15
n_2^I (cm^2/W)	3.3×10^{-16}	2.2×10^{-15}	2.2×10^{-12}	1.2×10^{-13}
β_2^I (cm/W)	5.5×10^{-15}	7.2×10^{-13}	$< 5.0 \times 10^{-10}$	$\approx 0^b$
n_4^I (cm^4/W^2)	?	?	-8×10^{-22}	-5×10^{-23} [143]

^{a} absorption at $\lambda_f = 1.3\mu$m used [158]
^{b} three-photon absorption is estimated at $\beta_4^I = 0.055 \times 10^{-18}$ cm^3/W [127]

Table D.1: Linear and nonlinear properties of promising materials for nonlinear optical switching. The values for the linear absorption coefficient are valid for slab waveguide geometries and are dominated by waveguide scattering.

j	resonance wavelength λ_j (μm)	oscillator strength B_j
1	0.0684043	0.6961663
2	0.1162414	0.4079426
3	9.896161	0.8974794

Table D.2: Sellmeier coefficients for fused silica.

A plot of index dispersion over visible to near IR is shown in Figure D.1. The refractive index n determines the phase

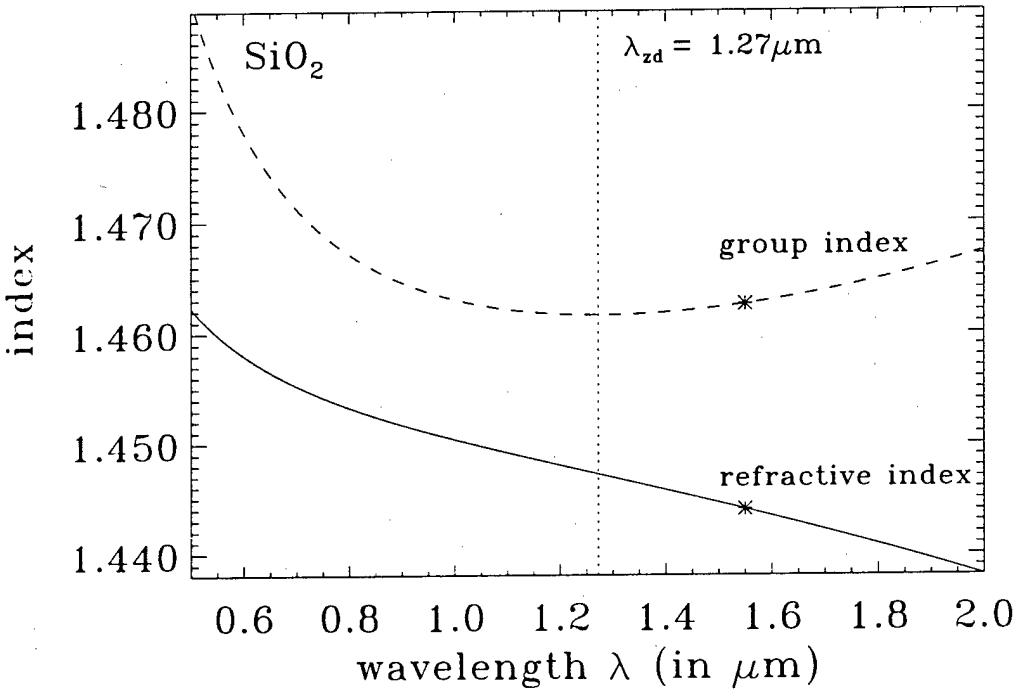

Figure D.1: Linear refractive index n and group index n_g for fused silica. The zero dispersion wavelength $\lambda_{zd} = 1.27\,\mu$m divides the boundary between the normal dispersion regime ($\lambda < \lambda_{zd}$) and the anomalous dispersion regime ($\lambda > \lambda_{zd}$). The curves are marked for their values at 1.55 μm.

velocity $v_p = c/n$, where c is the speed of light in free-space. The material propagation constant $k = \omega n/c$ is also referred to here as the phase delay coefficient, since it is related to the inverse phase velocity. Of more relevance to this thesis, though, are the group velocity and the group delay coefficient. The group velocity is the velocity at which a quasi-monochromatic wavepacket travels, which is in general different than the phase velocity, and is most easily calculated from the group delay coefficient. The group delay coefficient is the frequency derivative of the phase delay:

$$k' = \frac{\partial k}{\partial \omega} = \frac{1}{c}\left[n + \omega\frac{\partial n}{\partial \omega}\right] \equiv \frac{n_g}{c}, \tag{D.2}$$

where n_g is the group index. Now, the group velocity is

$$v_g = \frac{1}{k'} = \frac{c}{n_g}. \tag{D.3}$$

The group index is also plotted in Figure D.1, showing that, over the spectral range plotted, the group velocity is less than the phase velocity, which is generally true away from resonance.

Another useful relation is the calculation of group delay based on the change of index with wavelength. Noting that

$$\omega = \frac{2\pi c}{\lambda} \Rightarrow \frac{\partial}{\partial\omega} = -\frac{\lambda^2}{2\pi c}\frac{\partial}{\partial\lambda}, \tag{D.4}$$

the group delay can be written

$$k' = \frac{1}{c}\left[n - \lambda\frac{\partial n}{\partial\lambda}\right]. \tag{D.5}$$

Group-delay dispersion describes the variation in group delay across a wave packet spectrum and is responsible for pulse broadening in linear propagation. The group-delay dispersion coefficient is calculated

$$\begin{aligned} k'' = \frac{\partial^2 k}{\partial\omega^2} &= \frac{1}{c}\left[2\frac{\partial n}{\partial\omega} + \omega\frac{\partial^2 n}{\partial\omega^2}\right] \\ &= \frac{\lambda^3}{2\pi c^2}\frac{\partial^2 n}{\partial\lambda^2}. \end{aligned} \tag{D.6}$$

Figure D.2 plots group-delay dispersion over the wavelength range 0.5 - 2.0 μm. The zero-dispersion wavelength is also shown

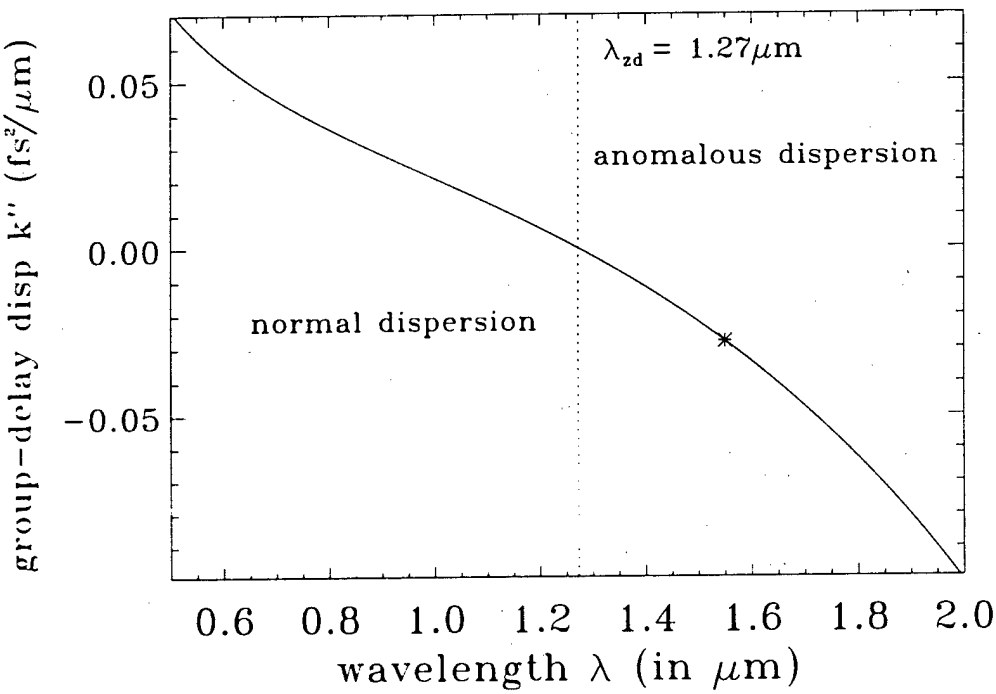

Figure D.2: Group-delay dispersion k'' for fused silica. The zero dispersion wavelength $\lambda_{zd} = 1.27\ \mu$m divides the boundary between the normal dispersion regime ($\lambda < \lambda_{zd}$) and the anomalous dispersion regime ($\lambda > \lambda_{zd}$). The curve is marked for its value at 1.55 μm.

on this plot to emphasize that, since group-delay dispersion is zero at this location, a wavepacket should propagate without change. Of course, this is not strictly true, because any wavepacket has nonzero bandwidth and will broaden because the slope (called third-order dispersion) and curvature (fourth-order dispersion) of group-delay dispersion are nonzero at this wavelength.

Higher-order dispersion becomes important for broad temporal bandwidths. The simulations of spatio-temporal solitons in this thesis use the higher-order dispersion coefficients because such broad bandwidths are present. Third-order dispersion is calculated from

$$\begin{aligned} k''' = \frac{\partial^3 k}{\partial\omega^3} &= \frac{1}{c}\left[3\frac{\partial^2 n}{\partial\omega^2} + \omega\frac{\partial^3 n}{\partial\omega^3}\right] \\ &= -\frac{\lambda^4}{4\pi^2 c^3}\left[3\frac{\partial^2 n}{\partial\lambda^2} + \lambda\frac{\partial^3 n}{\partial\lambda^3}\right]. \end{aligned} \tag{D.7}$$

Fourth-order dispersion is calculated from

$$k'''' = \frac{\partial^4 k}{\partial \omega^4} = \frac{1}{c}\left[4\frac{\partial^3 n}{\partial \omega^3} + \omega\frac{\partial^4 n}{\partial \omega^4}\right] \tag{D.8}$$
$$= \frac{\lambda^5}{8\pi^3 c^4}\left[12\frac{\partial^2 n}{\partial \lambda^2} + 8\lambda\frac{\partial^3 n}{\partial \lambda^3} + \lambda^2\frac{\partial^4 n}{\partial \lambda^4}\right].$$

Plots of third and fourth-order dispersion for fused silica are shown in Figure D.3.

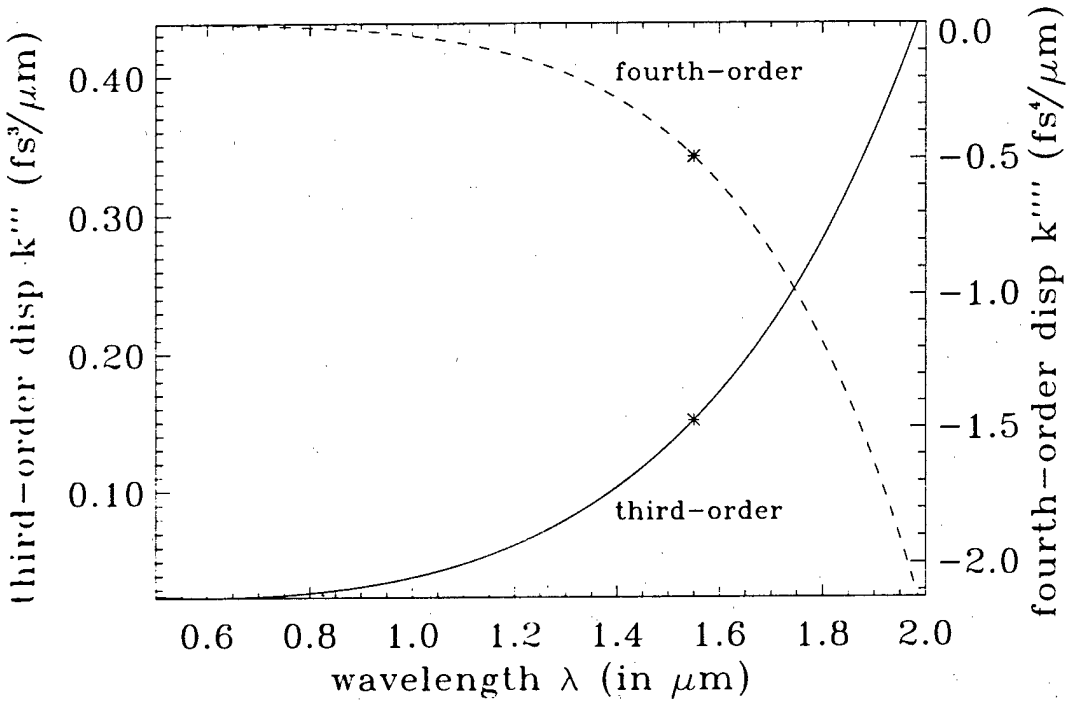

Figure D.3 Higher-order dispersion for fused silica. Third- (solid curve) and fourth-order (dashed curve) dispersions are plotted versus wavelength. The curves are marked for their values at 1.55 μm.

As a summary of this section, the appropriate dispersion coefficients for bulk fused silica at the communications wavelength $\lambda = 1.55\ \mu$m are listed in Table D.3.

coefficient	bulk SiO_2	units
n_0	1.444	
k_0	5.854	$1/\mu$m
k_0'	4.875	fs/μm
k_0''	-0.02791	fs$^2/\mu$m
k_0'''	0.1511	fs$^3/\mu$m
k_0''''	-0.4931	fs$^4/\mu$m

Table D.3: Calculated dispersion coefficients for bulk fused silica at $\lambda = 1.55\ \mu$m.

D.2 Properties of Glass Waveguides

The waveguide geometry of interest is shown Figure C.1. This sections derives the TE and TM eigenvalues and modal profiles in this three-layer slab case, and evaluates the modal phase delays β^{TE} and β^{TM} and the effective linear coefficients derived in Appendix C.

A cross-sectional view is shown in Figure D.4. Since the structure is piece-wise separable, the following definition is used which represents phase delay in each layer

$$k_j^2 = \omega^2 \mu_0 \varepsilon_j = \left[\frac{2\pi n_j}{\lambda}\right]^2, \tag{D.9}$$

where $n_j^2 = \varepsilon_j$. Note that it is assumed that the magnetic permeability is the same in all regions.

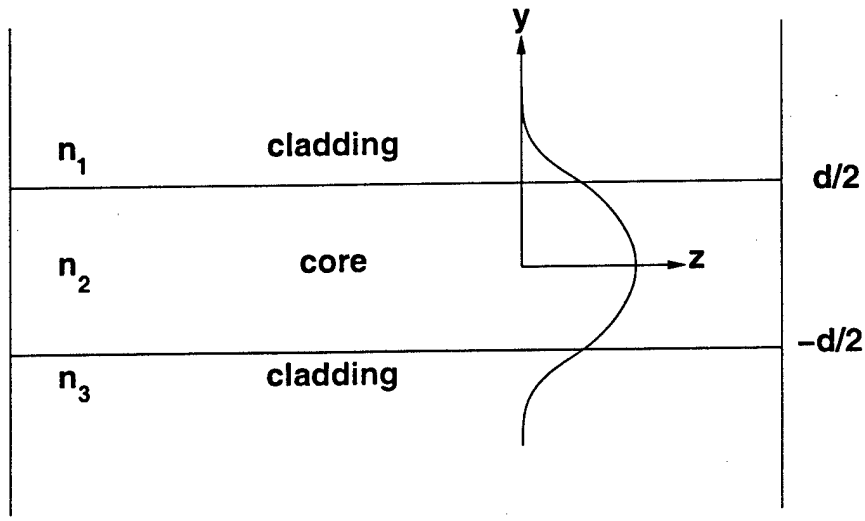

Figure D.4: Cross-sectional view of three-layer slab waveguide geometry. In general, the refractive indices of the two cladding layers are different, leading to an asymmetric structure.

D.2.1 Derivation of TE Mode

The solution for the TE mode must satisfy equation C.23, repeated here for convenience

$$\frac{\partial^2 U_x^{\mathrm{TE}}(y,\omega)}{\partial y^2} = \left\{\left[\beta^{\mathrm{TE}}\right]^2 - k^2(y,\omega)\right\} U_x^{\mathrm{TE}}(y,\omega), \tag{D.10}$$

along with the boundary conditions C.24. It is clear that, depending on the size of $\left[\beta^{\mathrm{TE}}\right]^2$ relative to $k^2(y,\omega)$, equation D.10 has two types of solutions:

$$\begin{aligned} U_x^{\mathrm{TE}} &= a_1 e^{\alpha_y y} + a_2 e^{-\alpha_y y} && \text{when } \left[\beta^{\mathrm{TE}}\right]^2 > k^2(y,\omega) \\ U_x^{\mathrm{TE}} &= b_1 e^{i\kappa_y y} + b_2 e^{-i\kappa_y y} && \text{when } \left[\beta^{\mathrm{TE}}\right]^2 < k^2(y,\omega). \end{aligned} \tag{D.11}$$

The transverse wave numbers are defined

$$\begin{aligned} \alpha_y^2 &= \left[\beta^{\mathrm{TE}}\right]^2 - k^2(y,\omega) \\ \kappa_y^2 &= k^2(y,\omega) - \left[\beta^{\mathrm{TE}}\right]^2. \end{aligned} \tag{D.12}$$

It is clear that in order to satisfy the boundary condition of finite one-dimensional power, the modal profiles must decay in the cladding regions, implying that the effective longitudinal wave number β^{TE} is greater than the bulk propagation constant of the cladding. This also implies that, in order to satisfy the continuity boundary conditions, the field in the core region cannot decay, such that the effective longitudinal wave number is less than the bulk propagation constant of the core.

With that in mind, the following piecewise solution is posed

$$U_x^{\mathrm{TE}}(y,\omega) = \begin{cases} a_1 e^{-\alpha_{1y} y} & y > d/2 \\ b\cos(\kappa_{2y} y + \phi) & -d/2 < y < d/2 \\ a_2 e^{\alpha_{3y} y} & y < -d/2 \end{cases} \tag{D.13}$$

where the solution in the core region is written in the form of a cos() function without loss of generality. Note that the non-decaying solutions in the cladding regions have been eliminated. Imposing the boundary conditions at $y = d/2$ yields the following constraints

$$a_1 e^{-\alpha_{1y} d/2} = b\cos(\kappa_{2y} d/2 + \phi) \tag{D.14}$$

$$-\alpha_{1y} a_1 e^{-\alpha_{1y} d/2} = -\kappa_{2y} b \sin(\kappa_{2y} d/2 + \phi), \tag{D.15}$$

which can be divided to obtain

$$\frac{\alpha_{1y}}{\kappa_{2y}} = \tan(\kappa_{2y} d/2 + \phi). \tag{D.16}$$

Similarly for the fields at $y = -d/2$,

$$\begin{aligned} a_2 e^{-\alpha_{3y} d/2} &= b\cos(-\kappa_{2y} d/2 + \phi) \\ \alpha_{3y} a_2 e^{-\alpha_{3y} d/2} &= -\kappa_{2y} b \sin(-\kappa_{2y} d/2 + \phi) \\ \Rightarrow \frac{\alpha_{3y}}{\kappa_{2y}} &= \tan(\kappa_{2y} d/2 - \phi). \end{aligned} \tag{D.17}$$

Now there are two equations and one unknown - ϕ. Forcing both equations to give the same value for ϕ results in the condition

$$\frac{1}{2}\phi_1^{TE} + \frac{1}{2}\phi_3^{TE} = \kappa_{2y} d \pm p\pi, \tag{D.18}$$

where p is a nonzero integer and the phases are defined

$$\phi_1^{TE} = 2\tan^{-1}(\alpha_{1y}/\kappa_{2y}) = \kappa_{2y} d + 2\phi \pm n\pi \tag{D.19}$$

$$\phi_3^{TE} = 2\tan^{-1}(\alpha_{3y}/\kappa_{2y}) = \kappa_{2y} d - 2\phi \pm m\pi. \tag{D.20}$$

Defining the effective index

$$\kappa_{2y} = \sqrt{k_2^2 - [\beta^{TE}]^2} \equiv k_0 \sqrt{n_2^2 - n_{eff}^2}, \tag{D.21}$$

the equation for the modal eigenvalue can be written

$$2k_0 d\sqrt{n_2^2 - n_{eff}^2} - \phi_1^{TE} - \phi_3^{TE} = 2p\pi, \tag{D.22}$$

which can be solved numerically via the bisection method. The phases are rewritten as

$$\phi_1^{TE} = 2\tan^{-1}\left(\frac{\sqrt{n_{eff}^2 - n_1^2}}{\sqrt{n_2^2 - n_{eff}^2}}\right) \tag{D.23}$$

$$\phi_3^{TE} = 2\tan^{-1}\left(\frac{\sqrt{n_{eff}^2 - n_3^2}}{\sqrt{n_2^2 - n_{eff}^2}}\right). \tag{D.24}$$

With n_{eff}, and hence β^{TE}, known, κ_{2y}, α_{1y}, α_{3y}, and ϕ can be calculated. From this information, the overall profile can be calculated

$$U_x^{TE}(y,\omega) = b \begin{cases} \cos(\kappa_{2y} d/2 + \phi) e^{-\alpha_{1y}[y - d/2]} & y > d/2 \\ \cos(\kappa_{2y} y + \phi) & -d/2 \le y \le d/2 \\ \cos(\kappa_{2y} d/2 - \phi) e^{\alpha_{3y}[y + d/2]} & y < -d/2 \end{cases} \tag{D.25}$$

where b is an arbitrary (real) constant. In Appendix C, this constant is taken as unity.

D.2.2 Derivation of TM Mode

The solution for the TM mode must satisfy equation C.28, repeated here for convenience

$$\frac{\partial^2 V_x^{TM}(y,\omega_0)}{\partial y^2} - \frac{\partial \ln \varepsilon_{\mathcal{R}}^{L}(y,\omega_0)}{\partial y}\frac{\partial V_x^{TM}(y,\omega_0)}{\partial y} = \left\{[\beta^{TM}]^2 - k^2(y,\omega_0)\right\} V_x^{TM}(y,\omega_0), \tag{D.26}$$

along with the boundary conditions C.29. When taking the boundary conditions into account at each interface, the eigenvalue equation to be solved in each homogeneous region is [159]

$$\frac{\partial^2 V_x^{\mathrm{TM}}(y,\omega_0)}{\partial y^2} = \left\{ \left[\beta^{\mathrm{TM}}\right]^2 - k^2(y,\omega_0) \right\} V_x^{\mathrm{TM}}(y,\omega_0), \tag{D.27}$$

which has the same form as for the TE mode.

Following the same steps used in the previous section yields the equation for the TM effective index

$$2k_0 d\sqrt{n_2^2 - n_{\mathrm{eff}}^2} - \phi_1^{\mathrm{TM}} - \phi_3^{\mathrm{TM}} = 2p\pi. \tag{D.28}$$

The phases are defined

$$\phi_1^{\mathrm{TM}} = 2\tan^{-1}\left(\frac{n_2^2\sqrt{n_{\mathrm{eff}}^2 - n_1^2}}{n_1^2\sqrt{n_2^2 - n_{\mathrm{eff}}^2}}\right) = \kappa_{2y}d + 2\phi' \pm n\pi \tag{D.29}$$

$$\phi_3^{\mathrm{TM}} = 2\tan^{-1}\left(\frac{n_2^2\sqrt{n_{\mathrm{eff}}^2 - n_3^2}}{n_3^2\sqrt{n_2^2 - n_{\mathrm{eff}}^2}}\right) = \kappa_{2y}d - 2\phi' \pm m\pi, \tag{D.30}$$

and the overall profile can be written

$$V_x^{\mathrm{TM}}(y,\omega) = \begin{cases} \cos(\kappa_{2y}d/2 + \phi')e^{-\alpha_{1y}[y-d/2]} & y > d/2 \\ \cos(\kappa_{2y}y + \phi') & -d/2 \le y \le d/2 \\ \cos(\kappa_{2y}d/2 - \phi')e^{\alpha_{3y}[y+d/2]} & y < -d/2 \end{cases} \tag{D.31}$$

D.2.3 Linear Waveguide Dispersion Properties

This section calculates the dispersion coefficients for the TE and TM modes, taking into account both the material and waveguide dispersions. The waveguide structure is assumed to be three-layer, as illustrated in Figure D.4.

The Sellmeier coefficients for three glass compositions [160] are given in Table D.4. These compositions are representative

coefficient	SiO_2	GeO_2:SiO_2 (0.135:0.865)	B_2O_3:SiO_2 (0.133:0.867)
λ_1	0.069066	0.064270	0.061900
λ_2	0.115662	0.129408	0.123662
λ_3	9.900559	9.425478	9.098960
B_1	0.696750	0.711040	0.690618
B_2	0.408218	0.451885	0.401996
B_3	0.890815	0.704048	0.898817

Table D.4: Sellmeier coefficients for representative glass compositions suitable for waveguide fabrication.

of glasses which are common for fiber and integrated waveguide devices. Because of the variability of glass properties between different melts and processing conditions, the coefficients for fused silica (SiO_2) in this table are slightly different than those listed in Table D.2.

The three most important effective waveguide quantities to this thesis are the difference in the phase delays between the TE and TM modes, the difference in the group delays, and the effective group-delay dispersion coefficients. The first quantity leads to a beat length between the modes defined by

$$l_{\mathrm{beat}} = \frac{2\pi}{|\beta^{\mathrm{TE}} - \beta^{\mathrm{TM}}|} = \frac{\lambda_f}{|n_{\mathrm{eff}}^{\mathrm{TE}} - n_{\mathrm{eff}}^{\mathrm{TM}}|}. \tag{D.32}$$

When the propagation distance is much greater than the beat length, then phase-dependent terms in the nonlinear polarization can be neglected as done for the simulations in Chapters 5 and 6, and the phase-dependent linear couplings derived in Appendix C for the slab waveguide geometry can also be neglected.

The second quantity leads to temporal walkoff, defined by

$$\tau_{\text{walkoff}} = \Delta\beta' z, \tag{D.33}$$

where $\Delta\beta' = \beta^{TE'} - \beta^{TM'}$ is the differential group delay coefficient, z is the propagation distance, and the effective TE and TM group delay coefficients are defined by equations C.50 and C.54. When the walkoff time is greater than the temporal duration of interacting pulses, then the interaction distance is limited to the walkoff distance, as defined by equation 1.33. As shown in Chapter 6 though, this birefringent walkoff can be beneficial in order to counteract the temporal walkoff due to the strong Raman down-shift of the pump solitary wave.

The final quantity, group-delay dispersion, is only important for the spatio-temporal studies in Chapter 6. In this case, a negative group-delay dispersion (AGDD) coefficient allows for the formation of a bright solitary wave. The magnitude of this coefficient determines the ratio between transverse width and duration (and spatial width), with small magnitude leading to short duration and large magnitude leading to long duration.

These three quantities for $\lambda = 1.55$ μm are plotted as a function of core thickness in Figures D.5 and D.7 for symmetric waveguides, and in Figures D.6 and D.8 for asymmetric waveguides, with air serving as the upper cladding layer. The waveguide compositions shown consist of SiO_2 core with B_2O_3:SiO_2 cladding, and GeO_2:SiO_2 core with SiO_2 cladding. These figures indicate that the use of asymmetric guides leads to shorter beat lengths and greater differential group delays.

For the spatial soliton logic gates studied in section 5.4, the gate lengths were 2.63 cm, indicating that $l_{\text{beat}} \ll 2.63$ cm. Numerical simulation has shown that the phase-dependent effect of the vectorial four-wave mixing terms is nearly eliminated when the device length is greater than about 5 l_{beat}. Therefore, for the spatial dragging gates, $l_{\text{beat}} < 5$ mm. This criterion is met by the asymmetric waveguide of Figure D.8, for core thicknesses of about 4.5 μm or less.

The spatio-temporal logic gates of section 6.3 have gate lengths of 8 Z_0 = 13.2 cm, so that $l_{\text{beat}} < 25$ mm. This constraint can be met by all waveguide structures except for the first symmetric waveguide with SiO_2 core. There is an additional constraint in the spatio-temporal case, however. As discussed in section 6.3, due to the Raman down-shift, in cascaded operation, group delay birefringence is necessary to equalize the group velocities of the downshifted signal and clean pump in all cascaded stages. This differential group delay is about 2.3 to 2.8 fs/μm, which can only be obtained by the second asymmetric guide of Figure D.8 with core thickness about 2 μm. Note, though, that the first asymmetric guide nearly fulfills this additional requirement as well.

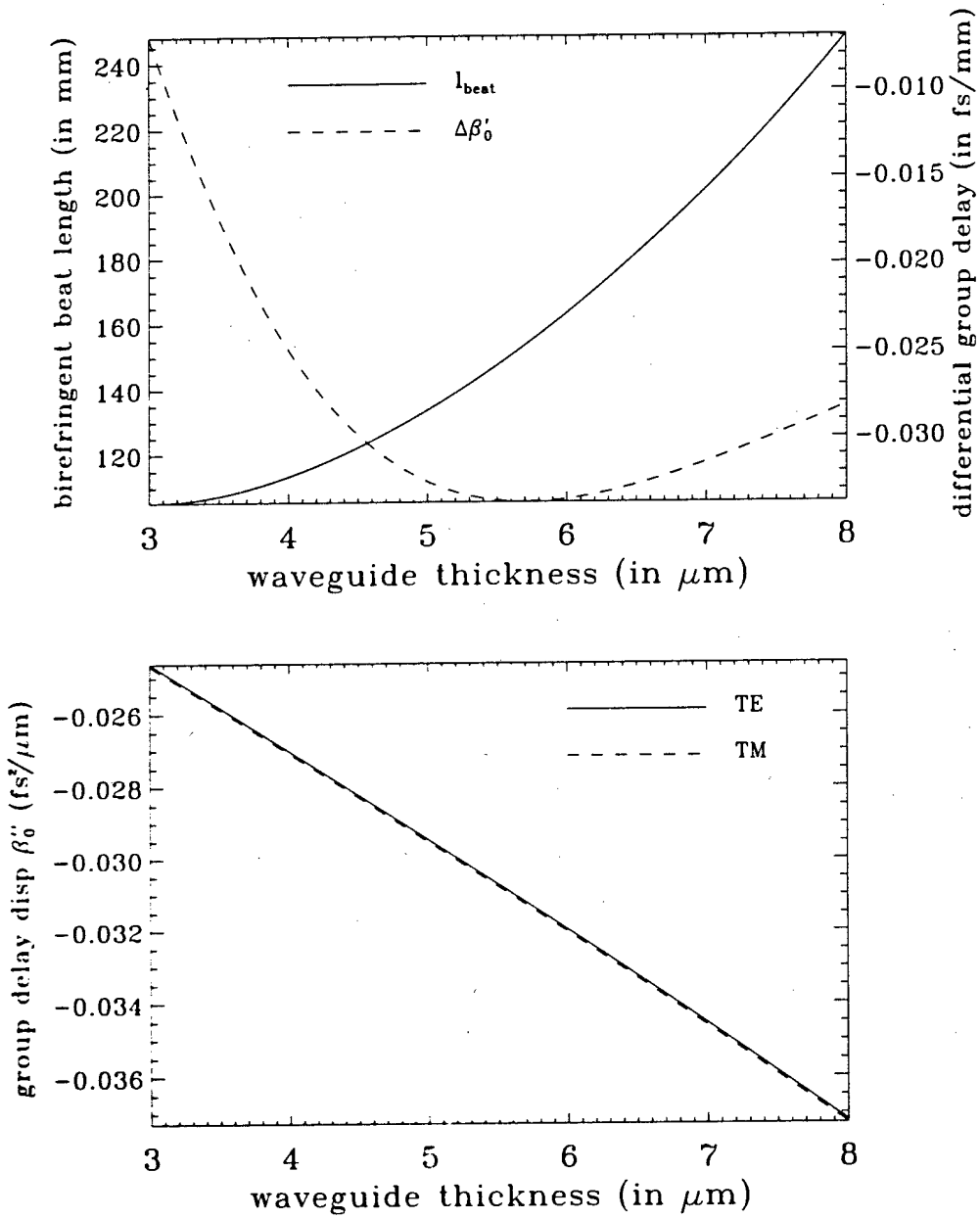

Figure D.5: Linear properties of silica (SiO_2) core, B_2O_3:SiO_2 symmetric clad slab waveguide versus core thickness. All quantities are evaluated at λ_f = 1.55 μm. The birefringent beat length l_{beat} is defined by equation D.32, and the differential group delay $\Delta\beta_0'$ leads to temporal walkoff defined by equation D.33. For comparison, the GDD coefficient for the core material is -0.02745 fs^2/μm, and -0.03865 fs^2/μm for the cladding.

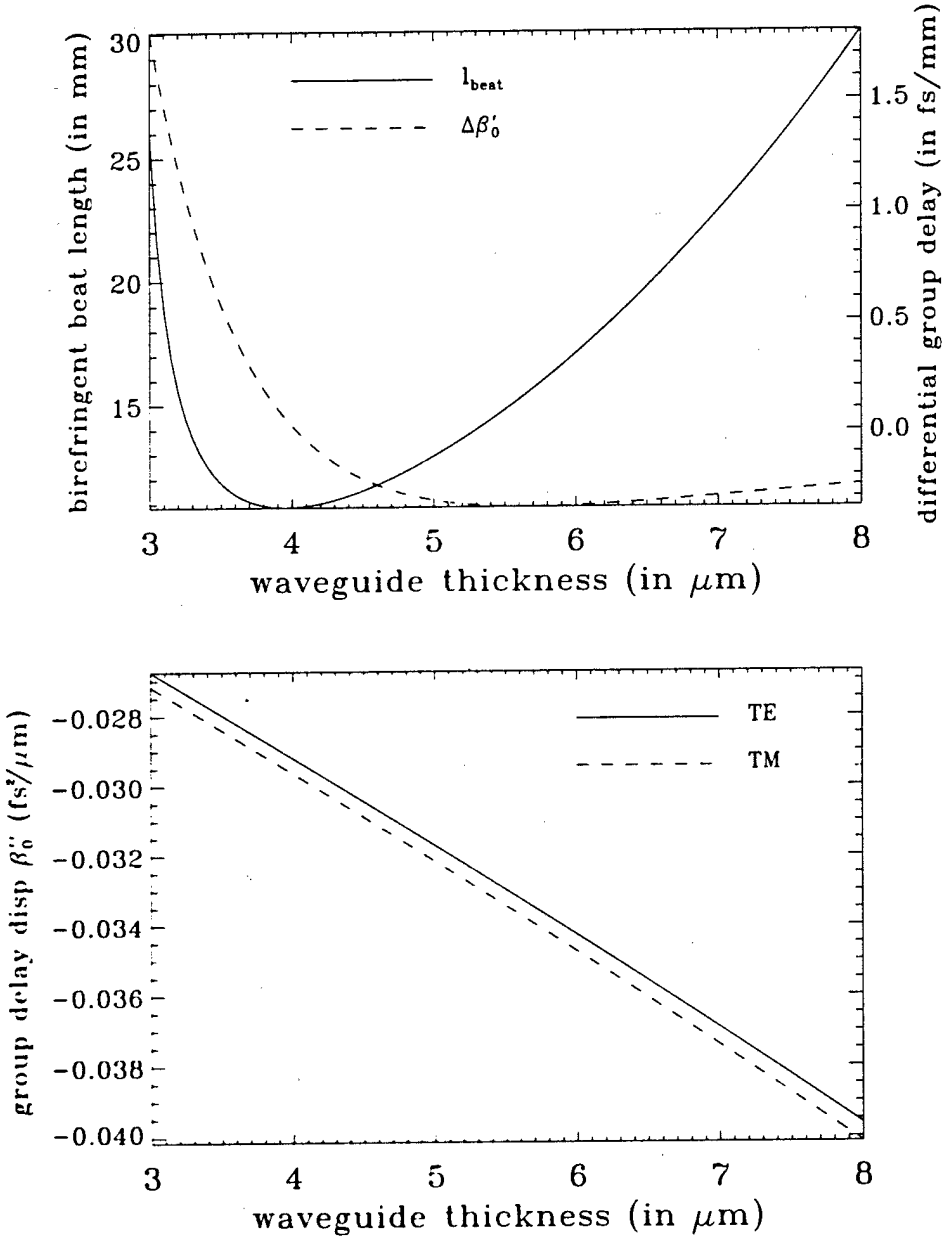

Figure D.6: Linear properties of silica (SiO_2) core, B_2O_3:SiO_2 lower clad and air upper clad slab waveguide versus core thickness. The dispersive properties of air are neglected for simplicity. All quantities are evaluated at λ_f = 1.55 μm. The birefringent beat length l_{beat} is defined by equation D.32, and the differential group delay $\Delta\beta_0'$ leads to temporal walkoff defined by equation D.33. For comparison, the GDD coefficient for the core material is -0.02745 fs^2/μm, and -0.03865 fs^2/μm for the lower cladding.

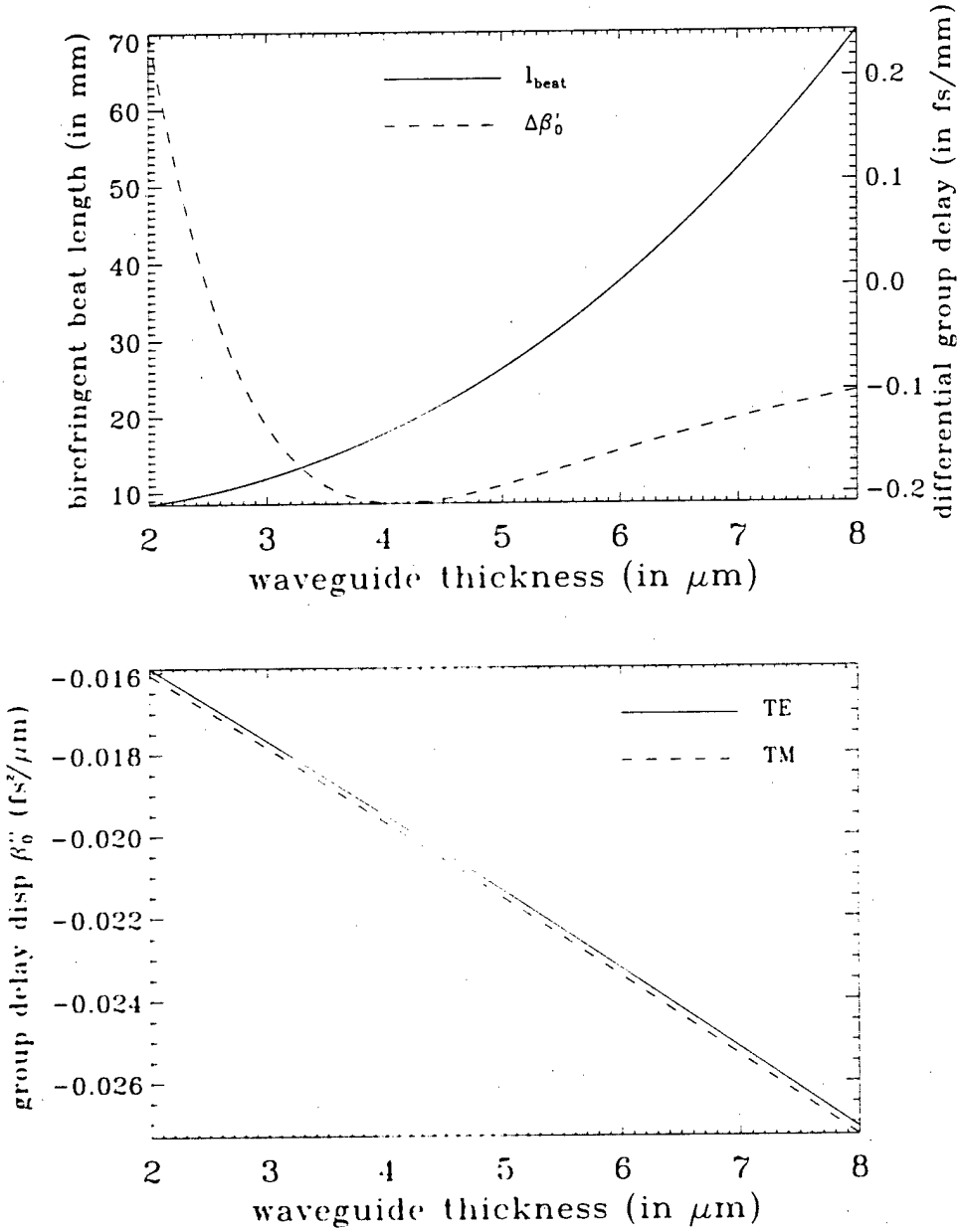

Figure D.7: Linear properties of GeO_2:SiO_2 core, silica (SiO_2) symmetric clad slab waveguide versus core thickness. All quantities are evaluated at λ_f = 1.55 μm. The birefringent beat length l_{beat} is defined by equation D.32, and the differential group delay $\Delta\beta_0'$ leads to temporal walkoff defined by equation D.33. For comparison, the GDD coefficient for the core material is -0.01733 fs^2/μm, and -0.02745 fs^2/μm for the cladding.

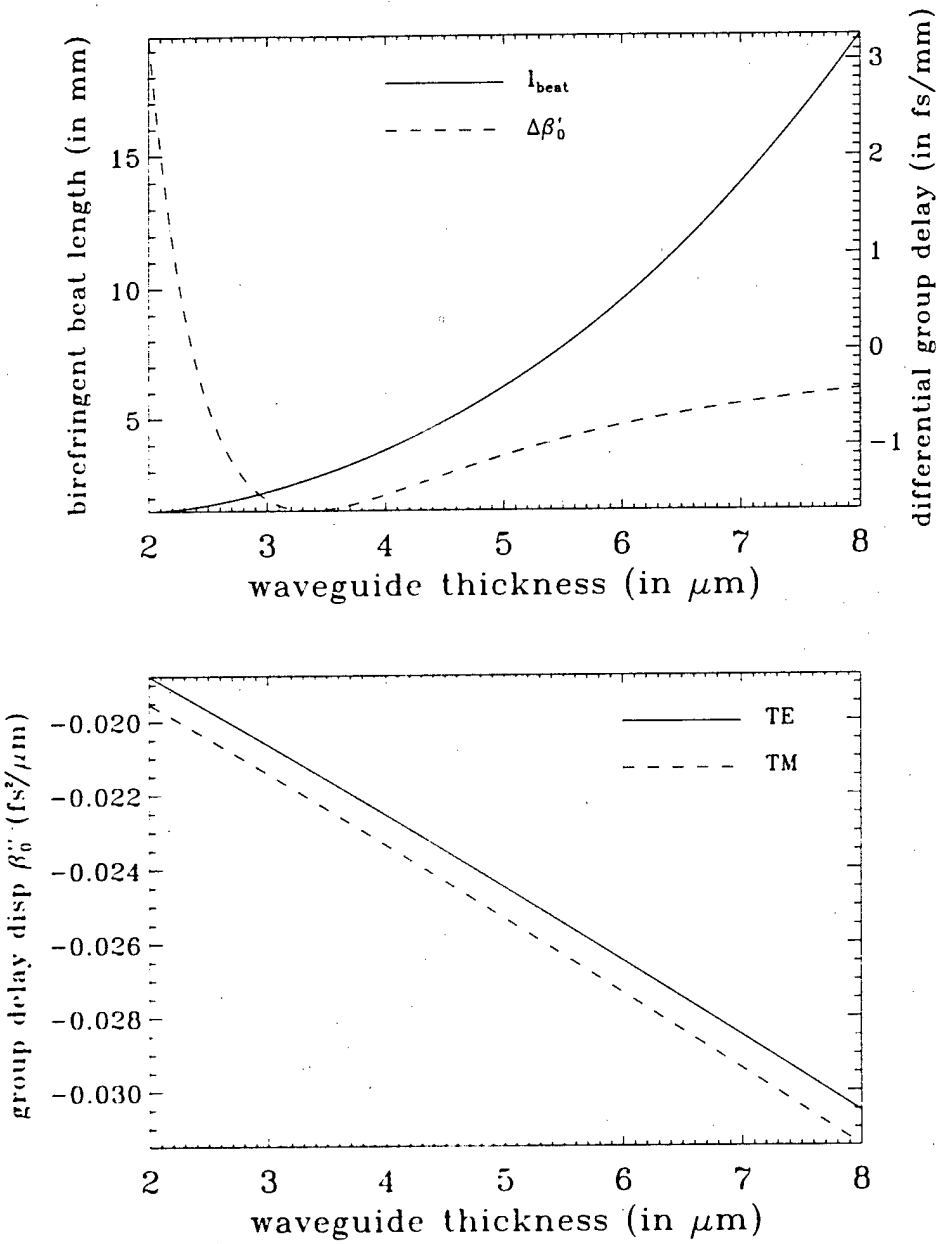

Figure D.8: Linear properties of GeO_2:SiO_2 core, silica (SiO_2) lower clad and air upper clad slab waveguide versus core thickness. The dispersive properties of air are neglected for simplicity. All quantities are evaluated at λ_f = 1.55 μm. The birefringent beat length l_{beat} is defined by equation D.32, and the differential group delay $\Delta\beta_0'$ leads to temporal walkoff defined by equation D.33. For comparison, the GDD coefficient for the core material is -0.01733 fs^2/μm, and -0.02745 fs^2/μm for the lower cladding.